DUBLIN CITY UNIVERSITY

GROWTH OF ZINC OXIDE NANOWIRES FOR FIELD EMISSION APPLICATION

by

ÉANNA MCCARTHY BSC.

A DISSERTATION SUBMITTED IN FULFILMENT OF THE REQUIREMENTS

FOR THE DEGREE OF

DOCTOR OF PHILOSOPHY

Presented to:

DUBLIN CITY UNIVERSITY

Research Supervisor

PROF. JEAN-PAUL MOSNIER

JANUARY 2013

I hereby certify that this material, which I now submit for assessment on the programme of study leading to the award of Doctor of Philosophy is entirely my own work, that I have exercised reasonable care to ensure that the work is original, and does not to the best of my knowledge breach any law of copyright, and has not been taken from the work of others save and to the extent that such work has been cited and acknowledged within the text of my work.

Signed: ______________________ ID No.: 54400232 Date: __________

Acknowledgements

First and foremost I would like to thank my supervisor, Dr. Jean-Paul Mosnier, for his support, guidance, patience, and constant positive attitude in the face of the various problems and surprises encountered. I would also like to thank Dr. Enda McGlynn for all his help and support during the project and the years prior.

I'd like to express my appreciation to the staff at DCU in particular Lisa Peyton and Sheila Boughton, and also to the technicians in the department, in particular Des Lavelle for correcting our confusing blueprints and turning them into a reality, and Pat Wogan for help with all our circuitry problems.

I want to express my gratitude to all my colleagues over the years, Dr. Conor McLoughlin, Dr. Richard O'Haire, Dr. Brendan Dogget, Dr. Satheesh Krishnamurthy, Dr. Mahua Biswas, Dr. Daragh Byrne, Dr. Jack Connolly, and Saikumar Inguva. Very special thanks to Dr. Séamus Garry for his long hard work in supplying me with samples to destroy, as well as support, discussion, ideas, insight and camaraderie through-out the project.

Thanks to my other comrades and cohorts in DCU: the office crew; Colm Fallon, Nicky Walsh, Conor Coyle, Vincent Richardson, Jiang Xi, Mossy Kelly, and Padraig Hough, and those further afield; Ruth Salholm, Catherine Doyle, Joe Cullen, Mairead Hurley, Hoi Ling Lee, Barry Foy, Ciaran Gray, Eoin O'Leary, John Dardis, Caroline Banahan, Paddy Hayden, and Paddy Kavanagh.

Finally I'd like to thank my parents for their constant support, without which none of this would've been possible.

Contents

Abstract

There is much interest in the development of field emitters for a number of applications, such as field emission displays and small x-ray sources. For these applications robust, sharp field emitters, capable of delivering sufficient current densities are needed. This thesis describes the development of an apparatus to test the field emission properties of a variety of samples. This apparatus included a metal electrode to measure current-voltage characteristics, and a phosphor electrode to determine distribution and uniformity of emission. Results are presented from a variety of zinc oxide (ZnO) nanostructures (grown by vapour phase transport, chemical bath, and pulsed laser deposition), and zirconium alloy films. The samples were analysed by a variety of techniques such as scanning electron microscopy and x-ray diffraction, and their field emission properties determined using the field emission apparatus developed. A new treatment for analysing field emission results was developed and applied to the data. The results of these analyses were evaluated in the context of the current literature. The suitability of the aforementioned growth methods for growing ZnO nanostructures for field emission applications was investigated. The effect of inter-rod spacing and aluminium doping on the field emission properties of ZnO nanostructures was also investigated.

List of Tables

List of Figures

List of Abbreviations

CBD - Chemical Bath Deposition

EDX - Energy Dispersive X-ray spectroscopy

FE - Field Emission

FESEM - Field Emission Scanning Electron Microscopy

FN - Fowler-Nordheim

FWHM - Full-Width Half Maximum

NSL - Nano-Sphere Lithography

PLD - Pulsed Laser Deposition

SEM - Scanning Electron Microscopy

UHV - Ultra High Vacuum

VPT - Vapour Phase Transport

XRD - X-Ray Diffraction

Publications

S. Garry, E. McCarthy, J.P. Mosnier, E. McGlynn, Control of ZnO nanowire arrays by nanosphere lithography (NSL) on laser-produced ZnO substrates, Applied Surface Science, 257, 5159-5162 (2011)

E. McCarthy, S. Garry, D. Byrne, E. McGlynn, J.P. Mosnier, Field emission in ordered arrays of ZnO nanowires prepared by nanosphere lithography and extended Fowler-Nordheim analyses, Journal of Applied Physics, 110, 124324 (2011)

M. Novotny, J. Cizek, R. Kuzel, J. Bulir, J. Lancok, J. Connolly, E. McCarthy, S. Krishnamurthy, J.P. Mosnier, W. Anwand, G. Brauer, Journal of Applied Physics D, 45, 225101 (2012)

Conferences

S. Garry, E. McCarthy, C. McLoughlin, S. Krishnamurthy, E. McGlynn, J.P. Mosnier, Growth and Characterisation of ZnO Nanowires for Field Emission Applications. Poster presentation at European Materials Research Society 2009, Strasbourg, France

E. McCarthy, S. Garry, J. Connolly, E. McGlynn, J.P. Mosnier, Optimisation of ZnO nanowires for field emission application. Poster presentation at European Materials Research Society 2010, Strasbourg, France

E. McCarthy, S. Garry, E. McGlynn, J.P. Mosnier, Growth of Zinc Oxide Nanostructures by Pulsed Laser Deposition for Field Emission Application. Poster presentation at Photonics Ireland 2011, Dublin, Ireland

Chapter 1

Introduction

1.1 Current Developments in Field Emission

Field emission is the emission of electrons from the surface of a condensed phase of matter, into another phase, under the action of electrostatic fields. Field emission most frequently takes place from a solid into a vacuum. It is a quantum effect, distinct from other kinds of emission such as Schottky emission, in that electrons quantum tunnel through the potential barrier at the material's surface, rather than overcoming the barrier. [1]

There has been much interest in the development of field emission electron sources, for use in new technologies such as flexible displays [2] or small x-ray sources [3, 4]. For these applications robust, sharp emitters of conductive, low work function materials, such as metals, are required.

Field emission was first reported in 1897 [5], by R.W. Wood, who was attempting to produce intense x-rays. It was first described mathematically by Ralph H. Fowler and Lothar W. Nordheim in 1928 [6]. They developed the Fowler-Nordheim (FN) theory, which still serves as the basis for modern field emission analysis. They determined that the main factors affecting field emission were the work function of the emitter, and the electric field strength. Though emission was initially considered from planar emitters, single sharp metallic tips became the focus of much research [1, 7, 8]. Microelectronics devices composed of 2D-arrays of molybdenum emitting tips were also successfully developed by Spindt *et al* [9]. These emitters are well suited to field emission, as sharper, higher aspect ratio emitters will experience a greater field at the point of emission than planar emitters.

With continuing research into nanomaterials, development of new fabrication methods have led to an increased interest in the use of nanostructures for field emission research [10]. Nanostructures can be grown with various materials in a variety of morphologies, and importantly for field emission, allow for very high aspect ratios.

The wide band gap material zinc oxide has received particular attention for this application, due to its favourable properties.

1.2 Zinc Oxide Properties

In this section, we detail the general properties of zinc oxide, and specifically the key properties which relate to field emission. We include our review of the possible work function values for different configurations of ZnO.

Zinc oxide (ZnO) is a popular material for research in many fields due to its versatility in chemical, physical, or engineering applications. It has potential and current uses in many areas such as electronics [11], optoelectronics [12], and spintronics [13]; and it is a good material for the fabrication of nanostructures, including nanorods and nanowires [14].

Zinc oxide is a II-VI semiconductor [15] with a wide direct band gap [16]. A wide band gap is generally considered to be one larger than three electron volts. The accepted value for zinc oxide's band gap is 3.37 electron volts [17]. This wide direct band gap is one of the properties that make it suitable for optoelectronics, particularly light emitting diodes (LEDs) and laser diodes (LDs).

The band gap energy of 3.37 eV corresponds to a wavelength of 369 nm. This is similar to other wide band gap semiconductors being slightly longer wavelength than gallium nitride or zinc sulphide. 369 nm is just inside the ultra violet (UV) area of the spectrum (known as UVA).

A direct band gap means that the maximum energy state in the valence band and minimum energy state in the conduction band have the same momentum. Thus in a direct band gap semiconductor its possible for an electron to transition between the valence band and the conduction band with little or no momentum change (see Figure 1.1). This is what makes these materials apt for use in optical devices, as photons have a very small amount of momentum; suitable for these kinds of direct band gap transitions, but not indirect transitions, where a large momentum change is required. An electron in the valence band can be promoted to the conduction band by a photon, which is a single body absorption. Two body absorptions (for example a photon and a phonon) are required for similar promotion in an indirect gap semiconductor, as momentmum must be conserved, and these absorptions are rare compared to single body absorptions.

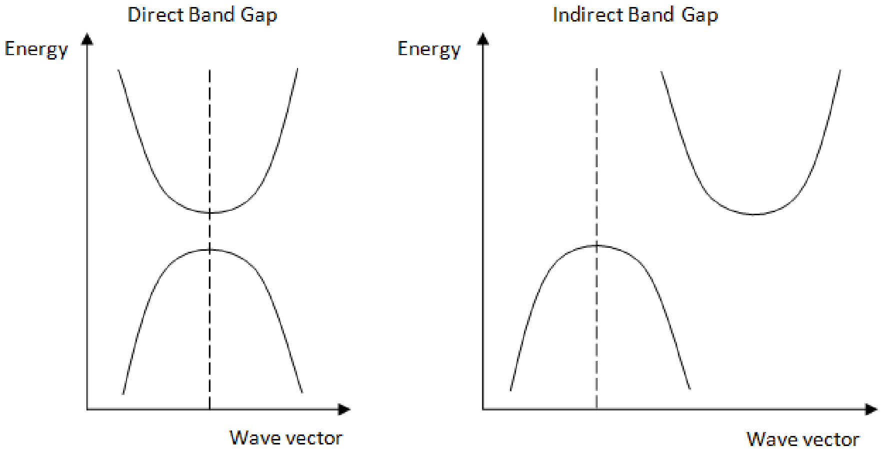

Figure 1.1: Direct and Indirect Bandgaps

The advantages to zinc oxide over similar wide direct band gap semiconductors are its large exciton (a bound electron-hole pair) binding energy of ∼60 meV, its availability in large high quality single crystals, and that it can be grown and processed efficiently using both bottom up and top down techniques. [18]

The exciton binding energy of 60 meV corresponds to an exciton dissociation temperature of ∼464 K, well above room temperature (∼293 K or ∼37 meV). Radiative emission due to exciton recombination has a higher transition probability than emission from an un-bound electron-hole transition. There are other wide band gap semiconductors with potential for UV optical devices, for example gallium nitride and zinc sulphide. However, these have lower exciton binding energies, 21 meV and 39 meV respectively. These correspond to temperatures of ∼162 K and ∼301 K, well below and slightly above room temperature, respectively. This comparatively higher chance of radiative emission at room temperature is one of the reasons for interest in using zinc oxide in LEDs and LDs.

Under normal circumstances (unlike extremely high pressures, or crystal seeding) zinc oxide has a hexagonal wurtzite structure [19] (see Figure 1.2), where each zinc atom is surrounded by four oxygen atoms, and each oxygen atom is surrounded by 4 zinc atoms. The lattice parameters are:

$a = b = 0.32488$ nm

$c = 5.2059$ nm

This forms a hexagonal layered structure, which can be thought of as two hexagonal close packing lattices overlaid on each other (see Figure 1.3). One interesting result of this structure is that when cleaved along the basal planes polar faces (the (0001) and ($000\underline{1}$) planes) - faces which terminate with a single element, either oxygen or zinc can be obtained.

The most useful morphological property of zinc oxide for nanostructure growth is its tendency to align and grow preferentially along the c-axis [17, 21]. This property is one that makes zinc oxide appropriate for epitaxial growth (thin films/buffer layers), and nanostructures. Zinc oxide lends itself well to deposition methods such as Chemical Vapour Deposition (CVD), Pulsed Laser Deposition (PLD), Molecular Beam Epitaxy (MBE) and sputtering [18]. The thin films created by these deposition methods will tend to

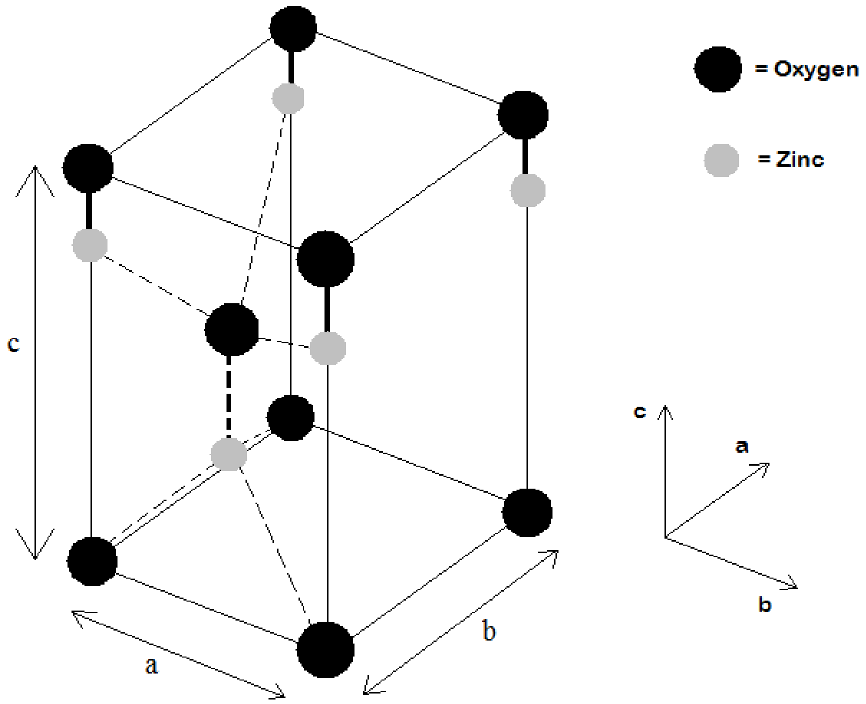

Figure 1.2: Wurtzite Unit Cell

have a natural crystallographic texture due to the tendency to align along the c axis. It is easy to produce thin films that are mosaic crystalline. This means that while they are not perfect single crystals, but rather polycrystalline. However the individual crystallites in the polycrystal are all only slightly misaligned. These thin films are ideal for nanorod growth because the c-axis alignment provides the surface with nucleation points for aligned nanorods to begin growth on [22].

ZnO is also radiation hard, significantly more so than silicon or gallium nitride, making it appropriate for use in space applications such as low-orbit satellites [23].

These properties make zinc oxide an appropriate candidate for fabricating field emitters, in particular its ease of nanostructure growth, providing

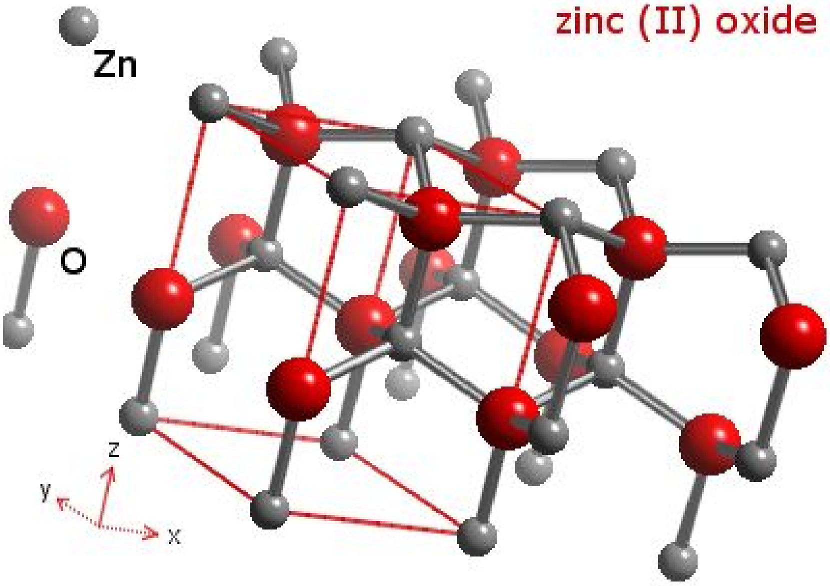

Figure 1.3: Zinc oxide crystal structure [20]

sharp emitters, and it's favourable electronic properties, such as its work function and the ease of n-type doping.

There has been much work on the field emission of zinc oxide emitters, typically disordered assemblies of vertically oriented nanowires [3, 4]. Works generally analyse the field emission characteristics by use of the Fowler-Nordheim theory, and report favourable results [24–28].

The work-function of the emitting material is a key factor in field emission. The work-function value of 5.3 eV is very commonly used by authors working in the ZnO nanowire FE field, obtained by Minami *et al* for magnetron-sputtered ZnO thin films [29]. However there are a wide range of potential values for ZnO structures. We have undertaken a review of these values, and summarise the appropriate values from the literature, along with the electron affinity (χ), and the band bending at the surface (BB), in Table 1.1.

Reference	**ϕ Zn (eV)**	**ϕ O (eV)**	**χ Zn (eV)**	**χ O (eV)**	**BB Zn (eV)**	**BB O (eV)**
Clean [30] annealed surfaces	3.7	6.0	3.7	4.5	-0.2	1.3
Reconstructed, [30] adsorbed	3.3	4.3	3.3	3.9	-0.2	0.15
[31]	3.15	4.85	3.35	5.05	-0.3	
[32]			4.1			
Polycrystalline [33] thin film	5.3	5.3				

Table 1.1: Work function (ϕ), electron affinity (χ), and band bending (BB) for the hexagonal faces of ZnO

Jacobi *et al* have carried out detailed angle-resolved ultraviolet photoelectron spectroscopy (UPS) measurements on clean, annealed ZnO polar (0001) and (000-1) faces[30] and measured the corresponding values of the work function, electron affinity, and band bending. The work function values were found to rapidly change as a function of time due to surface reconstruction, defect creation, and gas adsorption effects and reach asymptotic values of 3.3 eV and 4.3 eV, respectively. These asymptotic values would be more appropriate for most ZnO samples, which have been exposed to ambient conditions for extended periods. Marien [31] has measured the work function of the polar faces of ZnO needles using a combination of FN characteristics and low-field ionization characteristics, independently of any possible field enhancement factors. The Fermi level is placed 0.2 eV below the conduction band minimum in the bulk in these works. A value of 4.1 eV is quoted in Reference [32] for the electron affinity of the (0001) face, based on Schottky contact barrier measurements. Semet *et al* [34] accounted satisfactorily for their experimental observations on $\langle 002 \rangle$ vertically aligned ZnO nanowires if they assume an actual work function of the order of 1 eV due to severe modification of the electronic and structural properties of the emitting surface after prolonged field emission. On the basis of the above review, we believe that work function values of between 3.3 eV and 4.3 eV, rather than 5.3 eV found by Minami *et al*, may be more appropriate values for ZnO polycrystalline material or disordered nanowire assemblies.

1.3 Growth of ZnO Nanostructures for Field Emission

1.3.1 General Principles for ZnO Growth

There are a variety of methods used for the growth of ZnO films and nanostructures, on a variety of substrates. In this section we will give a brief outline of the methods relevant to this work, and their advantages and disadvantages. There are two types of epitaxial growth: homoepitaxy, where a material is grown on a substrate composed of the same material, and heteroepitaxy, where a material is grown on a substrate composed of a different material. For heteroepitaxial growth, the plane presented at the surface of the substrate must have a reasonable match to a plane of zinc oxide. In epitaxial growth, the deposited material will attach to the atomic sites at the substrate surface, causing the material to grow in a given orientation. This type of growth ensures control of the crystal orientation, and good crystal quality, which in the case of nanowire growth will ensure better alignment. However good epitaxial substrates may have other properties that make their use unfavourable, for example sapphire is an insulator, making it inappropriate for field emission samples.

For non-epitaxial substrates, a seed layer is usually deposited. Due to ZnO's tendency to align along the c-axis as discussed in section 1.2, a thin film of ZnO deposited on the substrate surface will present a surface of reasonable crystal quality for epitaxial growth. This two-stage growth is widely used for growing ZnO nanostructures, with various deposition techniques.

The substrate commonly used in this work is phosphorus doped, n-type,

(100) Silicon, a non-epitaxial substrate that has many advantages. Silicon's high melting point makes it compatible with growth methods requiring high temperatures, such as pulsed laser deposition and vapour phase transport. Its electrical conductivity is advantageous for field emission, as it provides a conductive path from any material grown on the surface to the back of the sample. Finally it is readily available and relatively inexpensive. The methods and techniques used in the fabrication of the samples used in this work were vapour phase transport, pulsed laser deposition, chemical bath deposition, and nanosphere lithography, which we detail below.

1.3.2 Vapour Phase Transport

Vapour phase transport (VPT) is a method of zinc oxide nanorod growth. A typical VPT apparatus can be seen in Figure 1.4. In VPT a mixture of zinc oxide powder and carbon, in the form of graphite powder, is heated and evaporated. The resultant zinc vapour is introduced to the surface of a substrate or thin film, where it condenses and oxidises. In the evaporation the zinc oxide and the carbon react to form carbon monoxide and zinc vapour. When this evaporated material meets with the surface it condenses at the nucleation points, the zinc reacting with oxygen in the furnace, condensing into zinc oxide at the nucleation points. These reactions are called carbothermal reduction and are summed up in the chemical equations below [22]:

$$ZnO + C \rightarrow Zn + CO$$
$$\mathrm{Zn} + \tfrac{1}{2}\,\mathrm{O}_2 \rightarrow ZnO$$

Carbothermal reduction reduces the vaporisation temperature, compared to using zinc oxide powder alone, allowing VPT growths to be performed at lower temperatures [35]. With careful control of the parameters, the depositing zinc oxide can form nanostructures, notably nanowires [22], on the substrate. Silicon is a typically used substrate, as discussed in the previous section. As ZnO does not readily nucleate on the surface of a Si substrate, a direct growth of wires on the surface is not possible. Silicon coated with a metal catalyst layer can be used [36, 37], however due to poor lattice matching between Si and ZnO, wires grown tend to be poorly aligned. If a thin film of zinc oxide is deposited on the Si substrate, it can act as a template layer for the nanowires to give better alignment. These template layers are grown on directly [38], or with an Au catalyst coating [39]. The presence of catalysts is undesirable for field emitters, as catalyst grown samples often exhibit pieces of the catalyst material at the tip of the nanowire, where emission occurs [14, 37]. Rods grown by VPT typically present a single crystal hexagonal prism, with typical heights and widths of a few microns and a few hundred nanometres, respectively. An example of ZnO nanowires grown by VPT on a catalyst-free ZnO thin film can be seen in a work by Rajendra Kumar *et al* [22]. A SEM image of the ZnO nanowires shown in the work is reproduced in Figure 1.5.

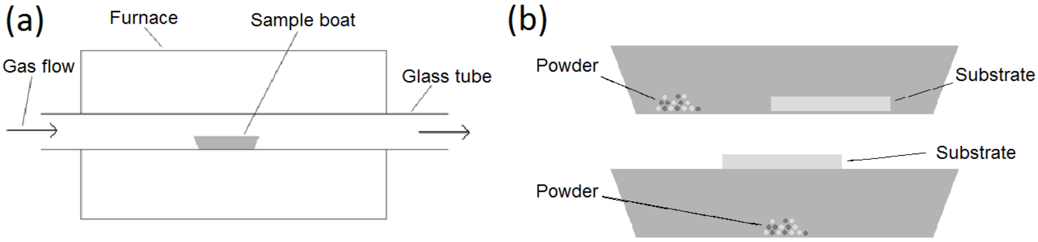

Figure 1.4: (a) A standard Vapour Phase Transport (VPT) growth chamber, (b) arrangement of powders, substrate, and alumina sample boat

The variables in a VPT growth are the temperature, deposition time, flow of gas through the furnace, amounts and composition of powders, the

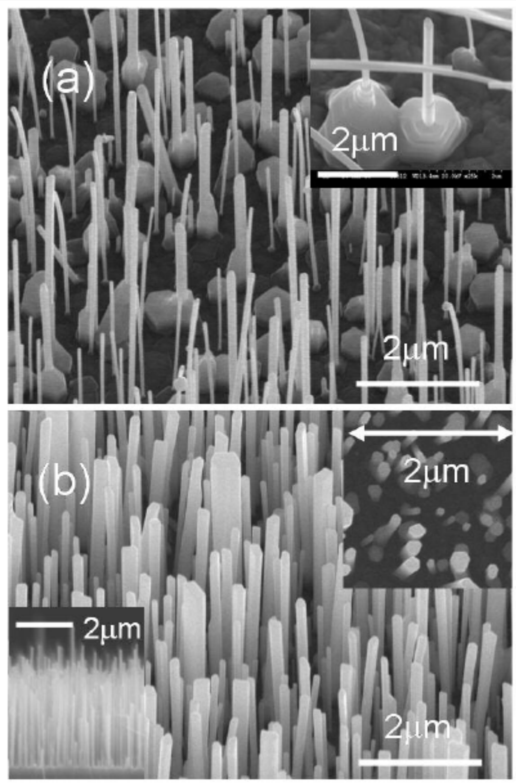

Figure 1.5: SEM image of VPT nanowires, grown with varied parameters by Rajendra Kumar et al [22]

substrate used, and the position of the substrate relative to the powders and flow of gas. Typical temperatures used in VPT zinc oxide nanowires growths range from ∼500-850 °C, and growth times ranging of ten minutes to one hour (not including temperature ramping times). A wide variety of substrates can be used. VPT can be used in combination with lithographic techniques, allowing for the growth of ordered, spaced arrays of nanowires suitable for field emission [39, 40].

1.3.3 Pulsed Laser Deposition

Plasma is a high energy phase of matter, where the matter is highly ionised and exhibits collective behaviour. There are many methods for producing plasmas, including through the use of laser ablation. When a laser irradiates a solid target, light is partially absorbed by the target. If the absorbed energy is high enough and concentrated enough, the bonds in the material will be broken, creating a plasma. Low wavelength lasers, typically UV, are required due to their low penetration depth. The minimum fluence (energy per unit area) required to create a laser induced plasma is known as the ablation threshold. For ZnO the ablation threshold is ~0.44 Jcm^{-2} [41]. The plasma created will expand outwards into the surrounding gas or vacuum; this jet of plasma is referred to as a plume.

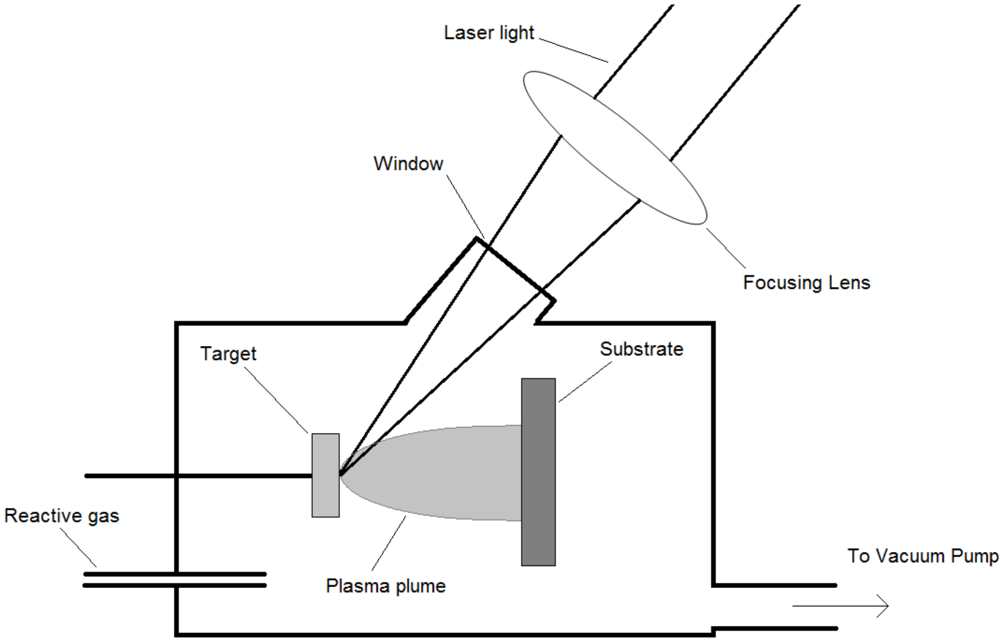

Figure 1.6: A typical PLD apparatus

Pulsed Laser Deposition (PLD) is a material deposition technique. In

PLD a short-pulse, low-wavelength laser is focused on to a target with fluence above the materials ablation threshold, such that a plasma plume is created which will expand in to the vacuum, to impinge upon a substrate and deposit material. An example of a PLD set up can be seen in Figure 1.6. The technique is well established as a method for depositing thin films [42]. The use of increased background pressures during deposition has also been shown as a viable method for the production of nanostructures, such as nanostructured columnar films [43], nanowalls [43] or nanowires [44]. An example of a nanostructured ZnO grown by PLD can be seen in the work by Premkumar *et al* [43]. SEM images presented in the work are shown in Figure 1.7. An example of PLD grown ZnO nanowires from a work by Tien *et al* [44] can be seen in Figure 1.8.

The deposition process can be varied by heating the substrate to different temperatures, changing the fluence incident on the target, the distance between the target and the substrate, and using different mixtures, pressures, or flow rates of background gases. Temperatures typically range from room temperature to ~1000 °C, with typical fluences of between the ablation threshold and ~20 Jcm^{-2}. Background pressures are typically 0.01 - 0.25 mbar for thin films, and 0.5 - 1.5 mbar for nanostructures. The advantages of PLD are that it can produce high quality thin films with thicknesses ranging from nanometres to microns, the possibility of stoichiometric transfer of multi-component materials, and the possibility of producing heterostructures by depositing multilayer thin films of different materials. The disadvantages of PLD are that it is difficult to achieve large scale uniformity of both films and nanostructures, the deposition area is small, and the turnaround time is quite long. PLD is useful in creating field emitters due to the facility to produce nanostructures, and the ease of doping by the use

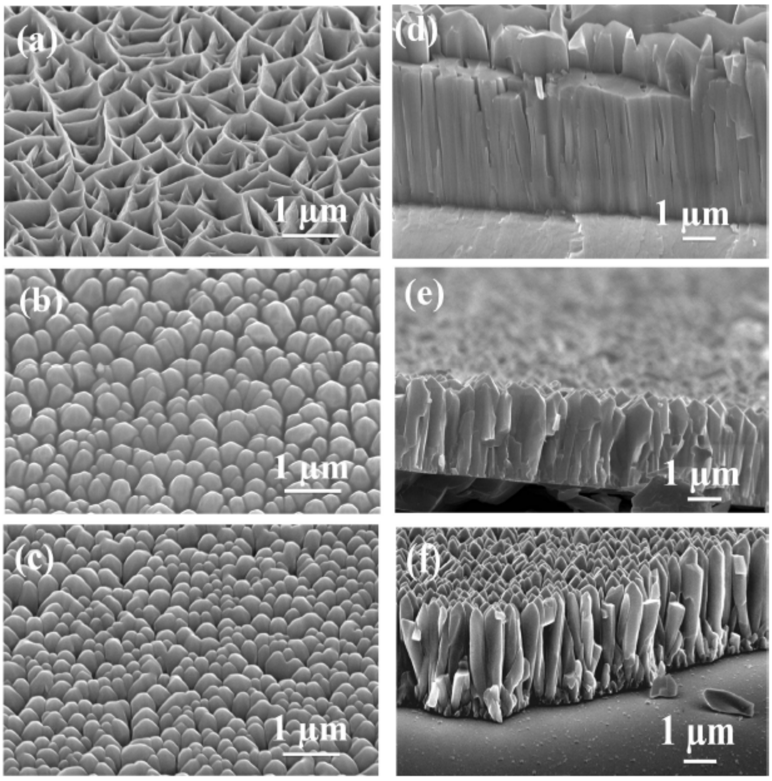

Figure 1.7: SEM image of PLD nanowalls and nanocolumnar film grown on (a,d) GaN, (b,e) Al_2O_3, and (c,f) Si , by Premkumar et al [43]

of doped targets [45].

1.3.4 Chemical Bath Deposition

Chemical Bath Deposition (CBD) is a method of depositing thin films [46] and nanostructures [47], where material is deposited by immersing a substrate in a chemical solution. A CBD apparatus typically consists of just a beaker, and a hotplate to control the solution temperature. The variables in CBD are the composition of the solution, the substrate used, temperature of the solution, and deposition time. Temperatures needed are typically low and a wide array of chemical configurations can be used, allowing for the

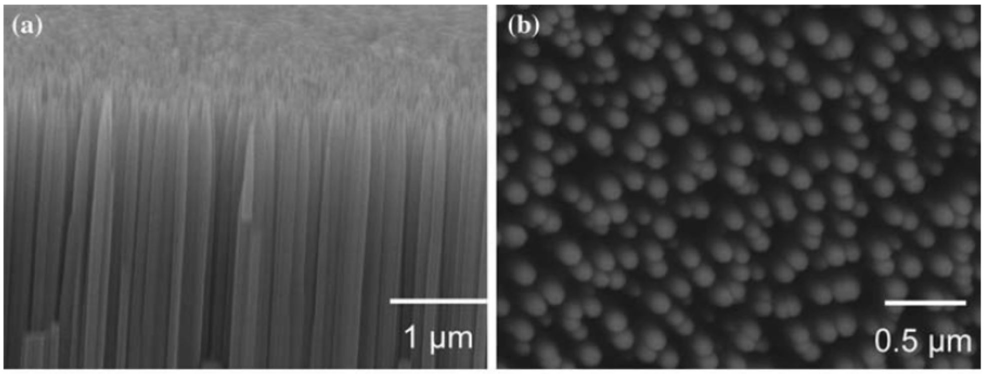

Figure 1.8: SEM image of PLD nanowires, grown by Tien et al [44]

use of substrates that would not be suitable for high temperature growth methods like VPT. Methods for deposition of zinc oxide are typical based around the decomposition of zinc salts, such as zinc acetate, zinc nitrate, zinc sulphate, zinc formate, and zinc chloride, either directly into zinc oxide or into zinc which is then oxidised.

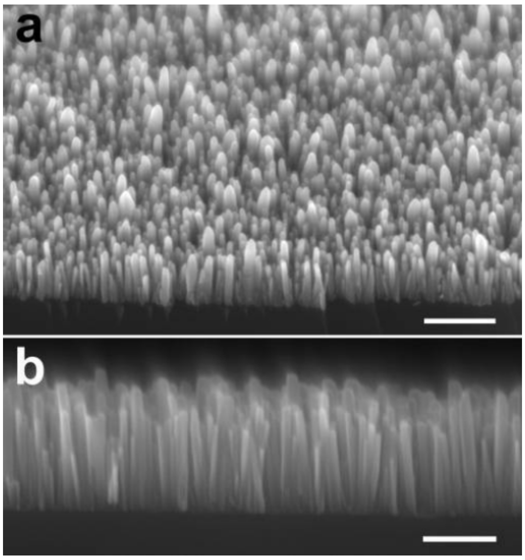

Figure 1.9: SEM image of CBD nanowires, grown by Greene et al [21], with scale bars of 500 nm and 200 nm for (a) and (b), respectively

At typical example of 2-stage seed layer and nanowire CBD deposition is presented in the work by Greene *et al* [21], where substrates were repeatedly drop coated and dried off, with a 0.005 M solution of zinc acetate dihydrate in ethanol, to deposit a layer of zinc acetate crystallites. The substrate was then annealed at 350 °C in air for 20 min, to decompose the zinc acetate into c-axis aligned zinc oxide nanocolloids. Zinc oxide nanowires were grown upon these seed layers by suspending the sample face down in an aqueous solution of 0.025 M zinc nitrate hydrate and 0.025 M diethylenetriamine at 90 °C. A SEM image of the nanowires grown can be seen in Figure 1.9.

The benefits of CBD are that it does not need expensive equipment or high temperatures, compatibility with lithographic techniques, and that it is easily scalable to produce large uniform samples.

1.3.5 Nanosphere Lithography

Nanosphere Lithography (NSL) is a method of creating an ordered, nanoscale pattern on a flat, solid surface. A hexagonally close-packed, self-assembled array of nanospheres (see Figure 1.10) is deposited on to the surface, forming a mask which can be deposited or etched through. Notable methods for depositing these arrays are drop coating [48], spin coating [49], or water transfer [50].

In drop coating, a fixed amount of liquid (e.g.: de-ionised water or a solvent) containing nanospheres in suspension is dropped by a pipette onto the surface of the substrate, and allowed to evaporate, at room temperature or with heating. In spin coating, a suspension of nanospheres in liquid is pipetted onto the surface of the substrate, which is then rotated at high speed in plane with the surface of sample, around the samples centre, to spread the mixture out, casting the liquid off the edges of the sample. In the water transfer method, a suspension of nanospheres in liquid is pipetted on

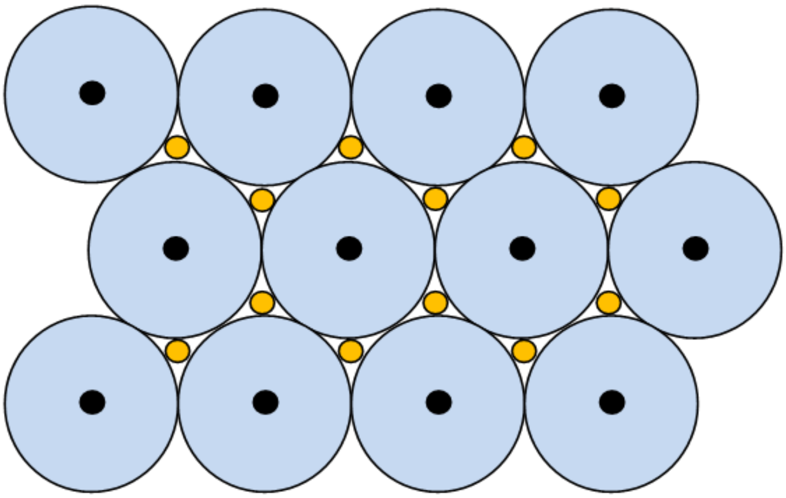

Figure 1.10: Hexagonal close-packed nanosphere monolayer, with black and gold dots marking the two possible patterns

to the surface of a body of de-ionised water. The spheres will float on the surface of the water, even if their density is greater, due to surface tension. The spheres will bunch up with each other, self-assembling into a hexagonal monolayer. The substrate can then be brought up from under the water, picking up the nanosphere array as it through the surface of the water. The substrate is then allowed to dry at room temperature or with heating. An example of a hexagonally close-packed nanosphere monolayer can be seen in Figure 1.11.

Once a nanosphere mask is present on the surface, material can be deposited through it leaving a nano-scale hexagonal array between the spheres. There are two main methods, the first based around the deposition of a catalyst material, such as gold [51], and the second based around the deposition of an inert material such as silica [52]. The first method can be seen in Figure 1.12 (a), where a hexagonally close-packed monolayer of nanospheres is deposited on the surface, and gold is deposited through the nanosphere

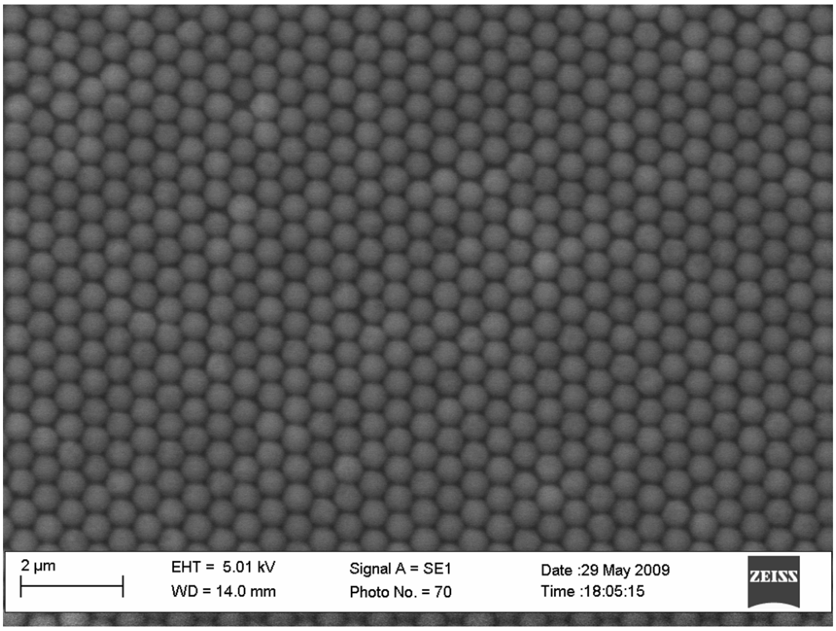

Figure 1.11: SEM image of a hexagonal close-packed nanosphere monolayer

mask. The spheres are removed, leaving a hexagonal array of gold catalyst, in the pattern denoted by the gold dots in Figure 1.10. The sample is then grown on with a method such as VPT or CBD. The zinc oxide will nucleate at the catalyst points, thus preferentially depositing at these points, causing the nanowires to grow in the same hexagonal array.

The second method can be seen in Figure 1.12 (b), where a hexagonally close-packed monolayer of nanospheres is deposited onto a sample. An inert layer of material, such as silica, is deposited through the nanosphere mask, and the spheres then removed. This will leave a silica mask with gaps only at the point of contact between a sphere and the underlying material, in the pattern denoted by the black dots in Figure 1.10. The sample is then grown on with a method such as VPT or CBD, with ZnO nanowires growing at the gaps in the silica mask. Due to the lack of catalyst material, this method requires a sample that can be directly grown on, such as a ZnO

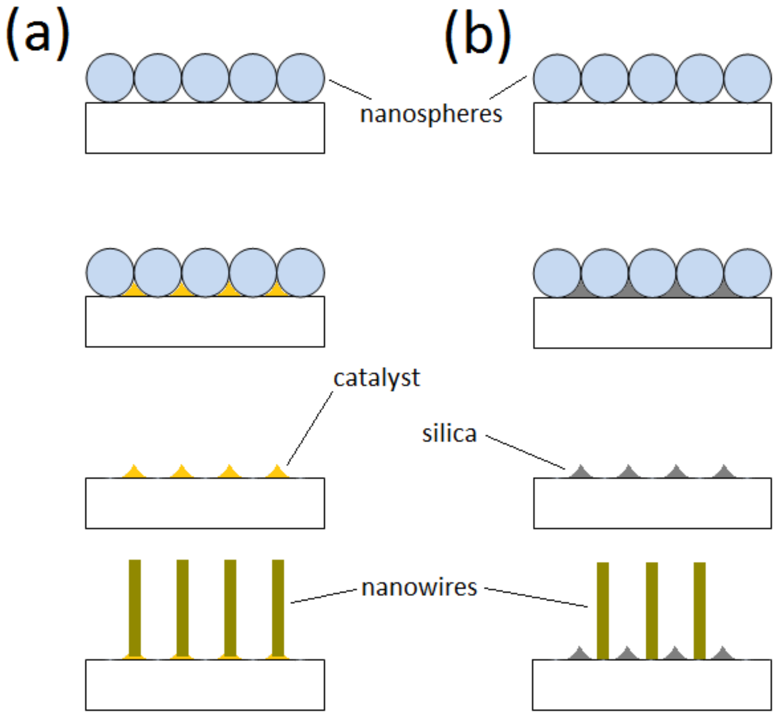

Figure 1.12: Example of two methods of producing ordered nanostructure arrays with NSL; (a) Using a metal catalyst, such as gold, (b) Using a silica mask

thin film. However, catalyst free growth is preferable for field emitters, as discussed previously. This inert method also has the advantage that gaps in the nanosphere layer will be filled with inert silica, and thus cause areas of no growth, whereas the catalyst method will fill gaps with catalyst material, and thus cause areas of heavy growth which may interfere with field emission. An example of a ZnO nanowire array grown using gold catalyst NSL patterning, reproduced from a work by Fan *et al* [53], can be seen in Figure 1.13.

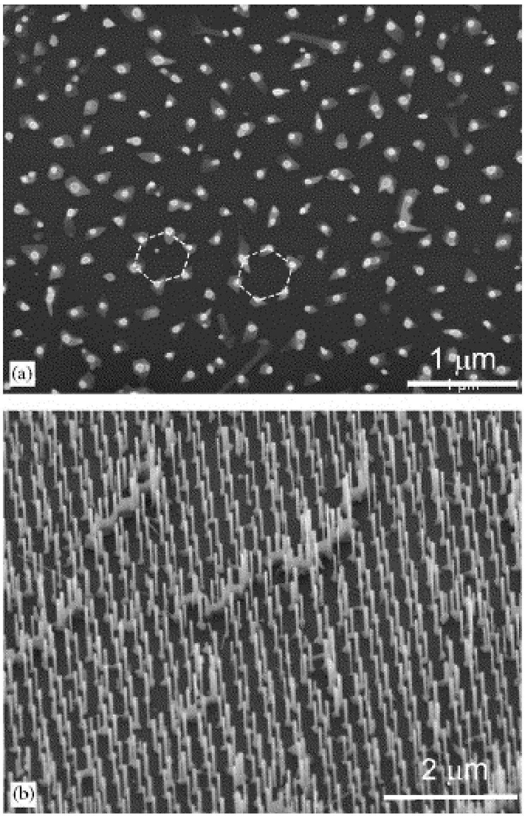

Figure 1.13: SEM image of an NSL ordered ZnO nanowire array made by Fan et al [53]

1.4 Motivation for and Aims of Present Work

As discussed in this chapter, there are a number of applications for reliable, efficient field emitters. The properties of zinc oxide are favourable for field emission. The motivation of this work is the investigation of the suitability of zinc oxide nanostructures for field emission applications. As outlined, the key parameters for field emission are the field enhancement due to the sample morphology and the work function of the material. We develop a new analytical treatment, which combines the general FN theory with new developments in the literature, to interpret experimental data. In Section 3.1 we describe the design and building of an apparatus to investigate the field emission properties of the various zinc oxide nanostructures. In Section 4 we investigate the field emission properties of morphologically varied ordered arrays of zinc oxide nanowires grown by VPT and CBD. In Section 5.1 we investigate the effective of n-type doping on the field emission properties of nanostructured columnar films grown by PLD. The motivation for these experiments is to optimise these two parameters, with a view to maximising the current densities achieved and minimising the voltage required to achieve these current densities.

Chapter 2

Theoretical Background on Electron Emission

2.1 Classical Electron Emission

Electron emission is any process in which electrons within a material escape from the material through the surface. In a metal, electrons are considered as a Fermi gas, able to freely move inside the metal. They are contained within the material's volume by a potential barrier at the surface called the work function. The work function is defined as the amount of energy required to move an electron in the Fermi level of a solid to a point outside the solid. For classical electron emission to occur electrons must be given sufficient energy to exceed the work function (Figure 2.1). In thermionic emission, this energy is provided by heat. In photoemission this energy is provided by incident photons.

The value of the work function is dependent on both the bulk and

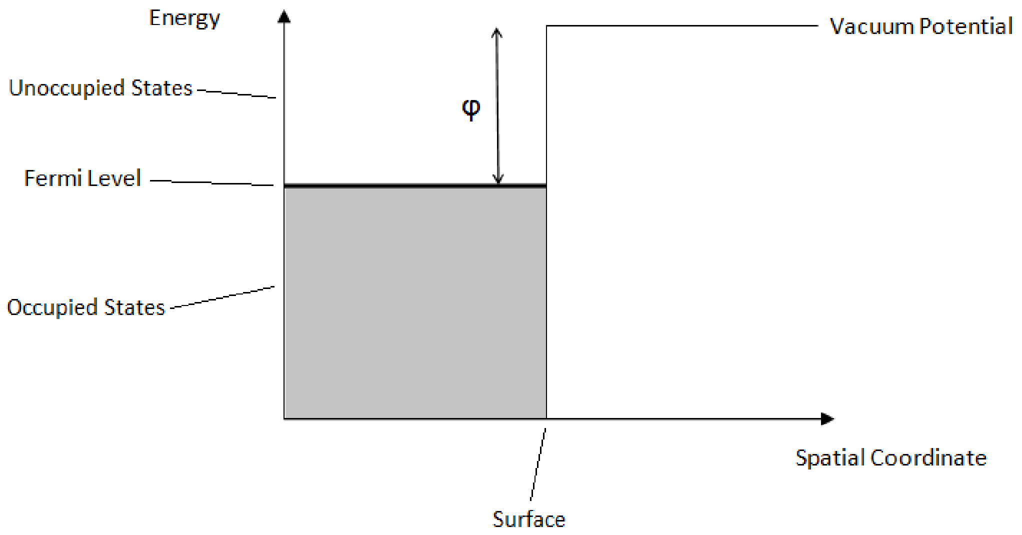

Figure 2.1: Schematic of Electron Energy at the surface of a free electron gas at 0 K, where ϕ is the work function

surface properties of a material, and in crystalline materials may differ for the various crystal planes [54]. A discussion of various work functions for zinc oxide is provided in Section 1.2.

2.1.1 Thermionic Emission

Thermionic emission occurs due to the transfer of energy, greater than the barrier height, from lattice vibrations to the electrons. At 0 K the distribution of electrons is a step function, such that the probability of finding an electron below the Fermi level is unity and the probability of finding an electron above the Fermi level is zero (see Figure 2.1).

$$f(E) = 0 \; when \; E > E_f \tag{2.1}$$

$$f(E) = 1 \; when \; E < E_f \tag{2.2}$$

where E is the energy and E_f is the Fermi level.

At above zero temperatures, electrons can be in energy levels above the Fermi level. The probability of an electron occupying any given energy level is determined by the equation:

$$f(E) = \frac{1}{\exp\left(\frac{E-E_f}{kT}\right)+1} \tag{2.3}$$

where k is Boltzmann's constant and T is the temperature

An equation to derive current density due to thermionic emission was developed by Owen Richardson in 1928 [55]:

$$J = \lambda_r \left[\frac{4\pi m_e k^2 e}{h^3}\right] T^2 \exp\left(\frac{-\Phi}{kT}\right) \tag{2.4}$$

where J is the current density, λ_r is a material dependant correction usually ~0.5, m_e and e are the mass and charge of the electron respectively, h is Planck's constant, and Φ is the work function.

2.1.2 Schottky Emission

Schottky emission is the emission of electrons from a material over the surface barrier, due to lowering of the barrier by an external electric field [56] (see Figure 2.2). In the absence of an electric field the electrons experience a barrier of height equal to the work function (Φ). Under the application of an electric field the barrier will be reduced by $\Delta\Phi$, increasing the rate of electron emission and thus the current density (J). Using the Richardson equation

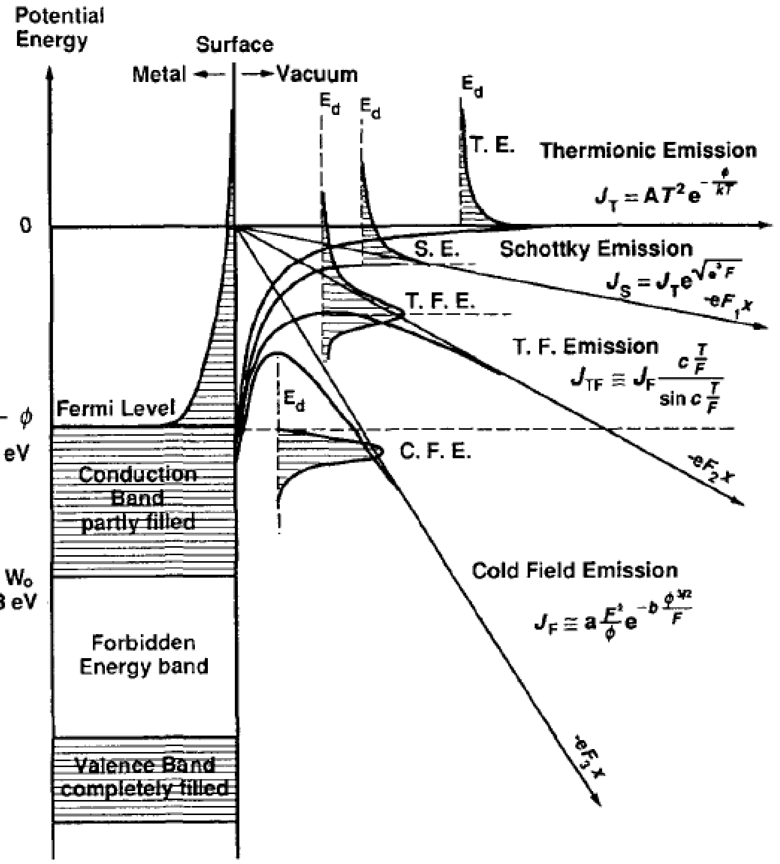

Figure 2.2: Electron Emission Processes, reproduced from a work by Charbonnier et al [8]

(Equation 2.4), modified for the lowered barrier[57], J will be given by:

$$J = \lambda_r \left[\frac{4\pi m_e k^2 e}{h^3}\right] T^2 \exp\left(\frac{-(\Phi - \Delta\Phi)}{kT}\right) \tag{2.5}$$

where $\Delta\Phi$ is given by:

$$\Delta\Phi = \left(\frac{e^3 F}{4\pi\epsilon_0}\right)^{\frac{1}{2}} \tag{2.6}$$

where F is the electric field strength, and ϵ_0 is the permittivity of free space.

The above equation is valid for field strengths lower than $\sim 10^8$ V/m [57]. For higher field strengths the equation becomes inaccurate due to quantum effects, specifically the contribution of Fowler-Nordheim tunnelling through the barrier.

2.2 Field Emission

In field emission, electrons do not gain enough energy to exceed the work function; the electrons are instead emitted by tunnelling through the potential barrier at the materials surface. The barrier is deformed by an applied electric field into a triangular shape, to the point that electrons can tunnel through the barrier (Figure 2.3). The barrier at the surface is not a sharp step function, due to the image force, as can be seen in Figure 2.3. Electrons at the surface of a solid can move a small distance outside the material. This leaves a positive image charge in the material, attracting the electron back to the material. This image potential is given by $-e^2/16\pi\epsilon_0 x$ [58]. Field emission was first reported in 1897 [5], by R.W. Wood, who was attempting to produce intense x-rays.

Field emission was first described theoretically by Ralph H. Fowler and Lothar W. Nordheim in 1928 [6]. They developed the Fowler-Nordheim theory, which still serves as the basis for modern field emission analysis.

2.2.1 Fowler Nordheim Theory

The Fowler-Nordheim model, which describes field electron emission from metals into vacuum under high electric field, is based on four assumptions:

1. the temperature of the metal is 0 K
2. the electrons in the metal follow the free-electron approximation
3. the surface is smooth and planar
4. the potential barrier near the surface (on the vacuum side) consists of the image force and the applied electric field (see Figure 2.3).

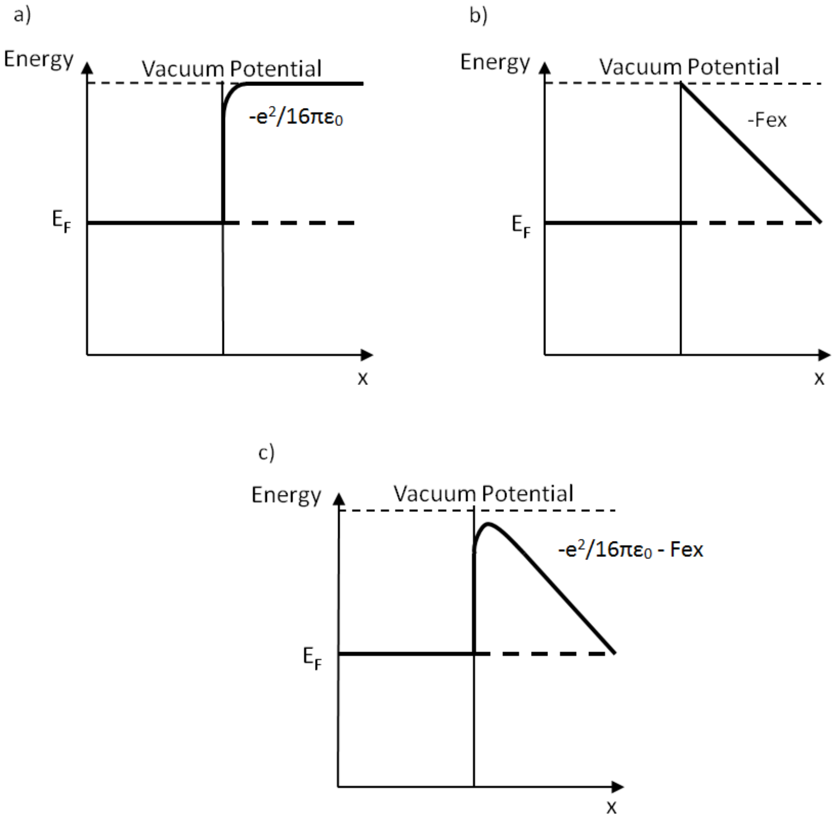

Figure 2.3: Bending of potential barrier, a) Image potential effect, b) External electric field, c) Sum of both effects, where e *is the charge of the electron,* x *is position and* F *is the field strength*

The effect of the image force was not accounted for in the original work by Fowler and Nordheim [6]. The theory was later modified by Nordheim to correct for the image force [59]. As stated previously, the image force is the force on the electron due to the positive image charge in the surface (see Figure 2.4). The force (F) is given by Coulombs law:

$$F = \frac{1}{4\pi\epsilon_0}\left(\frac{(q_1)(q_2)}{r^2}\right) \tag{2.7}$$

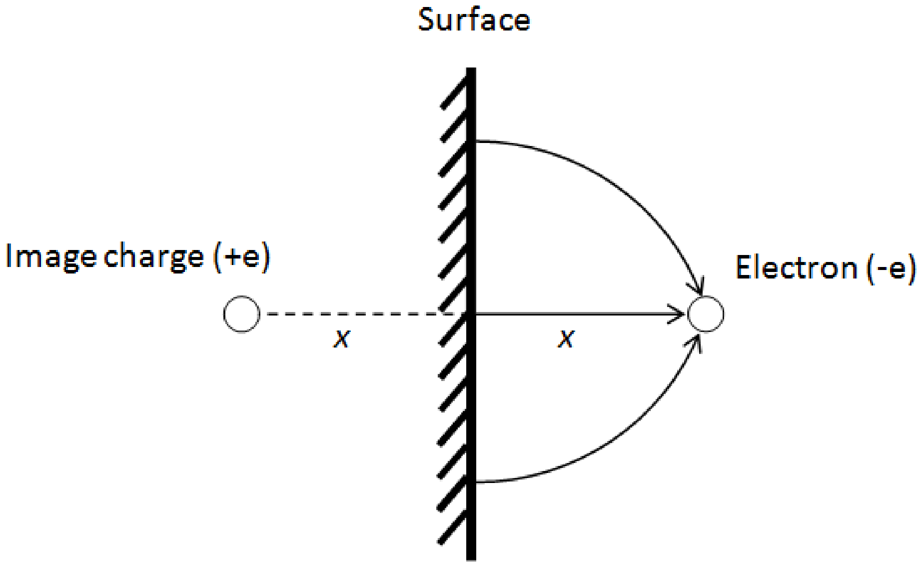

Figure 2.4: An electron outside the surface and its corresponding image charge, both a distance of x from the surface

where q_1 and q_2 are the charges and r is the distance between them. Solving for the situation shown in Figure 2.4, where $q_1 = +e$, $q_2 = -e$ and $r = 2x$, we get:

$$F(x) = \frac{1}{4\pi\epsilon_0}\left(\frac{-e^2}{4x^2}\right) \tag{2.8}$$

The electrostatic force ($F(x)$) is related to the electric potential ($V(x)$) by:

$$V(x) = -\int_{-\infty}^{\infty} F(x)dx \tag{2.9}$$

Thus the image potential will be given by:

$$V(x) = \frac{1}{4\pi\epsilon_0}\left(\frac{-e^2}{4x}\right) \tag{2.10}$$

Thus, combining the image potential with the applied field, the potential near the surface on the vacuum side ($x > 0$), will be:

$$V(x) = -\frac{e^2}{16\pi\epsilon_0 x} - Fex \tag{2.11}$$

where F is the electric field strength. We have plotted this potential for a number of field strengths, as presented in Figure 2.5. These plots show the effect of increasing field strength on the barrier, making it into a triangular shape. The range of the significance of the image force is clearly very close to the surface.

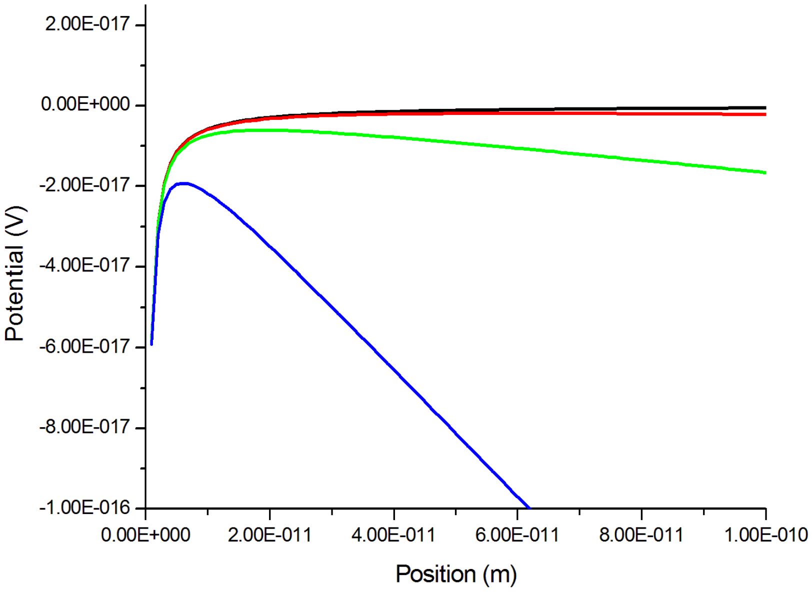

Figure 2.5: Potential barrier at the surface with no electric field (black), with 10^{11} Vm^{-1} (red), with 10^{12} Vm^{-1} (green), and 10^{13} Vm^{-1} (blue)

The following derivation is presented in cgs units, as these were the units used in the original, and much of the subsequent work. The final equations are converted for SI units, and SI units are used here in all the analyses. The energy of an electron under the surface energy potential $V(x)$ is given by:

$$U = \frac{P_x^2}{2m_e} + \frac{P_y^2}{2m_e} + \frac{P_z^2}{2m_e} + V(x) \tag{2.12}$$

where P_x, P_y, and P_z are the momentum in the x, y and z directions, and m_e is the mass of the electron. The x-component of this energy is given by:

$$U_x = \frac{P_x^2}{2m_e} + V(x) \tag{2.13}$$

It is assumed that only the x-component, U_x, affects the probability of an electron penetrating the barrier. A supply function $N(U_x)dU_x$ is defined as the number of electrons incident on the surface within the range U_x to $U_x + dU_x$ per unit area and time. The barrier penetration probability is defined as $D(U_x)$. The product of these two functions gives the number of electrons in the range U_x to $U_x + dU_x$ tunnelling from the metal into the vacuum per unit area and time:

$$P(U_x) = N(U_x)D(U_x)dU_x \tag{2.14}$$

and the current per unit area, or current density, is given by:

$$J = e\int_{-\infty}^{\infty} P(U_x)dU_x \tag{2.15}$$

The supply function is derived from the Fermi-Dirac energy distribution [6]:

$$N(U_x)dU_x = \frac{4\pi m_e kT}{h^3} \ln(1 + \exp\left[-\frac{U_x - \Phi}{kT}\right])dU_x \tag{2.16}$$

where h is Plancks constant.

The barrier penetration probability is calculated with a WKB approximation [60], using $V(x)$ from Equation (2.11) for the potential energy:

$$D(U_x) = exp\left[-c + \frac{U_x - \Phi}{d}\right] \tag{2.17}$$

where

$$c = \frac{4(2m_e\Phi^3)^{\frac{1}{2}}}{3\hbar eE} f(y) \tag{2.18}$$

$$d = \frac{\hbar eE}{2(2m_e\Phi)^{\frac{1}{2}} t(y)} \tag{2.19}$$

$$t(y) = f(y) - \frac{1}{2} y \left[\frac{df(y)}{dy}\right] \tag{2.20}$$

$$f(y) = 2^{\frac{1}{2}}[1 + (1 - y^2)^{\frac{1}{2}}]^{\frac{1}{2}}[E(k^2) - (1 - (1 - y^2)^{\frac{1}{2}})K(k^2)] \tag{2.21}$$

$$k^2 = \frac{2(1 - y^2)^{\frac{1}{2}}}{1 + (1 - y^2)^{\frac{1}{2}}} \tag{2.22}$$

$$y = \frac{(e^3 E)^{\frac{1}{2}}}{\Phi} \tag{2.23}$$

$K(k^2)$ and $E(k^2)$ are the complete elliptical integrals of the first and second kinds [61], given by:

$$K(k^2) = \int_0^{\pi/2} \frac{d\theta}{(1 - k^2 \sin^2 \theta)^{\frac{1}{2}}} \tag{2.24}$$

$$E(k^2) = \int_0^{\pi/2} (1 - k^2 \sin^2 \theta)^{\frac{1}{2}} \tag{2.25}$$

The Schottky barrier lowering parameter (y), sometimes referred to as the Nordheim parameter, describes the lowering of the barrier due to the electric field. Taking the barrier height as equal to the work function (Φ), $y = 0$ will correspond to a barrier height of Φ, and $y = 1$ will correspond to a barrier height of 0, relative to the Fermi level. The functions $f(y)$ and $t(y)$ are factors that correct for the effect of the image force. We have plotted the Schottky lowering parameter, y, and the barrier transmission probability, D, as a function of the electric field strength, for a work function value of 3.7 eV, which is presented in Figure 2.6.

Substituting from Equation (2.16) and Equation (2.17) into Equation (2.14) gives

$$P(U_x)dU_x = \frac{4\pi m_e(\Phi - U_x)}{h^3} \exp\left[-c + \frac{U_x - \Phi}{d}\right] dU_x \tag{2.26}$$

This can be inserted into Equation (2.15), giving

$$J = e \int_{-\infty}^{\infty} \frac{4\pi m_e(\Phi - U_x)}{h^3} \exp\left[-c + \frac{U_x - \Phi}{d}\right] dU_x \tag{2.27}$$

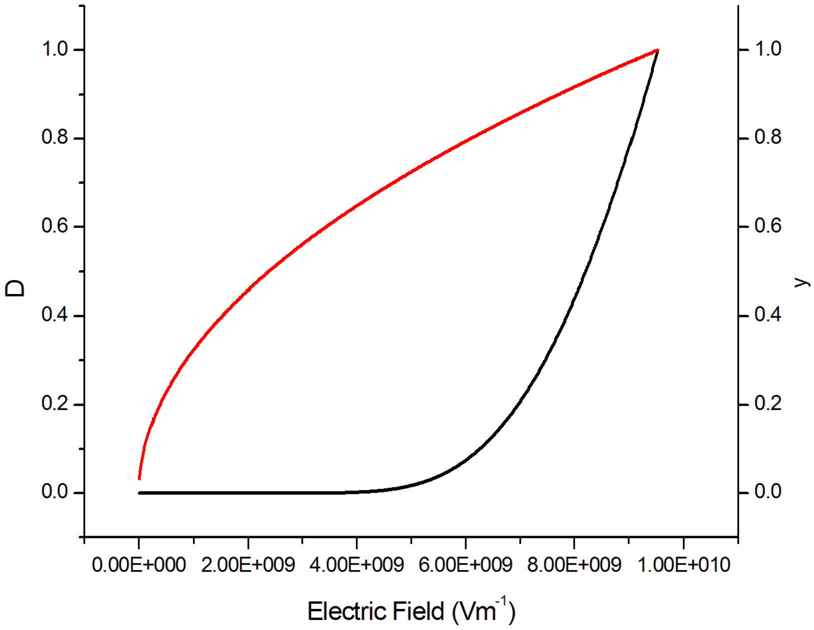

Figure 2.6: The Schottky lowering parameter (y) in red and the barrier transmission probability (D) in black vs. voltage

and integrating over all U_x gives

$$J = \frac{e^3 E^2}{8\pi h \Phi (t(y))^2} \exp\left[-\frac{4(2m_e)^{\frac{1}{2}}\Phi^{\frac{1}{2}}}{3\hbar e E} f(y)\right] \tag{2.28}$$

Finally, converting the equation for SI units, expressing J in Am^{-2}, E in Vm^{-1}, and Φ in eV, and applying the relevant constants, a final equation is obtained:

$$J = 1.54 \times 10^{-6} \frac{E^2}{\Phi(t(y))^2} \exp\left[-6.834 \times 10^9 \frac{\Phi^{\frac{3}{2}}}{E} f(y)\right] \tag{2.29}$$

The Schottky lowering parameter, y, must also be converted to SI units, and is then given by:

$$y = 3.79 \times 10^{-5} \frac{(E)^{\frac{1}{2}}}{\Phi} \tag{2.30}$$

In an experiment, the field emission is characterised by measuring the current, I, as a function of the potential difference, V, between the emitter/cathode and a flat anode, separated by a distance, d. The current and potential difference are related to J and V by:

$$J = \frac{I}{A} \tag{2.31}$$

$$E = \beta V \tag{2.32}$$

where A is the emitting area in m^2, and β is a geometrical factor relating the potential difference to the local field at the emitter surface, expressed in m^{-1}. For a planar emitter and flat anode, the electric field is given by:

$$E = \frac{V}{d} \tag{2.33}$$

Thus β is equal to $1/d$ for a planar emitter. A sharp emitter with a high aspect ratio will experience a greater field than that of a planar emitter, at the same potential difference and separation. In some works a factor, γ, called the field enhancement factor that relates the macroscopic applied field, F_M, to the field at the emitter surface, F_S, is used, such that:

$$F_S = \gamma F_M \tag{2.34}$$

From this we can relate β and γ by:

$$\gamma = \beta d \tag{2.35}$$

Expressing Equation (2.29) in terms of I and V gives us:

$$I = 1.54 \times 10^{-6} \frac{\beta^2 V^2 A}{\Phi(t(y))^2} \exp\left[-6.834 \times 10^9 \frac{\Phi^{\frac{3}{2}}}{\beta V} f(y)\right] \tag{2.36}$$

The current-voltage data taken in a typical field emission experiment is analysed by plotting $\ln(I/V^2)$ vs $1/V$. This plot is called a Fowler-Nordheim plot, and should be linear where field emission is the dominant emission process. The slope (m) is given by:

$$m = -6.834 \times 10^9 \frac{\Phi^{\frac{3}{2}}}{\beta} s(y) \tag{2.37}$$

where

$$s(y) = f(y) - \frac{y}{2}\left(\frac{df(y)}{dy}\right) \tag{2.38}$$

In a work by Charbonnier and Martin [62], they detail an approximation for the current density. In this work a $\log_{10}$ plot is used for the Fowler-Nordheim plot. In this the slope is given by:

$$m = -6.834 \times 10^9 \frac{\Phi^{\frac{3}{2}}}{2.3\beta} s(y) \tag{2.39}$$

By assuming $f(y)$ = 0.956 - 1.062y^2, $t(y)$ = 1.044, and $s(y)$ = 0.956, and substituting Equation (2.23) for y, and Equation (2.39) for β, the current density can be expressed in terms of m, V and Φ [62]:

$$J = 1.14 \times 10^{13} G(\Phi) \frac{\exp(-2.3\frac{m}{V})}{(\frac{m}{V})^2} \tag{2.40}$$

where

$$G(\Phi) = \Phi^2 \exp\left(\frac{10.4}{\Phi^{\frac{1}{2}}}\right) \tag{2.41}$$

which is roughly constant.

In Charbonnier and Martin's paper [62] where Equation (2.40) was first derived, $G(\Phi)$ was taken as ~2700, departing less than 7% for work functions greater or equal to 4 eV. This was re-evaluated in a paper by Spindt *et al* [9], who determined ~2250 to be a more appropriate value, being accurate within 10% for work functions between 3.4 eV and 11.6 eV. This is a low enough deviation to ensure sufficently accurate estimates of the current density using Equation (2.40), and thus the emitting area using Equation (2.31).

The image force correction functions based on the Schottky lowering parameter, $f(y)$, $t(y)$ & $s(y)$, can be calculated from Equation (2.20), (2.21), (2.22), (2.23), & (2.38). Calculation of these parameters is non-trivial, due to the elliptic integrals, E and K. Frequently, their values are assumed or very roughly approximated to simplify the analysis, as in Charbonnier's method [62] detailed above. In reference [7], Van Oostrom generates a table of values for these functions for different current densities and work functions, such that this table can be consulted to give a close value, without the need for calculation. Modern advances have made these calculations easier. The elliptic integrals can be solved using a MATLAB function ($[K, E] = ellipke(M)$). They can also be expressed as arithmetic series:

$$K(m) = \frac{1}{2}\pi\left[1 + \left(\frac{1}{2}\right)^2 m + \left(\frac{1}{2}\times\frac{3}{4}\right)^2 m^2 + \left(\frac{1}{2}\times\frac{3}{4}\times\frac{5}{6}\right)^2 m^3 + ...\right] \tag{2.42}$$

$$E(m) = \frac{1}{2}\pi\left[1 - \left(\frac{1}{2}\right)^2 m - \left(\frac{1}{2}\times\frac{3}{4}\right)^2 \frac{m^2}{3} - \left(\frac{1}{2}\times\frac{3}{4}\times\frac{5}{6}\right)^2 \frac{m^3}{5} - ...\right] \tag{2.43}$$

Forbes has found analytical expressions for the Schottky lowering parameter functions [63]. The following approximations are given for $f(y)$, $t(y)$ and $s(y)$:

$$f(y) = 1 - y^2 + \left(\frac{1}{3}\right) y^2 \ln(y) \tag{2.44}$$

$$t(y) = 1 + \left(\frac{1}{9}\right)\left[y^2 - y^2 \ln(y)\right] \tag{2.45}$$

$$s(y) = 1 - \left(\frac{1}{6}\right) y^2 \tag{2.46}$$

The approximation for $f(y)$ is accurate to within 0.33% over $0 \leq y \leq 1$. The approximations for $t(y)$ and $s(y)$ are accurate to within 0.4% over $0 \leq y \leq 1$. In Figure 2.7 we preset our calculation of $f(y)$ as a function of y by a number of methods, which illustrates the accuracy of these approximations compared to the use of MATLAB, or a simpler approximation from the literature. These approximations allow for convenient and accurate calculation of each of these functions for any given y value. However these approximations have yet to see practical use in the literature.

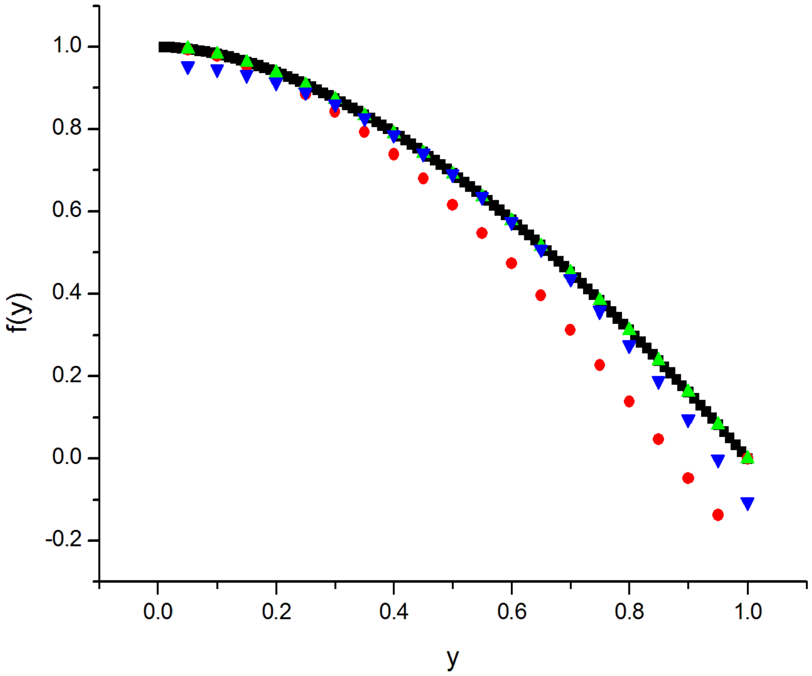

Figure 2.7: Plot of y vs. f(y) for calculated using the Forbes approximations (black), MATLAB functions (red), the arithemetic series (green), and the approximation used by Charbonnier [62] (blue)

The effect of the image force can be illustrated by plotting the current density as a function of electric field strength at the emission point both with, using these approximations, and without the image force correction, presented in Figure 2.8. We can also plot universal plots of current density as a function of electric field strength, for any given work function value. A number of these plots are presented in Figure 2.9. We now detail our method of combining these approximations with the FN equation in order to generate values for β, J and A which take full account of these functions at each data point.

If one fixes the value of the work function, then β can be evaluated using successive approximations based on the above equations. Calculation of the β factor is dependant on the function $s(y)$. The slope taken from an FN plot of

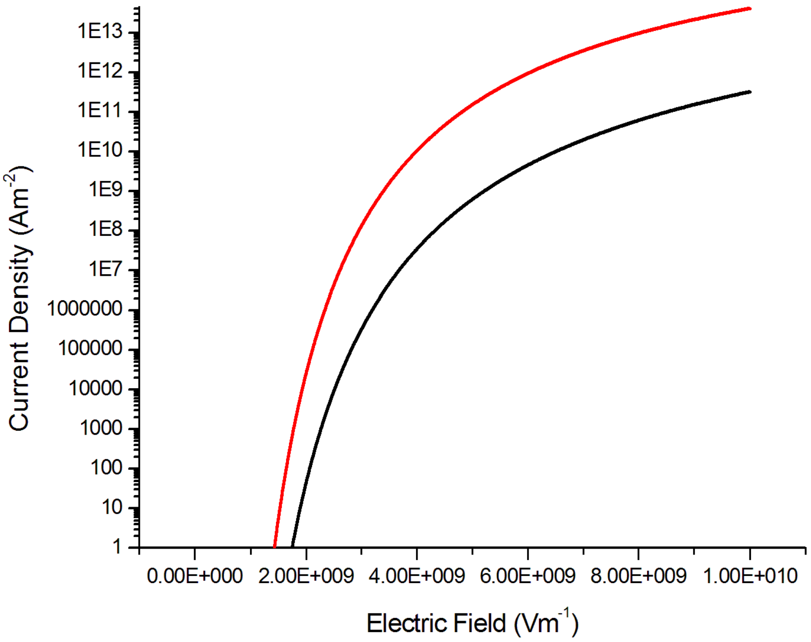

Figure 2.8: Plots of the FN current density vs. the electric field at the point of emission, without image force correction (black) and with image force correction (red) for a work function of 3.7 eV

experimental data can be used to calculate β using Equation (2.37), assuming $s(y) = 1$. With a value for β, y can be calculated using Equation (2.30), which in turn allows the calculation of $s(y)$ using the approximation above. This $s(y)$ value can be used to recalculate a new β value, and this procedure can be repeated until convergence, which typically takes $\sim$5 iterations.

This procedure can be used to calculate β, and the approximations to estimate $f(y)$ & $t(y)$ at any given I-V data-point. The current density can then be evaluated using Equation (2.29), and thus the emission area using Equation (2.31), for each data-point.

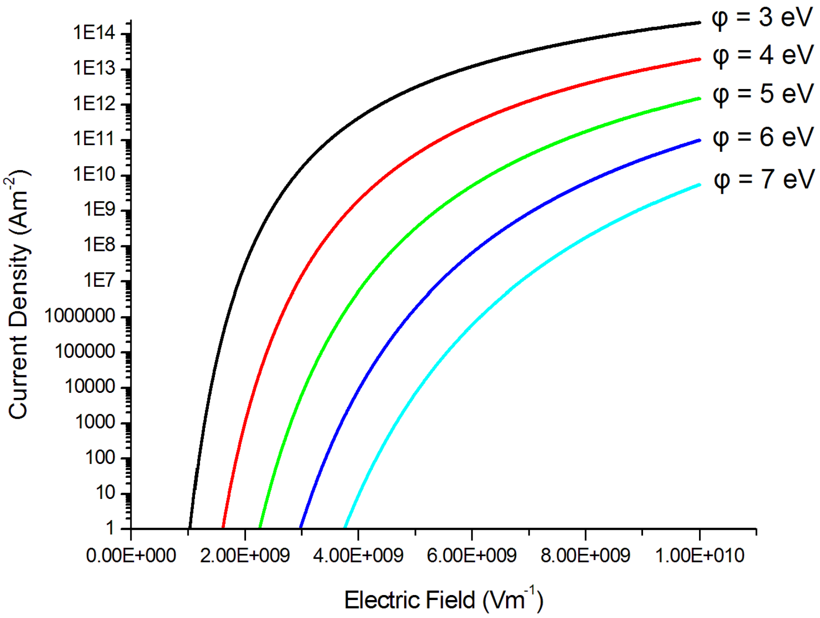

Figure 2.9: Plots of the FN current density vs. the electric field at the point of emission, for a number of work function values

2.2.2 Temperature Effects

One of the assumptions of the Fowler-Nordheim Theory set out in the previous section, is that the temperature of the metal or semiconductor emitting is 0 K, behaving as a degenerate electron gas. This greatly simplifies the analysis by assuming that all electrons will be below the Fermi energy, and by ruling out any contribution from thermionic emission. However in experimental situations the emitter will be at room temperature (∼300 K) or greater. Field emission where temperature is considered a significant factor is referred to as “thermal field emission” [64].

The current density for thermal field emission, J_{TFE}, can be obtained from a model reported in 1956 by Murphy and Good [65]:

$$J_{TFE} = J_{FN}\frac{\pi\rho}{\sin(\pi\rho)} \tag{2.47}$$

$$\rho = \frac{kT}{eh}\frac{2(2m_e e\Phi)^{\frac{1}{2}}}{F_S} \tag{2.48}$$

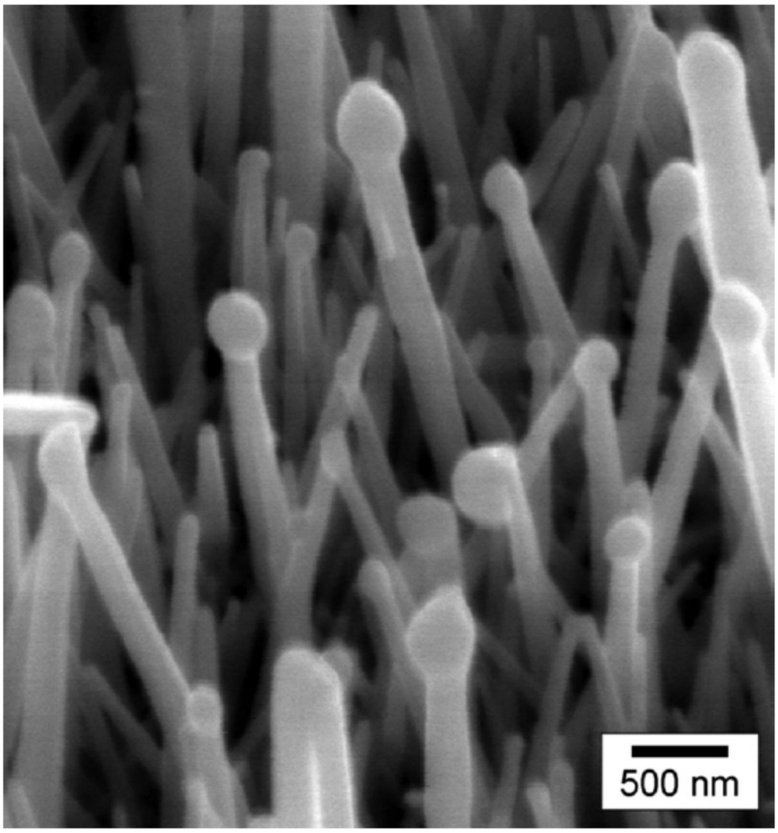

Figure 2.10: SEM image of bulbous tipped ZnO nanowires observed after field emission testing, in a work by Semet et al [34]

Field emission experiments are normally performed at room temperature, making ∼300 K seem an appropriate temperature for these calculations. However, as current passes through the emitter Joule heating takes place. Samples examined by scanning electron microscopy after field emission testing often exhibit signs of deformation consistent with melting [9, 34]. A typical feature is nanowire tips deforming into a bulbous shape. In Figure 2.10 an example is reproduced from a work by Semet *et al* [34], where bulbous tips were observed and attributed to surface diffusion. They also observed 5-10 μm scale areas of complete melting, presented in Figure 2.11. Similar areas of melting were observed by Spindt et al [9], which is reproduced in Figure 2.12. This melting may be caused by Joule heating during field emission, which would suggest performing calculations taking temperatures at or above the melting point. However melting, particularly the areas of complete melting, may be caused by electrical breakdown across the vacuum gap. As an emitter's temperature increases atoms or molecules adsorbed to the surface may be released, and at near melting temperatures gas may be released from the emitter itself. This localised pressure increase between the electrode and the sample can lead to the initiation of a vacuum arc, where high current is conducted through the gas. These high currents will give rise to much higher temperatures than those present during field emission, and thus may account for areas of significant melting. With these possible temperatures in mind, we have estimated the thermal field emission current density, using Equation (2.47), for a typical work function and electric field strength of 3.7 eV and 10^{10} Vm^{-1}, respectively. The results can be seen in Table 2.1, for temperatures of 0 K, 300 K, 2248 K, and 3813 K, which are the FN assumption, room temperature, the melting point of ZnO, and the melting point of ZrC, respectively. We can see that, even for this large temperature range, the current density does not vary significantly. This supports the use of the 0 K assumption implicit in applying FN analysis to experimental data.

The heat energy produced by Joule heating is given by:

Temperature (K)	**Current Density (Am^{-2})**
0	4.09×10^{13}
300	4.09×10^{13}
2248	4.12×10^{13}
3813	4.16×10^{13}

Table 2.1: Current density for a work function of 3.7 eV and electric field of 10^{10} Vm^{-1}, for a number of temperatures, estimated using Equation (2.47)

$$\frac{Q}{t} = I^2 R \tag{2.49}$$

where Q is the energy, I is the current, R is resistance, and t is time.

The energy lost by radiation is given by:

$$\frac{Q}{t} = A\sigma\epsilon(T^4 - T_0^4) \tag{2.50}$$

where Q is the energy, A is the surface area, σ is the Stefan-Boltzmann constant, ϵ is the emissivity of the material, and T_0 is the ambient temperature.

Another temperature factor is the Nottingham effect [66], which arises from the energy difference between the emitted electrons and the electrons replacing them. If the average energy of the electrons leaving the emitter is greater than the average energy of the electrons replacing them, there will be a net energy loss in the emitter, constituting a cooling effect. If the average energy of the electrons leaving the emitter is lower than the average energy of the electrons replacing them, this will cause a net gain in energy, constituting a heating effect. Nottingham identified that for thermionic emission the effect

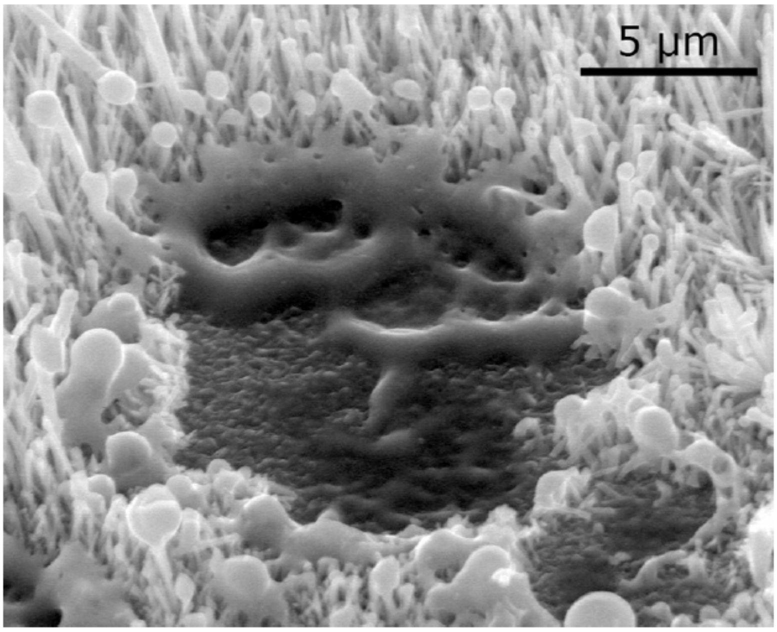

Figure 2.11: SEM image of melted area observed on a ZnO nanowire sample after field emission testing, in a work by Semet et al [34]

was cooling. An average energy ω is lost with each emitted electron, where ω is given by:

$$\omega = e\Phi + 2kT \tag{2.51}$$

In thermionic field emission, the effect can be either a heating or a cooling one, depending on the emitter temperature. For an emitter temperature below the "inversion" temperature, T_i, the effect will heat the emitter, and above this temperature the effect will cool the emitter [67]. Hence the Nottingham effect tends to stabilize the tip temperature at a value near the inversion temperature [8]. This inversion temperature is given by:

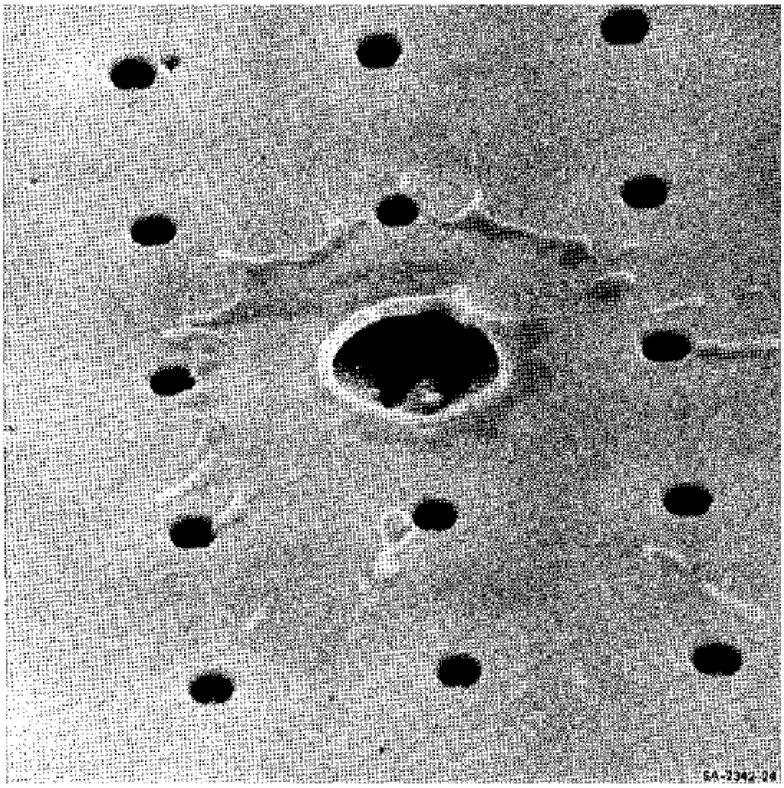

Figure 2.12: SEM image of melted area observed on an array of molybdenum cones after field emission testing, in a work by Spindt et al [9]

$$T_i = 5.32 \times 10^{-7} \frac{F}{\Phi^{\frac{1}{2}}} \tag{2.52}$$

A plot of the inversion temperature as a function of the electric field strength, for a work function of 3.7 eV, can be seen in Figure 2.13.

The average energy of an emitted electron, ϵ_e, can be approximated by the following expression [68]:

$$\epsilon_e = -\pi k T \cot\left(\frac{\pi T}{2T_i}\right) \tag{2.53}$$

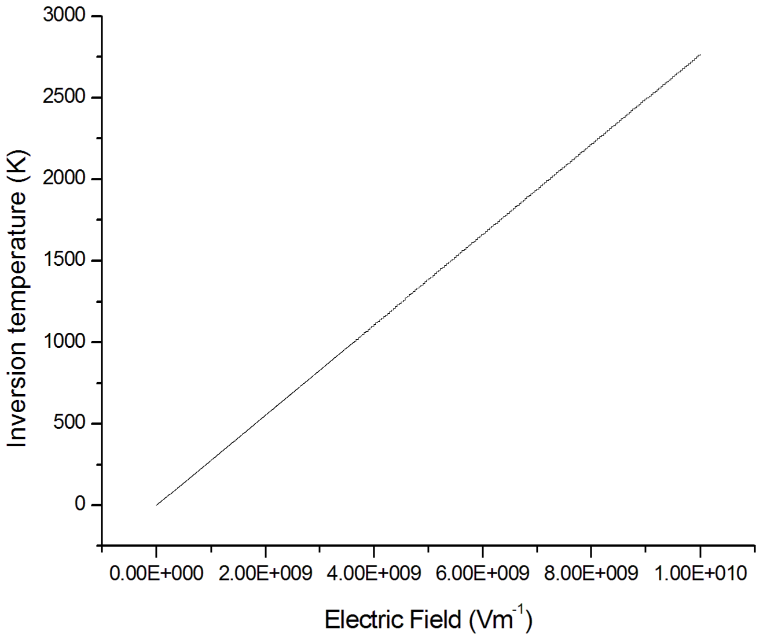

Figure 2.13: A plot of inversion temperature vs. electric field

2.2.3 Semiconductor Effects

The Fowler-Nordheim theory assumes a free electron gas behaviour for the emitter. This theory and analysis based on it are often applied to field emission from semiconducting materials. However, the specific band structure of semiconductors may have a significant effect on their field emission.

In a crystalline solid, the atomic energy levels coalesce into bands, separated by forbidden regions corresponding to the gaps between atomic levels, with each band having fine structure corresponding to the original atomic levels [1]. The conduction band is the higher energy band of energy levels where electrons have enough energy to become non-localised. The valence band is the lower energy band of energy levels that are occupied at 0 K. In a metal, these bands overlap. As such, there are electrons in the conduction band at any temperature. Electrons in the conduction band are delocalised, and thus metals are conductors.

In an insulator, these bands are distinct, separated by a large forbidden region called the band gap. The valence band is mostly occupied, with very few, if any, electrons in the conduction band, causing them to be insulating. In cases where the band gap is sufficiently small, electrons from the filled valence band can be thermally excited into the conduction band, allowing for conduction at some temperatures. These materials are semiconductors. A band diagram for these three types of material can be seen in Figure 2.14.

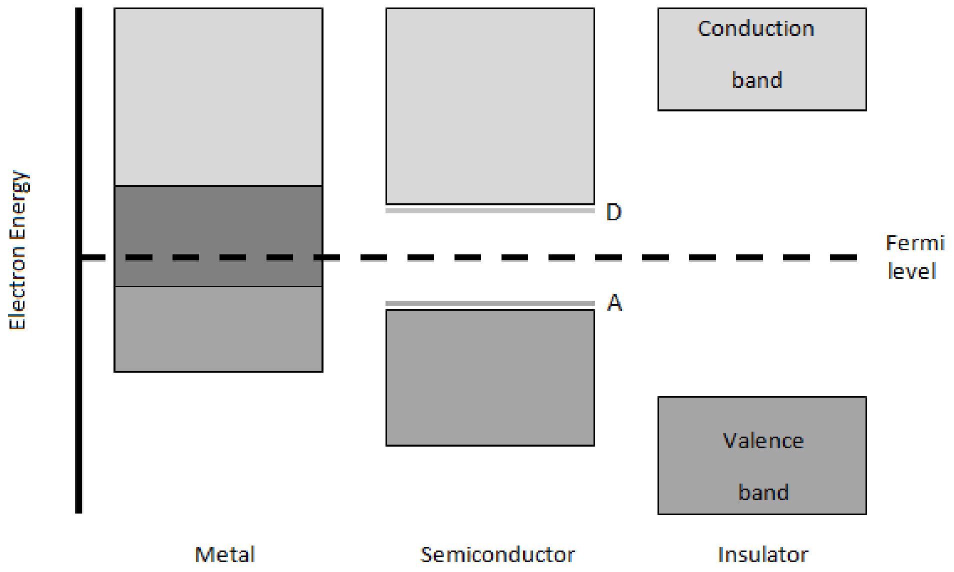

Figure 2.14: Band diagram for metal, semiconductor and insulator, with D and A denoting the donor and acceptor levels, respectively

In an intrinsic semiconductor the Fermi level is found in the middle of the band gap[1]. For an n-type semiconductor the Fermi level will be closer to the conduction band, and in a p-type semiconductor it will be closer to the valence band. FN theory considers emission exclusively from the Fermi level, which in the case of a pure semiconductor is not physically appropriate as the Fermi level cannot be occupied if it is in the forbidden region. Thus field emission from a semiconductor must be from either the conduction band, the valence band, from donor or acceptor states due to doping, or from defect states within the band gap caused by impurities.

In a free electron gas, emission comes from the top of the Fermi sea. Thus, for 0 K, the emitted electrons will be from the Fermi level, where the barrier encountered at the surface by electrons will equal the work function. To evaluate these other scenarios we can replace the work function, Φ, in the FN equations with the value of the barrier that will be experienced by electrons in the other situations. Given the operating temperatures in field emission experiments, discussed in Section 2.2.2, levels at the bottom of the conduction band may be occupied. The energy between the bottom of the conduction band and the vacuum level in a semiconductor is known as the electron affinity (χ), and will be smaller than the work function, for example in zinc oxide the difference is 0.2 eV [31]. However, Al-Tabbakh *et al.* [69, 70] found that at high field values, there is sufficient lowering of the barrier for emission to occur from the top of the valence band. The barrier encountered by electrons at the top of the valence band will be the electron affinity plus the band gap, which in the case of zinc oxide is 3.37 eV [17].

As they are conductors, there is no electric field penetration into metals. However electric fields can penetrate significantly into the surface of semiconductors [71]. If a positively biased electrode is positioned near the materials surface, as in standard field emission experiments, the field penetrating into the material will cause electrons to accumulate at the surface. This has the effect of bending the bands downwards at the surface [72]. This can be seen in Figure 2.15.

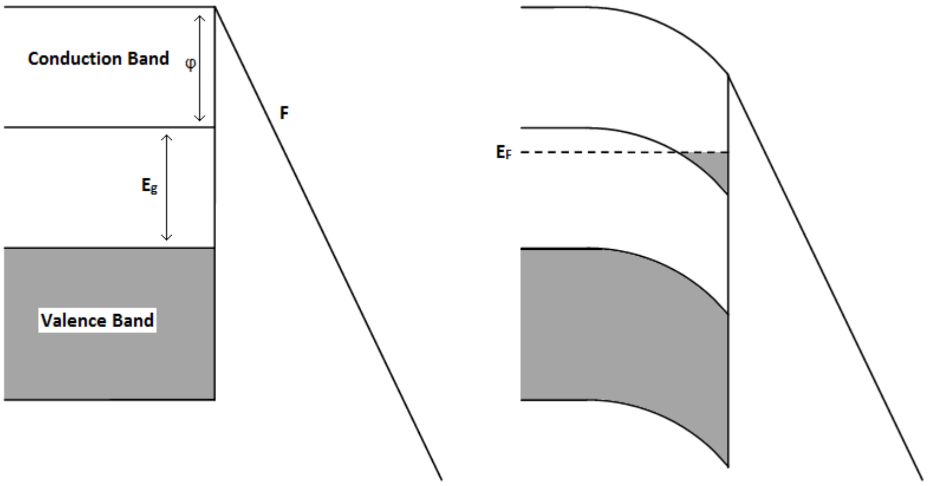

Figure 2.15: Band diagram at emitter surface without and with field penetration respectively

The diagram on the right of Figure 2.15 shows an n-type semiconductor with field penetration and subsequent band bending. As discussed, the Fermi level, E_f, is close to the bottom of the conduction band in an n-type semiconductor. If the band bending is sufficient, the bottom of the conduction band can dip below the Fermi level (as shown in the diagram). This will cause a "pool" of electrons at the surface, with the highest filled level being at the Fermi level, for a temperature of 0 K [1].

However, the field penetration into a semiconductor may be inhibited due to screening by occupied surface states. Surface states are electronic states that occur only at the surface, due to the sudden termination of the periodic lattice. For a clean semiconductor, the bonds left open on atoms at the surface will give rise to a narrow band of states, within the band gap [72]. In doped semiconductors, surface states causes band bending within the material, bending the bands down near the surface in n-type, and bending them upwards in p-type.

In experimental practice, the emitters used will not be fully clean, as even short exposure to atmospheric conditions will lead to adsorption to the surface. Adsorption is the process where atoms or molecules, present in the surrounding medium, adhere to the surface of a material. For a typical experimental pressure of 10^{-8} mbar it will only take $\sim$0.01 s for a monolayer to adsorb to a clean surface. Atoms or molecules that bond with the surface can act as donors or acceptors, with donors causing upward band bending and acceptors causing downward band bending.

If the surface states are sufficiently densely populated, they will screen the bulk of the material from the electric field, such that there is no field penetration. This gives effectively metallic behaviour. The degree of band bending due to surface states in various zinc oxide surfaces can be seen in Table 1.1.

In cases where these semiconductor effects influence the current voltage characteristics of a sample's emission, logarithmic plots of I/V^2 vs $1/V$ will be non-linear, due to the deviation from traditional FN behaviour [71]. An example of non-linear plots from various semiconductor samples can be seen in Figure 2.16. If FN plots from a semiconductor sample are linear, while the barrier height may be defined by the semiconductor nature of the sample, the effect of semiconductor effects on the current voltage response can be considered negligible. Any deviation from linearity observed can be attributed to the influence of these semiconductor effects. Such deviation from linear behaviour has been observed in the field emission of ZnO nanostructures, typically with a sharp change in slope between two linear regions at high and low field. For example, as discussed in Section 1.1, Al-Tabbakh *et al* have

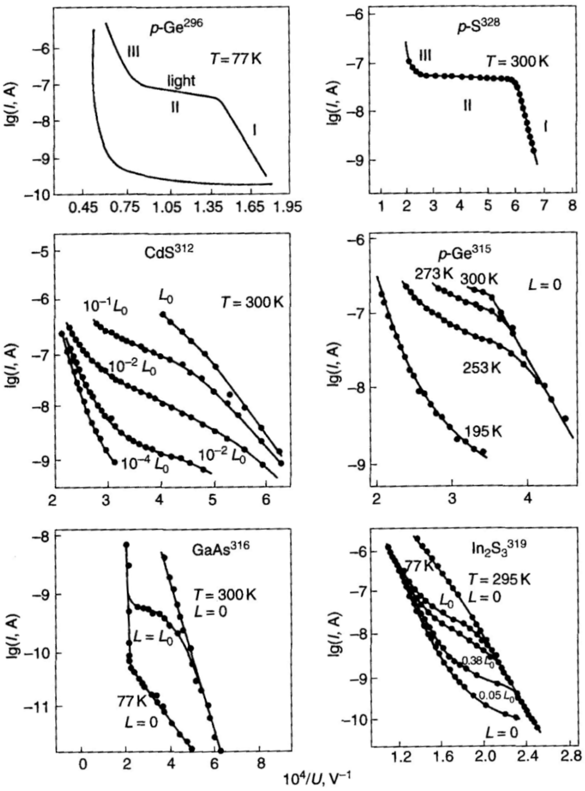

Figure 2.16: Examples of non-linear behaviour from various semiconductors, reproduced from Field Emission in Vacuum Microelectronics by Fursey [71]

obtained I-V data which produces these non-linear FN plots, for ZnO tetrapod nanostructures [69, 70]. They have interpreted this deviation as being due to emission of valence band at high field values due to the saturation of the conduction band current.

Chapter 3

Experimental Details

3.1 Field Emission Apparatus

An apparatus was designed to test the field emission properties of various samples. The general configuration for field emission characterisation is parallel plates (see circuit diagram in Figure 3.1), with the sample acting as the cathode, and a flat metal electrode as the anode. The separation between the cathode and anode, d, is typically on the order of a hundred microns and the bias on the anode on the order of kilovolts to achieve the electric fields necessary for field emission. When field emission occurs, electrons will be emitted from the sample cathode, and attracted to the anode. The emission is characterised by measuring the current as a function of the voltage. Due to the small gap size and high voltage, ultra-high vacuum (UHV) is necessary to minimise the chance of breakdown across the gap between the anode and cathode.

Our main goals in designing this system were achieving the necessary

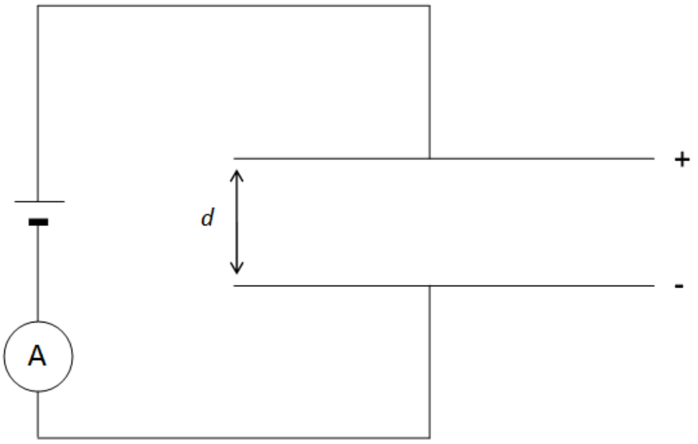

Figure 3.1: Parallel plate configuration

high vacuum, the faculty to hold multiple samples at once to decrease the overall turnaround time, the faculty to take I-V data with good control over the spacing, d, and the ability to use a transparent phosphor electrode to image the emission. In this section we describe how the system was designed and built to achieve these goals. A schematic of the apparatus can be seen in Figure 3.2. Photographs of the completed apparatus can be seen in Figures 3.3 and 3.4.

3.1.1 Vacuum Setup

As discussed, a requirement for the field emission apparatus is a high or ultra-high vacuum. The presence of background gases can lead to these gases being ionised by the strong electric fields required in field emission experiments, resulting in breakdown, or arcing, between anode and cathode. This could potentially do damage to the samples, as well as making it difficult to obtain results. Some arcing will always take place, as it is impossible to completely eliminate the background gases in the chamber, as well as out-gassing from

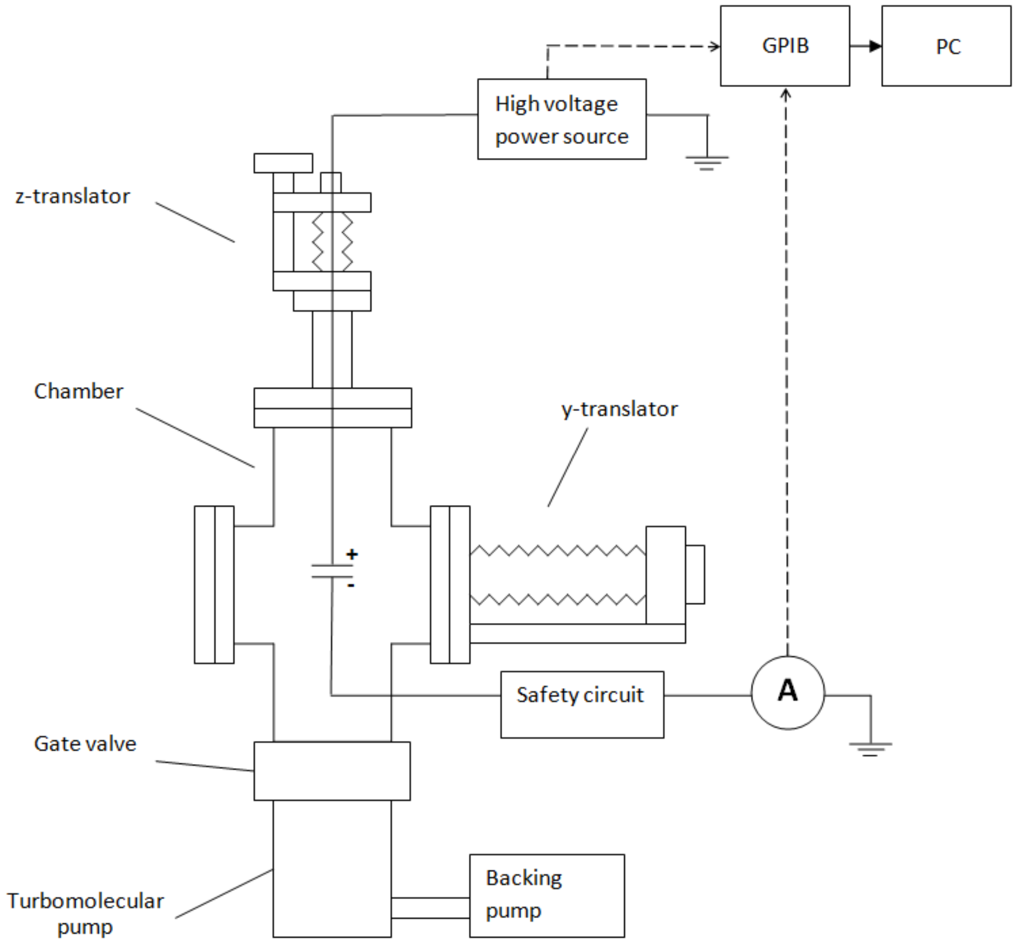

Figure 3.2: *Field emission apparatus*

the samples. However a high vacuum will minimise the amount of arcing.

A stainless steel CF vacuum chamber was used for the experiments (see Figure 3.3 and 3.2). It was equipped with a ∼500 l/s Edwards EXT 555HE turbomolecular pump, with an Edwards rotary RV12 backing pump. Under normal operation, the turbomolecular pump was kept running constantly. When opening the chamber was necessary, a gate valve between the pump and chamber was closed, and the chamber was vented to the atmosphere. To re-pump, the chamber was evacuated, or roughed, with an Edwards rotary

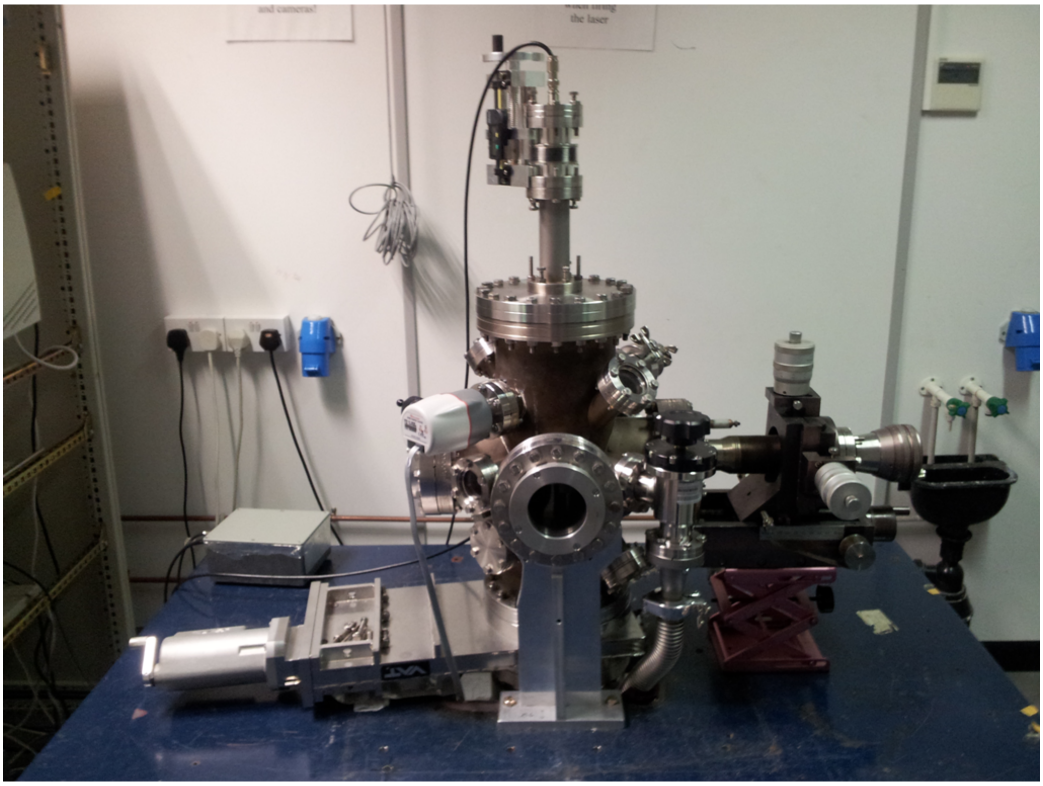

Figure 3.3: Field emission apparatus exterior

E2M-18 pump connected to the chamber through a valve. When the chamber reached a sufficiently low pressure ($\sim10^{-4}$ mbar) the valve to the rotary pump was closed, and the valve to the turbo opened.

The vacuum in the chamber was monitored with an Edwards WRG-S-NW35 combitron gauge, and between the turbomolecular pump and its backing pump using a Leybold pirani gauge. This setup was capable of reaching an ultimate base pressure of ~1 x 10^{-8} mbar. The operating pressure was taken to be $< 10^{-7}$ mbar, which could be achieved in ~24 hours. This time to reach operating pressure gave rise to a slow turnaround time, which provided motivation to allow loading of multiple samples at once.

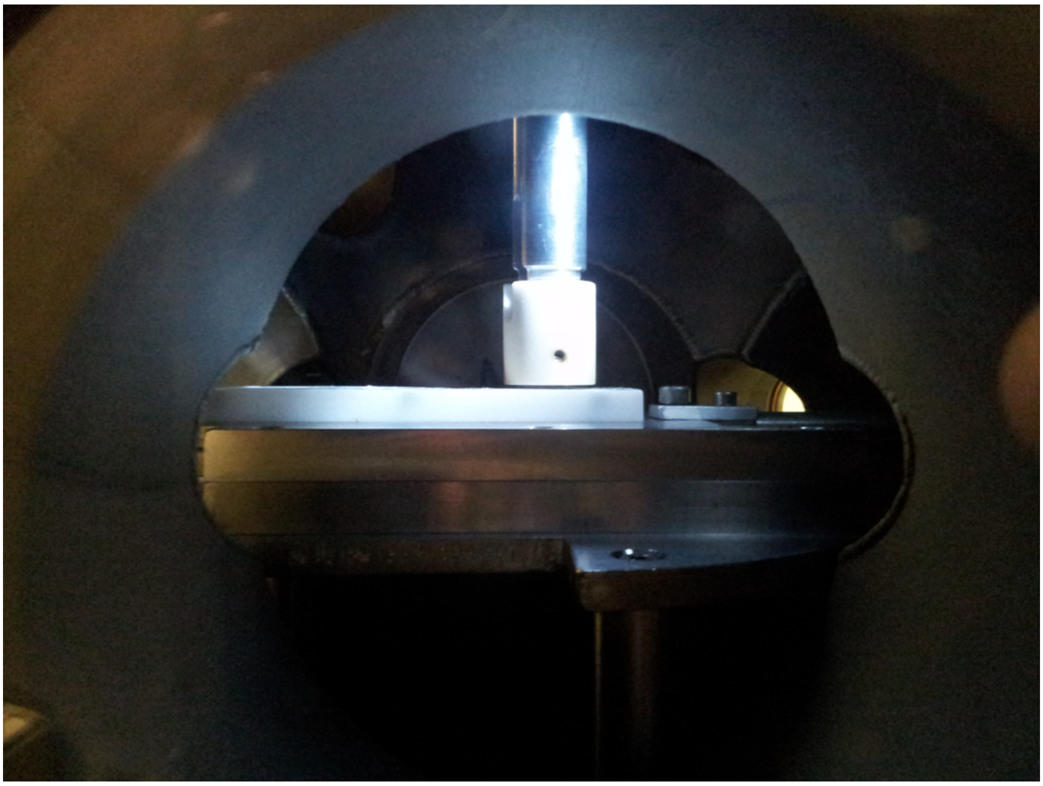

Figure 3.4: Field emission apparatus interior

3.1.2 Current Voltage Measurement

Once sufficient vacuum had been achieved, the next consideration was the design of the internal set up of the chamber (see Figure 3.5). In order to allow for multiple samples to be loaded into the chamber at once, a sample holder with four stainless steel contacts in Teflon was designed. This holder sits at roughly mid height in the chamber. One of the four contacts is left exposed, and samples to be tested are affixed to the other three contacts using silver paste (SPI Supplies, Silver Paste Plus). As the silver paste is conducting, this ensured an electrical connection between the surface of the sample and the stainless steel in the sample holder (for conductive substrates). This sample holder could be moved horizontally with the y-translator (see Figure 3.2).

A flat, polished, circular, stainless steel electrode, of radius 8 mm, sits in a Teflon holder on a rod attached to a linear z-translator at the top of the chamber (see Figure 3.5). Using this z-translator, the gap between the samples on the holder and the electrode could be controlled. The z-translator has a digital scale with a step size of 0.01 mm.

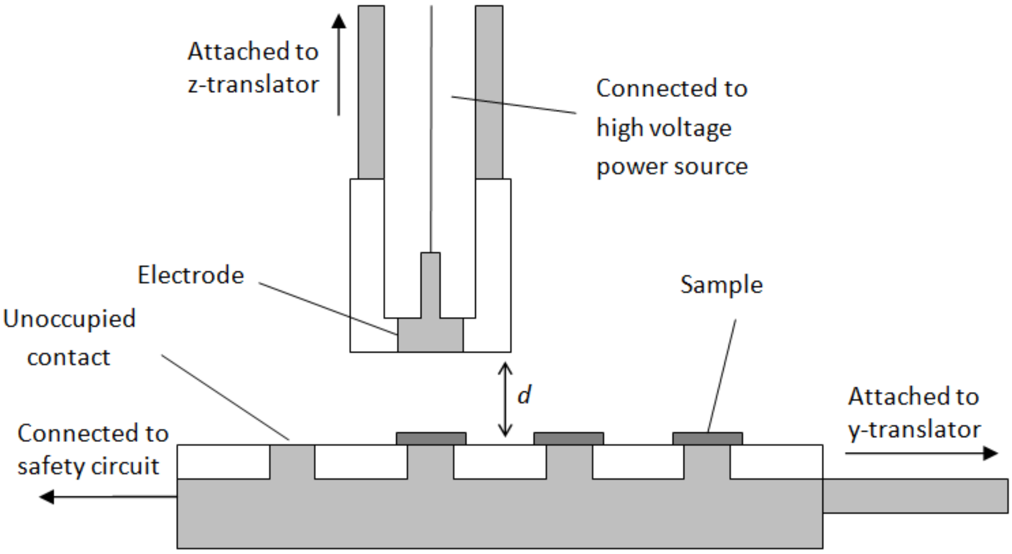

Figure 3.5: Field emission chamber interior cross-section

By moving the sample holder so the unoccupied contact was directly below the electrode, the electrode was slowly lowered until electrical contact was made (determined using a multimeter), and zero the digital scale on the linear translator to this point. The thickness of the (100) silicon wafers used in this work is 0.5 mm. With the linear translator zeroed on the unoccupied contact, the height of a sample's surface should be the known thickness of the sample, plus a number of other factors. The factors are the thickness of the silver paste layer, the difference in height between the unoccupied contact and the other contacts, and the error of the linear translator. Evaluating these factors was vital to accurately controlling the separation, d.

To investigate the height of the relative height contacts and the accuracy of the linear translator, the electrode was brought in to electrical contact with the first sample holder contact, and the linear translator zeroed. The electrode was then brought into contact with each of the other three contacts, and the height taken from the linear translator. The measurements were performed 20 times, to determine average heights and the reproducibility of those heights. The results are presented in Table 3.1. A typical plot of the values for a contact can be seen in Figure 3.6, with a Gaussian curve fitted to it, giving a full-width half maximum of ~0.009 mm. The height differences found were ~10 - 20 μm, as was the standard deviation. This suggests that the heights of the contacts were roughly equal, within the accuracy of the linear translator.

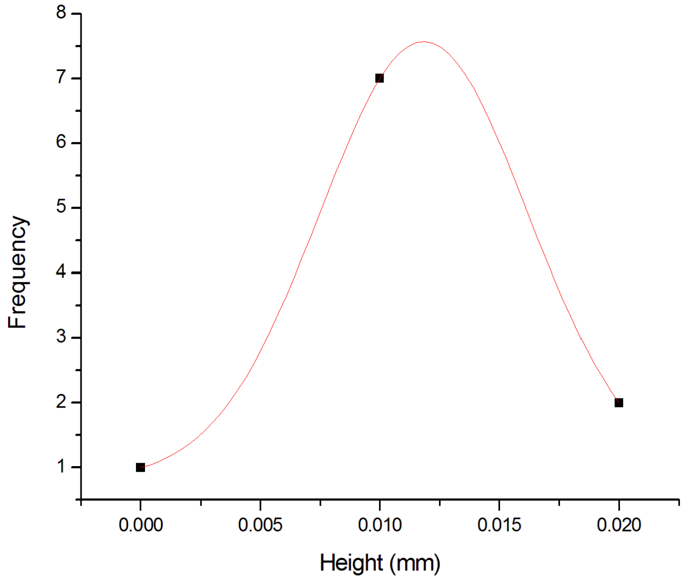

Figure 3.6: Typical height measurement distribution, fitted with Gaussian curve

To investigate the thickness of the silver paste layer, the first contact was left unoccupied, and 0.5 mm thick silicon samples were attached to the

Contact	Average Height (mm)	Standard Deviation (mm)
2	0.01	0.01
3	-0.02	0.02
4	-0.02	0.02

Table 3.1: The 20 measurement average height of the three contacts, relative to the first contact, and the standard deviation for these averages

other three contacts with silver paste. The electrode was brought into electrical contact with the first contact, and the linear translator zeroed. The electrode was then brought into contact with each of the silicon samples, and the height take from the linear translator. The measurements were performed three times to get an average value, then the samples changed and the process repeated. This was done for 4 sets of silicon samples. The results are presented in Table 3.2. We see heights ranging from 0.52 - 0.63 mm, with an average of ∼0.56 mm and a standard deviation of ∼0.04 mm. This indicates the thickness of the silver paste layer ranges from ∼20 - 130 μm, with an average of ∼60 μm. This is a significant variance, that would appreciably limit the controllability of the sample-anode separation, d.

Sample set	C2 Height (mm)	C3 Height (mm)	C4 Height (mm)
1	0.53	0.52	0.54
2	0.57	0.61	0.52
3	0.63	0.56	0.53
4	0.54	0.60	0.52

Table 3.2: The 3 measurement average height of the Si samples at the three contacts (C2, C3, C4), relative to the first contact, for 4 sets of Si samples affixed with Ag paste

The silver paste is viscous and lumpy. It may be possible to achieve a more controllable silver layer thickness, by dilution of the silver paste. To investigate this silver paste was diluted with an equal amount of acetone, and used to affix 0.5 mm silicon samples to the last three sample holders, with the first contact being unoccupied. The measurement process from above was repeated, for 8 sets of samples. The results are presented in Table 3.3. The heights range from 0.50 - 0.60 mm, with an average of ∼0.53 mm and a standard deviation of ∼0.02 mm. This indicates the thickness of the dilute silver paste layer ranges from within the error of the linear translator to ∼100 μm, with an average of ∼30 μm. While dilution has reduced the average thickness, the variance is still significant.

Sample set	**C2 Height (mm)**	**C3 Height (mm)**	**C4 Height (mm)**
1	0.52	0.52	0.50
2	0.57	0.51	0.50
3	0.55	0.52	0.55
4	0.54	0.60	0.52
5	0.55	0.53	0.51
6	0.56	0.55	0.52
7	0.55	0.53	0.51
8	0.55	0.53	0.50

Table 3.3: The 3 measurement average height of the Si samples at the three contacts (C2, C3, C4), relative to the first contact, for 8 sets of Si samples affixed with Ag paste diluted with acetone

This lack of reproducibility in the thickness of the silver paste layer limits the control of the separation. We developed our procedure to eliminate this uncertainty, by directly measuring the height. Before mounting the sample holder in the chamber, the height of each sample relative to the empty contact is measured using a micrometer. With the electrode zeroed to the unoccupied contact and knowing the relative height of the surface of the samples, the spacing between the electrode and the samples could be controlled to within the accuracy of the linear translator. Our standard operating distance for obtaining I-V curves was 250 μm.

A circuit diagram for the apparatus can be seen in Figure 3.7. The resistors and diodes make up a safety circuit, to protect the picoammeter (Keithley 6485 picoammeter, 10 fA resolution) from high currents in the case of arcing between the electrode and the sample. The resistors limit the current, and the two opposite facing, low leakage, fast response time diodes serve to bypass the picoammeter in the case of a sudden current surge.

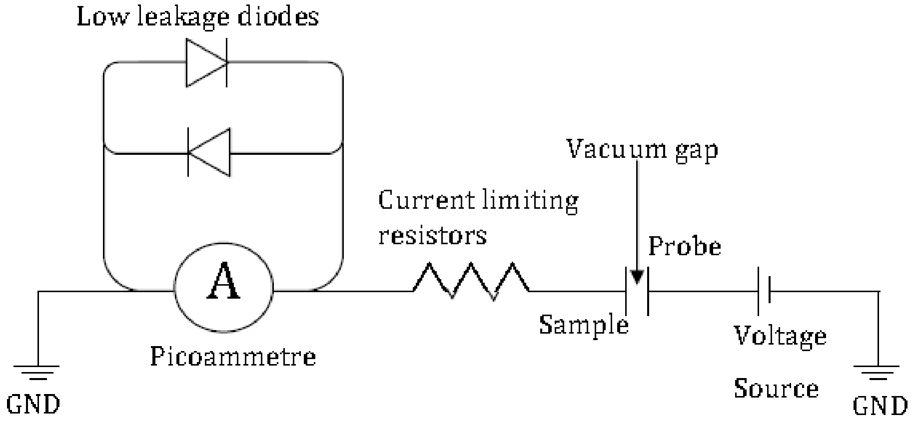

Figure 3.7: Circuit design of the field emission apparatus

However the resistors between the sample and the earth means that the sample is not grounded, but floating at a low voltage. The voltage can be obtained by calculating the voltage drop over the resistors using Ohm's law, and thus the potential difference between the electrode and the sample can be determined. The electrode was positive biased using a programmable Stanford PS350 high voltage power source capable of up to 5 kV and 5 mA. For example if the electrode was biased at 2 kV, and the picoammeter read 100 μA, taking into account the total resistance of the current limiting resistors being 231 kΩ, by taking V = IR, it can be seen that the potential difference between the electrode and sample is 1976.9 V. Any I-V data presented in this work were adjusted as described.

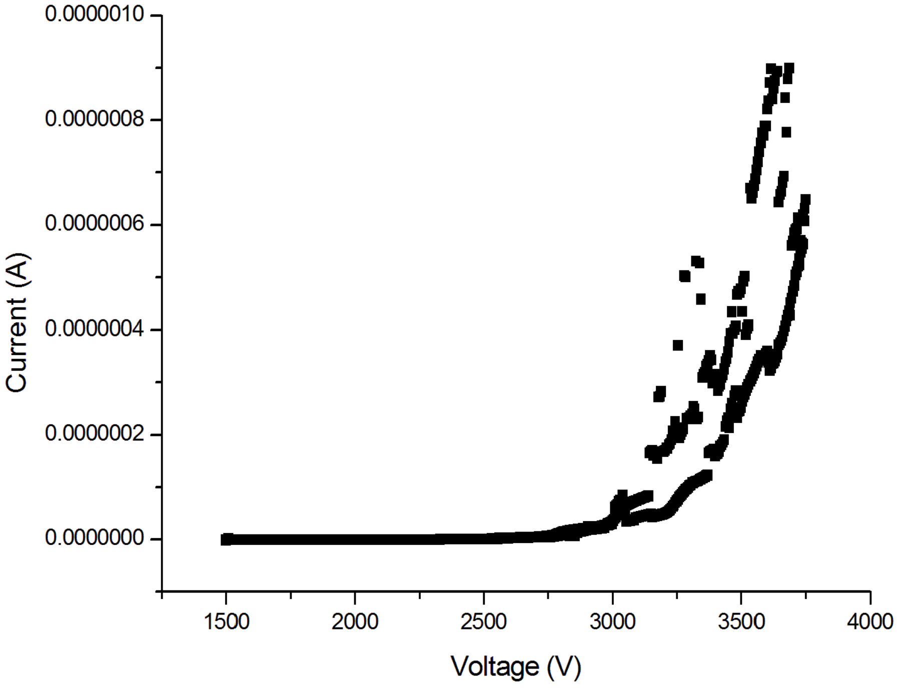

Figure 3.8: Plot of an initial set of I-V data, exhibiting noise and hysteresis

The standard experimental procedure was as follows. Three samples were affixed to the sample holder, leaving the first contact unoccupied for zeroing. The heights of the samples were measured by making a measurement at each corner and an average taken for each sample. The sample holder was loaded into the chamber, and the chamber pumped down to the operating pressure of $< 10^{-7}$ mbar, which typically takes ~24 hours. The electrode was positioned over the empty contact, lowered until electrical contact was made, and the z-translator was zeroed. The z and y translators were then adjusted to position the electrode 250 μm over a sample. As shown in Figure 3.2, the high voltage power source and picoammetter are connected to a PC through a GPIB interface. The data was taking using a LabVIEW program to control the Stanford HVPS and the picoammeter through this interface. The voltage was ramped to a set voltage and back down, the currents read by the picoammeter, and the corresponding voltages, stored by the computer. Thus I-V curves the samples were obtained. Initially a low max voltage was used, with it slowly being increased until a reasonable current, of the order of μA, was obtained.

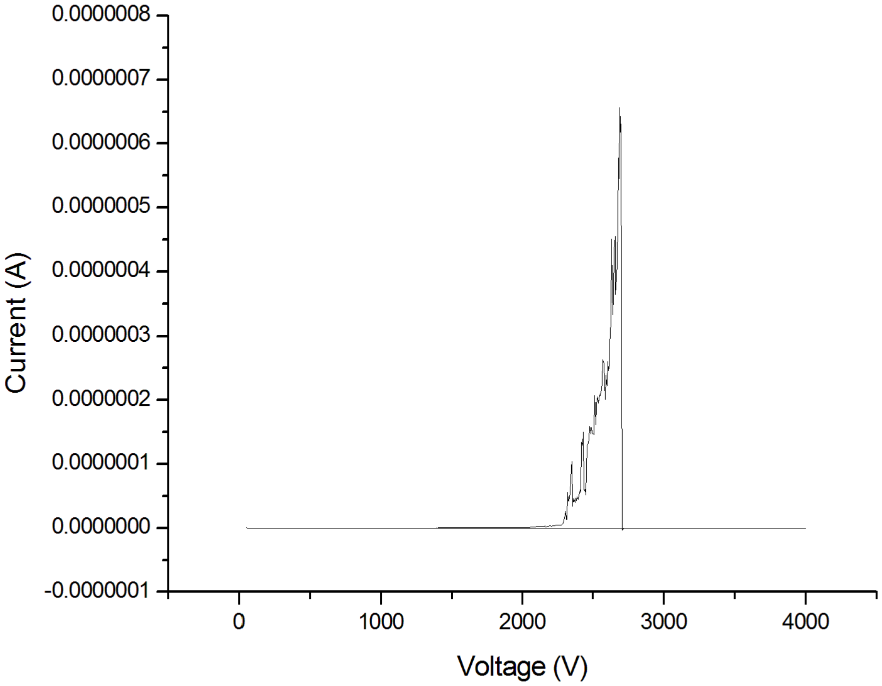

Figure 3.9: Plot of a set of I-V data where an arc took place

Initially curves may be noisy or unstable (see Figure 3.8) due to adsorbates on the surface of the sample, Joule heating of the sample, and the presences of defective nanostructures, which may be melted, or ionised in what is known as field ionisation [1]. During initial testing the vacuum pressure, which is stable outside of testing, was seen to spike at times, by up to $\sim 10^{-8}$ mbar. Vacuum breakdown arcs were also observed in initial testing. The Stanford HVPS has a safety feature, which trips if the current exceeds 1 mA, turning off the voltage. When breakdown occured, the current rose and the HVPS tripped quickly, such that the data showed no sign of the arc current, instead appearing to quickly drop off due to the voltage turning off (see Figure 3.9). A bright blue flash from the sample-anode gap was observed when these events occurred. Hysteresis (see example in Figure 3.8) was also observed in the initial data, and has in the past been attributed to adsorbates [73]. Samples were conditioned by continuously taking I-V curves until a reproducible, clean curve, where the current for the voltage rise and voltage fall roughly match, could be obtained (see example in Figure 3.10). Typically 100 - 200 cycles of ramping the voltage up and down were required.

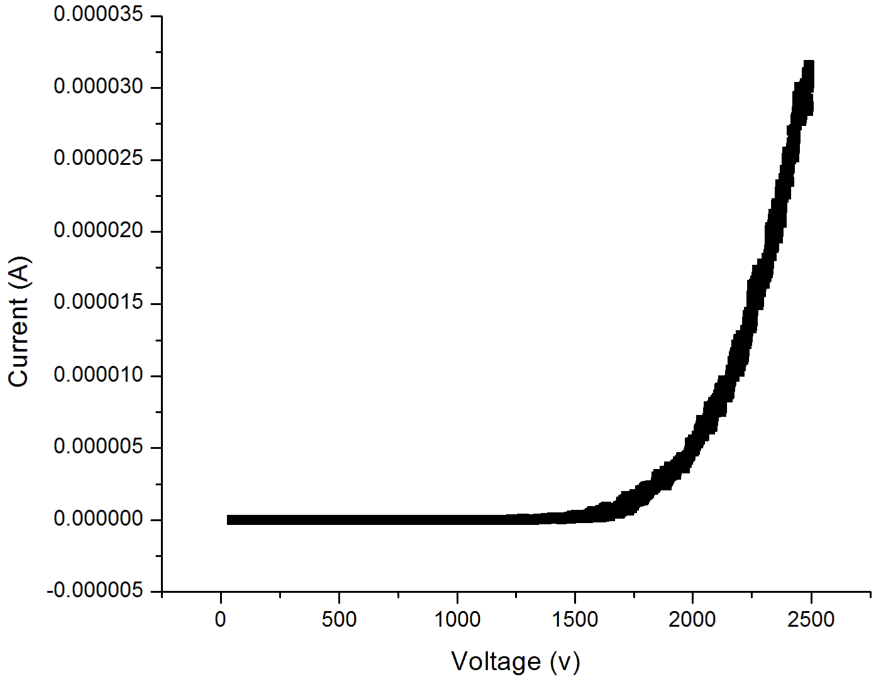

Figure 3.10: Plot of a set of I-V data obtained after conditioning

3.1.3 Imaging

One of the goals outlined at the beginning of this section was the development of a transparent phosphor electrode, to characterise the distribution and uniformity of the emission across the sample. A transparent phosphor electrode is composed of a transparent conductor, such as indium tin oxide (ITO), coated with a phosphor layer. The conducting layer is used as the anode in a parallel plate field emission experiment, as described above. The field emitted electrons colliding with the phosphor layer will cause light emission. By imaging the phosphor layer, we can image the distribution of the emission.

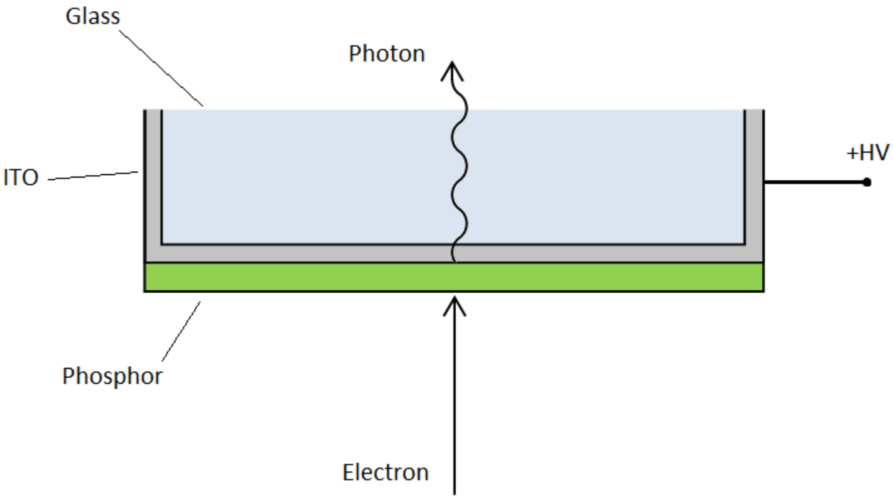

Figure 3.11: Transparent phosphor electrode cross-section

A diagram of the transparent phosphor electrode designed and constructed in this work can be seen in Figures 3.11 and 3.12. The transparent phosphor electrode was made up of a cylinder of BK7 glass, with a coating of ITO on one face and on the sides. The ITO coated face was coated with a layer of type P22G phosphor, which is composed of zinc sulphide, copper, and aluminium. It has an emission peak at a wavelength of 530 nm, an efficiency of 25% and decays to 10% intensity in 35 μs. The electrode was held in a teflon cylinder mounted on a hollow stainless steel shaft. A 90° prism resting directly on the back of the glass redirected the light. Electrical contact was made at the side of the electrode cylinder.

Due to a modular design, the stainless steel electrode seen in Figure 3.5 could be removed and replaced with the phosphor electrode without disrupting the rest of the apparatus. As with the stainless steel electrode, the phosphor electrode could be raised and lowered with the z-translator and used to address each sample with the y-translator. The phosphor was imaged through a chamber window using an Artcam 150p2 camera. The camera has

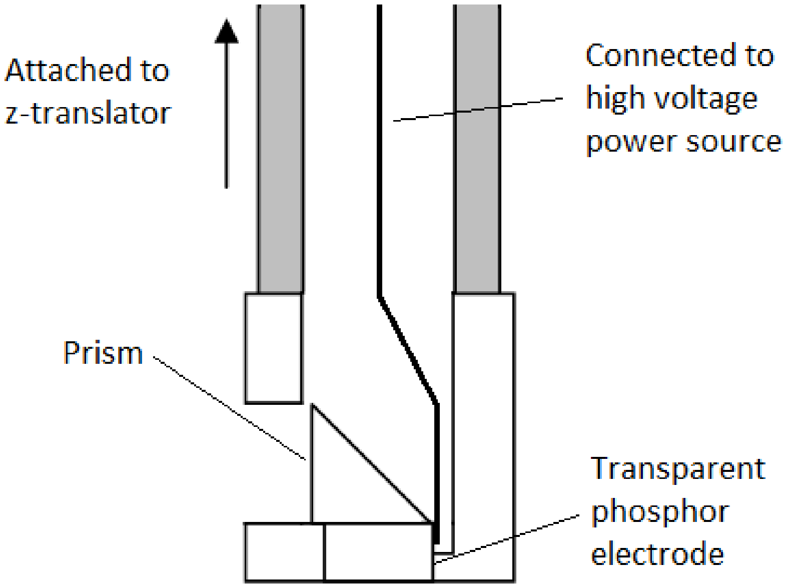

Figure 3.12: Transparent phosphor electrode module cross-section

a resolution of 1360 × 1024 pixels, and when in place and focused, each pixel corresponds to an area of ~8 × 10^{-11} m^2 on the phosphor. The phosphor electrode was connected to the Stanford high voltage power source, as with the stainless steel electrode, thus I-V data could be taken while imaging the emission. However, this does not eliminate the need for the stainless steel electrode. The arcing which takes place during conditioning could significantly damage the phosphor. The stainless steel electrode was much more robust, and could be re-polished if any damage does occur. All transparent phosphor electrode testing was peformed after first conditioning the sample with the stainless steel electrode. An example of an image of the phosphor can be seen in Figure 3.13.

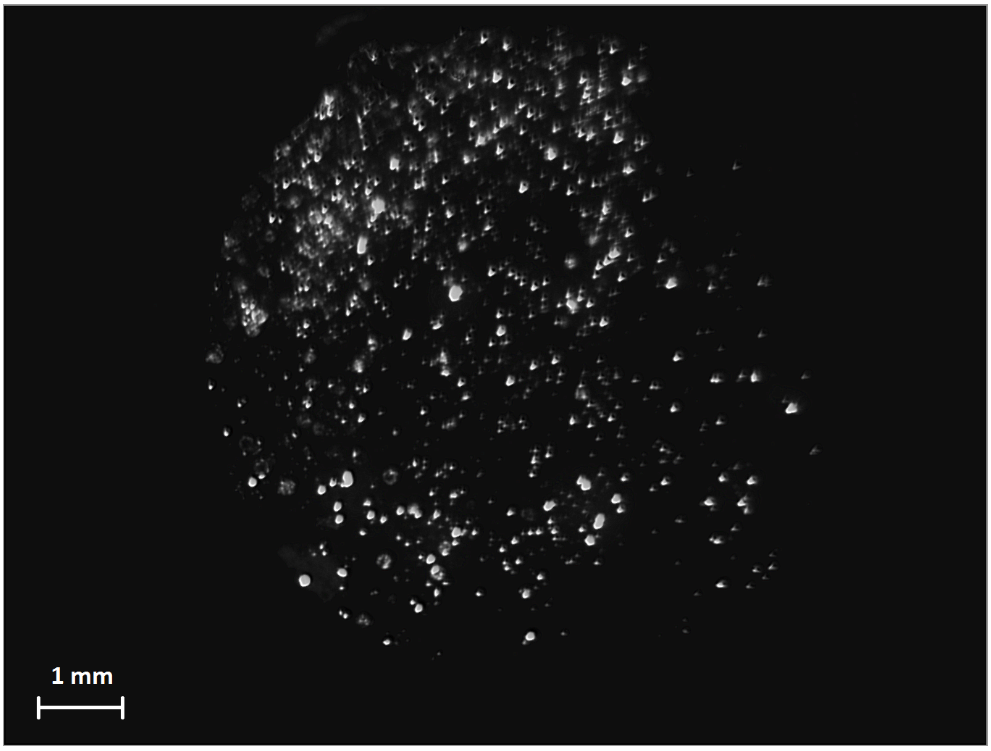

Figure 3.13: An example of a phosphor image

3.2 Pulsed Laser Deposition

The pulsed laser deposition (PLD) experiments were performed using a vacuum system designed specifically for PLD. The system consisted of a ~50 L stainless-steel main chamber, with a 4 L stainless-steel 'load lock' chamber. These chambers are connected through a gate valve suitable for a high pressure difference, and can be pumped and vented independently. This allows the loading and unloading of samples into the main chamber through the load lock, without breaking vacuum on the main chamber.

The main chamber is pumped with a 500 L/s Pfeiffer TMU 521P turbomolecular pump, with an oil-free, MVP 055 backing pump. This configuration is capable of evacuating the chamber to 10^{-7} mbar in ~12 hours, with

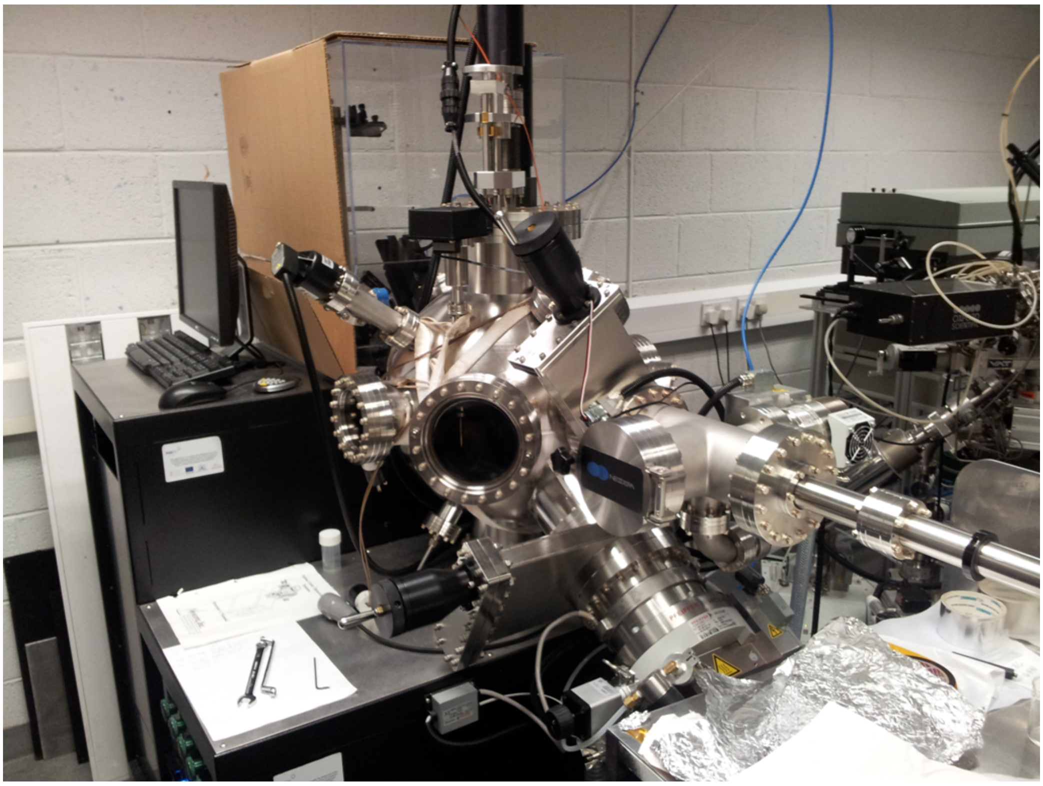

Figure 3.14: PLD apparatus

an ultimate base pressure of ∼3 by 10^{-8} mbar in ∼24 hours. Pumping down after depositions, where background gases up to 10^{-1} mbar may be used, the system reaches 10^{-7} mbar in roughly 30 minutes, reaching base pressure in ∼2 hours. The load lock chamber is pumped with 60 L/s Pfeiffer TMU 071 turbomolecular pump, with an oil-free, MVP 015 backing pump. This set up is capable of evacuating the load lock chamber from atmospheric pressure (after venting with nitrogen to reduce contamination of the chamber) to 10^{-7} mbar in ∼1 hour. The pressure in the main and load lock chamber was measured with Pirani gauges, for high pressures ($>10^{-4}$ mbar), and with cold-cathode gauges, for low pressures ($>10^{-10}$ mbar).

Substrates to be deposited on are attached to a substrate mount with

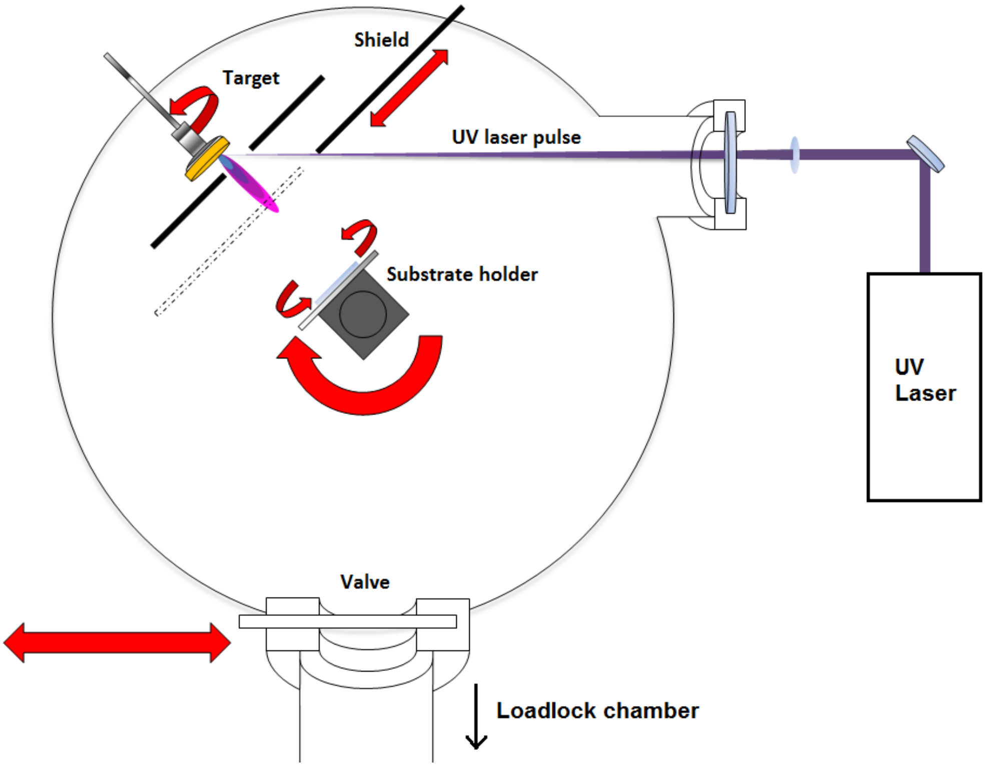

Figure 3.15: PLD system

silver paste (SPI supplies, Silver Paste Plus). The substrate mount is heated at 300 °C for ~30 min after affixing the sample, to dry the silver paste. This is necessary for good adhesion and also decreases pumping time, as the silver paste will outgas less when dried. The substrate mount is attached to an extendable arm in the loadlock chamber, which transfers the mount to a holder in the main chamber.

The sample holder in the main chamber is equipped with a heating coil, with a digital control unit, which allows it to be controlled by computer. The coil is capable of a maximum temperature of 1050 °C. The sample holder is positioned opposite to the deposition targets. The sample can be rotated about the axis perpendicular to the surface of the substrate via a computer controlled motor. Rotating by a whole number multiple of 360° during deposition ensures an even coverage over a substrate placed in the centre of the sample mount, in the event of the plume being unsymmetrical or not fully centred on the centre of the sample mount.

The targets are held on motorised carousels. The carousel has six equally spaced poles on which one inch diameter cylindrical solid targets can be mounted. The carousel can be rotated, allowing switching of which target is in position to be fired on by the laser (this position being opposite the centre of the sample mount). Thus, by mounting six different targets, depositions can be performed using six different compositions, without needing to break vacuum in the main chamber to change targets. In addition to rotation of the carousels, the posts themselves can be rotated about the axis of the post, thus rotating the targets. By rastering the rotation of the carousel and rotating the targets, the laser spot will be move around the surface in a spirograph pattern, maximising the surface area used. This will minimise the cratering of the surface, and increase the lifetime of the target.

A shield can be lowered between the target and the substrate. This allows the target to be irradiated during laser is set up, without any unwanted deposition on the substrate.

The laser used in this experiment was a Continuum Powerlite Precision II Laser. This laser has a fundamental wavelength of 1064 nm, which is frequency quadrupled using harmonic crystals to a wavelength of 266 nm. The energy output at this wavelength is approximately 150 mJ per shot, at a maximum repetition rate of 10 Hz. The pulse duration is 6 ns, and the spot size was adjusted to 0.05 mm to give a fluence of ∼2 J/cm. Movable optics allow the laser to be directed into either system as needed. The laser is directed into the chamber by two mirrors, and focused by a 30 cm focal length lens. All optics used are UV compatible.

The target used in the zinc oxide depositions was a sintered 99.999% purity ZnO, cylindrical target of 2.54 cm diameter and 1 cm height. For doped zinc oxide depositions, there were three targets of ZnO mixed with 0.02 wt%, 0.2 wt%, and 2 wt% Al_2O_3 respectively. The substrates used were Si (100). Prior to deposition substrates were cleaned in an ultrasonic bath, first for 15 min in acetone, then for 15 min in isopropyl alcohol, drying with a gentle flow of dry nitrogen after both. Substrates were then affixed to the sample mount using silver paste, and heated on a hotplate at 300 °C to dry the silver paste. Pre-deposition, substrates were annealed in-situ using the sample holders heater coil at 900 °C for 5 minutes to further clean the surface of any contaminants.

The main chamber can be populated with background oxygen and/or nitrogen. In our experiments only oxygen (99.999% purity) was used. The gas enters the system through a stainless steel pipe, and the flow rate and chamber pressure were controlled with a flow rate controller and by varying the speed of the turbomolecular pump. Nitrogen was used to purge the turbomolecular pump on the main chamber, and for venting the chambers to atmospheric pressure.

3.3 Characterisation

3.3.1 X-Ray Diffraction

X-ray diffraction is a characterisation technique which was used on samples in this work to analyse their texture. A 4-circle diffractometer (D8 Advance by Bruker AXS) was used with an emitting Cu K_α wavelength of 0.154 nm. This apparatus allows for position in the circular ranges of motion, θ and ϕ (see Figure 3.16), as well as positioning of the sample holder in the x, y, and z directions.

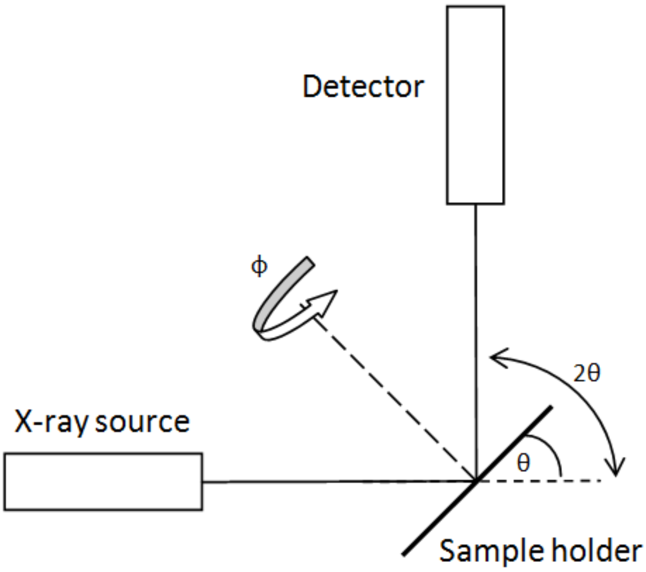

Figure 3.16: X-ray diffractometer

X-ray diffraction is based on the principle of Bragg diffraction [74] (see Figure 3.17). A single crystal is a solid made up of a regular, periodic array of atoms. They can be thought of as being made up of a series of parallel planes of atoms. Electromagnetic radiation incident on the crystal may be reflected by these atoms. Waves which are reflected by atoms in different planes will have a path difference, and thus are phase-shifted and may interfere with each other. Bragg determined the condition for constructive interference to be given by:

$$m\lambda = 2d \sin\theta \tag{3.1}$$

where n is the order, λ is the wavelength of the electromagnetic radiation, d is the spacing of the atomic planes, and θ is the glancing angle.

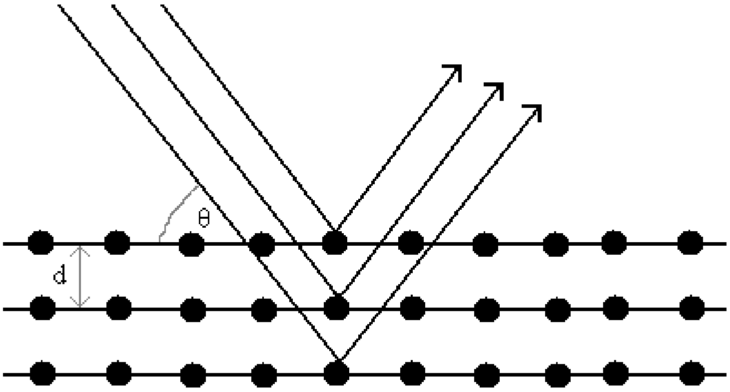

Figure 3.17: X-rays incident on a crystal being Bragg diffracted by the atomic planes

Thus by determining the angles at which constructive interference occurs, for incident radiation of known wavelength, the spacing between the planes can be determined and compared to literature values for the plane spacings of various crystal orientations of various materials. Due to the penetration of the x-rays into the surface this is a bulk characterisation. When analysing deposited samples such as thin films or nanostructure growth samples, peaks from both the deposited material and substrate will be observed.

In a typical characterisation in this work, the x, y, z, and ϕ positions were optimised with the source, sample, and detector aligned for a known constructive interference peak. In our case this peak was normally the peak of our commonly used substrate, (100) orientated silicon, which has a 2θ value of 69.132 ° [75]. Once the position has been optimised a θ-2θ scan can be performed, in which the x-ray source was held fixed, the sample holder was gradually rotated by an angle of θ while the x-ray detector was rotated by an angle of 2θ. Any peaks found in the θ-2θ scan can be further analysed by a rocking curve scan, where the x-ray source and detector were held static while the sample holder was rotated around the θ value for the peak. For a single crystalline material this peak should be extremely sharp, with any misalignment in the crystallites causing a broader peak. The full width half maxima of the same peak in different samples were compared for a qualitative comparison of crystal quality. In the case of c-axis aligned ZnO nanorods, each nanorod should be a single crystal, and as such any broadening of the rocking curve will be due to a misalignment of the rods. Thus the rocking curve full width half maxima can be used for a qualitative comparison of nanorod alignment. However due to the penetration of the x-rays, samples grown on c-axis ZnO seed layers will also have a contribution to the peak from the underlying film, which can interfere with these comparisons.

A typical θ-2θ scan can be seen in Figure 3.18. The (100) silicon substrate at 69.132° and the (002) zinc oxide peak at 34.3° can be seen. The sharp peaks at ∼62° and ∼66° are the characteristic peaks of the x-ray source. In some scans, a peak appeared at ∼33°, a forbidden silicon peak which arose due to double diffraction at certain ϕ angles [76].

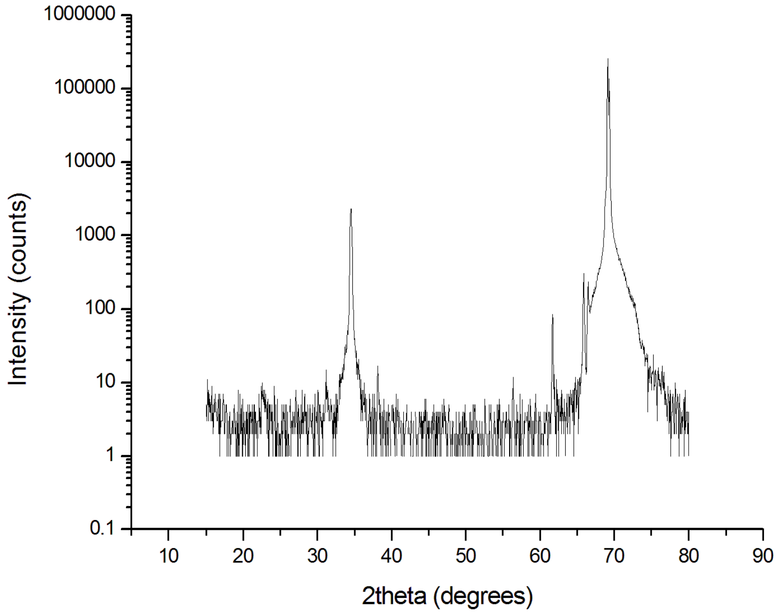

Figure 3.18: A typical θ-2θ scan of a zinc oxide sample

3.3.2 Scanning Electron Microscope

Scanning electron microscopy (SEM) was used to characterise the morphology of samples in this work. In SEM, a beam of electrons, typically of energies ranging from 0.2 keV to 40 keV, is focused on the surface of a sample under vacuum, and rastered across the surface in lines. The electrons are emitted from an electron gun by either thermionic emission, field emission, or combined thermal field emission. The emitted electrons are accelerated towards the sample and focused by an anode. The beam is further focused by magnetic lenses which bend the path of the electrons. An image of the sample's surface is constructed by detecting the secondary electrons, backscattered electrons, and emitted light caused by the electron beam [77]. The image of the surface morphology obtained is two dimensional, however the sample holder can be tilted, allowing for height and depth of structures to be investigated. The observation angle is taken from perpendicular to the sample surface, with 0° being the sample sitting flat, and 90° being a side view. An example of an image taken using SEM can be seen in Figure 1.5.

Electrons may be ejected from the surface by collision with the incident electrons. If electrons are ejected from low orbitals, an electron in a higher orbital may drop into the vacancy left by the emitted electron, releasing its energy as an x-ray photon. The energy of any x-rays emitted will be characteristic of the transition taking place, and as such by measuring these x-rays information can be gained about the material composition of the sample. This technique is called energy dispersive x-ray spectroscopy (EDX).

In this work a Carl Zeiss EVO series Scanning Electron Microscope (SEM) was used, as well as a Hitachi S5500 high resolution FE-SEM.

Chapter 4

Results and Analyses: Field Emission of Zinc Oxide Nanowires

4.1 Ordered Zinc Oxide Nanowire Array

As mentioned in Section 1.1, there is interest in the development of field emission (FE) electron sources for use in new technologies. The wide band gap material zinc oxide has received particular attention for this application, due to its ease of nanostructure growth in a variety of possible morphologies, and favourable electronic properties such as ease of n-type doping. These properties are directly related to the key factors controlling the field-emitted current, the applied electric field strength at the point of emission, F_S, and the work function, Φ, respectively; as they are the fundamental parameters entering the theory developed by Fowler and Nordheim (FN) to interpret

I-V data. The field emission behaviour of a single, sharp, metallic emitter has been studied and analysed using FN theory for several decades, e.g. References [1][7][8], to include a single carbon nanotube in recent work [78]. Microelectronics devices composed of 2D-arrays of molybdenum emitting tips were also successfully developed by Spindt *et al.* [9]. Significantly, these authors showed that the emission takes place in an effective, atomic-sized area of the order of 10^{-19} m^2 per tip.

The recent developments in nanotechnology fabrication methods have driven an intensive effort in the use of high aspect ratio ZnO nanostructures in field emission research due to advantageous physical and material properties [10]. Recent works typically study disordered assemblies of vertically oriented, parallel nanowires or nanorods with typical occupation density of 10^7 cm^{-2}, radii in the range 50-100 nm, heights in the range of 0.5-2 μm and overall sample surface areas of up to several cm^2 [4]. The authors generally report close to linear plots obtained via standard FN analyses, assuming a uniform field in the voltage gap (V/d). They report on the field enhancement factor, the turn-on field, and the threshold field, with typical values of several thousands, 1 V $\mu\mathrm{m}^{-1}$, and 10 V $\mu\mathrm{m}^{-1}$, respectively [24–28]. The apparent reported scatter of field parameters and field enhancement values out of these many studies indicate no clear trends for the understanding of the effects of ZnO nanowire topology and individual morphology on the field parameters. This may be a result in part of the lack of sample uniformity on the substrate, resulting in non-uniform electric field and emission patterns, respectively. Nanosphere lithography has proven to be an effective method of creating ordered, spaced, arrays of nanowires, nanodots or nanotubes, for a variety of materials including zinc oxide [79–81].

Peculiar emission behavior has also been reported recently by several authors. Xiao *et al.*[82] have observed an unstable oscillating behavior of the I-V data from single, cone-shaped ("agavelike") ZnO nanostructures, which they attribute to the combined effect of surface charging and surface atom diffusion on the nanostructure tip. Semet *et al.*[34] have reported linear FN plots for vertically aligned ZnO nanowire planar cathodes, but showed that the corresponding slopes could only be interpreted if an effective barrier height of about 1 eV was assumed, and attributed to structural changes at the nanowire tip due to temperature effects. As discussed in Section 1.2 most reports on the topic of FE assume the work function value $\Phi = 5.3$ eV for ZnO, irrespective of its morphology [29]. Al-Tabbakh *et al.* have recorded I-V data leading to highly non-linear FN plots for ZnO tetrapod nanostructures[69, 70], which they interpreted in terms of conduction band electrons or valence band currents at high field values due to the saturation of the conduction band current. It is apparent that the authors invoke differing electronic processes and work function values to explain the different results observed.

In this section, the field emission behaviour of hexagonally patterned arrays of vertically aligned ZnO nanowires is investigated. The control over emitter morphology should allow the determination of more valid field parameters. The method of the FN plot is extended by using Forbes' analytical expressions [63] discussed in Section 2.2.1, together with the plausible values of Φ discussed in Section 1.2. This provides for a general treatment of emission data within the physical framework of FN theory. The field enhancement factors computed by this treatment are compared with theoretical or modelling estimates, relating them to relevant geometrical parameters such as aspect ratio and surface density [83–85]. Effective emission areas and current densities are also calculated from the present treatment and compared with older approaches [9, 62, 86].

The ordered, spaced arrays of zinc oxide nanowires were produced by Daragh Byrne and Séamus Garry of the Semiconductor Spectroscopy Laboratory at Dublin City University, according to the following prescription. First, a zinc oxide seed layer was chemically deposited by dropping a 0.005 M solution of zinc acetate in ethanol on to a silicon substrate. This was left for 20 s, then rinsed with pure ethanol and repeated five times. The substrate was subsequently annealed at 350 °C for 20 min. Zinc acetate reacts with water which has diffused into solution from the atmosphere. This reaction creates zinc hydroxide which precipitates to the substrate surface (it takes time for the hydroxide to precipitate from the bulk to the sample surface, hence the 20 seconds before rinsing). Zinc hydroxide decomposes to ZnO at the high temperatures during the anneal. The ZnO seed layer was then grown, by chemical bath deposition (CBD) at 90 °C for 1 hour, in a solution of 0.025 M zinc nitrate dissolved in hexamine. This growth was repeated with fresh solution, giving a total growth time of 2 hour. This ZnO layer was then coated with a self-assembled monolayer of 1 μm diameter polystyrene nanospheres, using the water transfer method, and allowed to dry. The resulting sample was annealed at 110 °C for 40 s. An acid catalyzed silica sol, of 0.5 ml tetraethyl orthosilicate and 0.5 ml hydrochloric acid in 20 ml of ethanol, was deposited into the interstitial spaces left exposed by the close packed nanosphere pattern. The latter was then removed by ultra-sonication in toluene first, followed by acetone. The remaining hexagonal silica surface lattice was densified by annealing at 400 °C with a 10 °C min^{-1} ramp rate. This was finally used as the substrate to deposit the ZnO nanowire arrays by vapour phase transport (VPT), with carbothermal reduction of ZnO powders and graphite as the Zn vapour source, at 900 °C for 60 min, yielding the final sample to be used in the FE measurements. Full details of the growth methods may be found in References [52, 87]. The finished samples were characterised with scanning electron microscope, and x-ray diffraction, as described in Section 3.3.

4.1.1 Current Voltage Characterisation

The field emission I-V data were taken with a sample-anode separation $d = 250\ \mu\text{m} \pm 10\ \mu\text{m}$ using the apparatus and procedure described in Section 3.1. The voltage was swept between 50 V and 2500 V in 1 V steps, at a rate of 1 V s^{-1}, until stable, reproducible, non-hysteretic data were obtained, which took ~150 cycles.

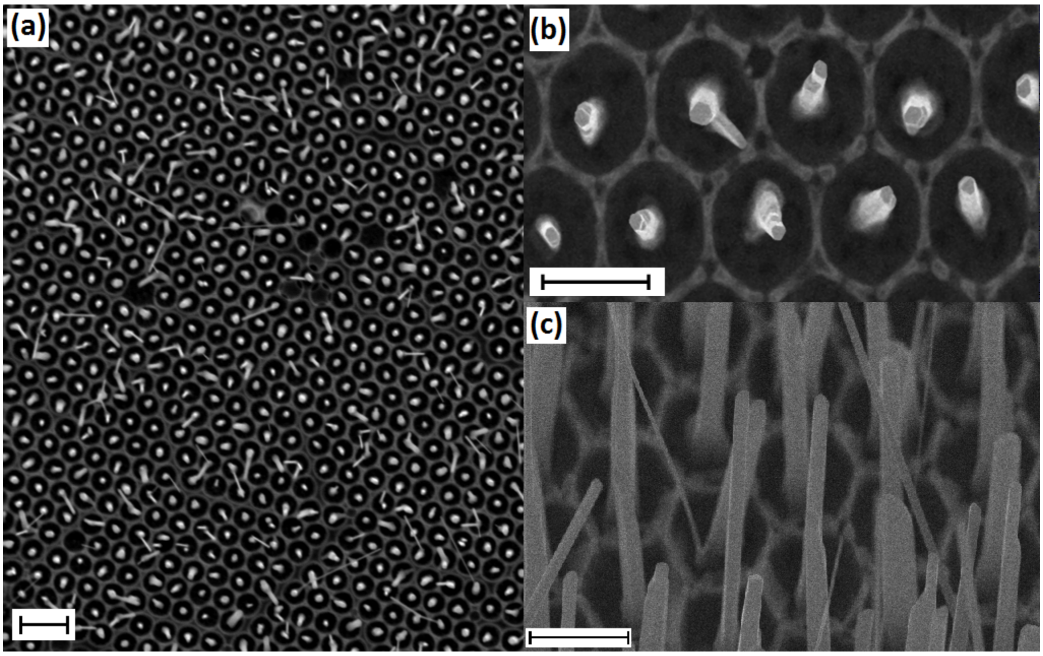

Figure 4.1: SEM and FE-SEM images of ZnO nanowire array, (a) SEM of sample viewed normal to surface taken before FE testing, (b) FE-SEM of sample viewed at 60° to the surface taken after FE testing, (c) FE-SEM of sample viewed at 50° to the surface taken after FE testing, with scale bars representing 2 μm, 1 μm, and 1 μm, respectively.

SEM images of the ZnO nanostructures are presented in Figure 4.1. Figures 4.1(a) was obtained before FE conditioning and measurements. Figures 4.1(b) and 4.1(c) were obtained with a higher resolution FE-SEM and after FE conditioning and measurements. Figure 4.1(a) shows a clear pattern of vertical ZnO nanowires, regularly spaced by a distance of 1 μm and positioned at the nodes of a 2D hexagonal close packed lattice. It is apparent that there are a number of void sites which are counted from the analyses of many areas of the sample at about 10 sites per 100 μm^2. Thus, the average site surface density is of the order of 0.9 per μm^2. As the electrode assembly covers an area of 5×10^{-5} m^2, a total of $\sim 4.5 \times 10^7$ nodes (nanowires) are sampled in a FE measurement.

From Figures 4.1(b) and (c), we observe that the typical morphology of a single nanowire is the familiar hexagonal prism oriented along the $\langle 002 \rangle$ direction; of average height around 2 μm, with a standard deviation of 0.29 μm; and average largest width/diameter of 0.2 μm, with a standard deviation of 58 nm (aspect ratio of 20). The ratio of inter-nanowire distance to nanowire length is therefore equal to 0.5. The nanowire dimensions imply a cross-sectional area of 2.6×10^{-2} μm^2 (or 3.1×10^{-2} μm^2 if a circular crosssection is assumed). This is close to the values of this ratio suggested in the literature as suitable for optimized FE [88]. The tip shape of the majority of the nanowires is curved outward rather than sharply pointed, and rarely seen to be flat-ended. We note from Figures 4.1(b) and (c) that the processes of conditioning and field emission do not appear to have a pronounced effect on the observable nanowire morphology. In particular, the change to a bulbous morphology at the tip, driven by temperature-dependent surface migration as seen by Semet *et al* [34], was not observed in the areas examined by SEM.

Figure 4.2 and Figure 4.3 shows x-ray diffraction data for the sample.

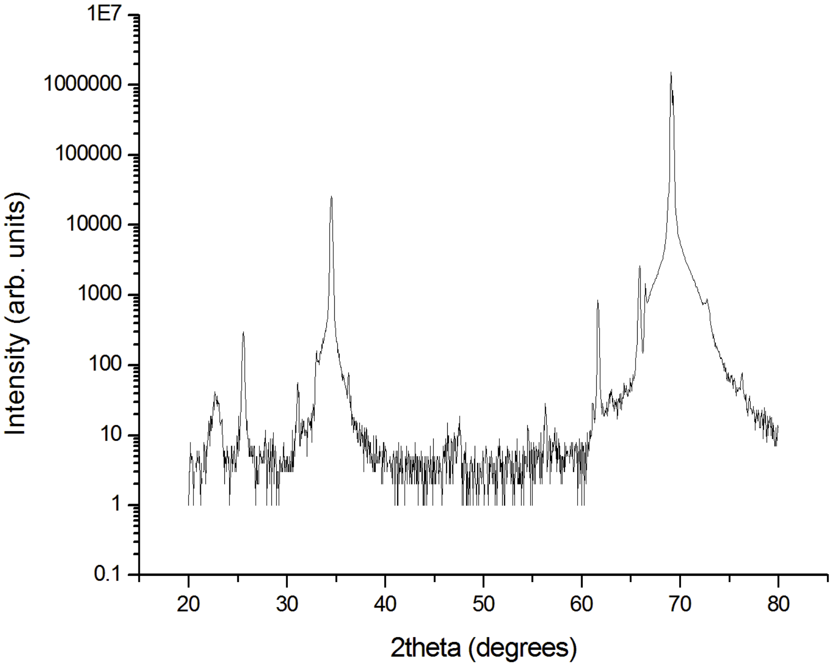

Figure 4.2: θ-2θ XRD scan of the sample

The θ-2θ scan in Figure 4.2 shows very intense diffraction peak at 34.3°, confirming the presence of crystalline zinc oxide in the (0002) orientation [89]. However, we are unable to determine from experiment whether the nanowires are either positively (0001) zinc- or negatively (000-1) oxygen-terminated or if a mixture of the two possible terminations prevails. Many other authors have reported, however, that the (0001) zinc terminated face tends to appear more tapered and this is consistent with the morphology we observe. The peak at ~69.1° is the (100) peak from the substrate [75].

The rocking curve scan in Figure 4.3, taken around the (0002) ZnO peak has a full width half maximum of 6.64°, which indicates reasonable alignment of the crystallites.

The final, reproducible I-V data set obtained after conditioning, and containing both the voltage ramping up and ramping down, which comprises

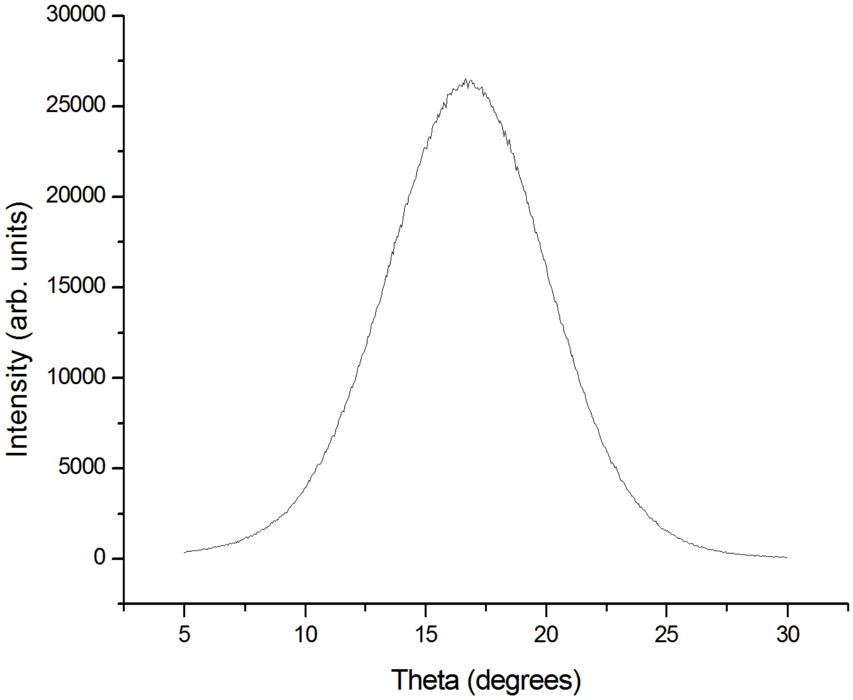

Figure 4.3: Rocking curve XRD scan of the sample

4900 data points is displayed in Figure 4.4. The full FN plot of $\log_{10}(I/V^2)$ vs. 1/V is displayed in Figure 4.5. An FN plot should be linear when field emission is the dominant process. This linear region can be seen on the left of Figure 4.5, with a curved region on the right in the low voltage regime. The turn-on voltage, the voltage at which detectable field emission begins, is taken as the lowest voltage of the linear regime. We can see that this is ∼1000 V. The linear region can be seen plotted in Figure 4.6.

Two linear regions can be observed on Figure 4.6, above and below 2000 V respectively, with a significant difference in slope between the two regions. The observed behaviour is typical of electron field emission with the distinct change in slope in the high voltage region often attributed to the buildup of a significant amount of space-charge at the tip[27, 90]. The

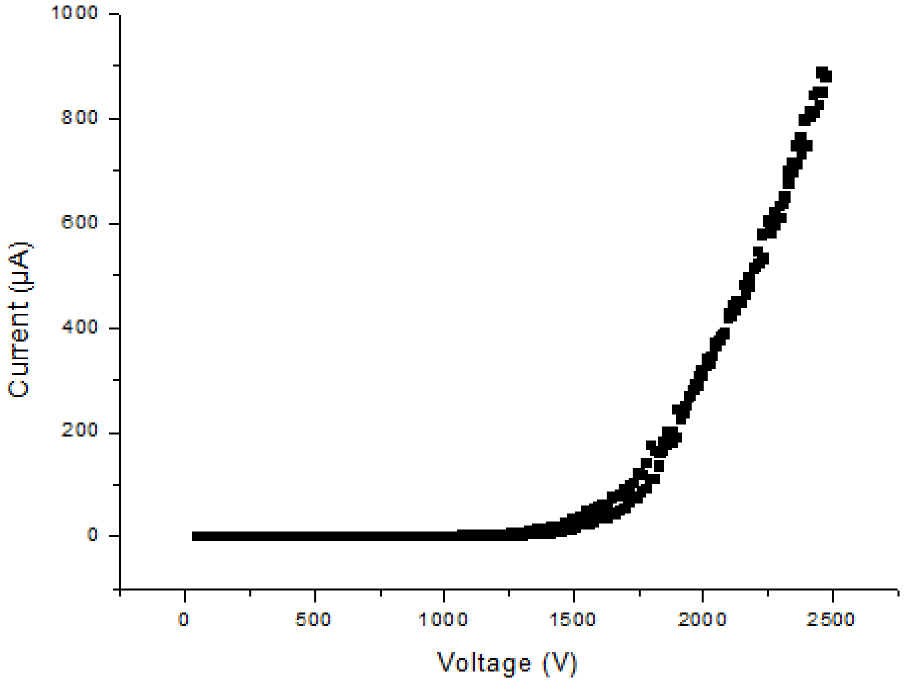

Figure 4.4: Current vs. Voltage plot of voltage ramping up from 50 to 2500 V and back down for the ZnO nanowire ordered array

deviations from linearity in the very low voltage region are not considered to be physically significant, and are mostly like noise due to stray fields and/or leakage currents.

The slope values of the low and high voltage linear regimes observed are measured at -5745 V and -2702 V, respectively. The slope, m, can be related to the field enhancement factor, β, and the work function, Φ, by Equation (2.37). The β factor is determined by local and large scale geometry, such that $F_S = \beta$V. This means that the β value obtained for an array of emitters represents the single tip current weighted average taken over the tip surface and the entire array [84]. The iterative approach outlined in Section 2.2.1 was applied using the appropriate work function values listed in Section 1.2, as well as the 1 eV estimated by Semet *et al* and a value for

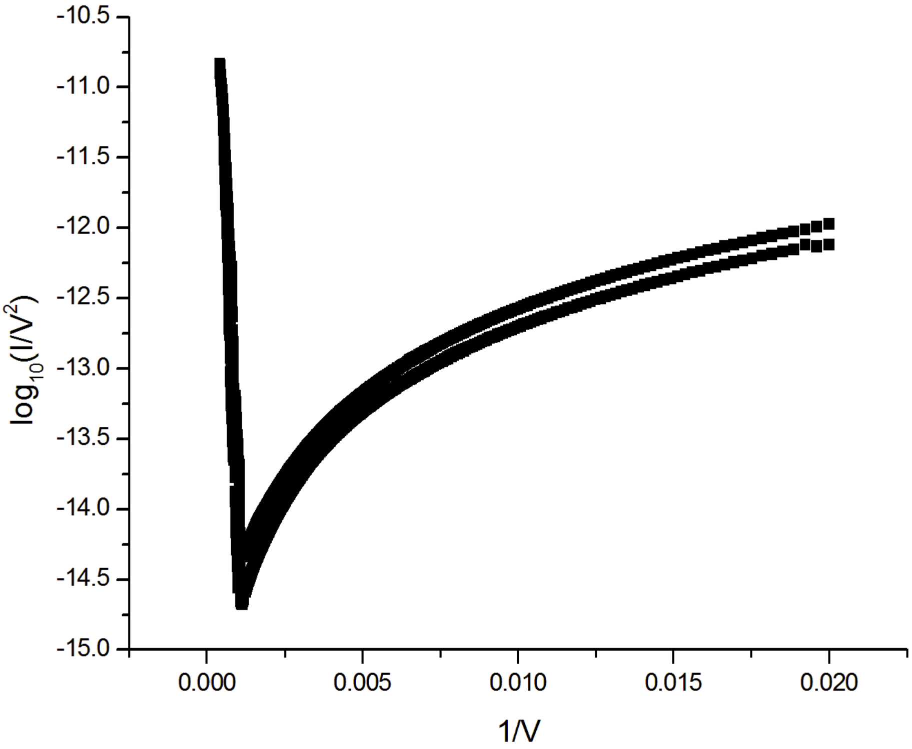

Figure 4.5: Full Fowler-Nordheim plot of the IV data, including ramp up and back down, for the ZnO nanowire ordered array

valence band emission [69, 70], for a voltage of 1500 V. The results are given in Table 4.1. Also provided are the Schottky lowering functions, which have been calculated using the Forbes approximations previously discussed, the current density (J_{FN}), emission area (A_{FN}), and the factor, γ, sometimes used in the literature, which is given by:

$$\gamma = \frac{F_S}{F_M} = \beta d \tag{4.1}$$

where d is the separation between anode and emitter, and F_M is the macroscopic applied field such that:

$$F_M = \frac{V}{d} \tag{4.2}$$

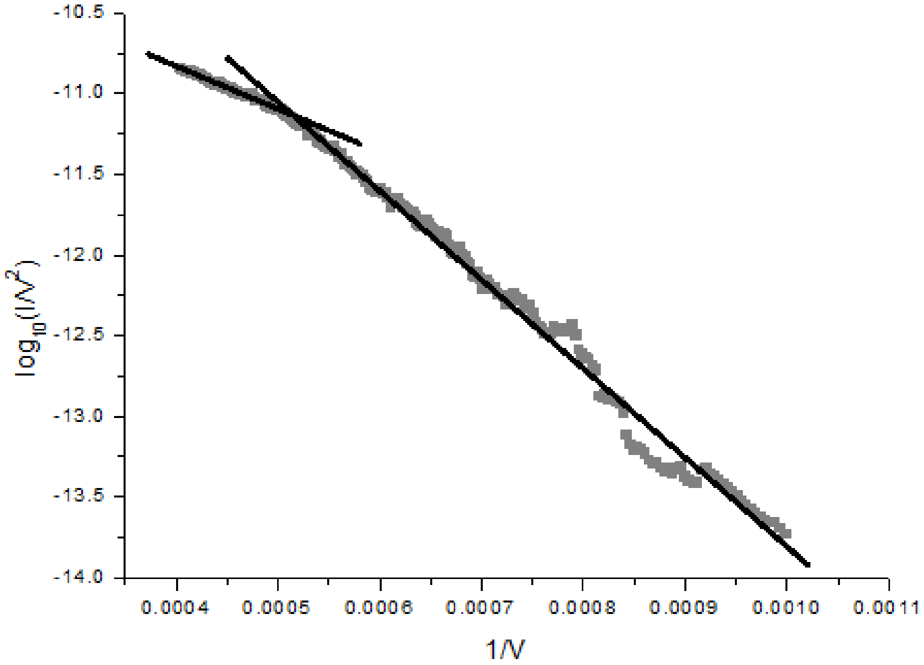

Figure 4.6: Linear region of Fowler-Nordheim plot for the ZnO nanowire ordered array, showing two distinct linear segments with differing slope

In this table, we can see typical surface field and current densities of $\sim 10^9$ Vm^{-1} and $\sim 10^{11}$ Am^{-2}, respectively. These are compatible with the results of similar types of FN analyses of sharp emitters [9]. We note that the use of a work function of 1.0 eV corresponds to a case of almost complete lowering of the barrier ($y \approx 1$), even at this moderate voltage. Thus, it would appear unsuitable for further interpretation of our data. For $3.3 \leq \Phi \leq 4.5$ eV, corresponding to conduction band electrons in the flatband diagram, the lowering of the barrier is more moderate (y = $\sim$0.7) and does not exceed the physical limit $y = 1$ at $V = 2500$ V, suggesting that the emission process is compatible with FN field emission. In this work function range, the field

ϕ **(eV)**	y	β **(m^{-1})**	γ	$s(y)$	$f(y)$	$t(y)$	F_S **(Vm^{-1})**	J_{FN} **(Am^{-2})**	A_{FN} **(m^{-2})**
1.0	0.97	0.4×10^6	109	0.84	0.05	1.11	7×10^8	3.2×10^{11}	7.7×10^{-18}
3.3	0.74	2.8×10^6	703	0.91	0.39	1.08	42×10^8	1.6×10^{11}	1.5×10^{-17}
3.7	0.73	3.4×10^6	839	0.91	0.42	1.08	50×10^8	1.6×10^{11}	1.5×10^{-17}
4.5	0.70	4.5×10^6	1135	0.92	0.46	1.08	60×10^8	1.7×10^{11}	1.4×10^{-17}
5.3	0.67	5.8×10^6	1460	0.93	0.49	1.07	88×10^8	1.8×10^{11}	1.4×10^{-17}
7.9	0.61	10.8×10^6	2693	0.94	0.57	1.06	162×10^8	3.2×10^{11}	1.1×10^{-17}

Table 4.1: Calculated Fowler-Nordheim parameters for various possible work function values

enhancement values (700-1100) are markedly lower than those reported in References [24, 27, 28, 90] based on the 5.3 eV value. The choice of a work function of $\Phi = 7.9$ eV corresponding to electrons emitted from the top of the ZnO valence band [69, 70] leads to even larger values of the enhancement factor and the surface field strength.

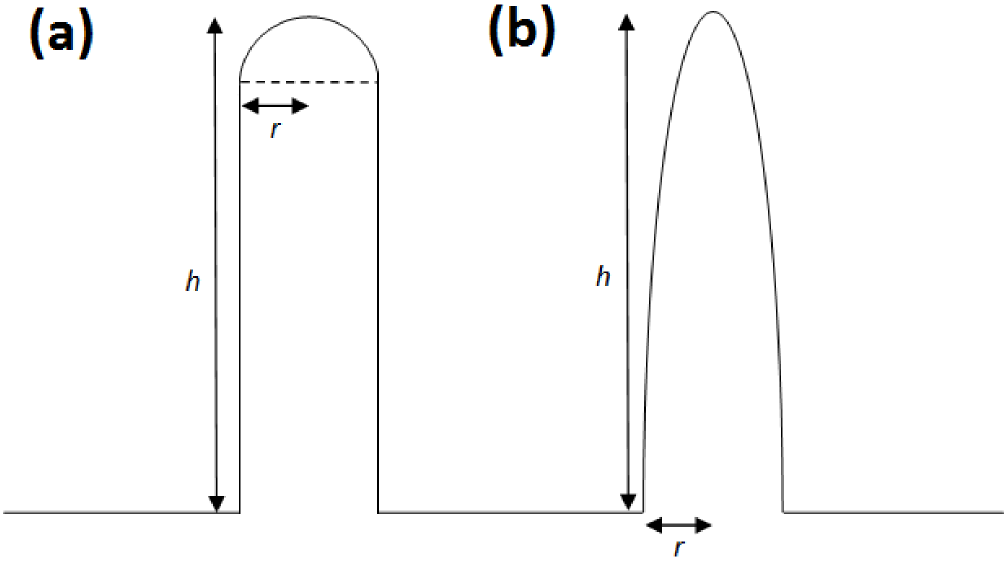

Figure 4.7: Geometrical models: (a) Hemisphere on a post, and (b) prolate hemi-ellipsoid

The β and γ factors are geometrical parameters, describing the field enhancement at the emitter tip as compared to a planar emitter, due to its sharp geometry. There are many models to estimate these factors for different emitter shapes using the dimensions of the emitters, which can be obtained using SEM. Forbes *et al* [85] have collected and summarized a number of models and approximations for γ from the literature. As previously stated, the average height and diameter of the nanowires was found by SEM to be $\sim$2 μm and $\sim$0.2 μm, respectively, giving an aspect ratio (ν) of $\sim$20. They give several author's different models for a hemisphere on a post emitter shape (see Figure 4.7 (a)), which are as follows:

$$\gamma = 2 + \nu \tag{4.3}$$

$$\gamma = \frac{\nu}{2^{\frac{1}{2}}} \tag{4.4}$$

$$\gamma = 0.72\nu \tag{4.5}$$

$$\gamma = 1.2(2.15 + \nu)^{0.90} \tag{4.6}$$

$$\gamma = 5.93 + 0.73\nu - 0.0001\nu^2 \tag{4.7}$$

Forbes *et al* also give two different models based on a prolate hemi-ellipsoidal of revolution (see Figure 4.7 (b)). The key dimensions for this shape are the base radius, r, the hemi-ellipsoid height, h, and the apex radius of curvature, r_a, which is given by:

$$r_a = \frac{r^2}{h} \tag{4.8}$$

$$\gamma = \frac{\zeta^3}{[\nu \ln(\nu + \zeta)] - \zeta} \tag{4.9}$$

where

$$\zeta = (\nu^2 - 1)^{\frac{1}{2}} \tag{4.10}$$

and

$$\gamma = 2 + \frac{h}{r_a} \tag{4.11}$$

These models were applied to the dimensions previously stated, and give γ values of 22, 14.14, 14.4, 19.50, 20.49, 148.17 and 402, for the models in Equations (4.3) - (4.7), (4.9), and (4.11), respectively.

Kirkpatrick *et al* [83] give another hemi-ellipsoidal model given by:

$$\gamma = \frac{2}{[\eta(\eta^2 - 1)][\ln(\frac{\eta+1}{\eta-1}) - \frac{2}{\eta}]} \tag{4.12}$$

where

$$\eta = \frac{h}{(h^2 - r^2)^{\frac{1}{2}}} \tag{4.13}$$

Applying this model gave a value of $\gamma = \sim 145$. Read and Bowring [84] detail a model to account for electrostatic shielding due to the space charge in the vacuum gap between emitter sample and anode. Most models calculate the field enhancement for an individual emitter, however in an array the field enhancement of any given emitter may be inhibited by electrostatic shielding by neighbouring emitters. Read and Bowring's model accounts for this shielding, for a square array of emitters, and is given by:

$$\gamma = \gamma_0(1 - 0.99\exp(-1.253(s/h)^{1.18})) \tag{4.14}$$

where γ_0 is the γ factor for an individual emitter, h is the emitter height, and s is the separation between emitters.

The zinc oxide ordered array under analysis is a hexagonal close-packed array, rather than a square array. However this model can be applied as an approximation, and gives a shielding effect of $0.43\gamma_0$. Thus it can be estimated that there is a shielding effect of ~50% in an array of this spacing.

When comparing these modelled γ values with those of Table 4.1, we observe a generally poor agreement, with discrepancies by factors of between 5 and 8. Similar disagreement levels between measurements and calculations are also common in the current literature on the topic of ZnO nanowire FE [28, 34, 90]. In order to obtain modelled values which would agree with the values determined from analysis of the I-V data, a radius of ~50 nm would have to be assumed.

The hemi-ellipsoidal models provide the nearest agreement in γ factors, however the exact tip shape cannot be clearly discerned from the SEM images, and as such it can't be determined if this model shape is physically accurate. However, similar zinc oxide nanowires investigated by tunnelling electron microscopy in reference [27] appear to support this shape.

The two linear regimes observed in the FN plot of Figure 4.6 have been briefly mentioned. The slope value in the high-field regime is measured at -2702 V and is significantly reduced compared with its value in the low field regime. We observe that the transition between these regimes occurs gradually around a voltage of 2 kV over a range of about 150 V. We note that these two distinct regimes are also observed by Jeong *et al* [27] in the case of ZnO nanowires and Al-Tabbakh *et al* [69, 70] in the ZnO tetrapods.

Such high-field deviations from the FN straight-line have been commonly observed in FE experiments and typically interpreted in terms of the occurrence of space-charge effects, where the volume of electrons above the sample due to emission screens the emitters inhibiting further emission, at higher currents [91–93]. Stern *et al* [91] detail a numerical criterion in cgs units, T, for judging the negligibility where T is given by:

$$\mathrm{T} = \left(\frac{16\pi}{3}\right)\left(\frac{m_e}{2e}\right)^{\frac{1}{2}} \frac{IV^{\frac{1}{2}}}{AF_S^2} \tag{4.15}$$

where m_e and e are the mass and charge of the electron respectively, and A is the area of the sample covered by the anode. When T << 1 the space-charge effects can be considered negligible. Calculating for this ZnO nanowire array gives a value for T of ∼0.06 and ∼0.4 at 1500 V and 2000 V respectively, showing that space-charge effects may contribute to observed behaviour in the high voltage region.

Besides space-charge effects, the lower slope of the FN plots at high field, within the framework of cold emission FN theory, can be due to two effects: changes in the work function [94] or the field enhancement factor [83]. As a larger surface area of the emitter will contribute to the emission at higher fields, the assumption of a non-uniform work function over the probe area is reasonable. Also, contributing tips having different crystallographic terminations may have a contribution and we have shown previously in this section that a small change in the value of the work function can significantly alter the outcome of the FN analysis. The work functions of other faces of

ZnO have been measured: 5.05 eV for the prismatic faces [30] and 4.05 eV for the (10-1-1) faces [31], and show sufficient variance to have an effect if engaged in the field emission process. Kirkpatrick *et al* [83] have shown that for an emitter with nanometric-sized tips of hemi-ellipsoidal shape the field enhancement factor γ decreases and the effective emission area α increases with increasing applied field, while a standard FN analysis would lead to the opposite conclusion (see also References [92, 93]). This is seen in the high-field region of the data, as an increased γ value of 1540 would be obtained at 2000 V if a constant work function of 3.7 eV were assumed. Furthermore, this analysis would yield a $y > 1$, indicating an inconsistency in the FN plot analysis. However the departure from FN linearity at high field could be satisfactorily accounted for by the field dependence of the work function and the enhancement factor. Alternative explanations, based on the semiconductor electronic structure of ZnO, have been put forward by other authors.

One such explanation, by Jeong *et al* [27], suggested that the emission proceeds from deep-level defect states in the low field regime whereas the high field regime consists of electrons emitted from near the Fermi level. Al-Tabbakh *et al* [69, 70] suggested that low-field emission in the conduction band ultimately saturates as the field is increased and leads to predominant emission from the valence band in the high field regime with a related increase in the work function value. However our results do not clearly support or contradict these possibilities.

From an I-V measurement, one can estimate a value for the emission area A when the current density J is obtained, via $A = I/J$. In the case of a large-area electron source composed of many identical sharp emitters, this area is an average over the tip surface weighted by the local value of the current density and extended to the macroscopic area of the sample

[27, 91, 95]. Such values for this emission area were extracted for the ordered ZnO nanowire array, A_{FN}, from the measured data using various approaches.

In Table 4.1, values for A_{FN} can be seen, determined by solving the FN equation using parameters calculated by the iterative method and Forbes approximations, as previously discussed. The values of A_{FN} are small compared to the surface area of the tip of one nanowire that would be obtained from its estimated dimensions and weakly dependent on the value of the work function in the 3.0-8.0 eV range. In Section 2.2.1, specifically Equation (2.40) and (2.41), a method outlined by Charbonnier [62] which utilises this weak dependence, to create a work function independent approximation for the current density, J. The variable in this approximation is m/V. A plot of m/V against $\log_{10}(J)$ should give a straight line. Such a plot can be seen in Figure 4.8, and a plot of J vs. V for the iterative method and Charbonnier's method in Figure 4.9.

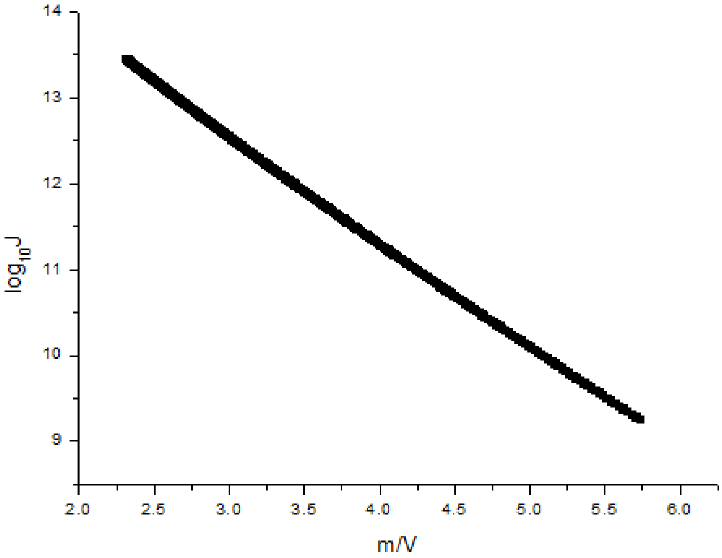

Figure 4.8: A log plot of current density, J, vs m/V

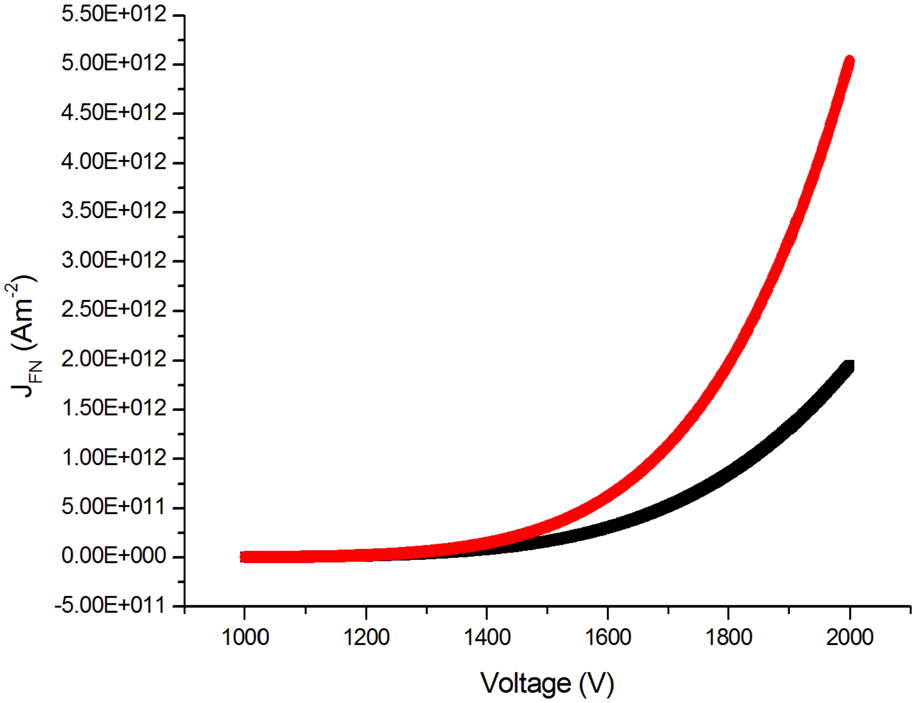

Figure 4.9: Plot of current density, J_{FN}, vs voltage, V, for the iterative method (black) and Charbonnier's method (red)

The two methods show good agreement at low voltage, with the difference becoming more pronounced at higher voltages. This discrepancy arises because Charbonnier's method is based on fixed values for $s(y)$ and $t(y)$, which are accurate at low voltage, whereas in the iterative method these values are calculated for each data point using the highly accurate Forbes approximations. In Figure 4.10 a plot of the corresponding area values for the current densities obtained by both methods is shown. The same discrepancy at high voltage can be seen in the area values. Area values are on the order of 10^{-17} m^2 (10^{-13} cm^2). In view of the number of nodes probed by the anode in the present conditions ($\sim$4.5 $\times$ 10^7), the effective emitting area per nanowire can only be of dimensions of the order of a few atomic sites, even if only 1% of the nanowires are actual emitters. Spindt *et al* [9] conclude identically although there are significant differences in the morphology, nature (metallic), and surface density of the molybdenum emitter cones used.

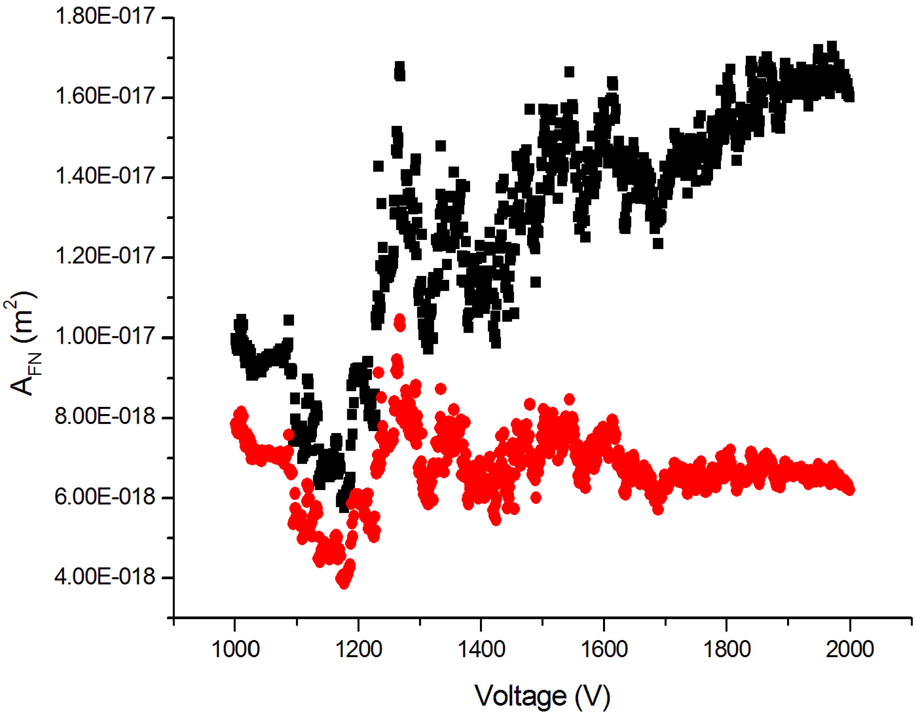

Figure 4.10: Plot of emitting area, A_{FN}, vs voltage, V, for the iterative method (black) and Charbonnier's method (red)

From the viewpoint of field emission applications, such as electronic display devices, we can compute the following figures of merit for this ZnO nanowire array cathode. The onset voltage of field emission was around 1000 V at which the device emitted a current of 14 nA, corresponding to a macroscopic current density of 2.7×10^{-3} Am^{-2} and an applied field of 4×10^6 Vm^{-1}. To obtain a threshold current of 10 mAcm^{-2} (the value required for field emission displays [2]) required a voltage of 1323 V, corresponding to an applied field of 5.3×10^6 Vm^{-1} with an emitted current of 513 nA. At 2000 V, the macroscopic current density is 0.62 Am^{-2}, corresponding to a current per nanowire of 31 nA (assuming 50% efficiency).

4.1.2 Imaging

Another ordered zinc oxide nanowire array, grown using the same techniques, was examined using the phosphor electrode described in Section 3.1.3, and high resolution FE-SEM. Transparent, phosphor coated electrodes are occasionally used to determine the uniformity of emission across a sample [25, 96–98]. However, these data are seldom analysed in depth. It is clear from the previous analyses that the γ factors determined experimentally are higher than modelled values, and that the emission areas determined by FN analysis are extremely small. By using the phosphor electrode data and the emitter geometry obtained by FE-SEM, it should be possible to estimate area and current density, independent of FN theory. FE-SEM images of the ZnO nanowire array are presented in Figures 4.11 and 4.12. The dimensions agree well with the sample in Part (a). However the higher resolution of the FE-SEM allows for detailed imaging of the nanowire tip. The hexagonal prism shape of the nanowire can be clearly observed. The tip shape appears to be curved rather than sharply or flatly terminated. In examination after field emission experiments, bulbous tips, similar to those observed by Semet *et al* [34] and attributed to melting, can be seen.

The voltage on the phosphor anode was increased in 1 V increments at a rate of 1 Vs^{-1}, and images of the phosphor were taken at 1250 V, 1500 V and 1750 V. These images can be seen in Figures 4.13, 4.14, and 4.15. These images were analysed by summing the number of lit pixels to determine a total lit area, and by summing the number of resolvable distinct dots. The 1750 V data exhibited significant saturation, and could not be accurately analysed in this way. However for the 1250 V and 1500 V images, this analysis allowed the determination of a maximum number of emitting rods, under the

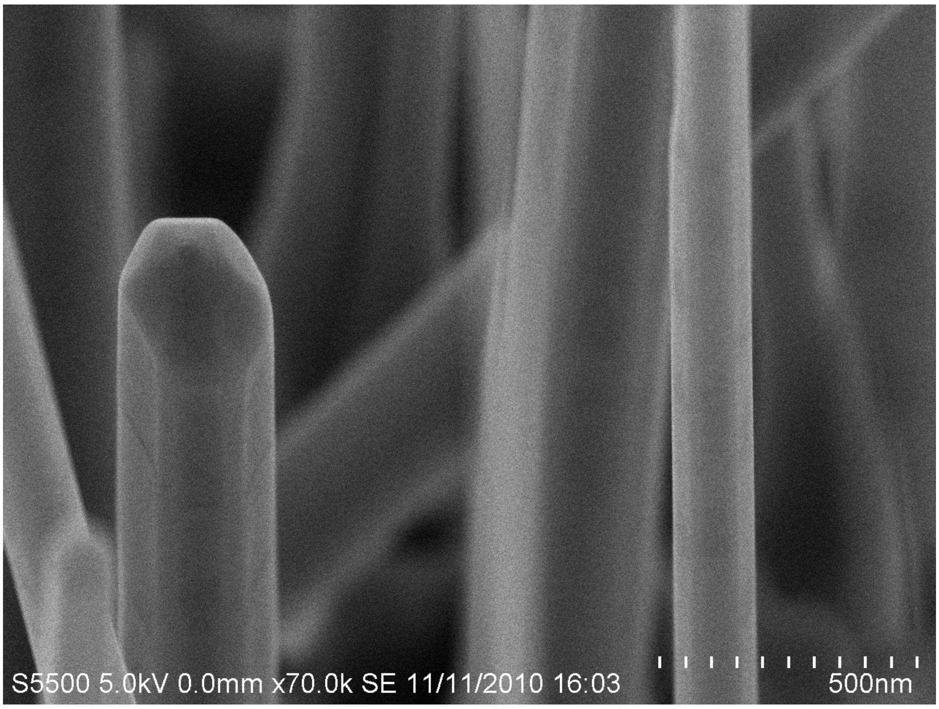

Figure 4.11: FE-SEM of a ZnO nanowire tip, taken before field emission testing

assumption that every nanowire covered by the lit area was emitting, and a minimum number of emitting rods, under the assumption that each dot was due to the emission of an individual nanowire. The maximum number of emitters was estimated to be 1.28×10^6 for the image taken at 1250 V and 8.16×10^6 for the image taken at 1500 V. The minimum number of emitters was estimated to be ~150 for the image taken at 1250 V and ~1300 for the image taken at 1500 V.

If we apply the maximum and minimum number of emitters to the small emission areas given by the FN treatments, we get values on the order of 10^{-19} - 10^{-23} m^2 per rod, suggesting emission at the tip coming from only a few atomic sites, which as we have noted was the conclusion in Reference [9]. The area can be estimated, independent of FN theory, by calculating the area of a tip based on the geometry observed by FE-SEM and applying the

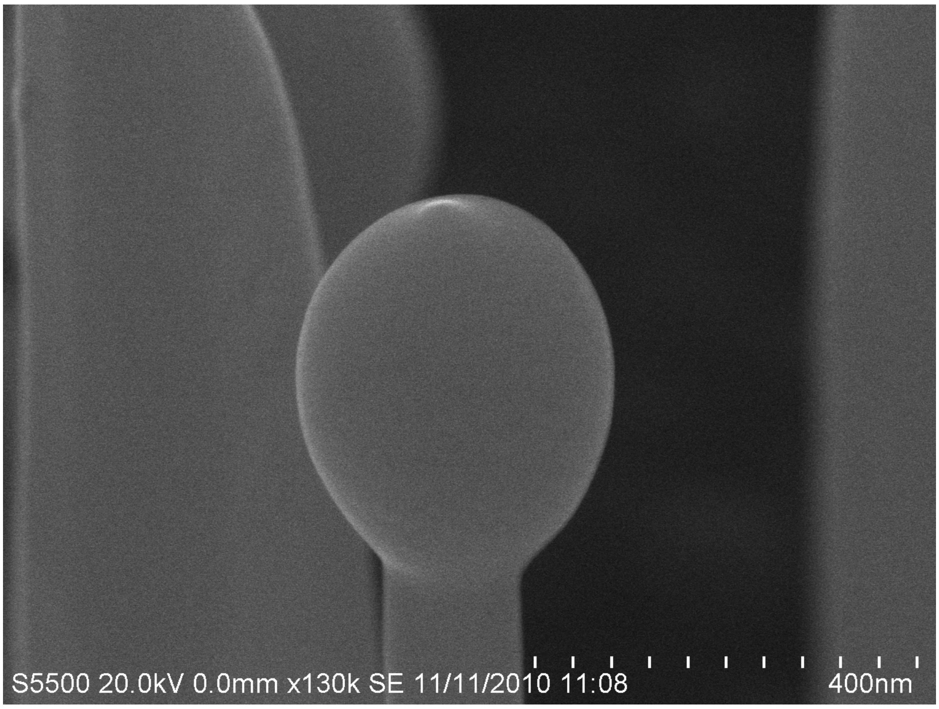

Figure 4.12: FE-SEM of a ZnO nanowire tip, taken after field emission testing

maximum and minimum number of emitters. These estimates can be seen in Table 4.2, based on three possible emitter radii: the radius of one of the typical hexagonal nanowires (pre-FE), the radius of one of the bulbed tips observed after field emission testing (post-FE), and the radius of the small bulbous protrusion on the tip (small bump).

The areas estimated by these methods are much larger than those determined from FN analysis. These areas can be used to calculate values for the current density using Equation (2.31). The results of these calculations can be seen in Table 4.3. Using these current densities, the FN equation, Equation (2.29), and the Forbes approximations, γ factor values can be estimated for an assumed work function. Values for an assumed work function of $\Phi = 3.7$ eV can be seen in Table 4.4. Unlike the areas and current densities, these γ factors are not independent of FN theory. We can see that they give

Figure 4.13: Image of phosphor taken at 1250 V

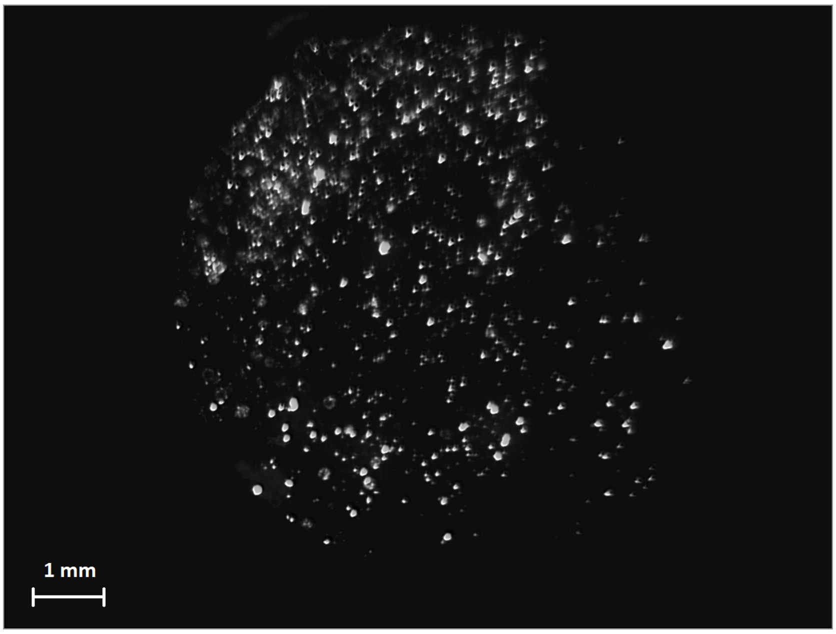

Figure 4.14: Image of phosphor taken at 1500 V

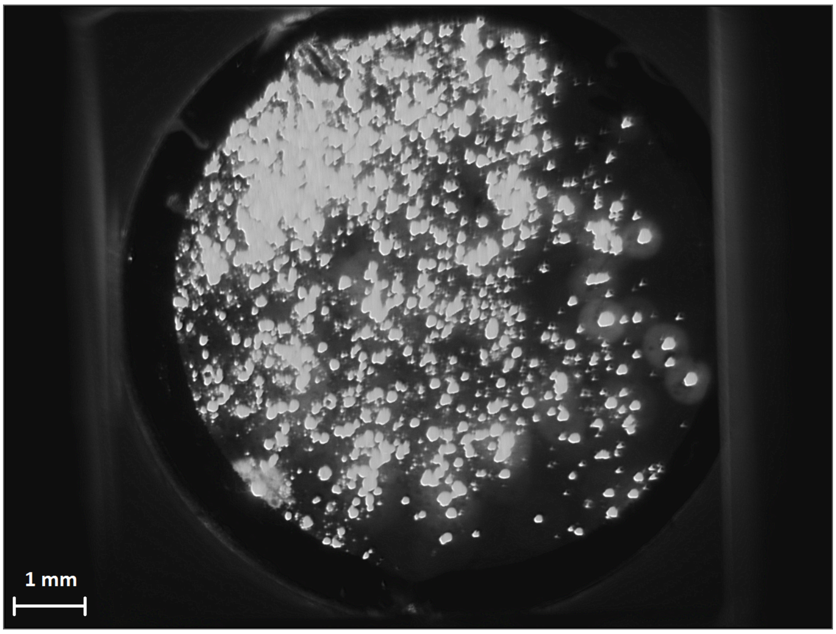

Figure 4.15: Image of phosphor taken at 1750 V

Tip type	**Tip area ($\mathbf{m^2}$)**	$\boldsymbol{A_{1250min}}$ ($\mathbf{m^2}$)	$\boldsymbol{A_{1250max}}$ ($\mathbf{m^2}$)	$\boldsymbol{A_{1500min}}$ ($\mathbf{m^2}$)	$\boldsymbol{A_{1500max}}$ ($\mathbf{m^2}$)
Pre-FE	6.53×10^{-14}	9.80×10^{-12}	8.36×10^{-8}	8.49×10^{-11}	5.33×10^{-7}
Post-FE	8.53×10^{-14}	1.28×10^{-11}	1.09×10^{-7}	1.11×10^{-10}	6.96×10^{-7}
Small bump	1.79×10^{-15}	2.69×10^{-13}	2.29×10^{-9}	2.33×10^{-12}	1.46×10^{-8}

Table 4.2: Phosphor areas for maximum and minimum number of emitters at 1250 V and 1500 V, for three possible emitter radii

Tip type	$\boldsymbol{J_{1250min}}$ ($\mathbf{Am^{-2}}$)	$\boldsymbol{J_{1250max}}$ ($\mathbf{Am^{-2}}$)	$\boldsymbol{J_{1500min}}$ ($\mathbf{Am^{-2}}$)	$\boldsymbol{J_{1500max}}$ ($\mathbf{Am^{-2}}$)
Pre-FE	4.90×10^{5}	5.74×10^{1}	3.88×10^{5}	6.19×10^{1}
Post-FE	3.75×10^{5}	4.40×10^{1}	2.98×10^{5}	4.74×10^{1}
Small bump	1.79×10^{7}	2.10×10^{3}	1.42×10^{7}	2.26×10^{3}

Table 4.3: Current densities for maximum and minimum number of emitters at 1250 V and 1500 V, for three possible emitter radii

better agreement with the modelled values than those determined from FN analysis of I-V data in Part (a).

Tip type	$\gamma_{1250min}$	$\gamma_{1250max}$	$\gamma_{1500min}$	$\gamma_{1500max}$
Pre-FE	452	322	373	269
Post-FE	447	319	369	267
Small bump	538	364	443	304

Table 4.4: γ factor for maximum and minimum number of emitters at 1250 V and 1500 V, for three possible emitter radii

From the average phosphor dot size and the tip radius as observed by FE-SEM, assuming each dot represents emission from one nanowire, the angle of the cone of emission from a nanowire can be estimated. All three tip radii used previously give a cone angle of 9 - 11°.

4.2 The Effect of Inter-wire Spacing on Field Emission

It has been established that nanosphere lithography is a useful tool for catalyst-free growth of ordered, spaced arrays of ZnO nanowires. An additional benefit of nanosphere lithography is the faculty to vary the spacing of the nanowires in the array, by use of different sphere sizes. In the previous section, a model which takes account of shielding by neighbouring nanowires on the field enhancement factor was discussed (Equation (4.14)). The further spaced the nanowires, the less effect each nanowire has on its neighbouring nanowires, and thus the greater the field enhancement factor. However, the further spaced the nanowires are, the less nanowires in a given unit area, decreasing the overall current density. The authors of this model [84] suggest the optimum spacing will be a ratio of separation (s) to nanowire height (h) of between 1 and 2.

To experimentally investigate the effect of inter-wire spacing, ordered ZnO nanowire arrays were grown by Séamus Garry, of the Semiconductor Spectroscopy Laboratory at Dublin City University, using 3 sizes of polystyrene nanospheres: 500 nm, 1 μm, and 1.5 μm diameter, respectively. Samples were grown by two methods, one based on vapour phase transport growth of the nanowires, the other based on chemical bath deposition of the nanowires.

The VPT method used was similar to the method used in Section 4.1, with some revisions. In brief, a seed layer was deposited on a (100) Silicon substrate by drop coating with a 0.005 M zinc acetate in ethanol solution. This was allowed to remain on the substrate for 20 seconds before rinsing with ethanol and drying under a stream of nitrogen. This procedure was repeated 5 times. The substrate was then annealed for ~30 mins at 350 °C. CBD deposition was then carried out on seeded substrate using an aqueous solution of Zn acetate at 0.025 M concentration heated to ~65 °C, for a deposition time of ~3 hours to produce thin film of ~250 - 300 nm thickness. Substrates are removed after 90 minutes and rinsed with de-ionised water to remove any material which has precipitated in the solution and attached to the surface and then growth was continued for the remaining 90 minutes in a fresh solution. A self-assembled monolayer of the polystyrene nanospheres was deposited on the surface by the water transfer method, and allowed to dry. The nanosphere coated sample was annealed at 110 °C for ~30 seconds. A silica sol was prepared by mixing 1 ml of TEOS and 1 ml of the chosen acid catalyst to 20 ml of absolute ethanol, and stirring for 3 hours. The acid catalyst may be 0.05 M sulphuric acid (H_2SO_4) or 0.1 M hydrochloric acid

(HCl). The choice of acid catalyst was not observed to affect the sol produced. The silica sol was mixed with an equal volume of ethanol before being applied to the surface and allowed to dry in air, to deposit silica in the interstitial spaces left exposed by the close packed nanosphere pattern. The spheres were removed by sonicating in toluene for 15 minutes, then rinsed with deionised water and dried with a stream of nitrogen. The remaining hexagonal silica surface lattice was densified by annealing at 450 °C with a 15 °C min^{-1} ramp rate. The sample was then grown on by a CBD deposition, using the same solution concentration and temperature, for 30 minutes. This serves two purposes, firstly it deposits a small nanostructure in the apertures in the silica mask which aids uniform nucleation in VPT deposition, and secondly due to the lateral growth exhibited by Zn acetate derived CBD deposition, it may cap off any grain defect present in the buffer layer, significantly reducing multi-wire nucleation in the VPT deposition. Finally, the sample was grown on in the VPT deposition. 60 mg of both ZnO and graphite powders are used and the samples are placed directly above the powders. The furnace temperature was set to 800 °C and held for 11 minutes. It was then raised at a rate of 10 °C min^{-1} until it reached 900 °C. This temperature was then held for the remainder of the growth time (1 hour in total). The growth was performed under a flow of 90 sccm argon. Unordered samples, with uncontrolled spacing can be grown by depositing the thin film as described above, then growing with VPT as described above, without any lithography. Two sets of samples were grown by this method, VPT1 which consisted of an unordered, 500 nm spaced, and 1 μm spaced sample, and VPT2 which consisted of an unordered, 500 nm spaced, 1 μm spaced, and 1.5 μm spaced sample.

The CBT method used the same steps as above in depositing the thin film and silica mask. The sample was then grown on by a CBD deposition, using the same solution concentration and temperature for 180 minutes to grow nanowires at the exposed points in the CBD mask. An unordered sample with uncontrolled spacing could not be grown by CBD, as omitting the silica mask and growing on the thin film with CBD simply causes further film growth. The set of CBD samples consisted of a 500 nm, 1 μm, and 1.5 μm spaced sample.

The arrays produced by the VPT method were analysed by SEM, the results of which can be seen in Figures 4.16 - 4.29. The lack of ordered and uniform spacing can be seen in the non-lithographic samples (Figures 4.16, 4.17, 4.22, and 4.23). In the lithographic samples, the ordered pattern and uniform spacing is evident, with defects in the pattern typically leading to areas with no growth. However there is some anomalous growth, usually in the form of thin, randomly oriented wires. The nanowires are vertically oriented, and aligned to within a few degrees of perpendicular to the substrate. For the ordered arrays the number of nanowires per unit area, or nanowire density, can be estimated from the pattern. For 500 nm spaced arrays there will be $\sim 4 \times 10^{12}$ nanowires per m^2, for 1 μm spaced $\sim 1 \times 10^{12}$ nanowires per m^2, and for 1.5 μm spaced $\sim 4.44 \times 10^{11}$ nanowires per m^2. For unordered samples, the nanowire density can be estimated from the SEM results. For the VPT1 unordered sample, this was $\sim 4.3 \times 10^{12}$ nanowires per m^2, and for the VPT2 unordered sample it was $\sim 5.6 \times 10^{12}$ nanowires per m^2. These nanowire densities are close to the density for 500 nm spaced samples. Samples were analysed by XRD. A plot of θ-2θ scans for a typical thin film, unordered, and ordered sample are shown in Figure 4.30. In the θ-2θ we observe the (100) silicon peak at $\sim 69.1^\circ$, and the (0002) zinc oxide peak at $\sim 34.4^\circ$. In Figure 4.31 we present a rocking curve scan taken around

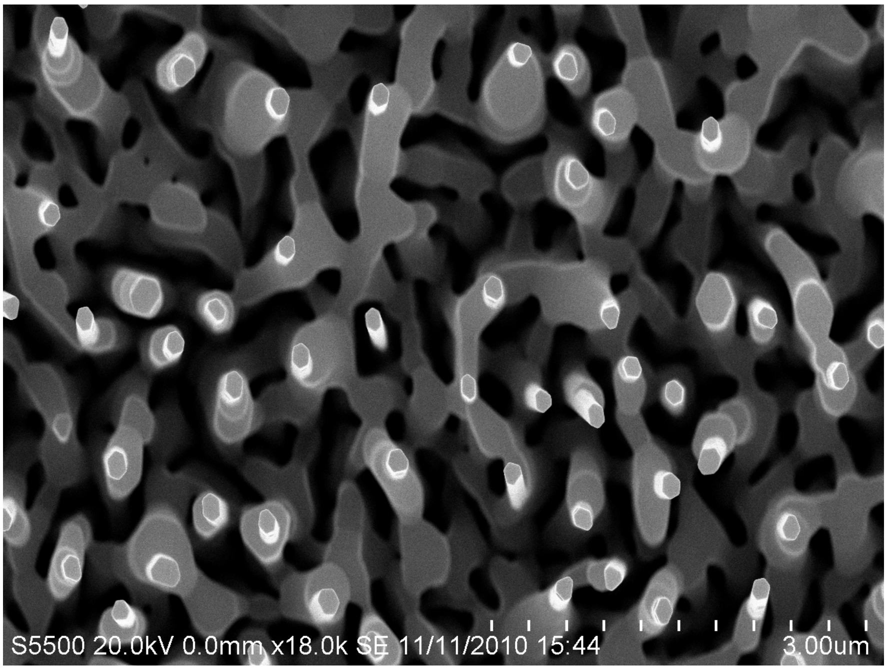

Figure 4.16: SEM image of VPT1 unordered sample at 0 ° observation angle

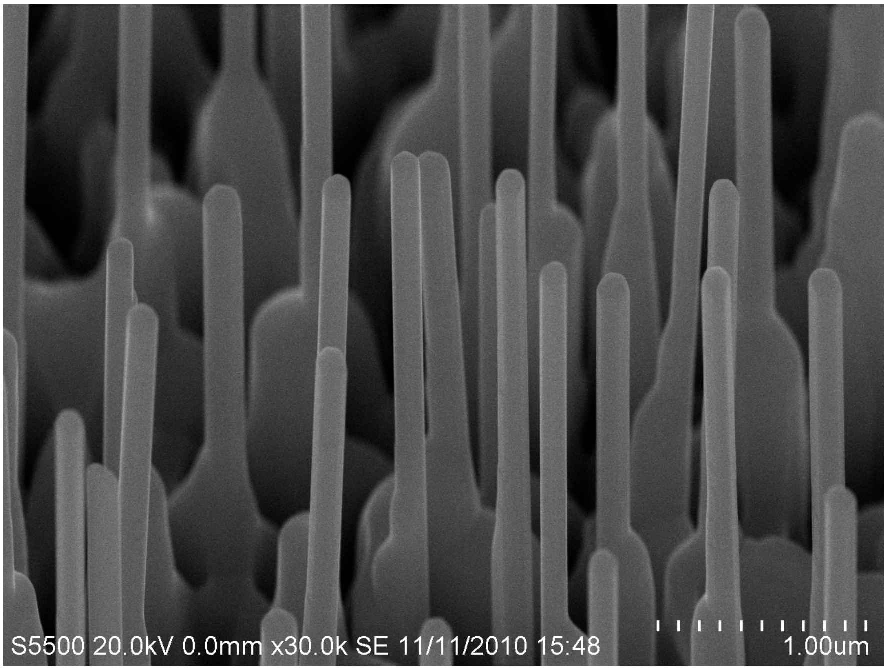

Figure 4.17: SEM image of VPT1 unordered sample at 60 ° observation angle

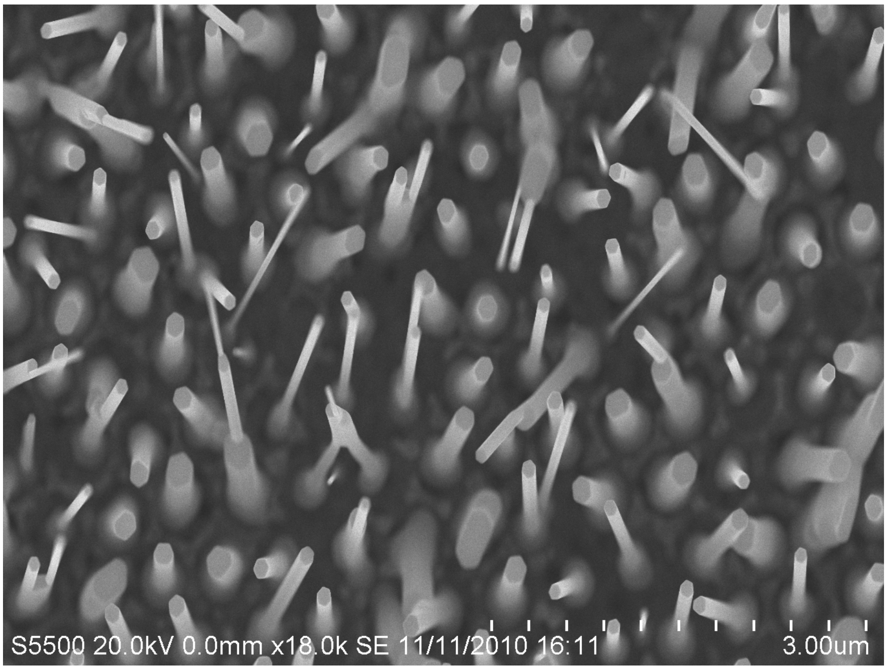

Figure 4.18: SEM image of VPT1 500 nm sample at 0 ° observation angle

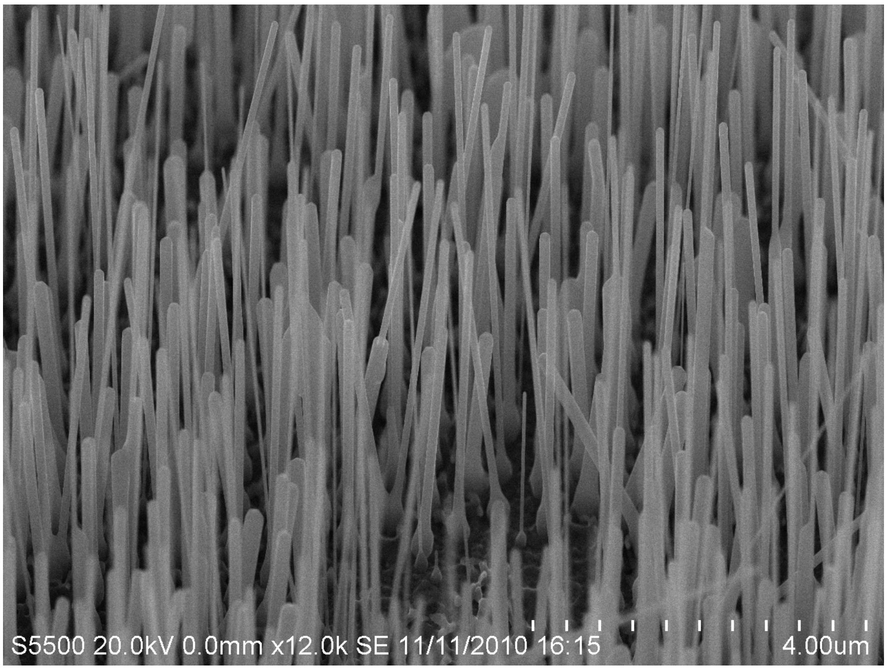

Figure 4.19: SEM image of VPT1 500 nm sample at 60 ° observation angle

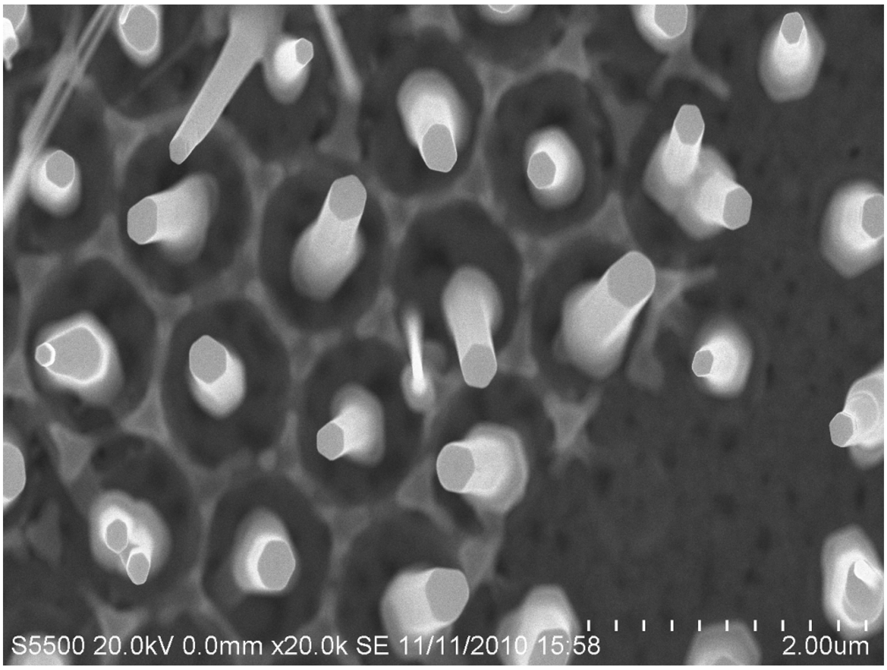

Figure 4.20: SEM image of VPT1 1 μm sample at 0 ° observation angle

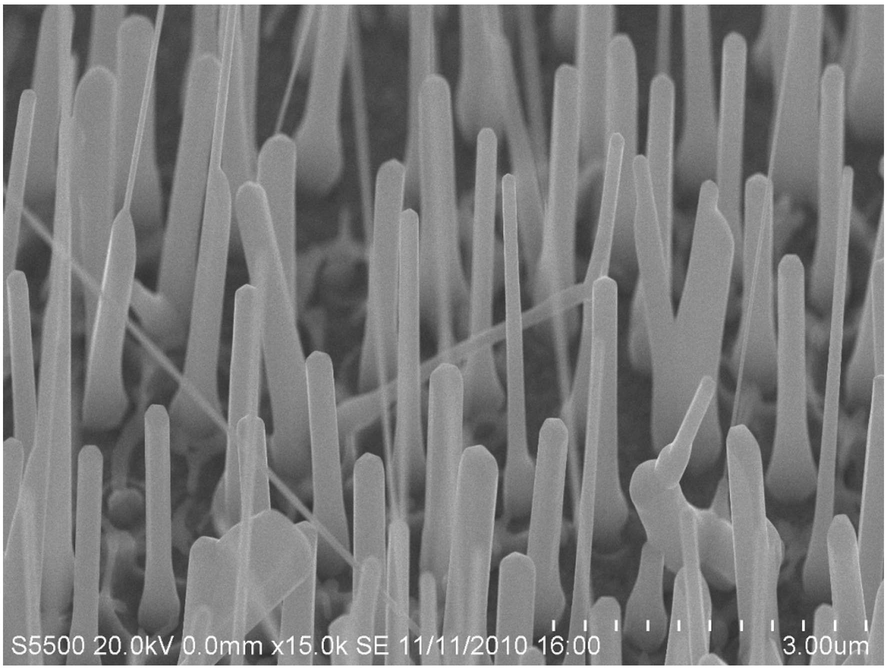

Figure 4.21: SEM image of VPT1 1 μm sample at 60 ° observation angle

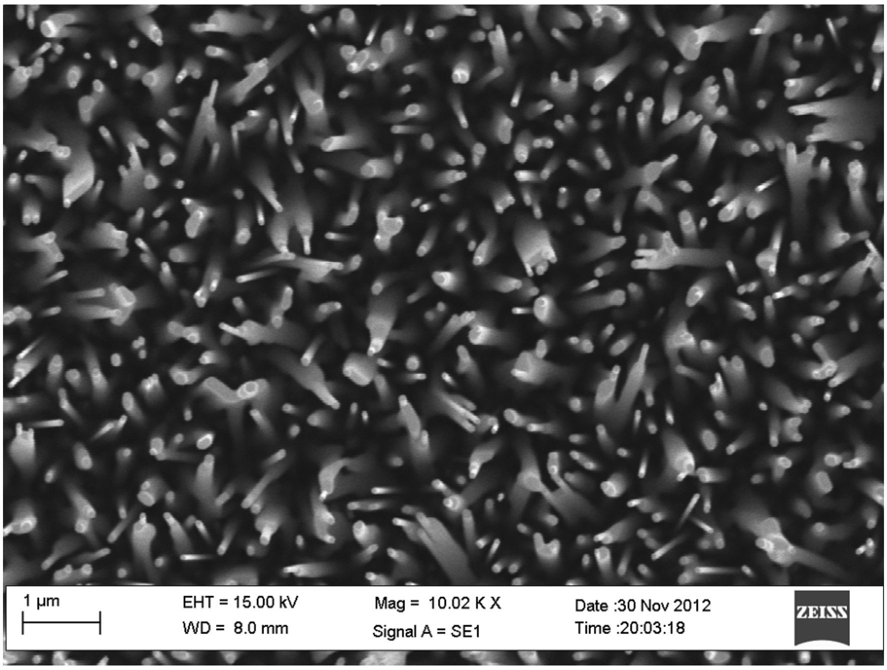

Figure 4.22: SEM image of VPT2 unordered sample at 0 ° observation angle

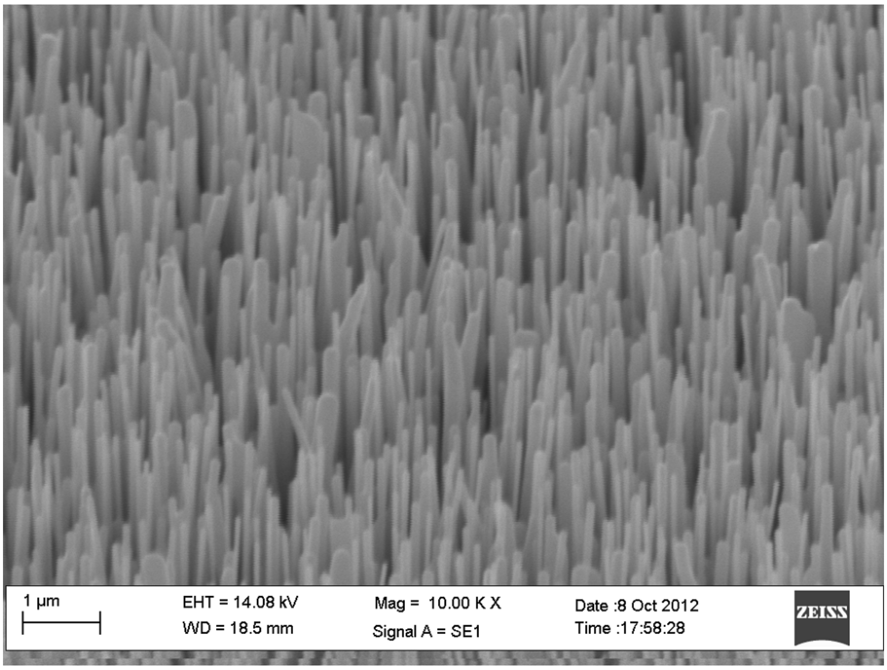

Figure 4.23: SEM image of VPT2 unordered sample at 60 ° observation angle

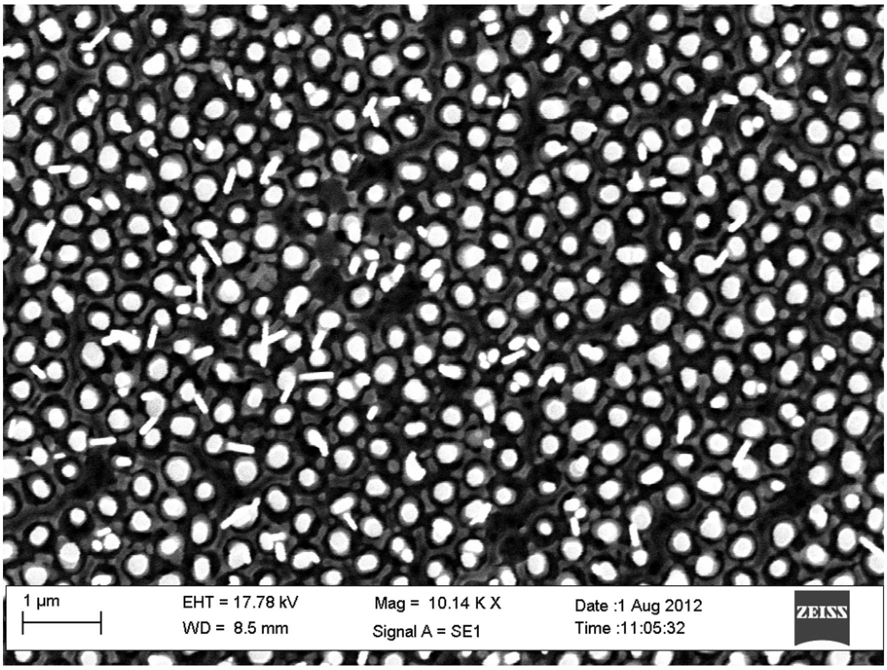

Figure 4.24: SEM image of VPT2 500 nm spaced sample at 0 ° observation angle

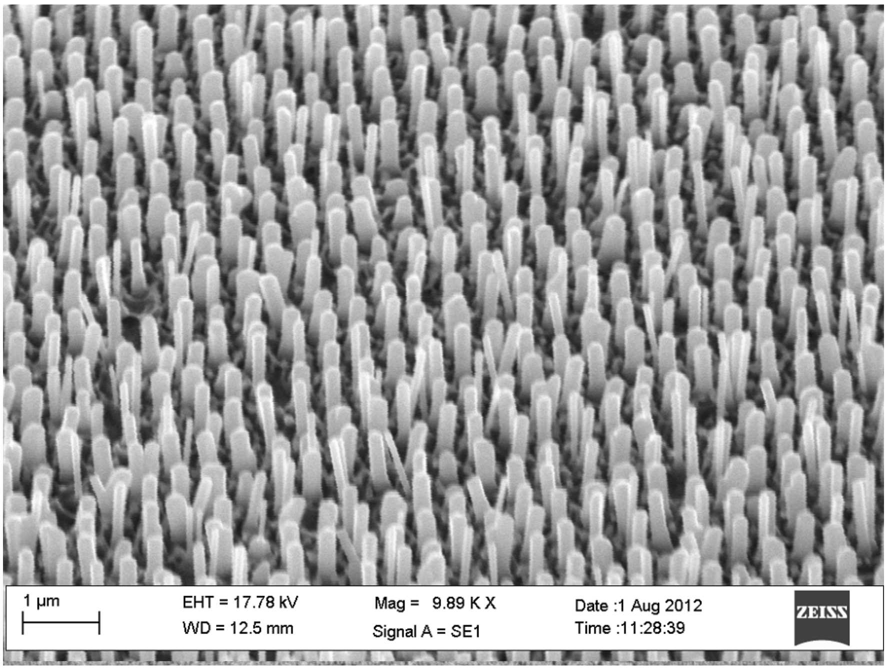

Figure 4.25: SEM image of VPT2 500 nm spaced sample at 60 ° observation angle

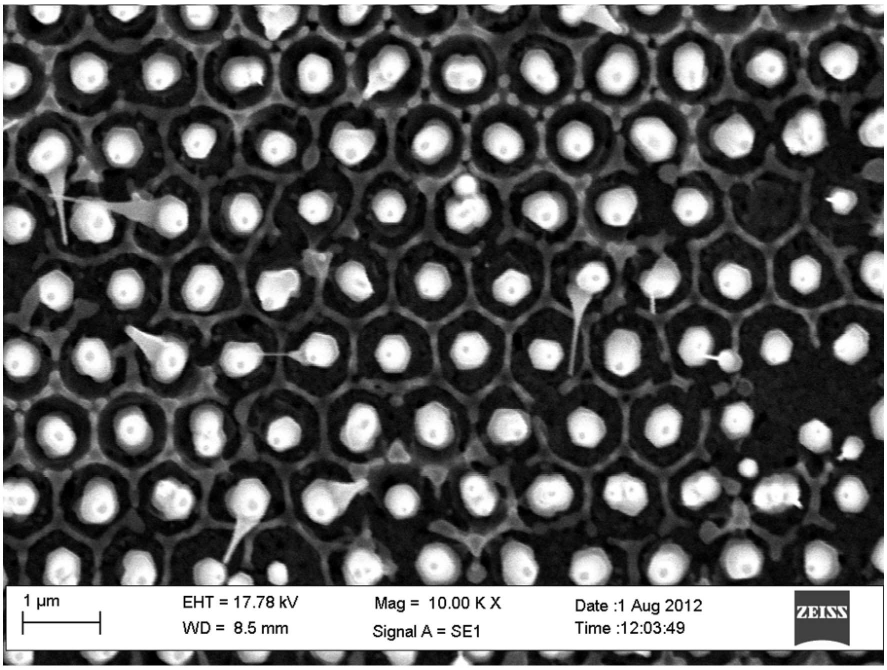

Figure 4.26: SEM image of VPT2 1 μm spaced sample at 0 ° observation angle

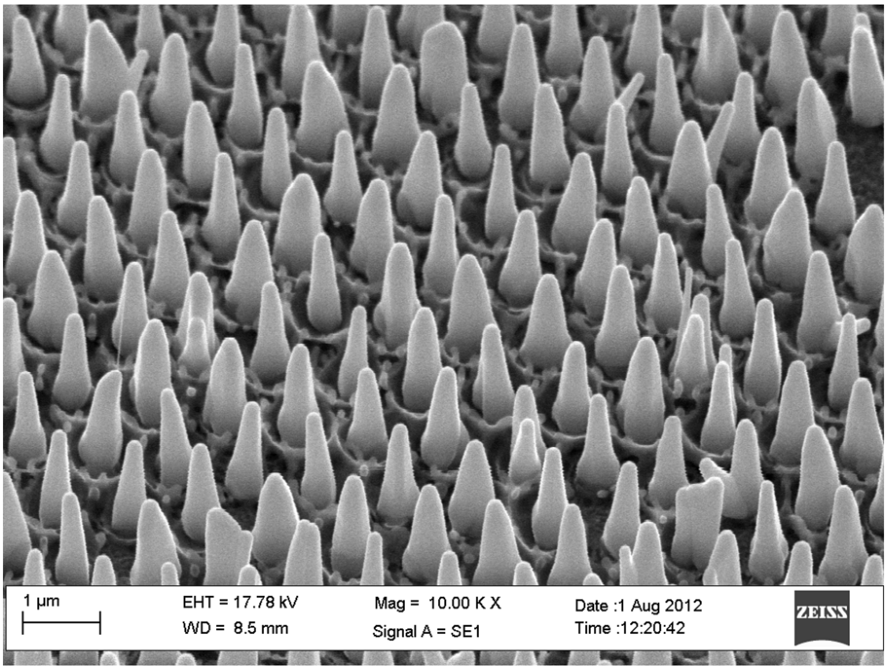

Figure 4.27: SEM image of VPT2 1 μm spaced sample at 45 ° observation angle

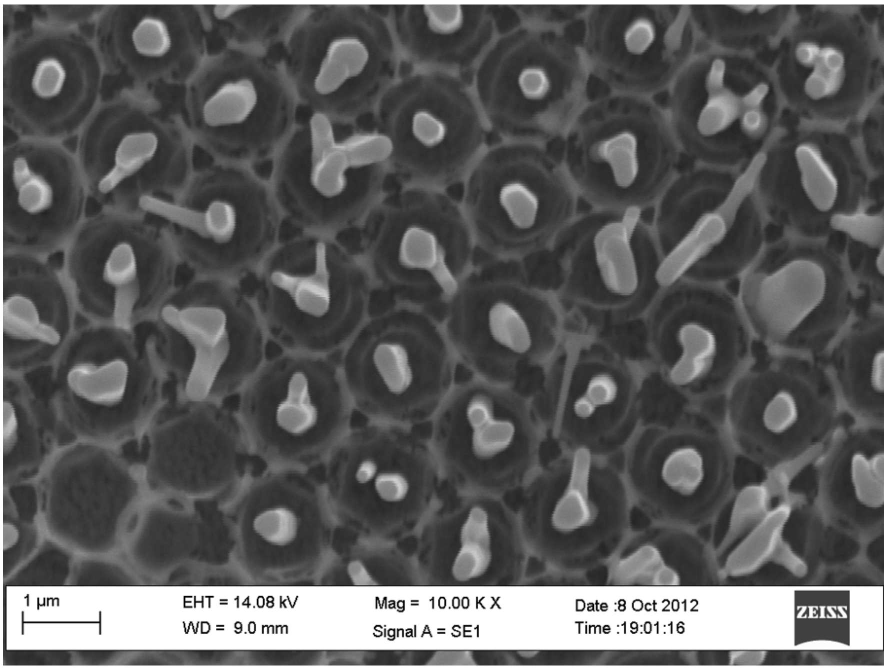

Figure 4.28: SEM image of VPT2 1.5 μm spaced sample at 0 ° observation angle

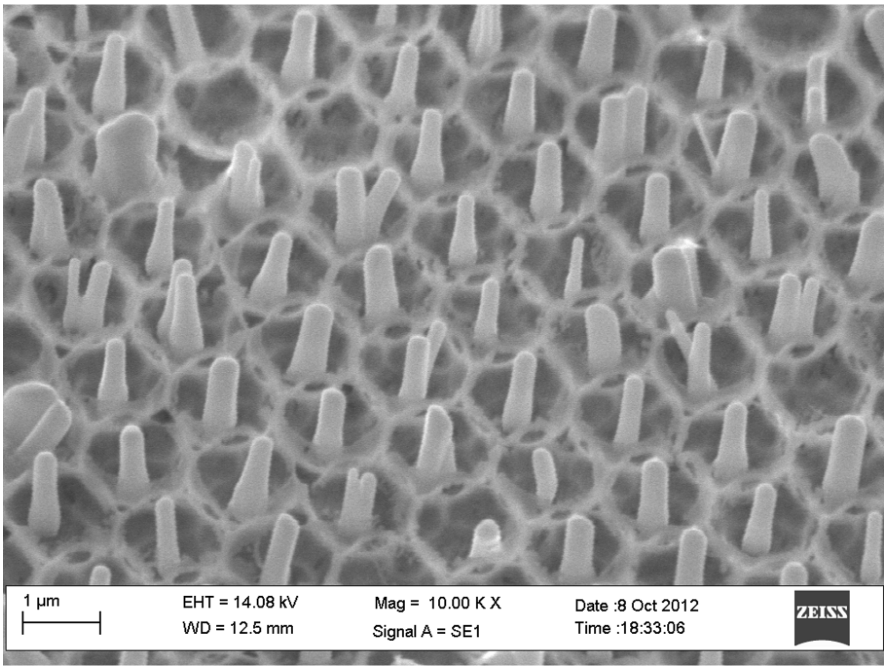

Figure 4.29: SEM image of VPT2 1.5 μm spaced sample at 45 ° observation angle

the (0002) ZnO peak. As discussed in Section 3.3.1, the full width half maximum (FWHM) of a rocking curve peak is dependent on the alignment of the crystallites, with a smaller FWHM indicating better alignment. The rocking curve FWHM for thin films is ~9°. Nanowire samples exhibit smaller FWHM than the buffer layer, indicating a better crystallographic alignment. As the nanowires appear to be predominantly single crystals, this suggests good alignment of the wires. There may also be an improvement in the alignment of the buffer layer, due to the high temperatures used in VPT growth annealing the thin film and improving its crystal quality. Unordered samples have rocking curve FWHM of ~2°, and ordered samples have rocking curve FWHM of ~7°. Ordered samples may exhibit worse alignment due to growth being forced into specific locations by the silica mask, rather than being allowed to nucleate at the optimal growth points. The dimensions of the wires, determined by SEM, are shown in Table 4.5.

Sample	**Diameter (nm)**	**Height (μm)**	**Shielding**
VPT1 Unordered	140	3	
VPT1 500 nm	200	4	$0.111\gamma_0$
VPT1 1 μm	200	3	$0.297\gamma_0$
VPT2 Unordered	100	4	
VPT2 500 nm	200	1.5	$0.297\gamma_0$
VPT2 1 μm	300	2.5	$0.353\gamma_0$
VPT2 1.5 μm	300	1.5	$0.717\gamma_0$

Table 4.5: Dimensions of VPT samples as observed by SEM, and the shielding factor

From the dimensions of the nanowires, γ can be calculated using the models detailed in Section 4.1. The values obtained for these models, for the various VPT grown samples, can be seen in Table 4.6.

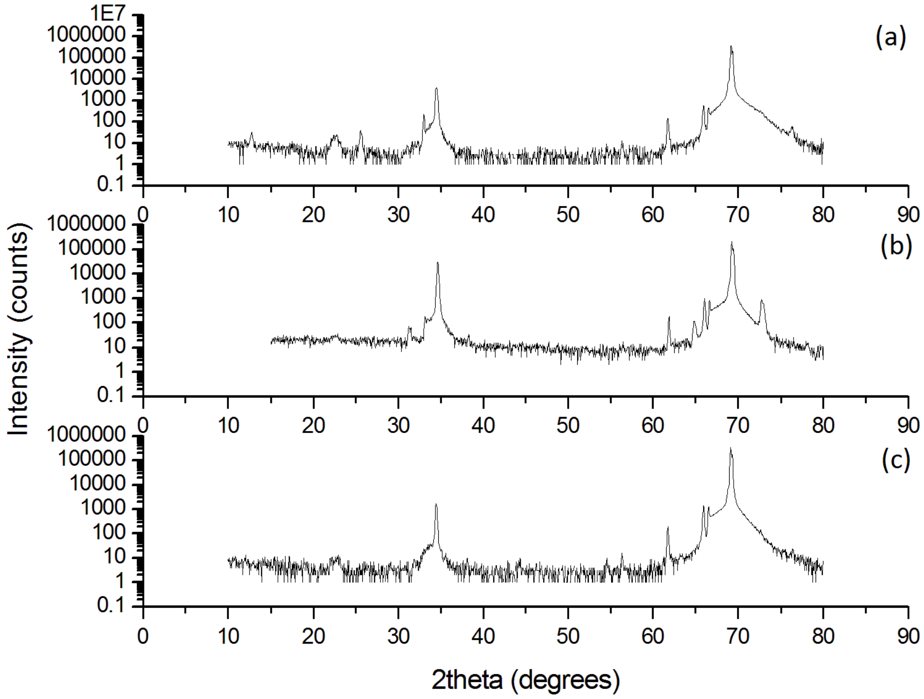

Figure 4.30: θ-2θ XRD scans for a typical (a) ordered ZnO nanowire array (b) unordered ZnO nanowire array, and (c) ZnO thin film

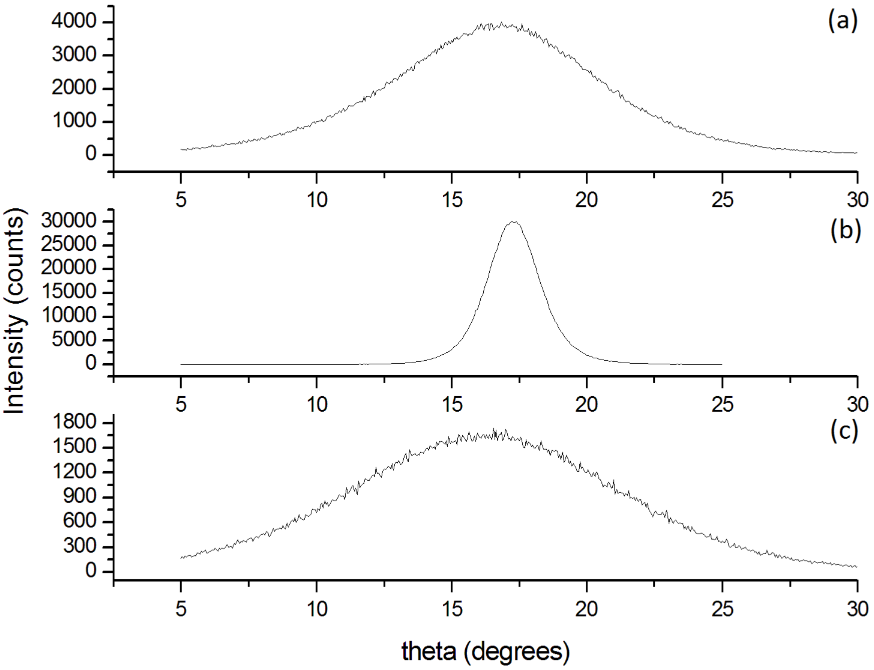

Figure 4.31: Rocking curve XRD scans of the (0002) ZnO peak for a typical (a) ordered ZnO nanowire array (b) unordered ZnO nanowire array, and (c) ZnO thin film

Sample	**Eq. 4.3**	**Eq. 4.4**	**Eq. 4.5**	**Eq. 4.6**	**Eq. 4.7**	**Eq. 4.9**	**Eq. 4.11**	**Eq. 4.12**
VPT1 Unordered	42.0	28.3	28.8	34.8	35.0	472.6	1602.0	472.6
VPT1 500 nm	42.0	28.3	28.8	34.8	35.0	472.6	1602.0	472.6
VPT1 1 μm	32.0	21.2	21.6	27.3	27.7	290.3	902.0	290.3
VPT2 Unordered	82.0	56.6	57.6	63.4	64.7	1570.1	6402	1570.1
VPT2 500 nm	17.0	10.6	10.8	15.5	16.9	93.0	227.0	93.0
VPT2 1 μm	18.7	11.8	12.0	16.8	18.1	110.2	279.8	110.2
VPT2 1.5 μm	12.0	7.07	7.2	11.4	13.2	49.3	102.0	49.3

Table 4.6: Modelled γ factors for the various VPT grown samples

Using Equation 4.14 a modified value for γ taking account of shielding from neighbouring nanowires can be calculated for each ordered sample. The shielding factors for the ordered arrays are presented in Table 4.5.

The arrays produced by the CBD method were characterised with SEM, the results of which can be seen in Figures 4.32 - 4.37. Ordered, spaced arrays of vertically oriented nanowires are evident. There are some defects in the pattern, where there is no zinc oxide growth. The nanowires produced by CBD are much shorter than typical VPT wires, and thus will have lower aspect ratios, which would be expected to give lower field enhancement. The dimensions of the wires, as determined from the SEM data, are listed in Table 4.7. The arrays were also characterised with XRD. We present a typical θ-2θ and rocking curve scans, in Figures 4.38 and 4.39, respectively. Again the θ-2θ shows the (100) Si peak at 69.1° and the (0002) ZnO peak at 34.3°. The FWHM of the (0002) ZnO rocking curve peak is ~6.1°, a slightly smaller value than the ordered ZnO nanowire arrays grown by VPT, indicating that the CBD wires may be more vertically aligned.

Sample	**Diameter (nm)**	**Height (μm)**	**Shielding**
CBD 500 nm	300	1.5	$0.297\gamma_0$
CBD 1 μm	500	1	$0.717\gamma_0$
CBD 1.5 μm	450	1	$0.869\gamma_0$

Table 4.7: Dimensions of CBD samples as observed by SEM, and the shielding factor

Modelled values of γ have been calculated from the nanowire dimensions, using the models detailed in Section 4.1. The values obtained for these models, for the three spacings, can be seen in Table 4.8.

Using Equation 4.14, the shielding effect for each spacing can be esti-

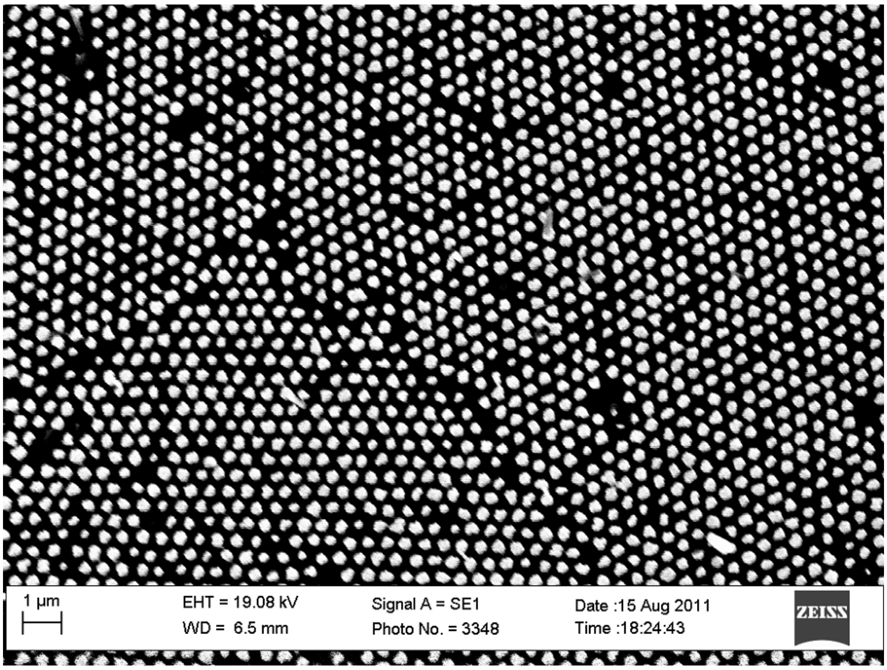

Figure 4.32: SEM image of CBD-grown 500 nm spaced sample at 0 ° observation angle

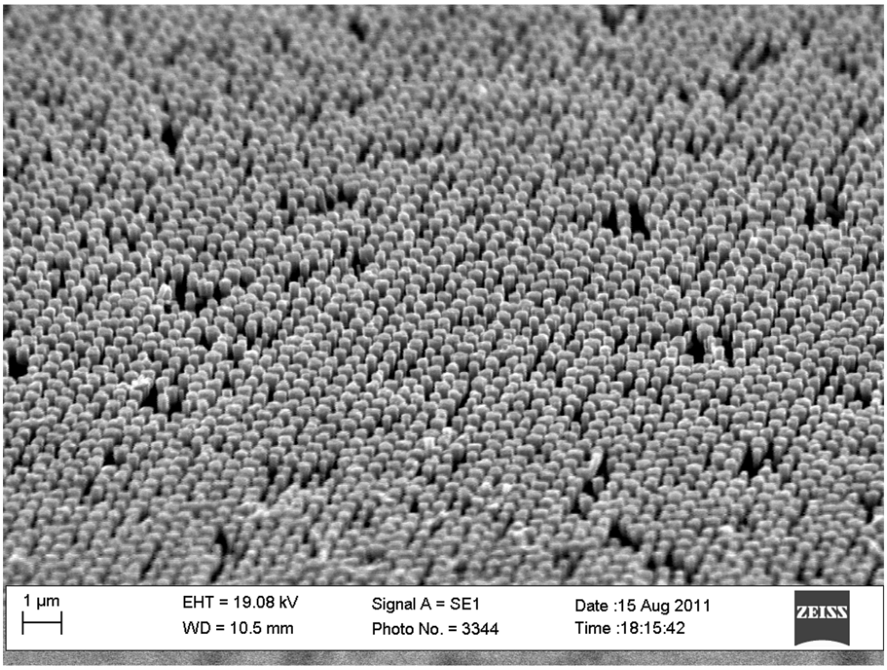

Figure 4.33: SEM image of CBD-grown 500 nm spaced sample at 60 ° observation angle

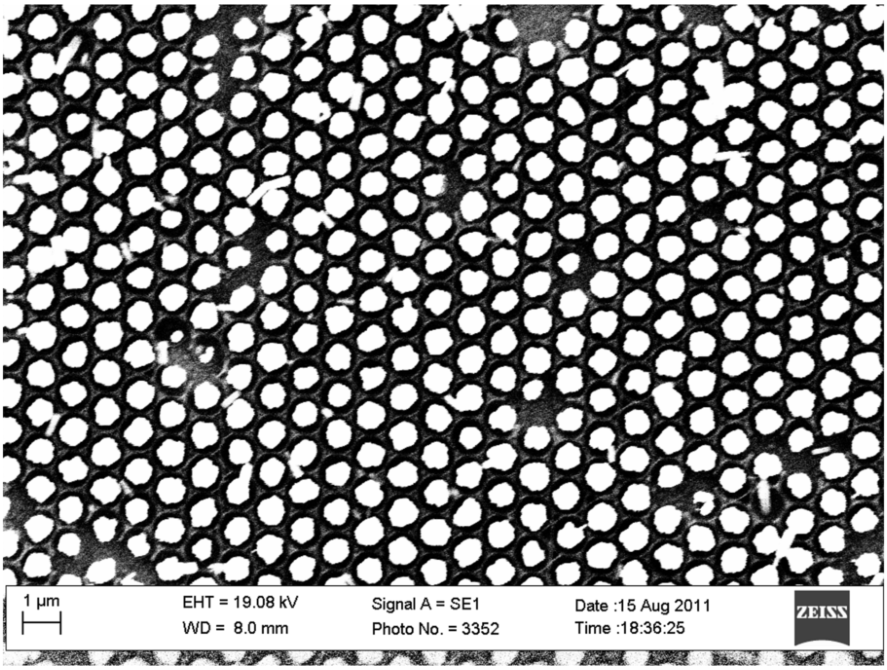

Figure 4.34: SEM image of CBD-grown 1 μm spaced sample at 0 ° observation angle

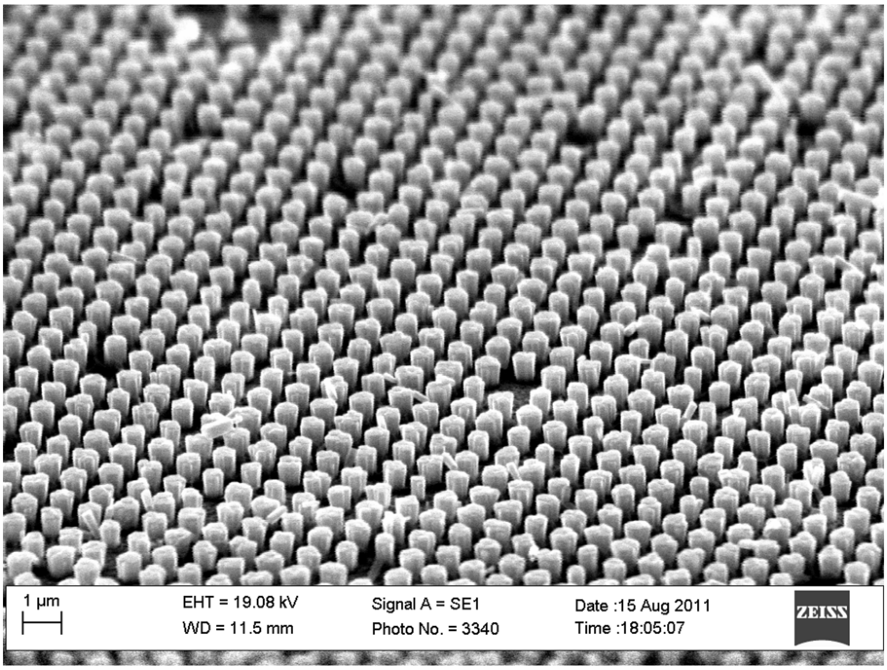

Figure 4.35: SEM image of CBD-grown 1 μm spaced sample at 60 ° observation angle

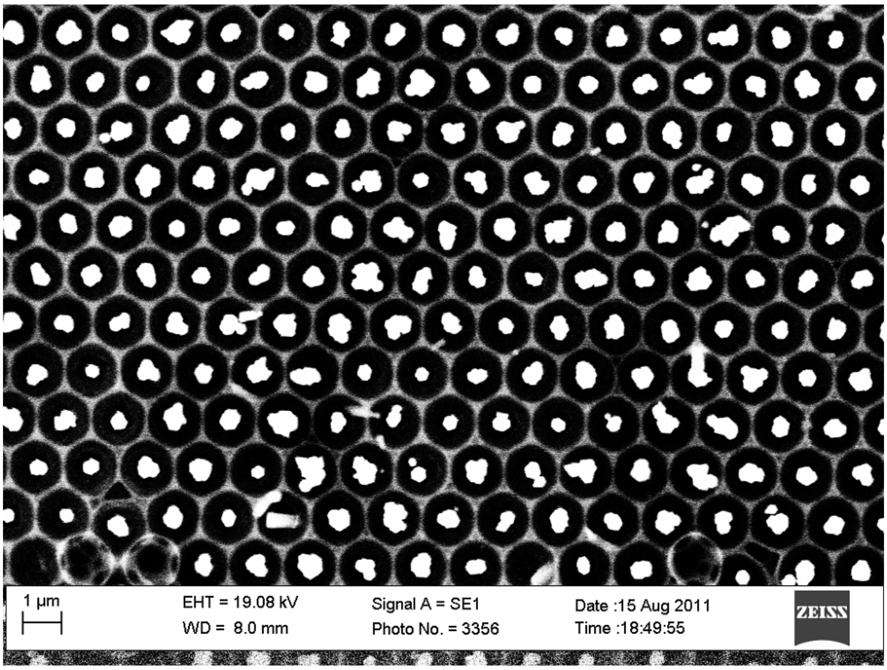

Figure 4.36: SEM image of CBD-grown 1.5 μm spaced sample at 0 ° observation angle

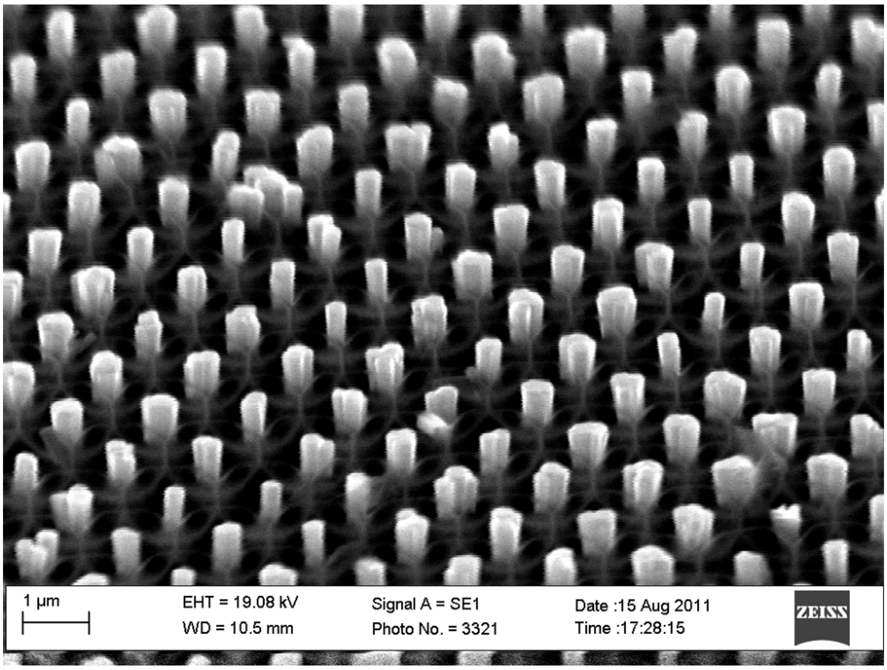

Figure 4.37: SEM image of CBD-grown 1.5 μm spaced sample at 60 ° observation angle

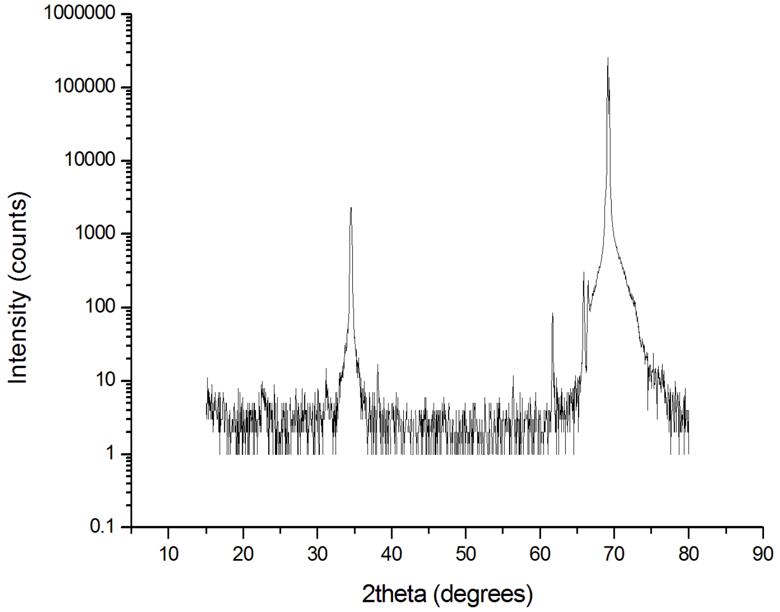

Figure 4.38: θ-2θ XRD scans for a typical CBD-grown ordered ZnO nanowire array

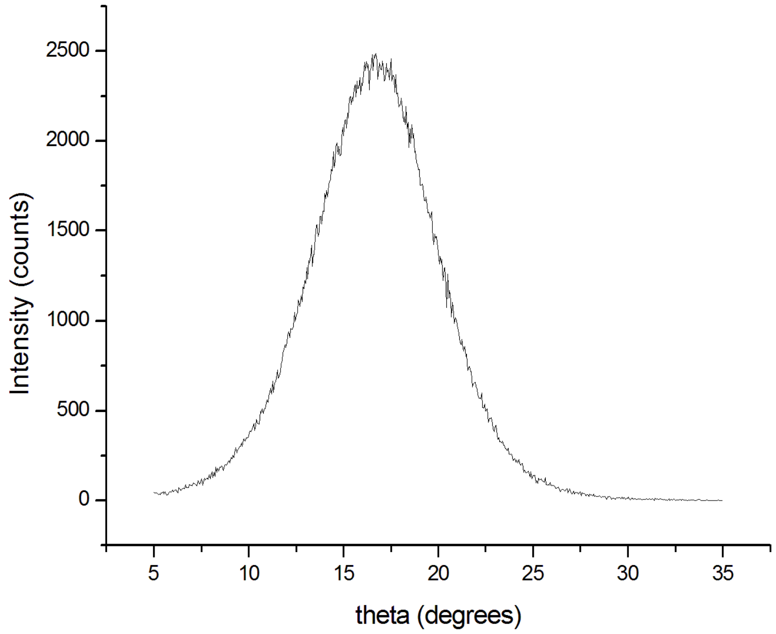

Figure 4.39: A typical rocking curve XRD scan of the (0002) ZnO peak for a CBD-grown ordered ZnO nanowire array

Spacing	**Eq. 4.3**	**Eq. 4.4**	**Eq. 4.5**	**Eq. 4.6**	**Eq. 4.7**	**Eq. 4.9**	**Eq. 4.11**	**Eq. 4.12**
500 nm	12.0	7.07	7.2	11.4	13.2	49.3	102.0	49.3
1 μm	6	2.8	2.9	6.2	8.9	13.3	18.0	13.3
1.5 μm	6.4	3.1	3.2	6.6	9.2	15.3	21.8	15.3

Table 4.8: Modelled γ factors for the 3 spaced CBD samples

mated. The shielding factors calculated are presented in Table 4.7. From these results we can see that although the γ values modelled for each sample, based on individual emitters, are roughly similar, the shielding should give rise to significantly different values of γ, and subsequently to the current.

The Field emission characteristics of the samples were tested. I-V data were taken with a sample-anode separation $d = 250\ \mu$m using the apparatus and procedure described in Section 3.1. The data was analysed using FN analysis and the iterative method we have described, for an assumed work function of 3.7 eV. Results are presented in the form of I-V curves, linear region FN plots, plots of J_{FN} vs. V, and plots of A_{FN} vs. V. The results for each sample set can be seen in Figures 4.40 - 4.43 for VPT1, Figures 4.44 - 4.47 for VPT2, and Figures 4.48 - 4.51 for the CBD samples.

The γ factors found by analysis of the FN plots are listed in Table 4.10, along with a modelled value (using Equation (4.12)), with and without shielding (using Equation (4.14)), for comparison. Turn-on voltages for the samples are presented in Table 4.9. For the VPT1 500 nm spaced sample, the turn-on was below the starting voltage, and thus could not be determined. The current densities and emission areas given by the analyses were on the order of 10^{12} Am^{-2} and 10^{-17} m^2, respectively.

The experimental γ factors are significantly larger than the modelled values, as commonly reported. The unordered samples show reasonable agreement, however the modelled values for these samples do not account for screening, as the model for shielding requires an ordered array with equal spacings. The VPT1 samples appear to indicate proportionality between the spacing and the experimental γ factor. The ordered VPT2 samples also reflect this trend, with the exception of the unordered sample which has a

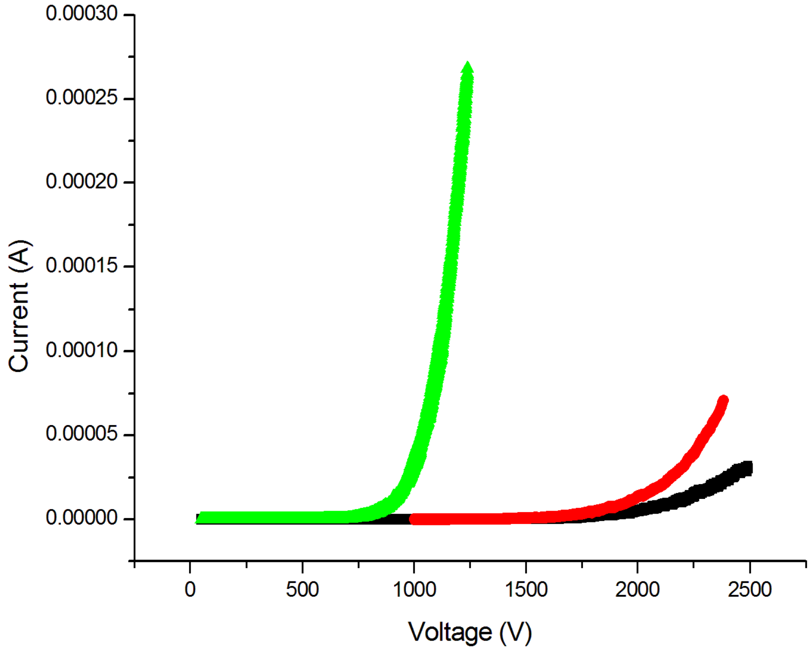

Figure 4.40: Current vs. Voltage for the VPT1 samples unspaced (black), 500 nm spacing (red), and 1 μm spacing (green)

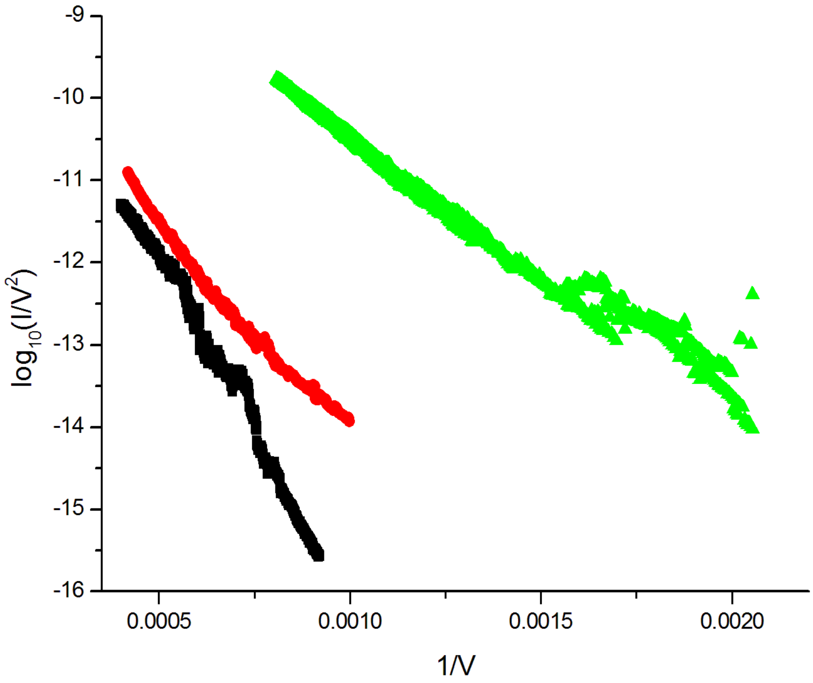

Figure 4.41: FN plot for the VPT1 samples unspaced (black), 500 nm spacing (red), and 1 μm spacing (green)

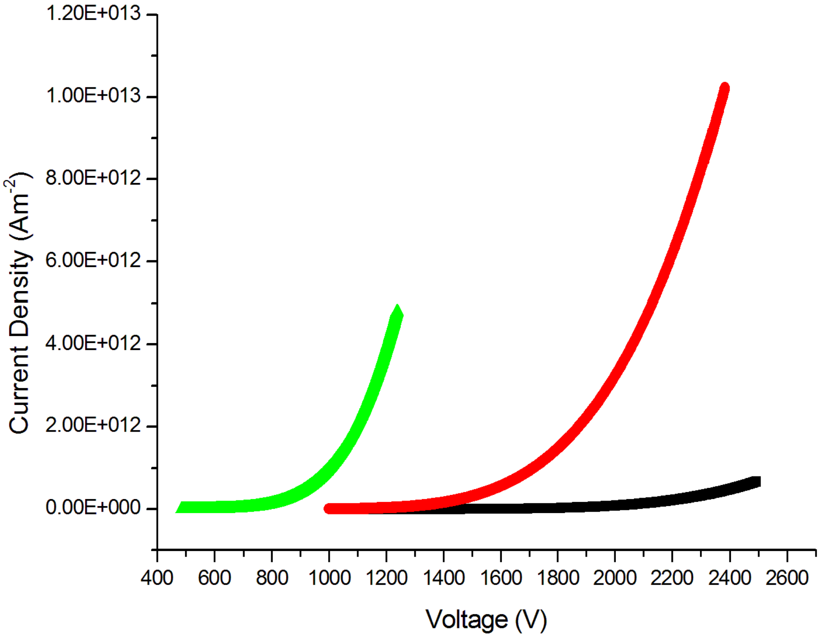

Figure 4.42: Current Density vs. Voltage for the VPT1 samples unspaced (black), 500 nm spacing (red), and 1 μm spacing (green)

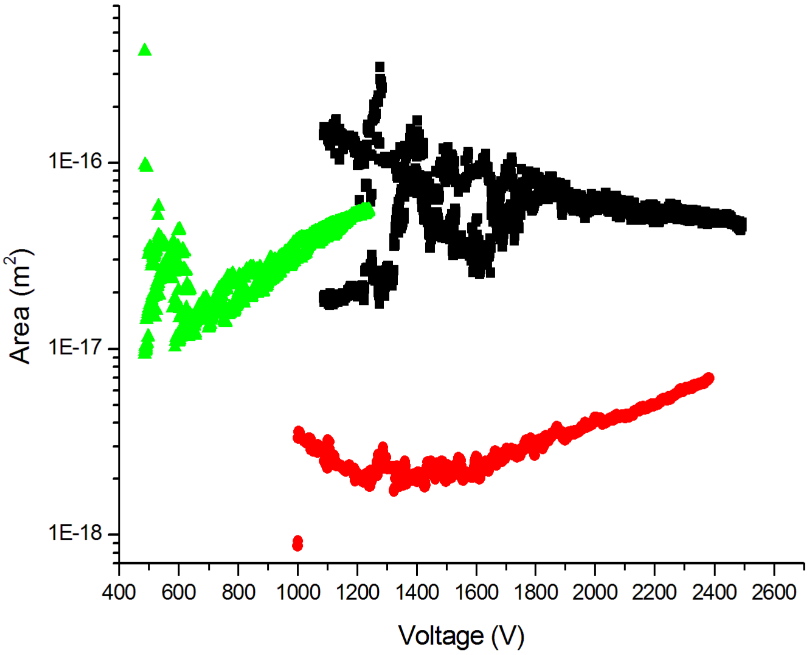

Figure 4.43: Emission area vs. Voltage for the VPT1 samples unspaced (black), 500 nm spacing (red), and 1 μm spacing (green)

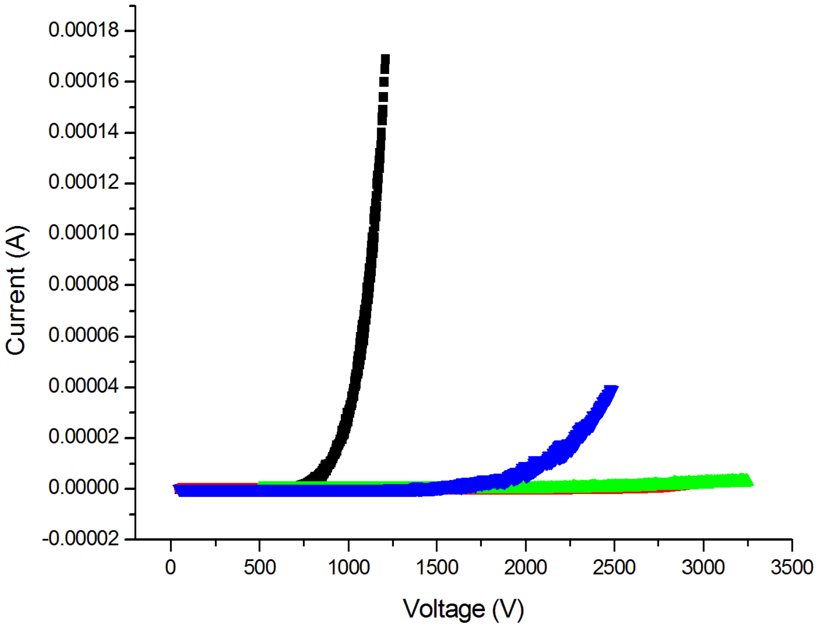

Figure 4.44: Current vs. Voltage for the VPT2 samples unspaced (black), 500 nm spacing (red), 1 μm spacing (green), and 1.5 μm spacing (blue)

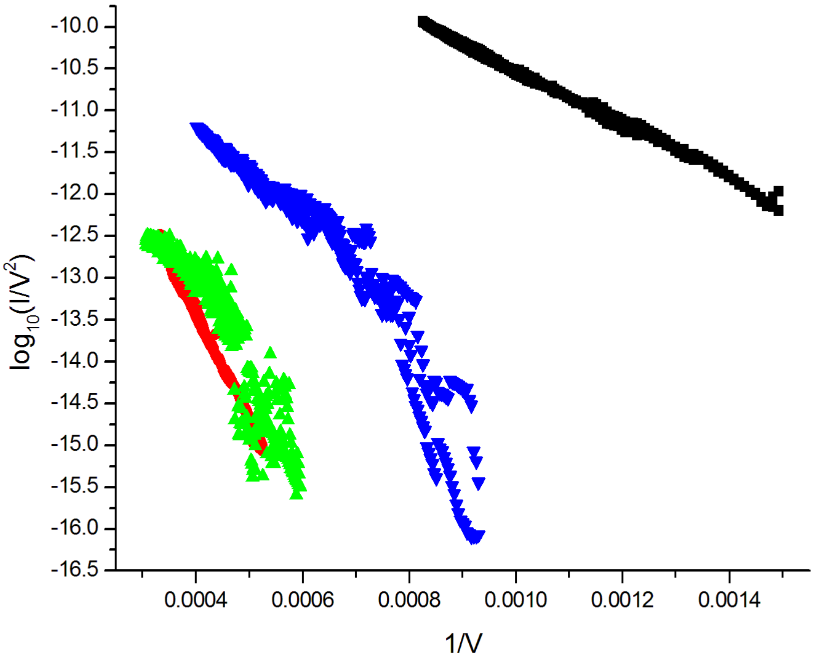

Figure 4.45: FN plot for the VPT2 samples unspaced (black), 500 nm spacing (red), 1 μm spacing (green), and 1.5 μm spacing (blue)

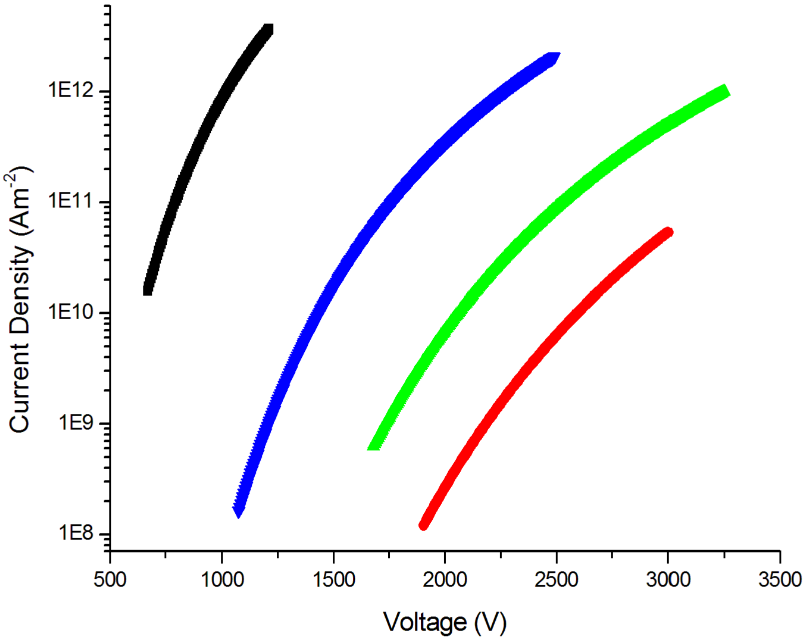

Figure 4.46: Current Density vs. Voltage for the VPT2 samples unspaced (black), 500 nm spacing (red), 1 µm spacing (green), and 1.5 µm spacing (blue)

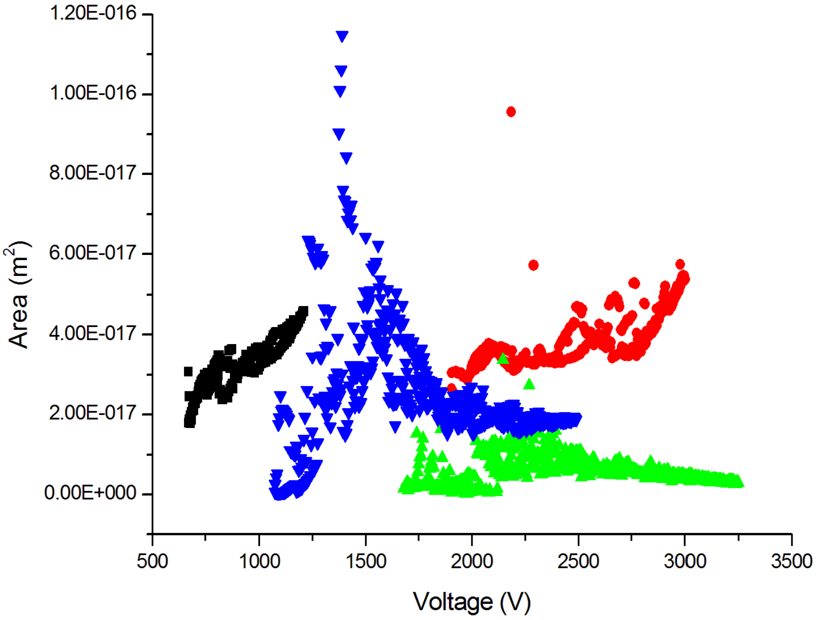

Figure 4.47: Emission area vs. Voltage for the VPT2 samples unspaced (black), 500 nm spacing (red), 1 µm spacing (green), and 1.5 µm spacing (blue)

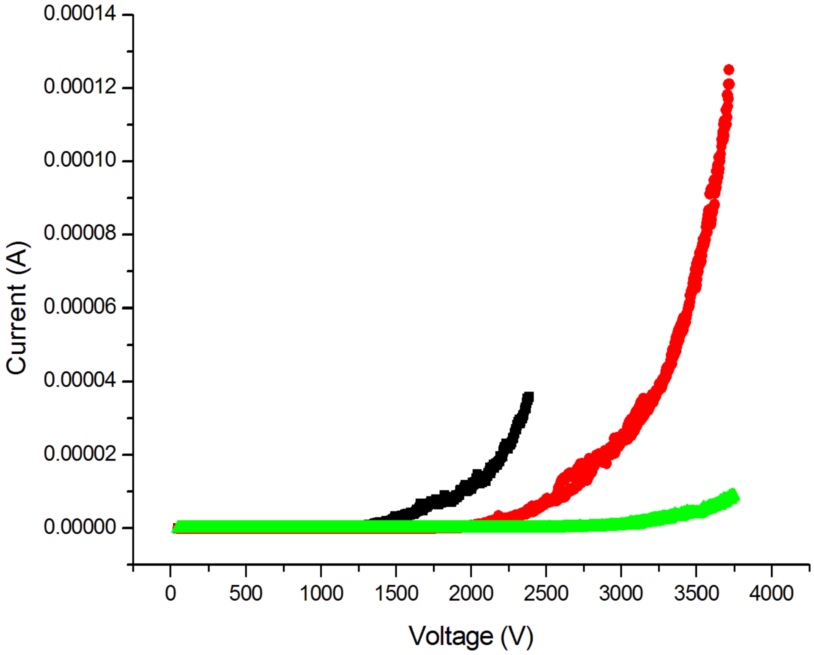

Figure 4.48: Current vs. Voltage for the CBD samples 500 nm spacing (black), 1 µm spacing (red), and 1.5 µm spacing (green)

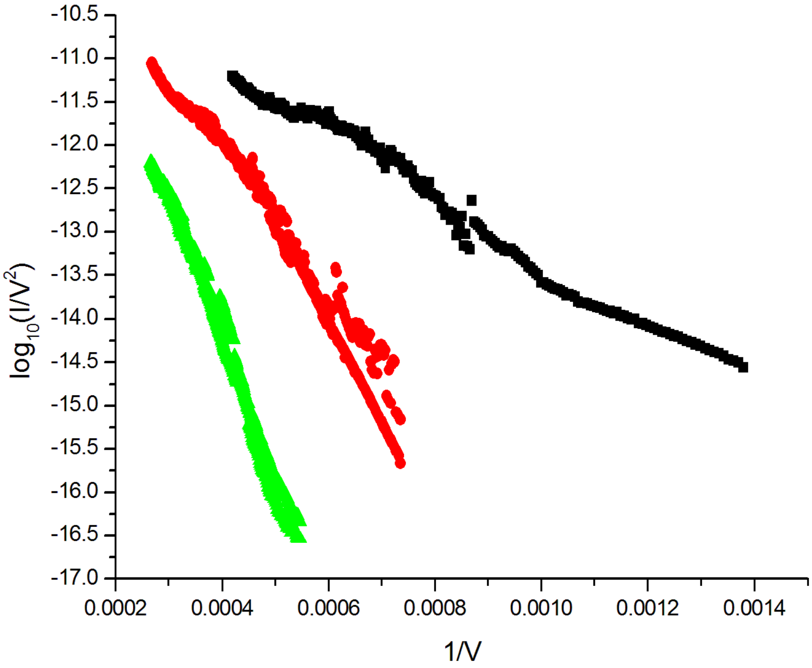

Figure 4.49: FN plot for the CBD samples 500 nm spacing (black), 1 µm spacing (red), and 1.5 µm spacing (green)

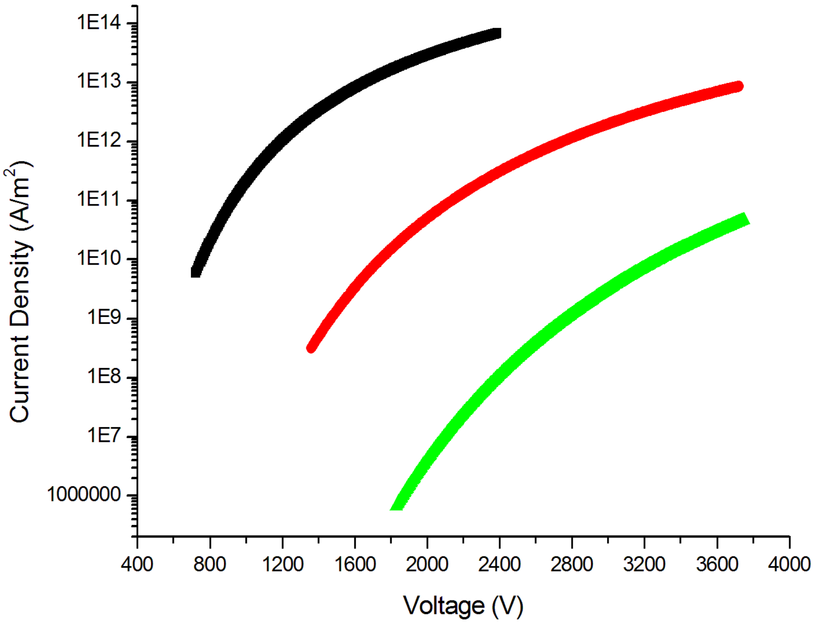

Figure 4.50: Current Density vs. Voltage for the CBD samples 500 nm spacing (black), 1 μm spacing (red), and 1.5 μm spacing (green)

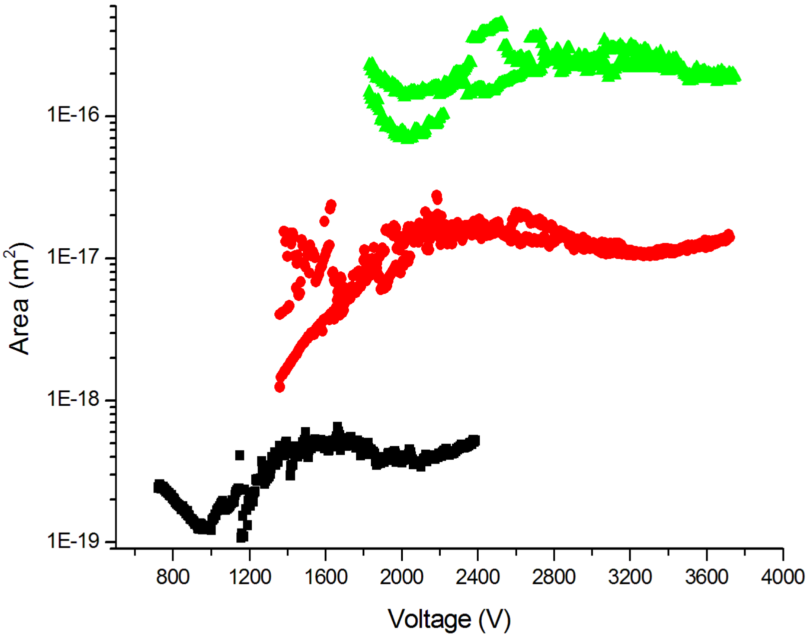

Figure 4.51: Emission area vs. Voltage for the CBD samples 500 nm spacing (black), 1 μm spacing (red), and 1.5 μm spacing (green)

Sample	**Turn-on Voltage (V)**
VPT1 Unordered	1091
VPT1 500 nm	<1000
VPT1 1 μm	489
VPT2 Unordered	671
VPT2 500 nm	1905
VPT2 1 μm	1680
VPT2 1.5 μm	1075
CBD 500 nm	724
CBD 1 μm	1360
CBD 1.5 μm	1830

Table 4.9: Turn-on voltages for the VPT and CBD samples

significantly higher experimental γ factor. However this may be due to the unordered samples significantly higher aspect ratio. In the CBD samples the trend appears to be reversed. The samples were re-examined by SEM after field emission testing. There were a number of new features present on the samples. SEM images showing these features observed are presented in Figures 4.52 - 4.68.

Figures 4.52 and 4.53 show nanowires with bulbous tips, similar to those observed by Semet *et al* [34]. This deformation of the tip suggests surface diffusion or melting of the nanowire tip during emission. The change in tip geometry will lead to a change to the field enhancement of the structure, which would have a corresponding effect on the field emission. One factor in the I-V hysteresis exhibited by emitters before they have been fully conditioned may be changing field enhancement due to tip melting. Not all the nanowires exhibit bulbed tips, and those that do are distributed across

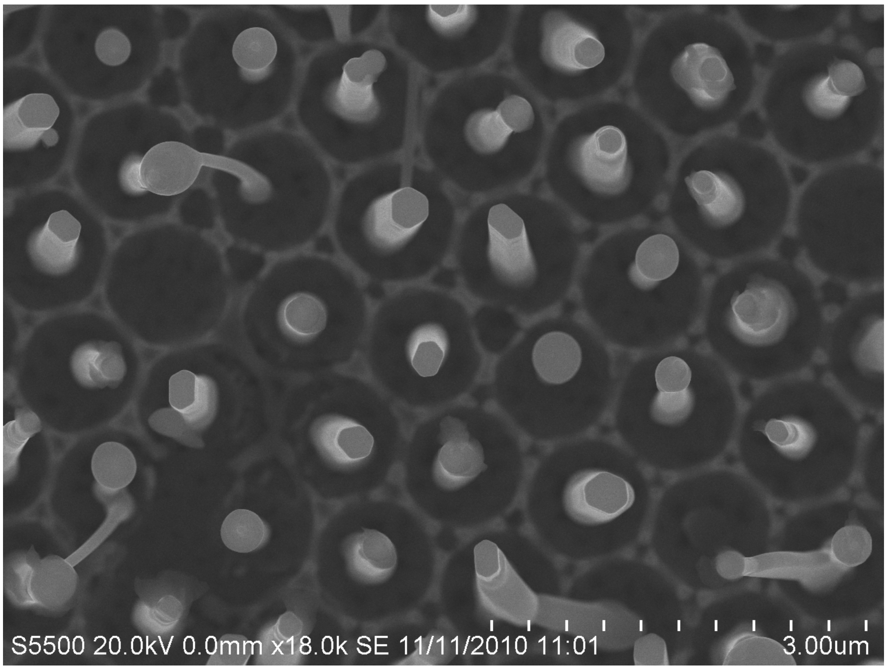

Figure 4.52: Post-field emission characterisation SEM image of VPT1 1 μm sample at 0 ° observation angle

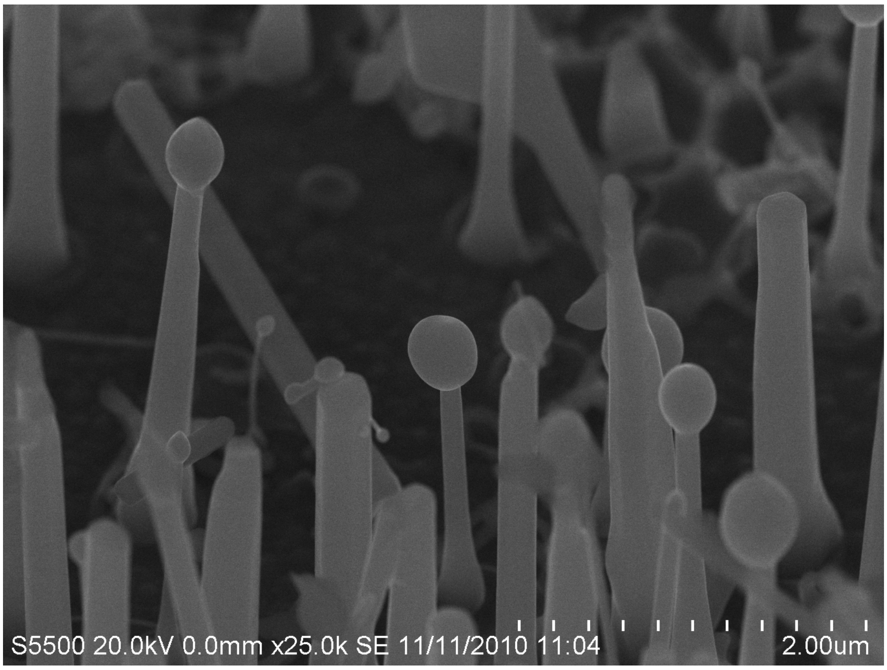

Figure 4.53: Post-field emission characterisation SEM image of VPT1 1 μm sample at 60 ° observation angle

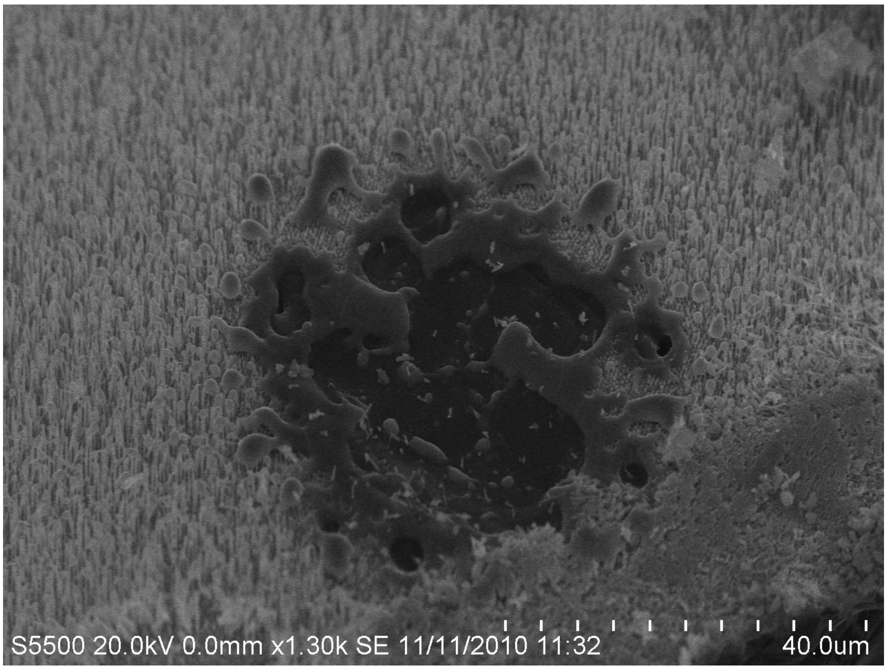

Figure 4.54: Post-field emission characterisation SEM image of VPT1 500 nm sample at 60 ° observation angle

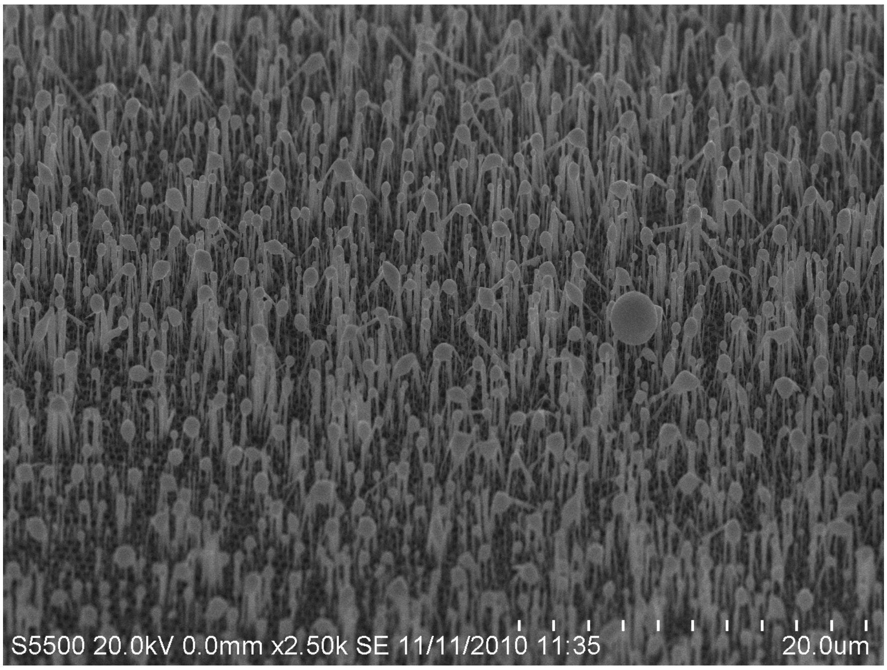

Figure 4.55: Post-field emission characterisation SEM image of VPT1 500 nm sample at 60 ° observation angle

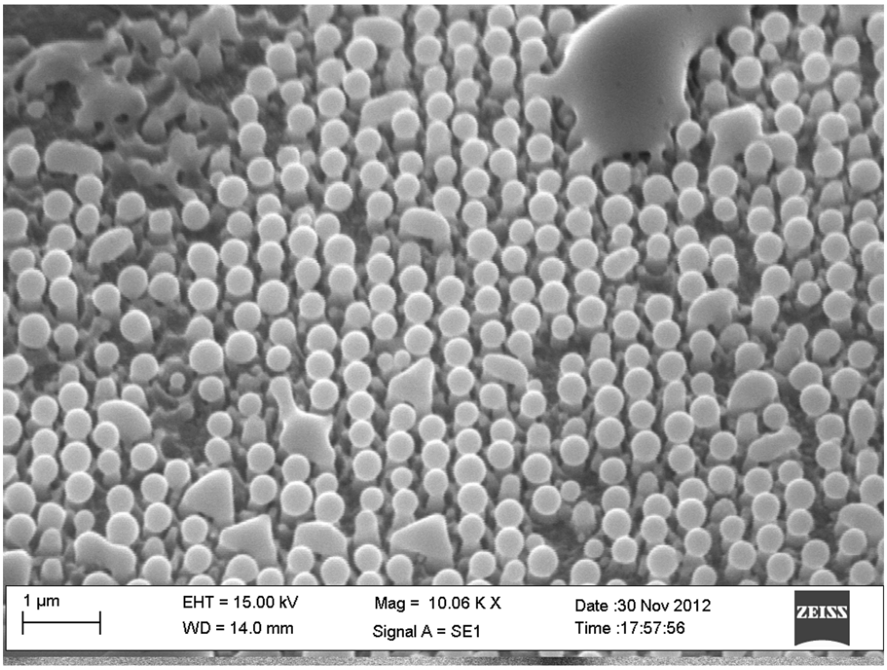

Figure 4.56: Post-field emission characterisation SEM image of VPT2 500 nm sample at 45 ° observation angle

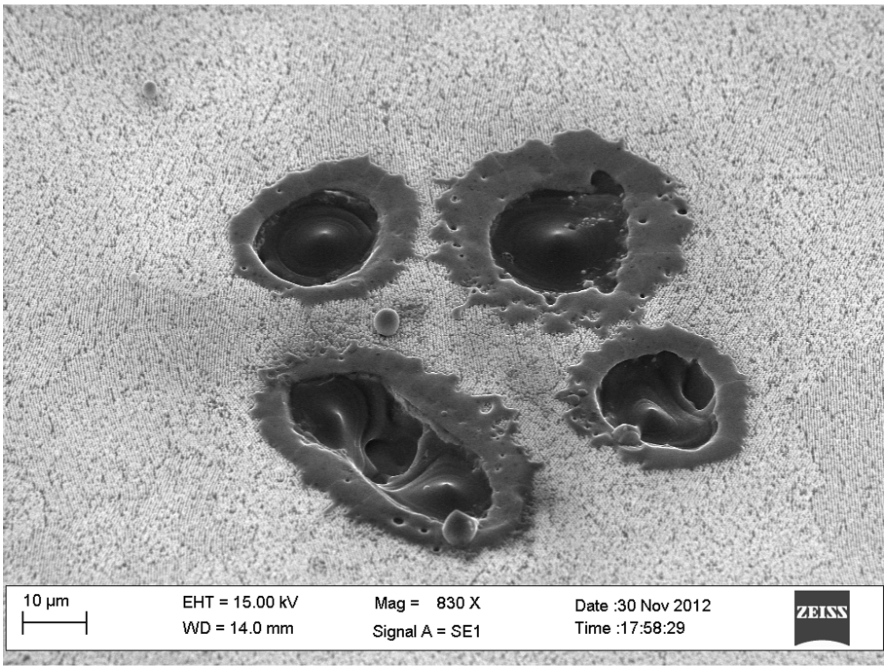

Figure 4.57: Post-field emission characterisation SEM image of VPT2 500 nm sample at 45 ° observation angle

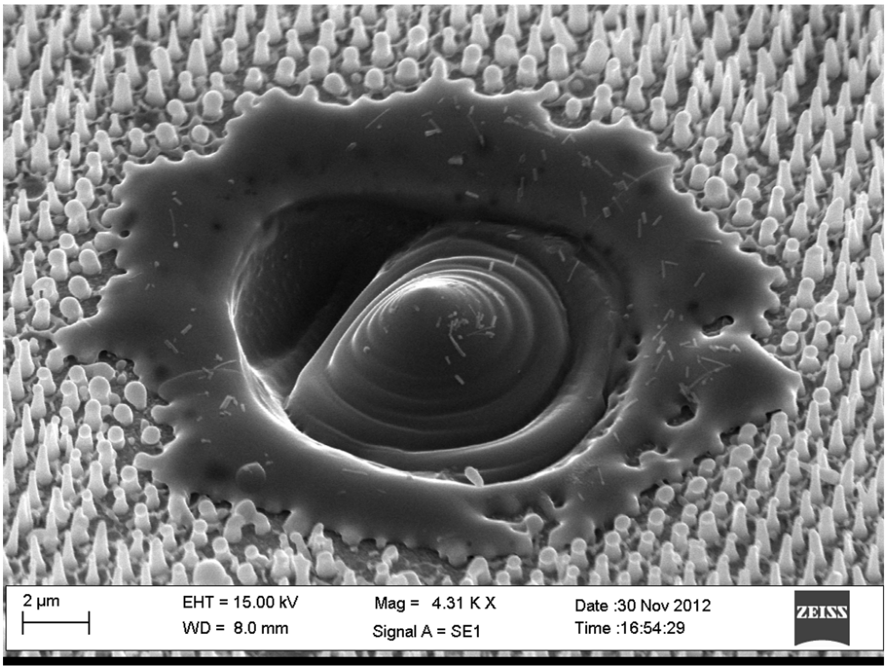

Figure 4.58: Post-field emission characterisation SEM image of VPT2 1 µm sample at 45 ° observation angle

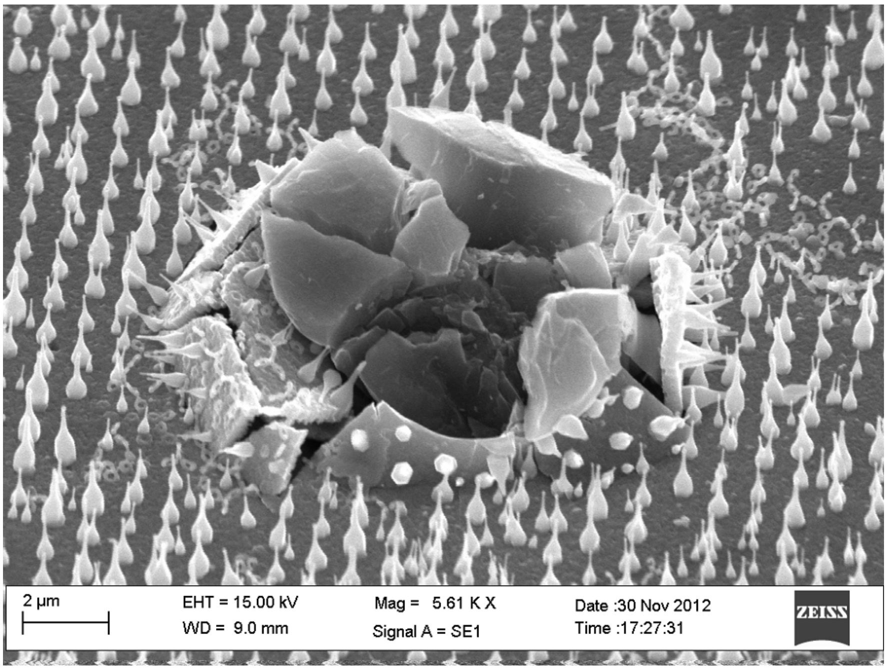

Figure 4.59: Post-field emission characterisation SEM image of VPT2 1 µm sample at 45 ° observation angle

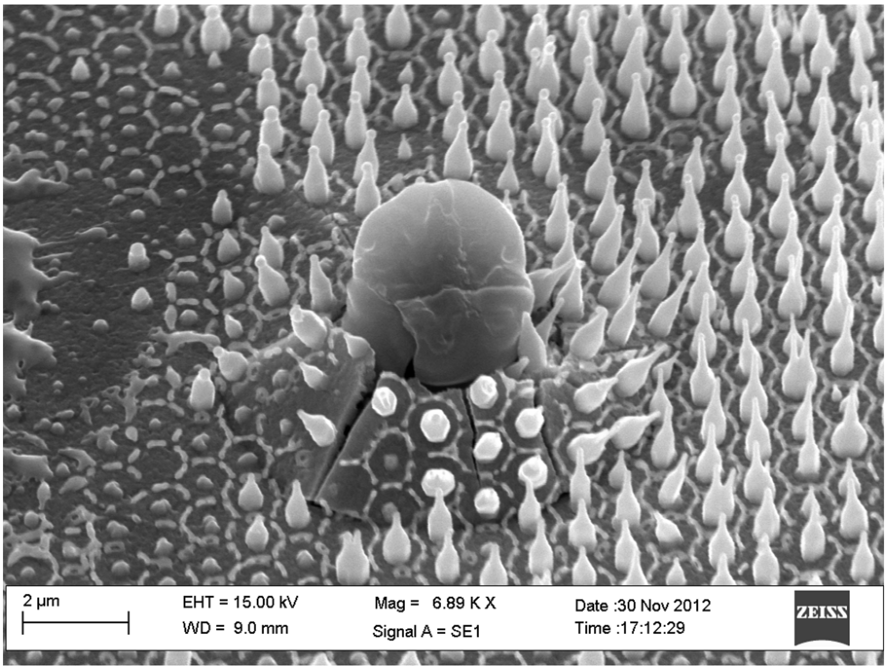

Figure 4.60: Post-field emission characterisation SEM image of VPT2 1 µm sample at 45 ° observation angle

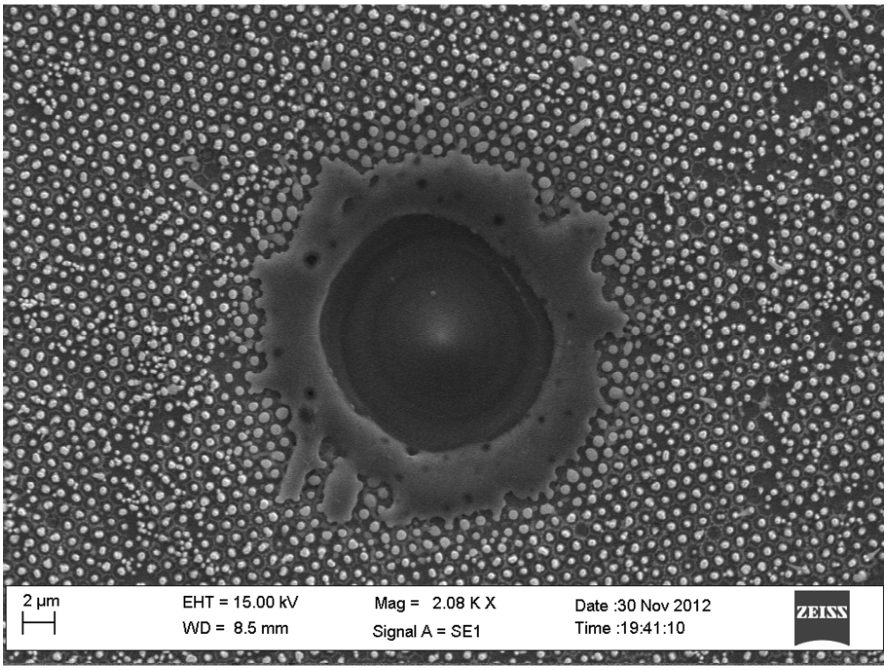

Figure 4.61: Post-field emission characterisation SEM image of VPT2 1 µm sample at 0 ° observation angle

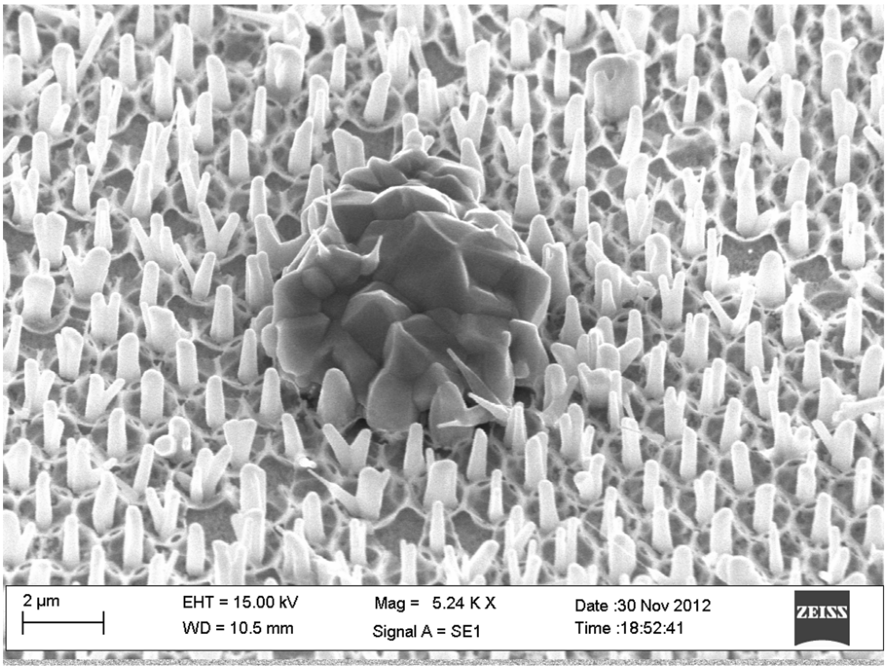

Figure 4.62: Post-field emission characterisation SEM image of VPT2 1.5 µm sample at 45 ° observation angle

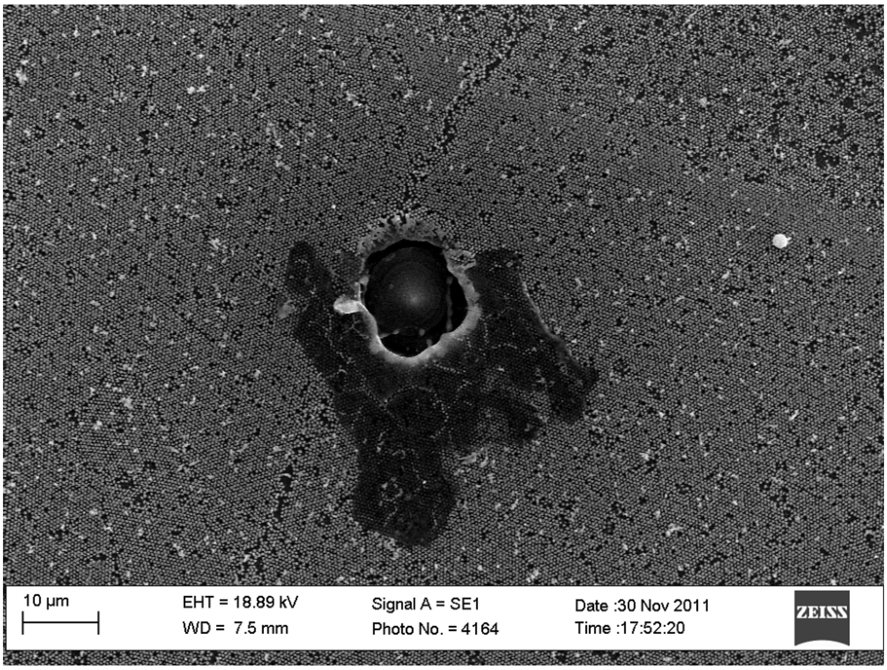

Figure 4.63: Post-field emission characterisation SEM image of CBD 500 nm sample at 0 ° observation angle

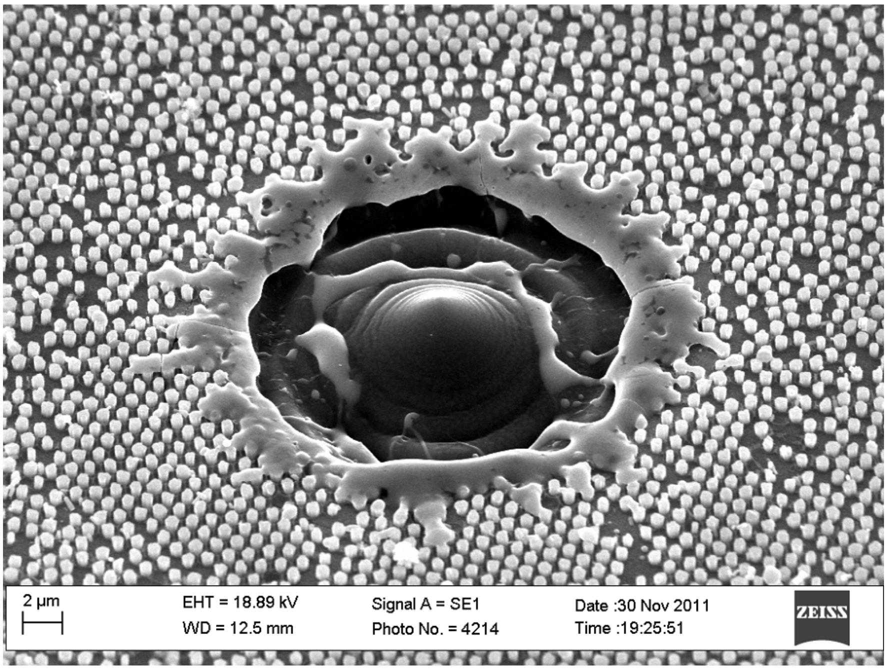

Figure 4.64: Post-field emission characterisation SEM image of CBD 1 µm sample at 45 ° observation angle

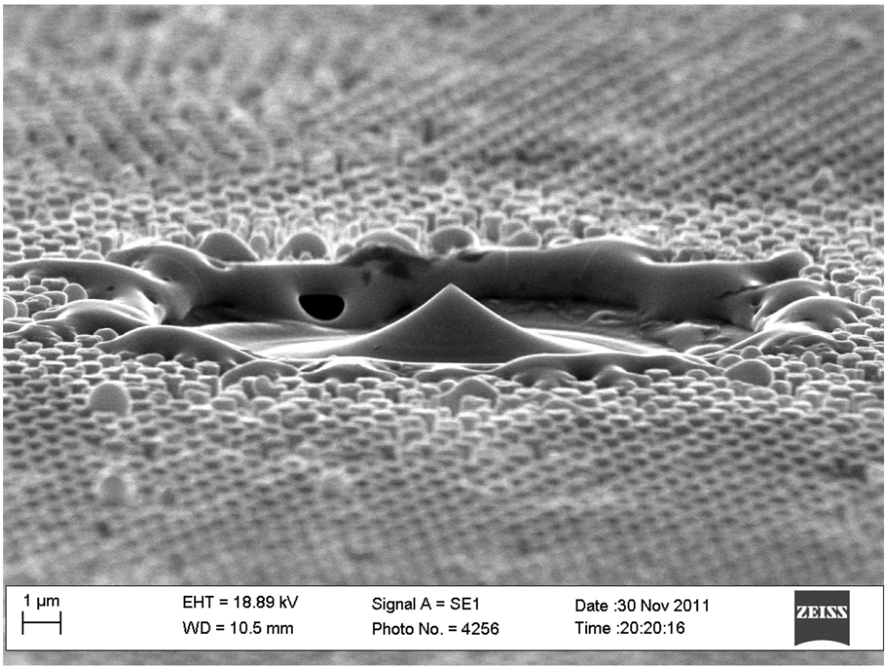

Figure 4.65: Post-field emission characterisation SEM image of CBD 1 µm sample at 80 ° observation angle

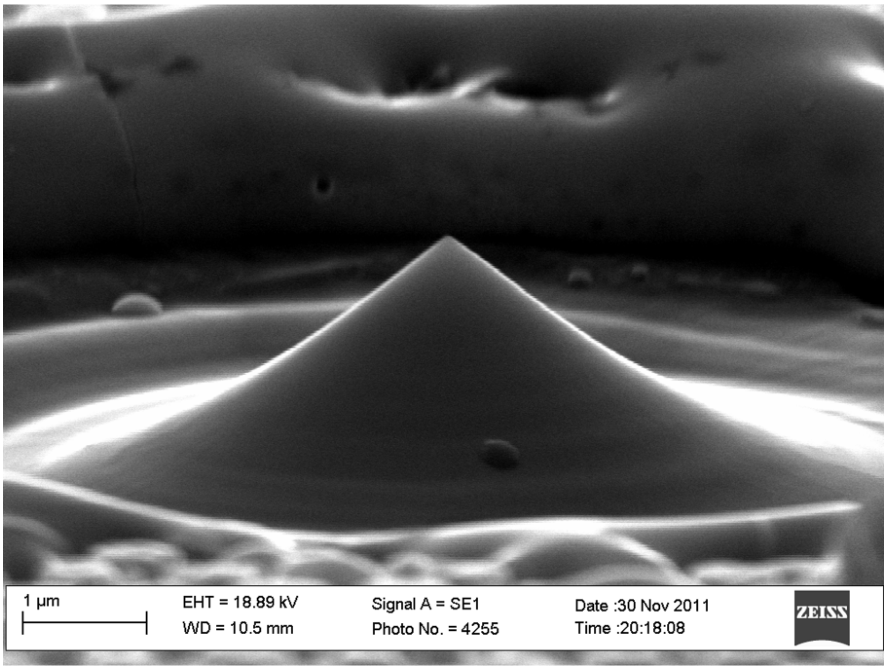

Figure 4.66: Post-field emission characterisation SEM image of CBD 1 μm sample at 80 ° observation angle

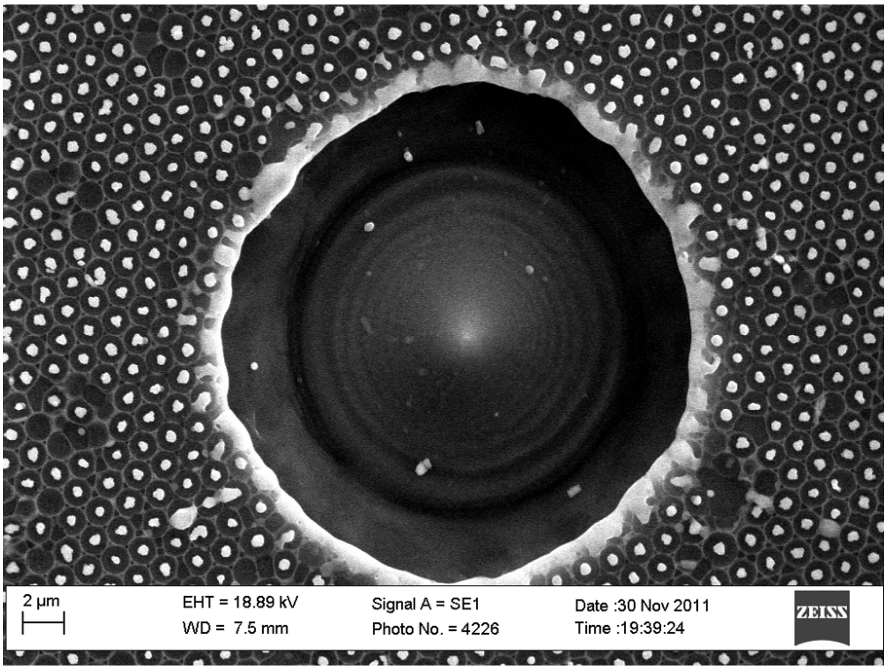

Figure 4.67: Post-field emission characterisation SEM image of CBD 1.5 μm sample at 0 ° observation angle

Sample	**Experimental γ**	**Modelled γ_0**	**Shielding factor**	**Modelled γ with shielding**
VPT1 Unordered	598	472.6		
VPT1 500 nm	883	472.6	$0.111\gamma_0$	52.5
VPT1 1 μm	1528	290.3	$0.297\gamma_0$	86.3
VPT2 Unordered	1495	1570.1		
VPT2 500 nm	385	93.0	$0.297\gamma_0$	27.66
VPT2 1 μm	477	110.2	$0.353\gamma_0$	38.9
VPT2 1.5 μm	682	49.3	$0.717\gamma_0$	35.4
CBD 500 nm	1230	49.3	$0.297\gamma_0$	14.7
CBD 1 μm	554	13.3	$0.717\gamma_0$	9.5
CBD 1.5 μm	307	15.3	$0.869\gamma_0$	13.3

Table 4.10: Experimental γ factors for the VPT and CBD samples

the sample. Large melted areas are also observed, as in Figure 4.54. Areas like this were also observed by Semet *et al* [34], and by Spindt *et al* [9]. In this area, the nanowires have been completely destroyed, and splattered material is present around the edges of the destroyed zone. Such a disturbance is most likely due to arcing between the sample and the anode. The loss of the emitters may affect the emission characteristics, however due to the small size of the melted area compared to the total area, the effect will be negligible if the number of melted areas is low.

In Figures 4.57, 4.58, 4.61, and 4.63 - 4.68, large craters can be seen. Again nanowires in the area have been destroyed, and the area is surrounded by a splatter of material that appears to have been resolidified after melting. However, in the craters there are signs of the silicon substrate having been melted, forming conical protrusions. The cones have dimensions on the order of microns, and have sharp tips. They bear some resemblance to Spindt valves (see example in Figure 4.69). The composition of the melted zone

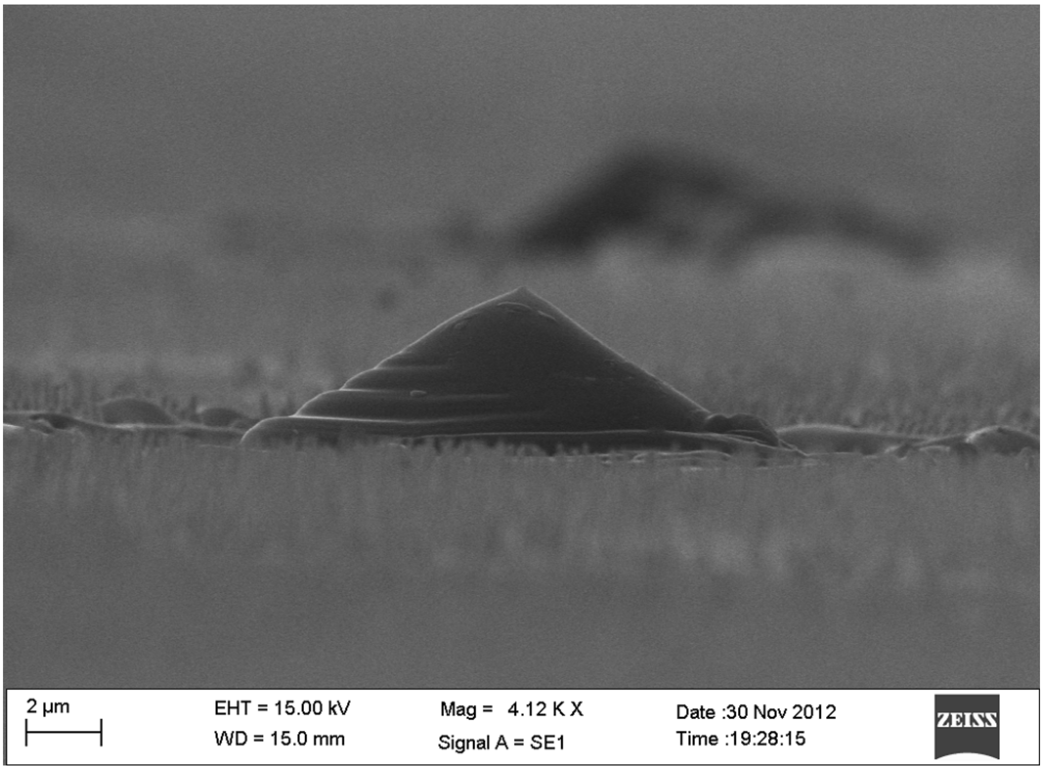

Figure 4.68: Post-field emission characterisation SEM image of CBD 1.5 μm sample with 80° tilt

shown in Figure 4.58 was investigated by energy dispersive x-ray spectroscopy (EDX), the results are presented in Table 4.11. The results indicate that the splattered material at the edge of the feature is melted ZnO, and that the feature in the centre of the melted region is composed of silicon. Silicon has a melting point of $\sim$1700 K, giving an indication of the temperatures that might be reached during field emission and arcing. In Figure 4.68, the tip of the cone appears to be several micron higher than any of the surrounding material. These cones will have a significant effect on a sample's observed field emission characteristics. Their geometry, in particular the sharp termination, is well suited to field emission, and due to the cratered area around each cone tip, shielding will be minimal.

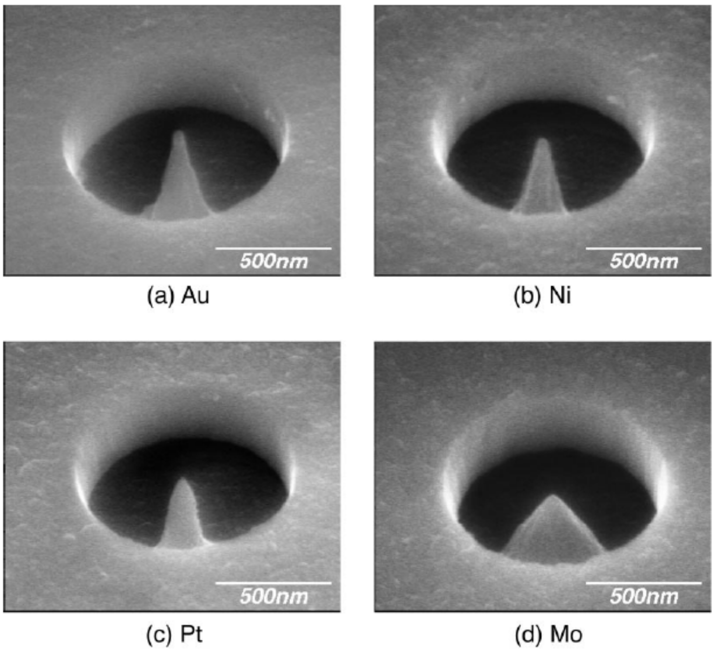
(a) Au (b) Ni (c) Pt (d) Mo

Figure 4.69: An example of Spindt valves from a work by Nagao et al [99]

Another feature is shown in Figures 4.59 and 4.60. This feature was observed only on the VPT2 1 μm spaced sample. Here we see a large mass of cracked material, in the case of Figure 4.59, and bulbous material, in the case of Figure 4.60, in the centre, each with cracked and buckled thin film surrounding it. EDX results for these features can be seen in Table 4.12. The results show that the material in the centre is composed mainly of silicon. It seems that material from the silicon substrate has pushed up through the zinc oxide thin film, causing the cracking and buckling. This may be due to heat expansion. The feature in Figure 4.60 in particular appears bulbous, consistent with melting, though there is no splattered material that has been seen with other large melts in either feature. The nanowires in this region exhibit an altered morphology, becoming very narrow towards the top, and terminating with a spherical tip. Like the conical features, these protuberances appear to be taller than the nanowires. They may field emit,

Area examined	Si (% weight)	Zn (% weight)	O (% weight)
Outside	2.57	65.91	22.92
Splatter	5.53	74.17	14.75
Centre	95.82	4.18	0.00

Table 4.11: Composition of material given by EDX on the feature in Figure 4.58 for the area outside the melted area, the splattered material at the edges of the melting, and the centre of the melted area

interfering with field emission characterisation of the wires, although their morphology is not as suited to field emission as the sharp cone shapes.

Feature	Area examined	Si (% weight)	Zn (% weight)	O (% weight)
Figure 4.59	Outside	9.29	54.07	26.65
	Centre	96.65	3.35	0.00
Figure 4.60	Centre	88.38	2.73	6.46

Table 4.12: Composition of material given by EDX on the feature in Figures 4.59 and 4.59 for an area outside the feature, and the material at the centre of each feature

In Figure 4.62 we present a feature observed on the 1.5 μm spaced VPT2 sample. The feature is a large, faceted piece of material on the surface of the sample. EDX results for the feature are presented in Table 4.13. These results show that the material is zinc oxide. The processes behind the formation of this kind of feature are unclear. The size of the feature is too large for it to be formed by melting rods coalescing together, and there is no obvious removal of material in the surrounding area that could have contributed to the feature. The feature is tall, and has faceted edges, and thus may field emit and interfere with field emission characterisation.

The observed features can be classified into those which do not significantly affect, and those which might significantly affect, field emission

Si (% weight)	**Zn (% weight)**	**O (% weight)**
0.00	64.50	25.81

Table 4.13: Composition of material given by EDX on the centre of the feature in Figure 4.62

characterisation. The samples from the VPT1 set and the unordered VPT2 sample exhibited only minor melting features. The samples from the CBD set and the 500 nm and 1 μm spaced VPT2 samples exhibited the conical features. The VPT2 1.5 μm sample did not have any of the conical features, but exhibited large, faceted pieces of material on the surface. While data from the latter samples may not represent emission from an ordered nanowire due to emission from these large features, it is safe to presume emission in the VPT1 set reasonably represents an ordered nanowire array, even if some emitters has been deformed or destroyed by melting. The values determined by experiment and FN analysis support the trend of γ increasing with spacing. While the experimental values for the ordered samples are much larger than the modelled values, as commonly reported, the ratios of the 1 μm spaced γ factor to the 500 nm spaced γ factor for experimental and modelled values are roughly equal, being 1.731 and 1.646, respectively.

The 1 μm sample, which had the highest enhancement factor and lowest turn-on voltage, was analysed by phosphor electrode imaging. The results were previously shown in Figures 4.13, 4.14, and 4.15. As the voltage increases the number of sites emitting increases with it. The turn-on voltage of this sample is $<$500 V, however, detectable light emission for the phosphor was not perceived until $\sim$1250 V. In Figures 4.70 - 4.72, we present phosphor electrode images for the 500 nm sample. These images exhibit a much lower amount of bright spots, even at significantly higher voltages. This may be

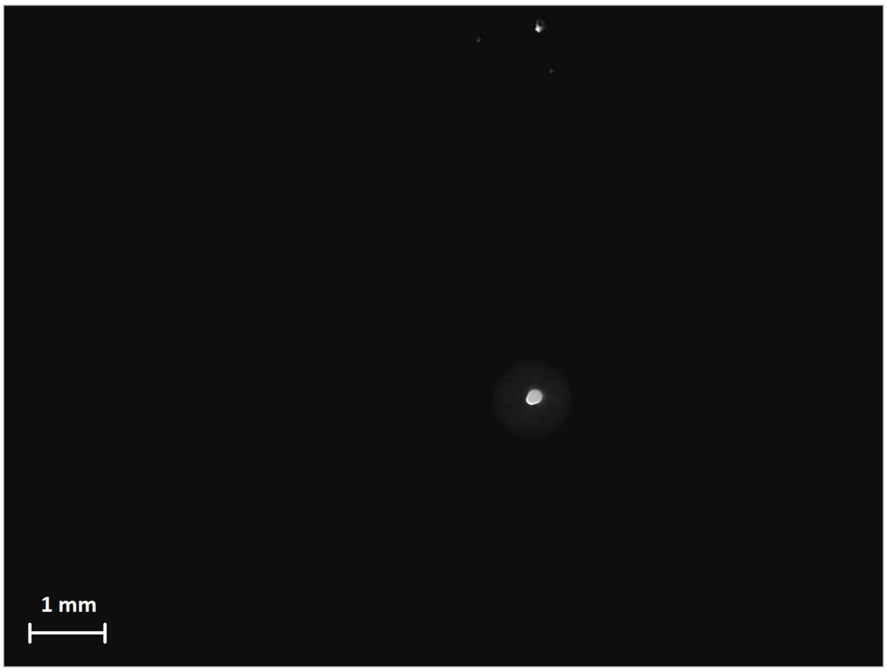

Figure 4.70: Image of phosphor electrode for the VPT2 500 nm spaced sample taken at 2250 V

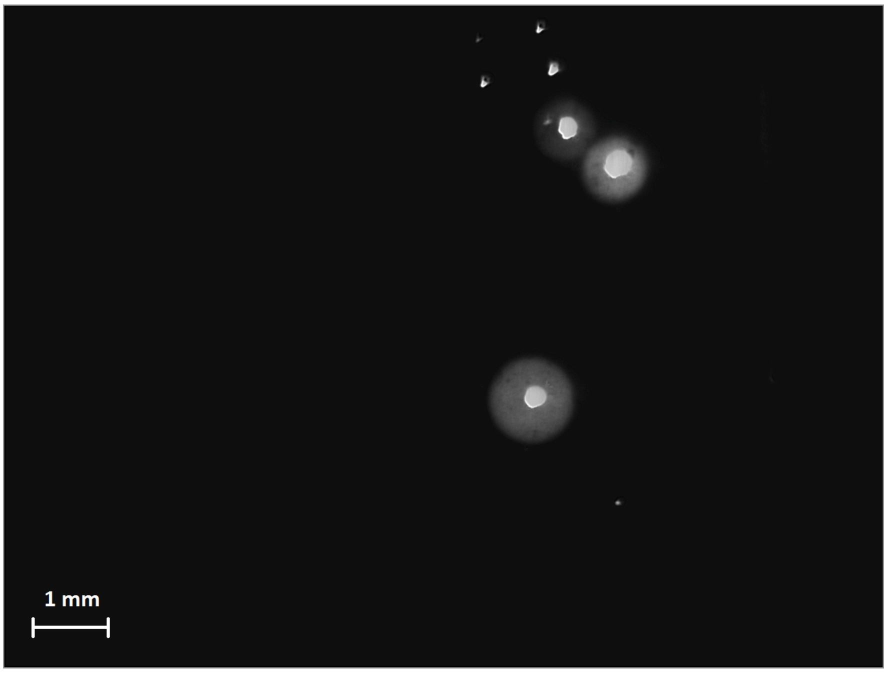

Figure 4.71: Image of phosphor electrode for the VPT2 500 nm spaced sample taken at 2500 V

Figure 4.72: Image of phosphor electrode for the VPT2 500 nm spaced sample taken at 2750 V

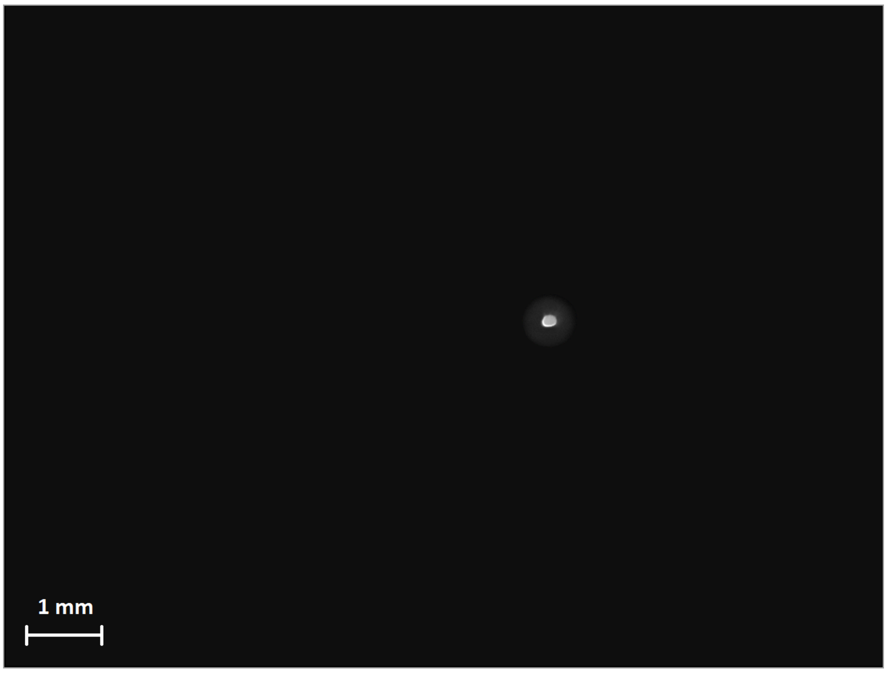

Figure 4.73: Image of phosphor electrode for the CBD 1.5 μm spaced sample taken at 2600 V

an effect of the spacing. However for the 1 μm spaced sample, more spots appeared at higher voltages. The emission levels saturate of the CCD array, indicating a high current densities. It is possible that if higher voltages could be stably achieved for the 500 nm spaced sample, the number of spots would be comparable to the 1 μm spaced sample. However higher voltages will increase the chance of arcing, which may damage the phosphor electrode. The samples that exhibited significant melting effects showed only one or two spots lighting. Again, this could be due to the lower turn-on and field enhancement requiring greater voltages for more bright spots, or it may be a sign that emission is primarily from melted features, such as the Si cones. A typical phosphor electrode image for one of these samples can be seen in Figure 4.73, showing just one bright spot.

Chapter 5

Results and Analyses: Field Emission of Nanostructured and Non-Nanostructured Films

5.1 Field Emission of Doped Zinc Oxide

Doping is the addition of trace amounts of impurities into a semiconductor to modify the electronic properties. While there are continuing difficulties with p-type doping of zinc oxide, there has been wide success in n-type doping. One method for doping in pulsed laser deposition growths is the use of targets containing dopants [45, 100, 101]. The work function of a material can be altered by using of doping, as discussed in Section 2.2.3. N-type doping will decrease the value of the work function, which should change the field emission characteristics. Improvements in field emission results have been reported for ZnO films by doping with cobalt [102], for a single ZnO nanowire by doping with indium [103], and for disordered ZnO nanowire arrays by doping with indium [104]. Aluminium has proven to be an effective n-type dopant for zinc oxide [105].

The variables in the FN equation (Equation (2.36)) are the current and voltage, which are acquired as data, and the work function and field enhancement factor. The analyses we have described thus far have assumed a value for the work function in order to obtain the field enhancement factor. If the field enhancement factor was known, the work function for a given sample could be calculated.

To experimentally investigate the effect of the work function on field emission characteristics, we deposited a number of doped and undoped columnar, nanostructured films using PLD. The targets used were pure zinc oxide, zinc oxide with 0.02 wt% Al_2O_3, zinc oxide with 0.2 wt% Al_2O_3, and zinc oxide with 2 wt% Al_2O_3. Samples were grown with each target, using the same growth parameters, in order to grow morphologically similar samples. If a work function is assumed for an undoped sample, a field enhancement factor can be determined from its field emission characteristics. As the field enhancement factor arises from geometry, it should be the same for morphologically similar doped samples. Thus the work function of these samples, relative to the assumed undoped work function, can be determined.

PLD is a widely established deposition technique for a variety of thin film materials [106]. In recent years, it has also been applied in the growing of nanostructures. It has been established that PLD growth of thin films with increasing background pressure during deposition, above about $\sim$0.1 mbar, shows a considerable increase in the surface roughness [107, 108]. By increasing the background pressures to on the order of 100 mbar, nanostructure growth can be achieved. Kawakami *et al* [109] attribute the growth of nanostructures to the formation of nanoparticles in the plume, due to the decreased mean free path for particles in the plume due to the higher pressure. High background pressures have proved effective in nanostructure growth for zinc oxide [44, 79, 109–111]. Tien *et al* present a study on the effect of background pressure and substrate temperature, for a two stage method in which a thin film of ZnO is deposited by low pressure PLD as a template layer, then grown upon by high pressure PLD [44].

We grew a number of nanostructured zinc oxide films on (100) silicon substrates by a two stage PLD method with a pure ZnO target. In the first stage, a clean (100) Si substrate was heated to 950 °C at a rate of 30 $°\mathrm{Cmin}^{-1}$, annealled for 5 min, and cooled to 300 °C at a rate of 20 $°\mathrm{Cmin}^{-1}$. This anneal is to clean the substrate of adsorbates. The substrate was deposited on by PLD at 300 °C for 5,000 shots at a rate of 10 Hz, with a background gas of O_2 at 1.33 mbar. After deposition, the sample was heated to 750 °C at a rate of 30 $°\mathrm{Cmin}^{-1}$, annealled for 5 min, and cooled to 150 °C at a rate of 10 $°\mathrm{Cmin}^{-1}$, in an oxygen background. Samples were allowed to cool from 150 °C to room temperature naturally. This first stage deposits a thin film, to be used as a template for nanostructure growth. Using spectroscopic ellipsometry, the thickness of such a film was found to be ∼120 nm. Figures 5.1 and 5.2 show XRD results for such a film, presenting a θ-2θ scan and rocking curve of the (0002) ZnO peak, respectively. The FWHM of the rocking curve is ∼2°, indicating good crystallite alignment.

In the second stage this thin film was grown upon by PLD, using various shot counts, background pressures and deposition temperatures. The sample was heated to its deposition temperature at a rate of 10 $°\mathrm{Cmin}^{-1}$, deposited on for the desired number of shots with the desired background pressure,

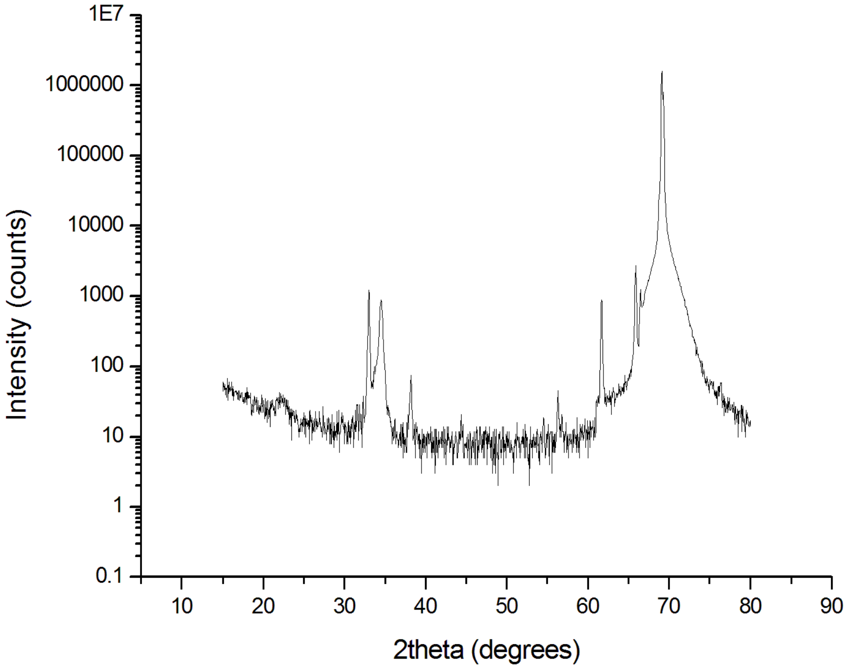

Figure 5.1: θ-2θ scans for a PLD-grown ZnO thin film

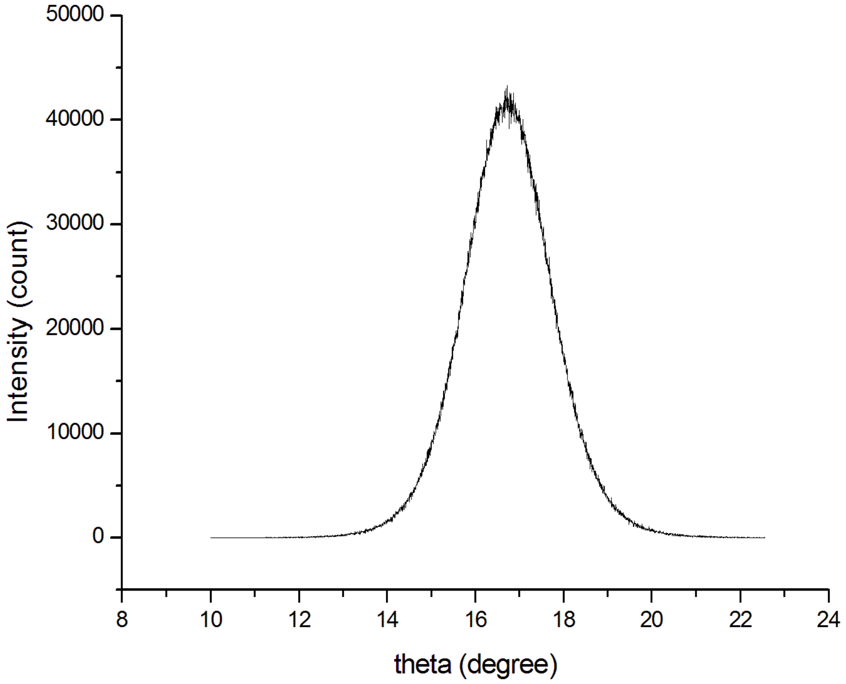

Figure 5.2: Rocking curve around the (0002) ZnO peak for a PLD-grown ZnO thin film

then cooled to 150 °C at a rate of 10 °Cmin^{-1}.

Sample	**Temperature (°C)**	**Background Pressure (mbar)**	**Number of Shots**
S01	800	0.533	20,000
S02	800	0.667	20,000
S03	800	0.800	20,000
S04	800	0.533	40,000
S05	800	0.667	40,000
S06	800	0.800	40,000
S07	800	1.000	40,000
S08	800	1.267	40,000
S09	650	0.800	40,000
S10	950	0.800	40,000
S11	650	1.000	40,000
S12	950	1.000	40,000

Table 5.1: Deposition parameters for undoped ZnO nanostructured films

We grew a number of undoped ZnO samples by this two stage method, using the parameters listed in Table 5.1 for the second stage. The samples were investigated by SEM, the results of which can be seen in Figures 5.3 - 5.15. The samples all exhibit nanostructured growth in some form. Samples S01 - S03, shown in Figures 5.3 - 5.5, show columnar film growth, with tips typically ∼300 nm across, with less frequent ∼100 nm diameter tips also present. Samples S04 - S06, shown in Figures 5.6 - 5.9, were grown with the same temperature and background pressures, but with an increased shot count. These samples also exhibit columnar growth, with tips of ∼100 - 300 nm. The sharp, hexagonal, faceted geometry of the tip can been seen clearly in Figures 5.8 and 5.9.

Samples S07 and S08, shown in Figures 5.10 and 5.11, used higher pressures than the previous 6 samples. Sample 07 shows similar growth to the previous samples. However, Sample 08 presents a different morphology, where the columns of the growth have coalesced giving a more uniform film. It also exhibits cracks, which are usually typical of temperature expansion

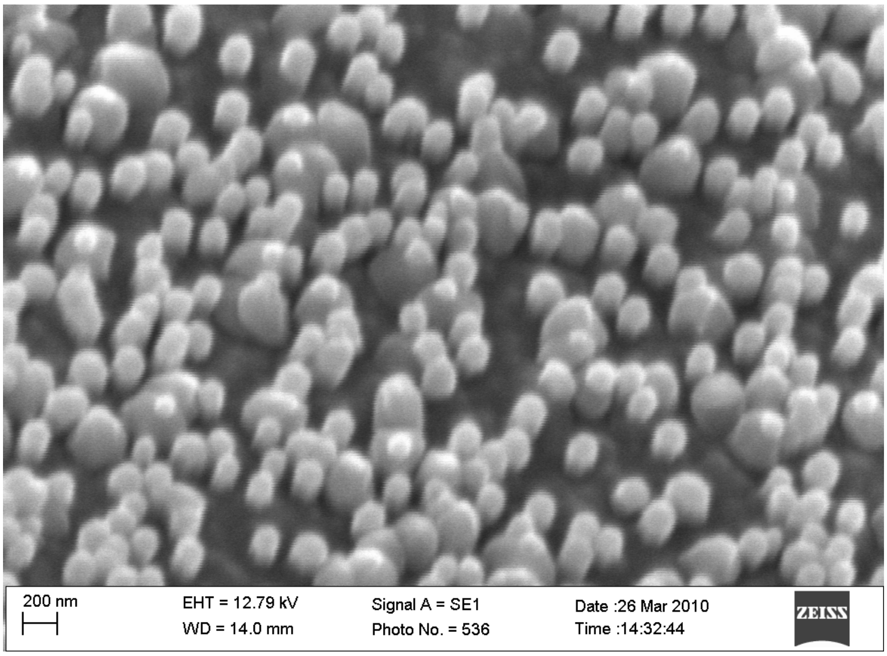

Figure 5.3: SEM image of sample S01 taken at 30 ° observation angle

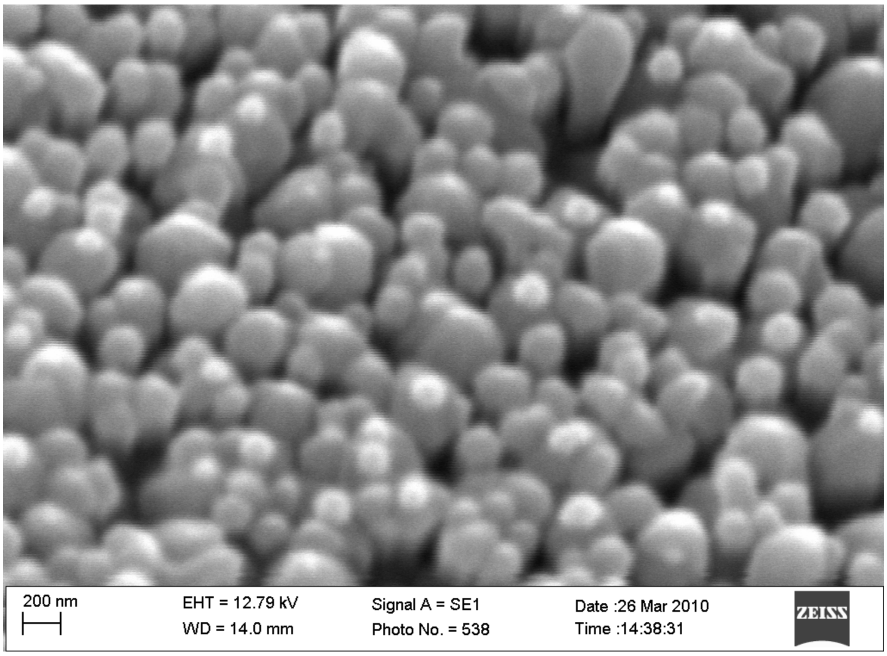

Figure 5.4: SEM image of sample S02 taken at 30 ° observation angle

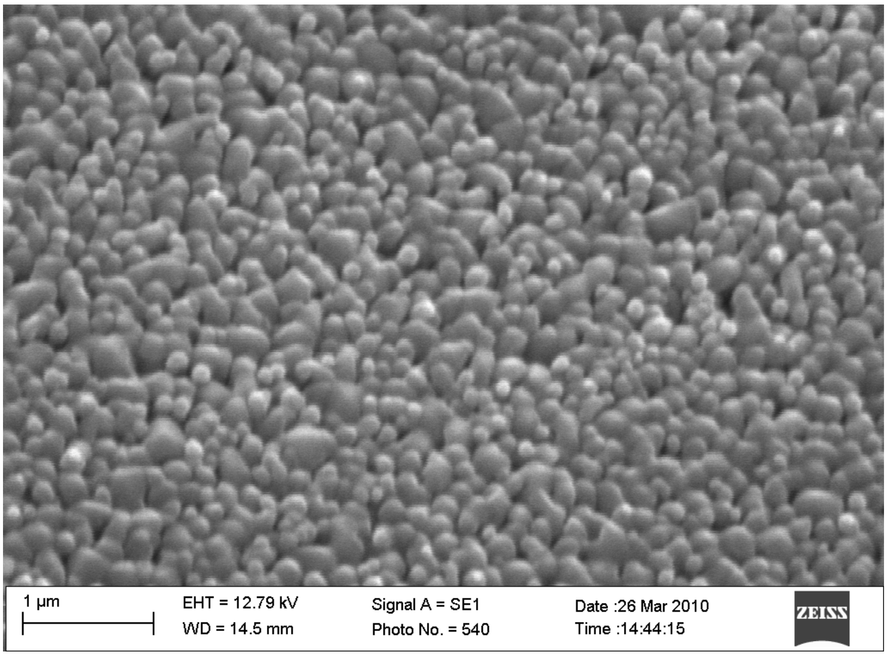

Figure 5.5: SEM image of sample S03 taken at 30 ° observation angle

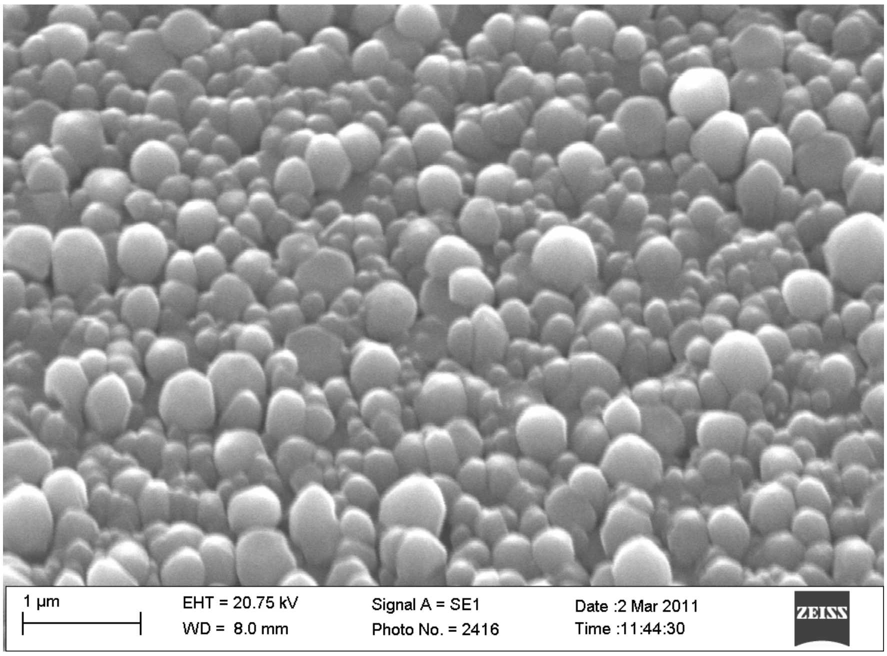

Figure 5.6: SEM image of sample S04 taken at 30 ° observation angle

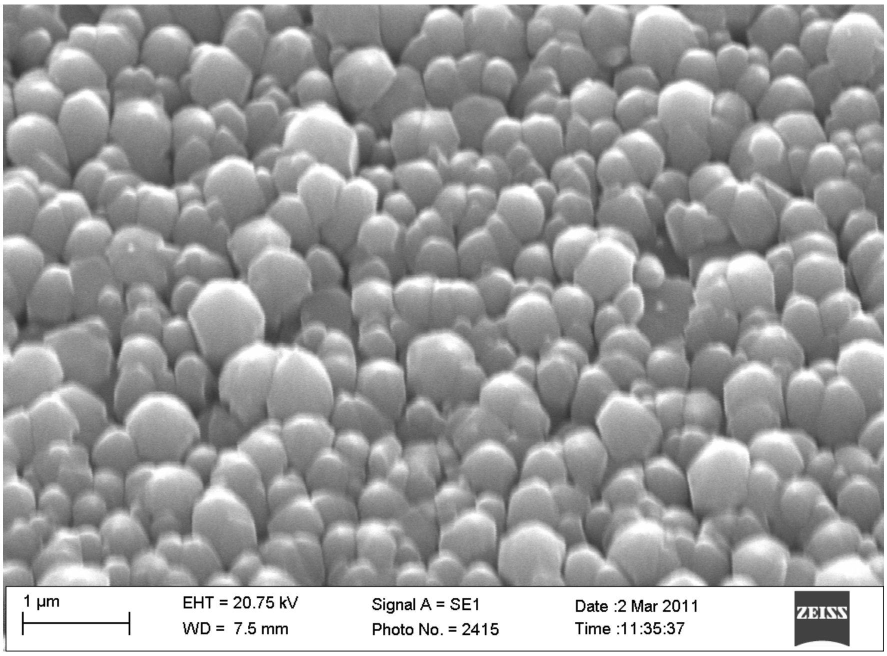

Figure 5.7: SEM image of sample S05 taken at 30 ° observation angle

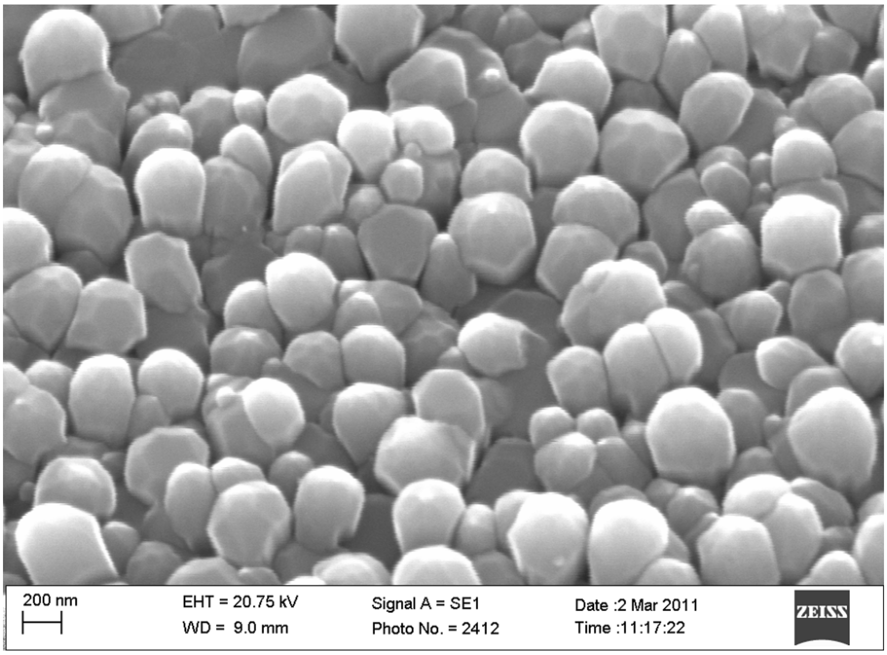

Figure 5.8: SEM image of sample S06 taken at 30 ° observation angle

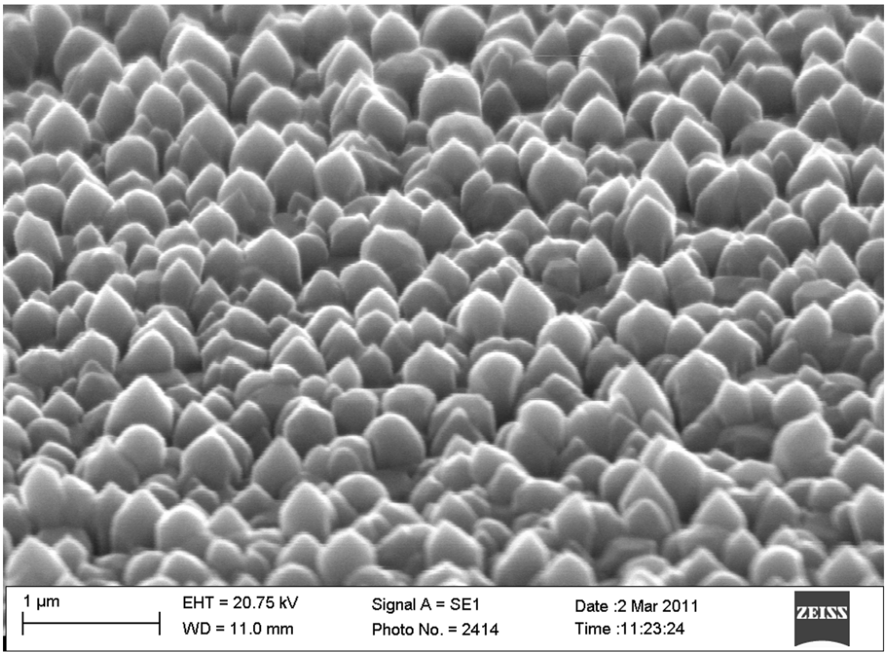

Figure 5.9: SEM image of sample S06 taken at 70 ° observation angle

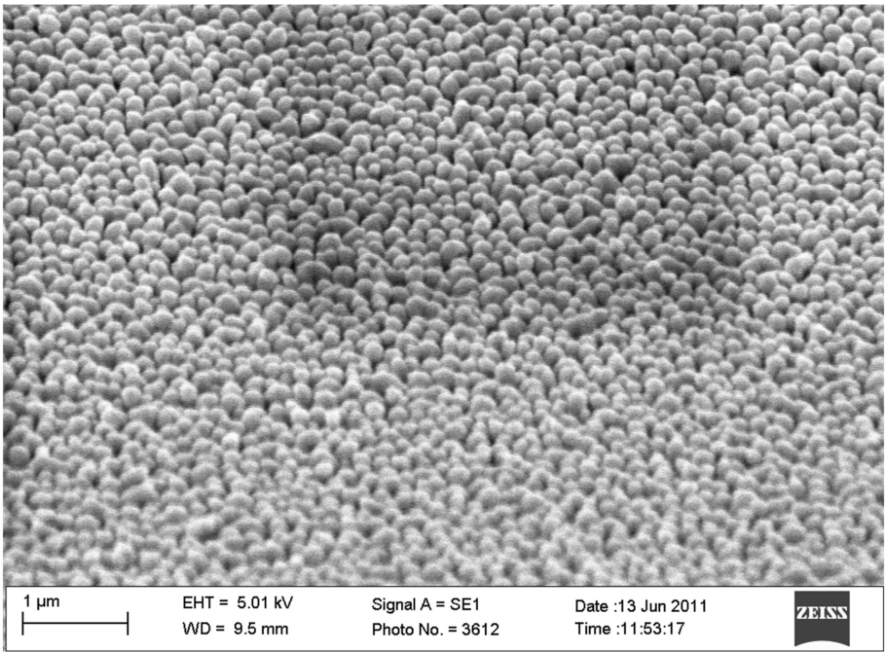

Figure 5.10: SEM image of sample S07 taken at 45 ° observation angle

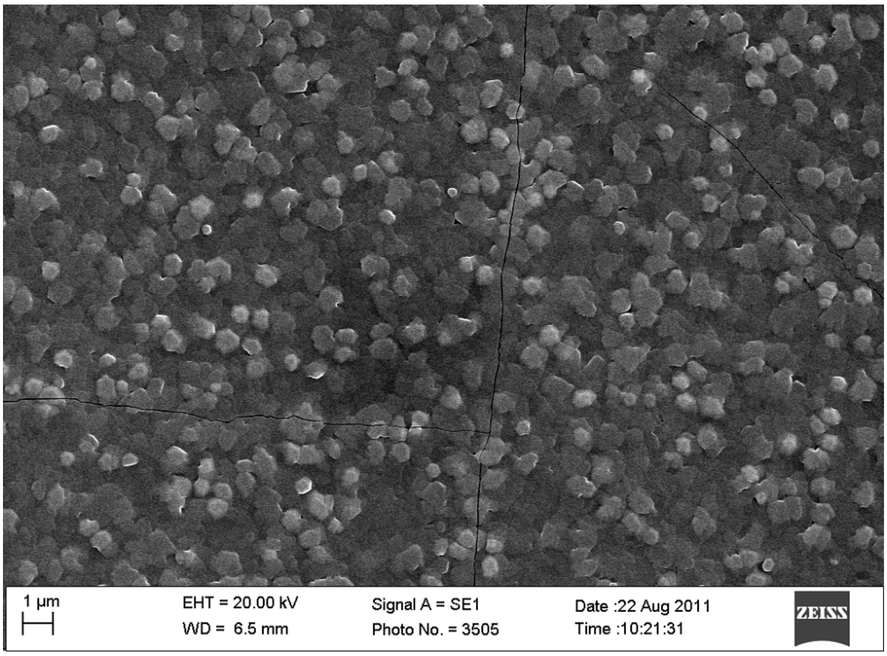

Figure 5.11: SEM image of sample S08 taken at 0 ° observation angle

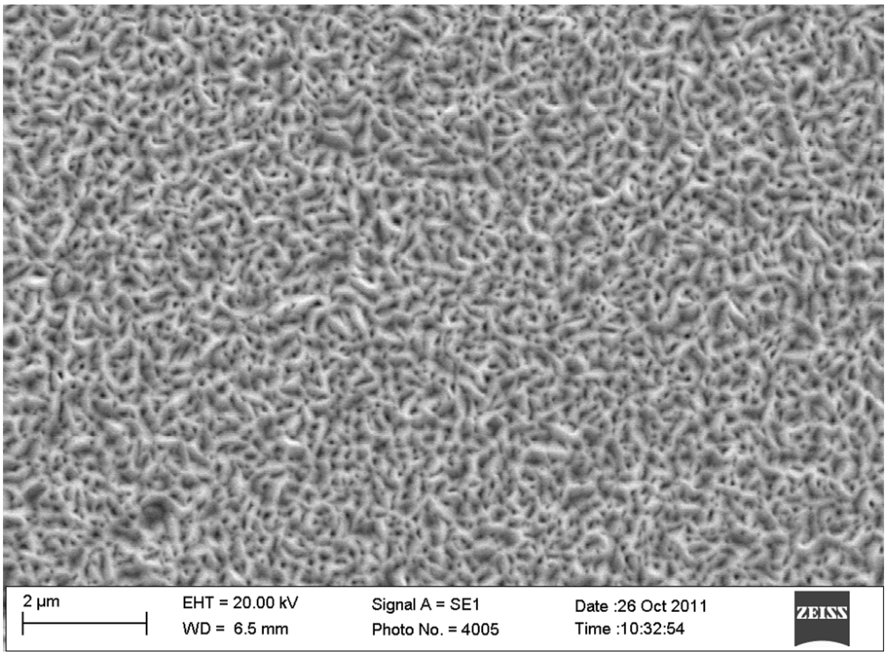

Figure 5.12: SEM image of sample S09 taken at 0 ° observation angle

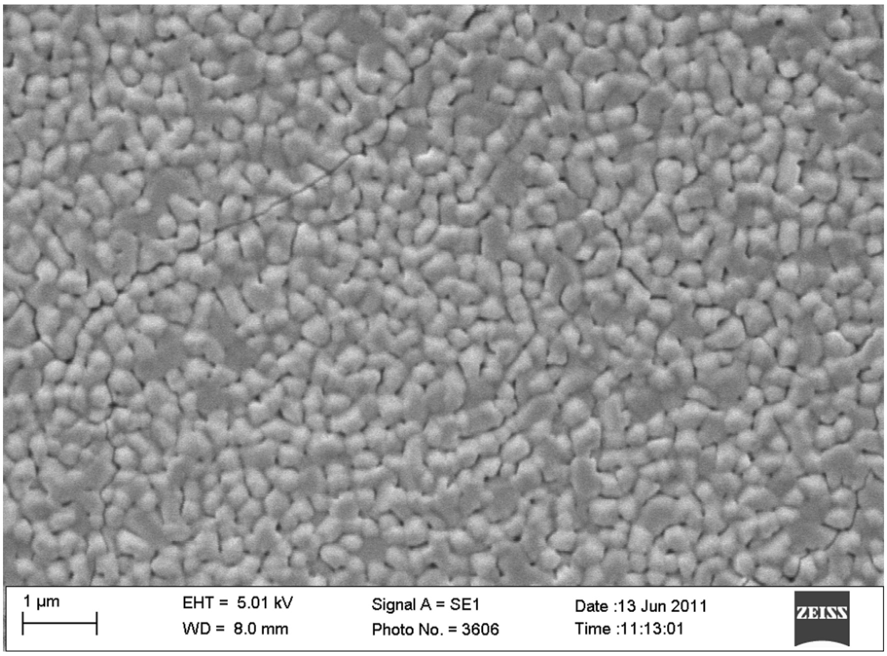

Figure 5.13: SEM image of sample S10 taken at 0 ° observation angle

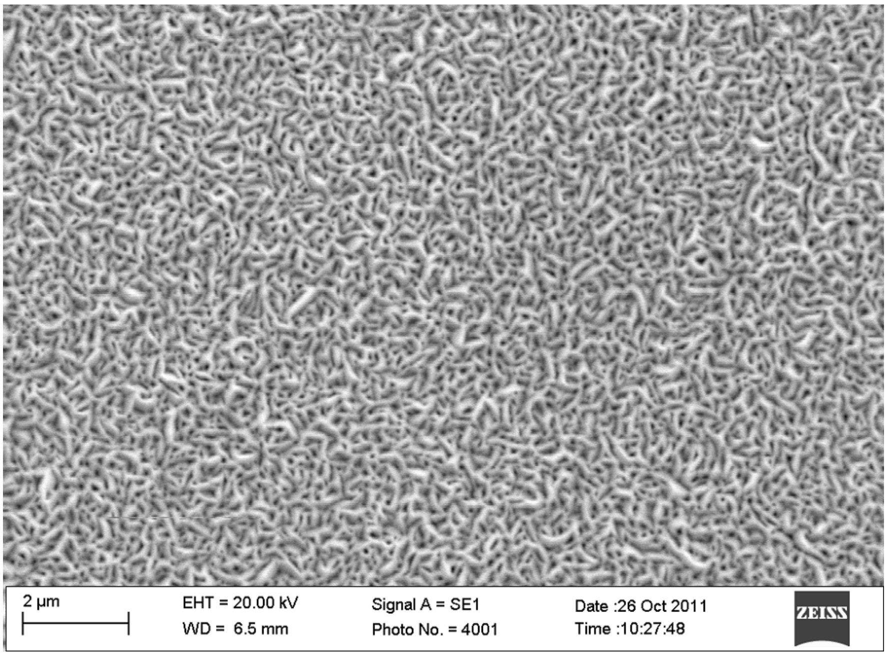

Figure 5.14: SEM image of sample S11 taken at 0 ° observation angle

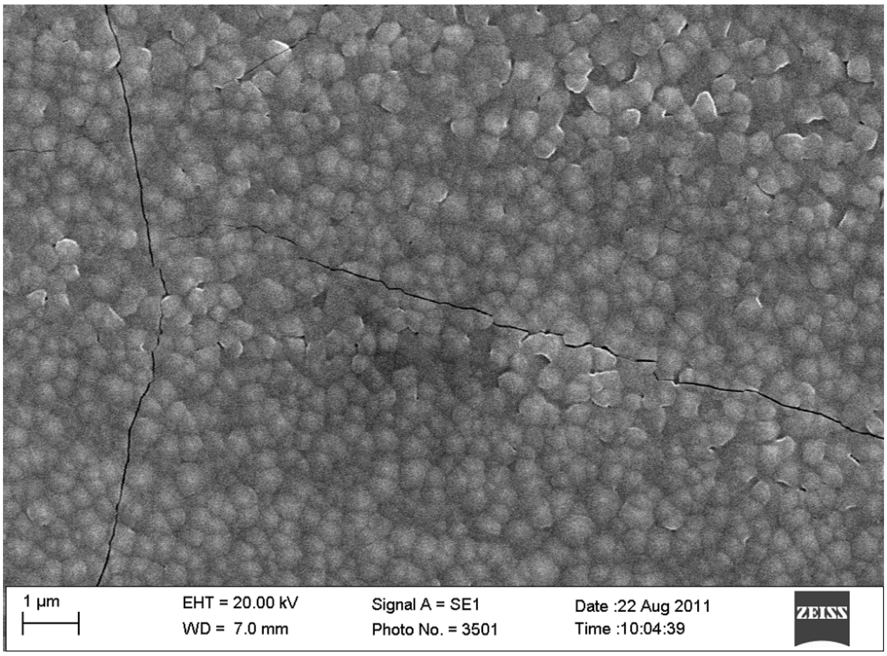

Figure 5.15: SEM image of sample S12 taken at 0 ° observation angle

effects, however it was deposited at the same temperature as the other PLD samples discussed thus far. Samples S09 - S12, shown in Figures 5.12 - 5.15, were grown at different temperature for two background pressures. The lower temperature growths, S09 and S11, lead to a markedly different structure to the samples previously discussed. The columnar growth terminating in hexagonal tips is not evident here. Instead a web of connected growth is seen across the surface. The higher temperature growths, S10 and S12, show growth that is more similar to the typical columnar growth, but with some coalescing of the columns and signs of cracking. Samples were analysed by XRD, and found no significant differences between samples. A typical θ-2θ scan and rocking curve around the (0002) ZnO peak are shown in Figures 5.16 and 5.17, respectively.

Based on the above results, the parameters of Sample S06 gives the best results morphologically, for field emission purposes. It presents sharp, faceted

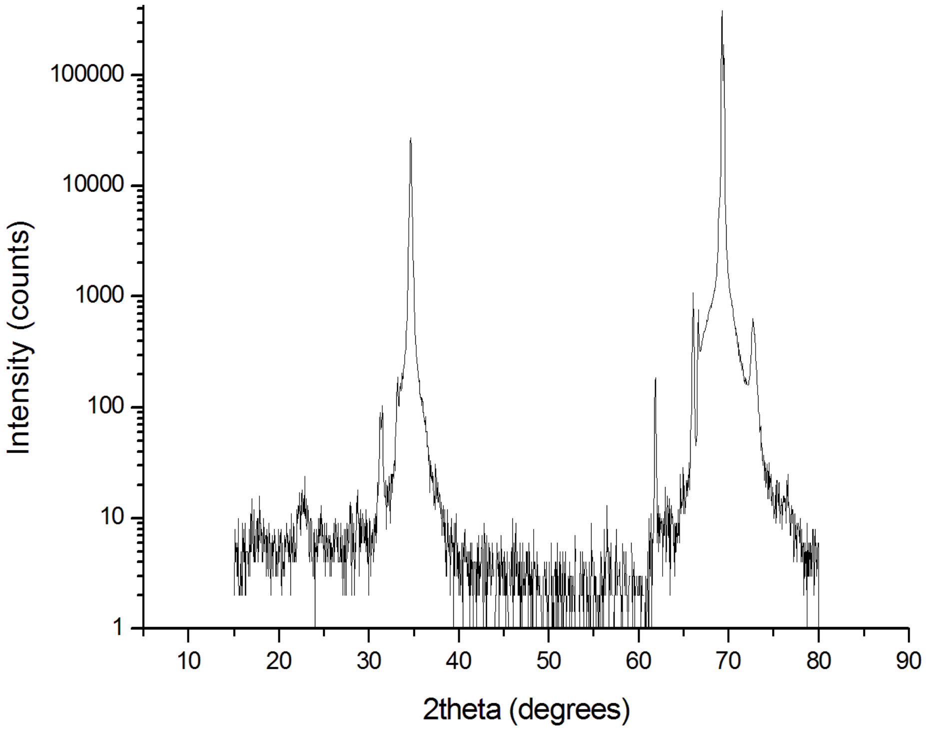

Figure 5.16: θ-2θ scan for a 2-stage PLD-grown ZnO nanostructure film

tips, with the most uniformity. It shows minimal non-columnar growth or coalescing/merging of columns, and no cracks. Aluminium doped zinc oxide nanostructure films were grown by performing a two stage deposition, as described above, using the same parameters as used for Sample S06, with $ZnO:Al_2O_3$ targets. Using three such targets composed of ZnO, with 0.02 wt%, 0.2 wt% and 0.02 wt% Al_2O_3, respectively, 3 doped ZnO nanostructure films were deposited. The sheet concentration and sheet resistance of the samples was estimated using a 4-point Hall effect probe, which can be used with the thickness of the deposited material (~1 μm) the results can be seen in Table 5.2. These measurements may be affected by possible discontinuities in the structure of the deposited material. This may have caused the p-type behaviour of the sample deposited with the pure ZnO target. How-

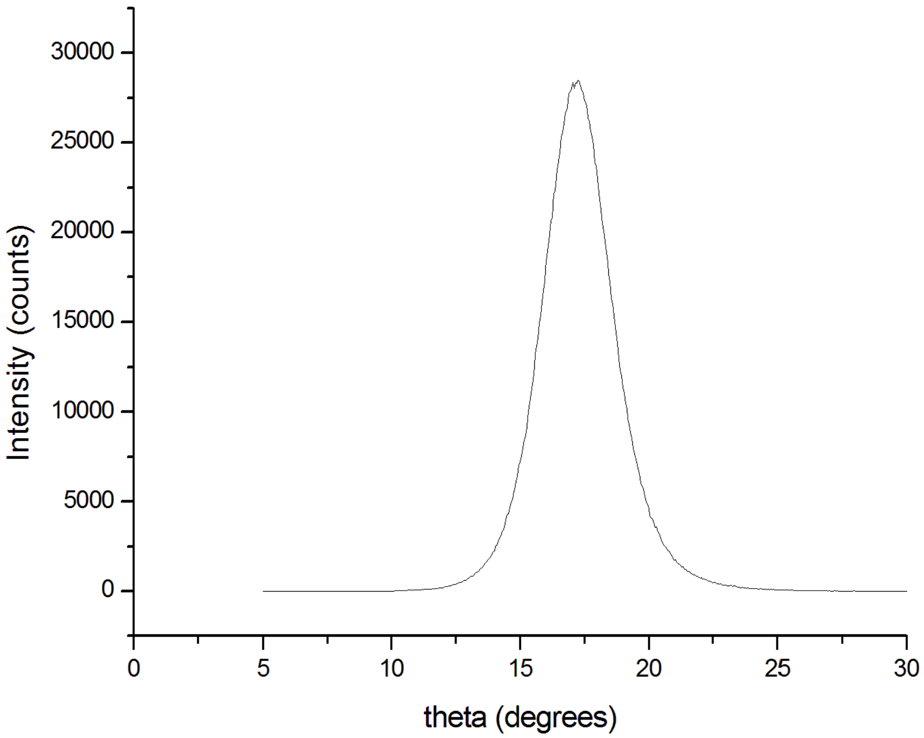

Figure 5.17: Rocking curve around the (0002) ZnO peak for a 2-stage PLD-grown ZnO nanostructure film

ever the behaviour may also be caused by the semi-insulating behaviour of the material, or the low carrier concentration. The values obtained for the samples grown with the ZnO:Al_2O_3 targets agree well with values reported in the literature for Al-doped ZnO [112, 113]. These values indicate increasing electron concentration with the amount of Al_2O_3, which is consistent with n-type doping.

The presence of dopants did not have any significant effect on the sample morphology. Samples were analysed by XRD, and found no significant differences between samples. A typical θ-2θ scan and rocking curve around the (0002) ZnO peak are shown in Figures 5.16 and 5.17, respectively. Rocking curves from these samples have FWHM of $\sim 3°$, slightly broader than the

Sample	**Sheet concentration ($\mathbf{cm^{-2}}$)**	**Carrier concentration ($\mathbf{cm^{-3}}$)**	**Sheet resistance ($\mathbf{\Omega}$/square)**	**Resistivity ($\mathbf{\Omega}$cm)**
Pure ZnO target	1.64×10^{7}	1.64×10^{15}	3.48×10^{7}	3.48×10^{-1}
0.02 wt%	-5.15×10^{11}	-5.15×10^{19}	5.90×10^{4}	5.90×10^{-4}
0.2 wt%	-1.86×10^{13}	-1.86×10^{21}	7.89×10^{4}	7.89×10^{-4}
2 wt%	-1.41×10^{15}	-1.41×10^{23}	9.94×10^{4}	9.94×10^{-4}

Table 5.2: Sheet concentrations for undoped and doped samples

template thin film. In Figure 5.18 we present representative SEM images for samples grown with the pure ZnO, 0.02 wt%, 0.2 wt% and 0.02 wt% targets. The field emission characteristics of these samples were tested with the apparatus and method previously described. The results are present as I-V curves in Figure 5.19, and linear FN plots in Figure 5.20.

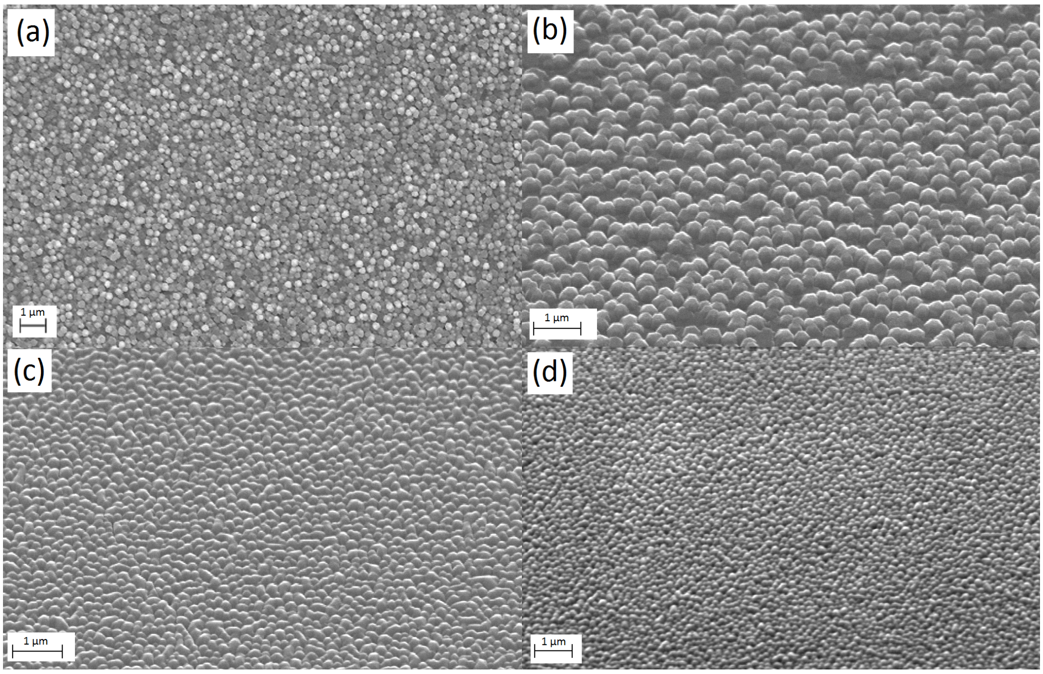

Figure 5.18: SEM image of samples grown with (a) undoped, (b) 0.02 wt%, (c) 0.2 wt%, and (d) 2 wt% targets

From the I-V and FN plots, it appears that the field emission properties from best to worst are the 2 wt%, undoped, 0.2 wt%, and the 0.02 wt%. This goes against expectations, as the samples should be geometrically similar, with higher doping leading to a smaller work function, and thus better field emission. The γ factor determined for the undoped sample by our analysis method is ~496, for an assumed work function of ~3.7 eV. Assuming that the samples are geometrically similar enough to assume a roughly equal γ factor, we can apply Equation (2.37) to determine a work function for each

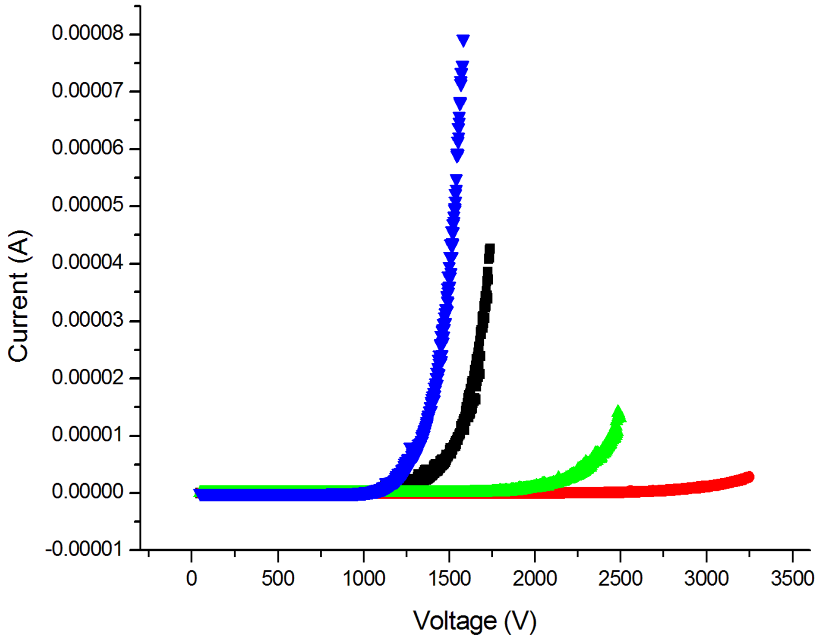

Figure 5.19: I-V curves for samples grown with undoped (black), 0.02 wt% (red), 0.2 wt% (green), and 2 wt% (blue) targets

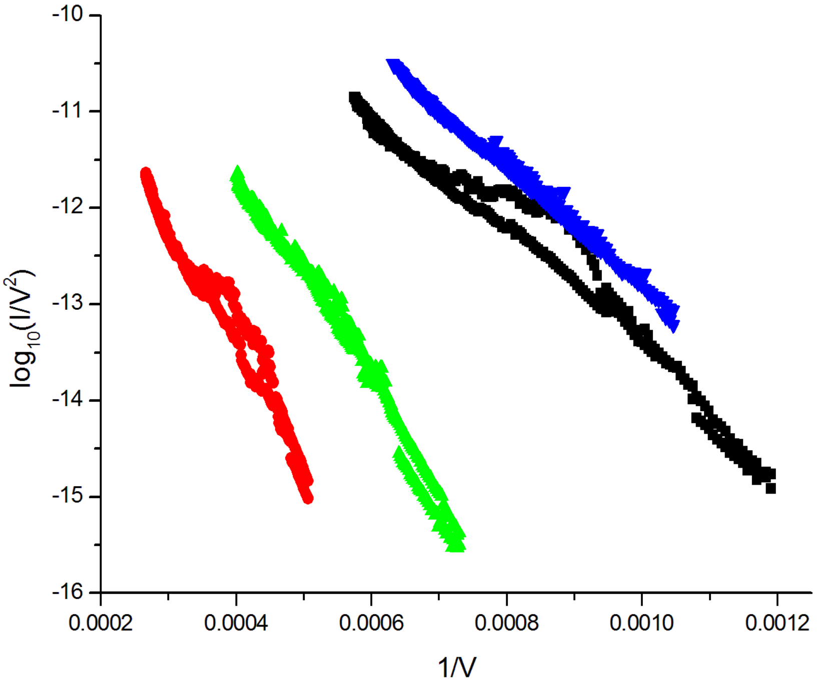

Figure 5.20: FN plots for samples grown with undoped (black), 0.02 wt% (red), 0.2 wt% (green), and 2 wt% (blue) targets

doped sample. This gave values of 5.51 eV, 5.35 eV, and 3.56 eV, for the 0.02 wt%, 0.2 wt% and 2 wt% target samples, respectively. These values seem unrealistic, as n-type doping should decrease the work function, and the sheet concentrations measured indicated increasing n-type doping with increasing Al_2O_3 levels in the target. The current densities (J_{FN}) and emission areas (A_{FN}) were calculated using these work function values, and are plotted in Figures 5.21 and 5.22, respectively.

The samples were examined by SEM after field emission characterisation. The results can be seen in Figures 5.23 - 5.26. In Figures 5.23 and 5.24 we can see a crater similar to those seen on the VPT and CBD samples in Section 4.2. Such craters were seen across all 4 samples. In Figures 5.25 and 5.26, a feature seen on the sample grown with the 2 wt% target is presented. In this area, the sharp tipped columns are no longer present, having undergone a complete morphology change. The area appears to have melted and cooled, allowing the material to re-form into this new morphology.

These craters and morphological changes will undermine analysis based on assuming a roughly uniform geometry. This may have given rise to the unexpected work functions determined by our analysis above.

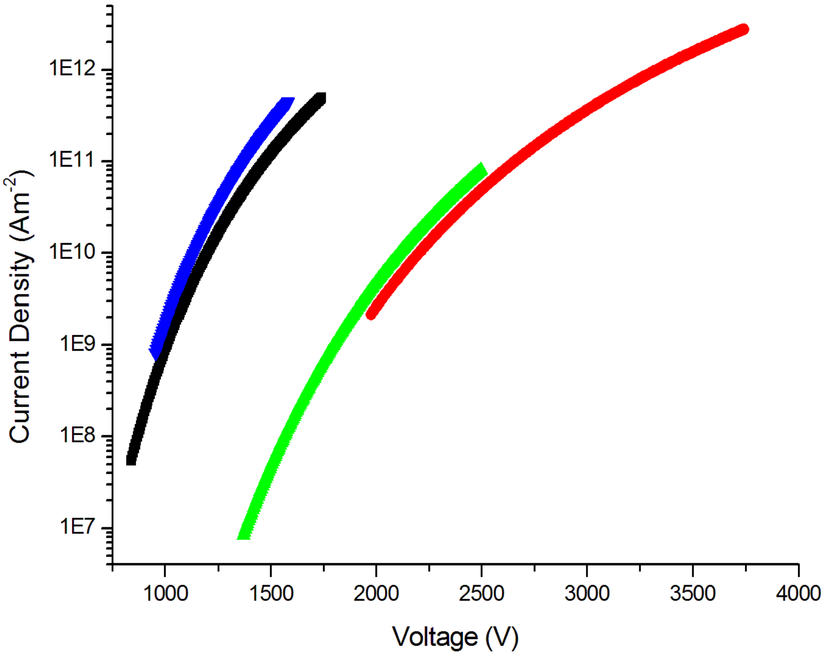

Figure 5.21: Plot of J_{FN} vs. Voltage for samples grown with undoped (black), 0.02 wt% (red), 0.2 wt% (green), and 2 wt% (blue) targets

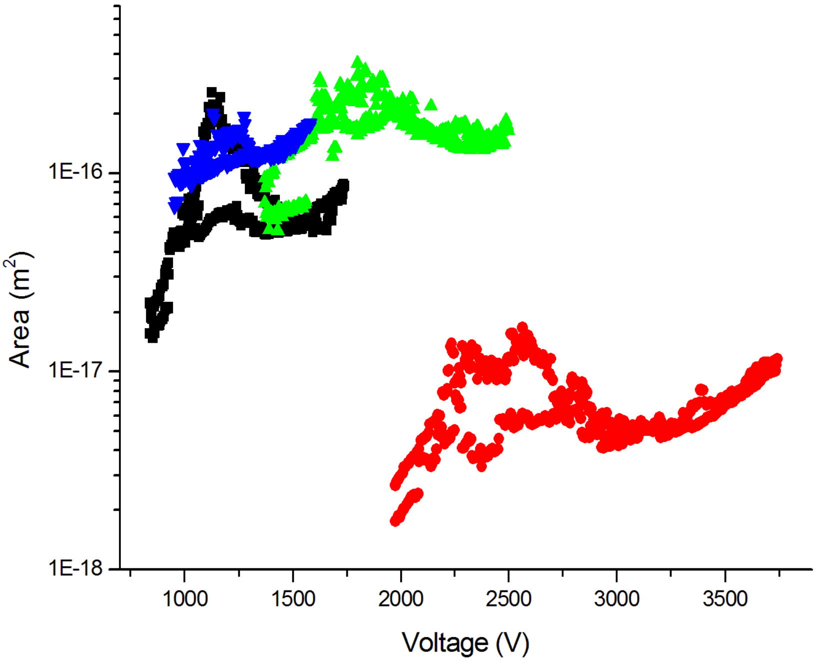

Figure 5.22: Plot of A_{FN} vs. Voltage for samples grown with undoped (black), 0.02 wt% (red), 0.2 wt% (green), and 2 wt% (blue) targets

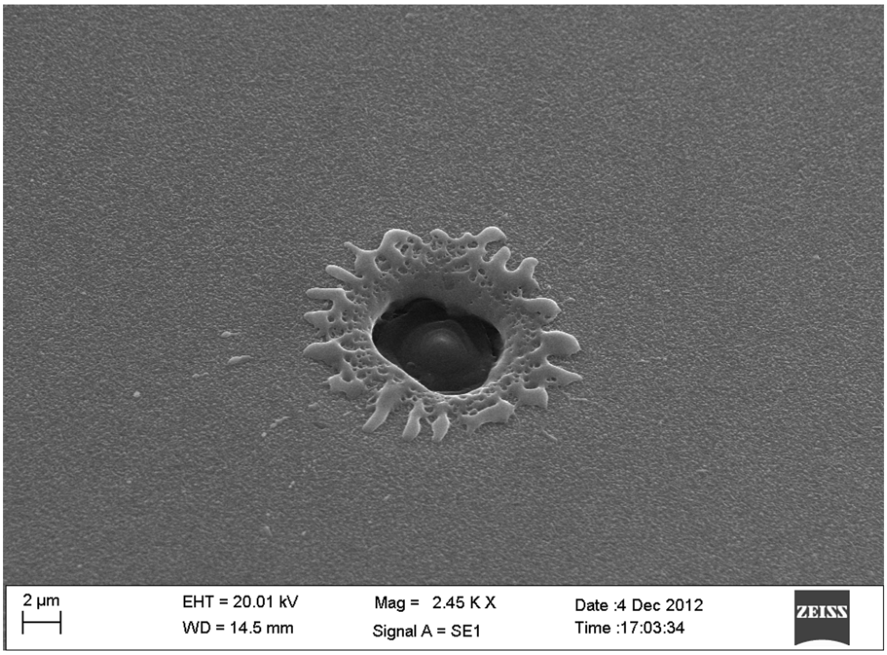

Figure 5.23: SEM image of the sample grown by PLD with a ZnO with 2 wt% Al_2O_3 target taken at 30 ° observation angle

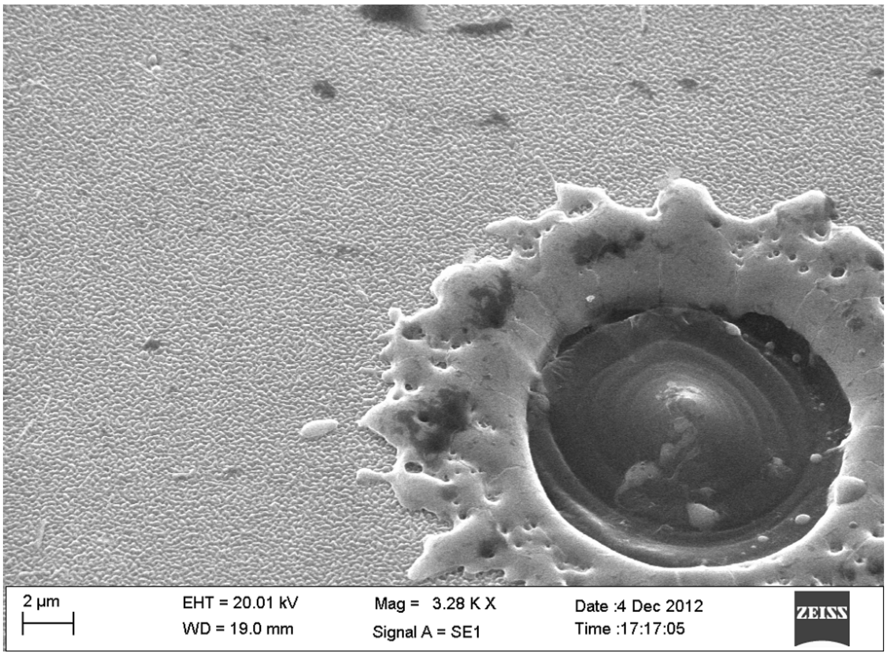

Figure 5.24: SEM image of the sample grown by PLD with a ZnO with 0.02 wt% Al_2O_3 target taken at 30 ° observation angle

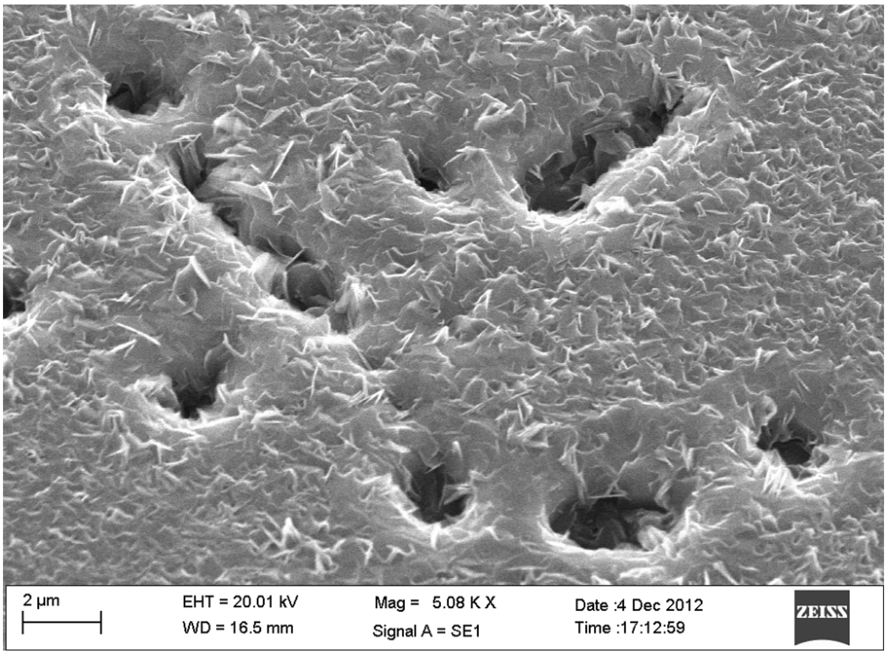

Figure 5.25: SEM image of the sample grown by PLD with a ZnO with 2 wt% Al_2O_3 target taken at 30 ° observation angle

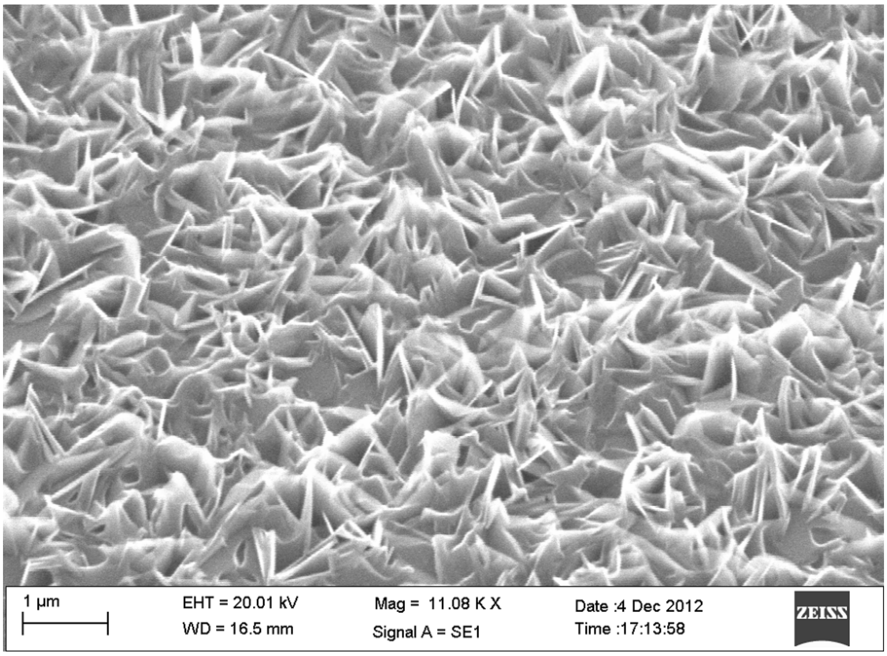

Figure 5.26: SEM image of the sample grown by PLD with a ZnO with 2 wt% Al_2O_3 target taken at 30 ° observation angle

5.2 Field Emission of ZrN and ZrC Films

There has been much research and development in transition metal carbide and nitride coatings, such as zirconium nitride (ZrN) and zirconium carbide (ZrC), in the last decades, due to their properties like high hardness [114], biocompatibility [115], and high melting point (2982 °C for ZrN [116], 3540 °C for ZrC [117]). These coatings have industrial applications such as hard coatings [118], semiconductor devices [119], and optical applications in heat mirrors [120].

Another potential use for these coatings is as a protective coating on field emitters. The high hardness and stability is desirable for field emission applications. As we have seen in the previous results, thermal destruction of field emitters can be significant, making the high melting points of these materials very suitable. In field emission, the work function at the surface is a key factor, therefore any coatings would need to have a reasonably low work function, in order to be viable. The work functions of ZrN and ZrC are reported to be ∼2.9 eV [121] and ∼3.5 eV [122], respectively.

In this section we have characterised the field emission properties of a ZrN thin film and a ZrC thin film, both on a (100) silicon substrate, which were fabricated by Dr. Valentin Craciun of the Department of Material Science and Engineering, at the University of Florida. In Figures 5.27 - 5.30 we present I-V curves and FN plots for the two samples.

The turn-on voltages for the ZrN and ZrC thin films are ∼1275 V and ∼1542 V, respectively. The emitters are thin films, and thus if they are sufficiently flat, they can be considered approximately planar. In this case, there will be no field enhancement due to geometry, meaning a γ factor of 1.

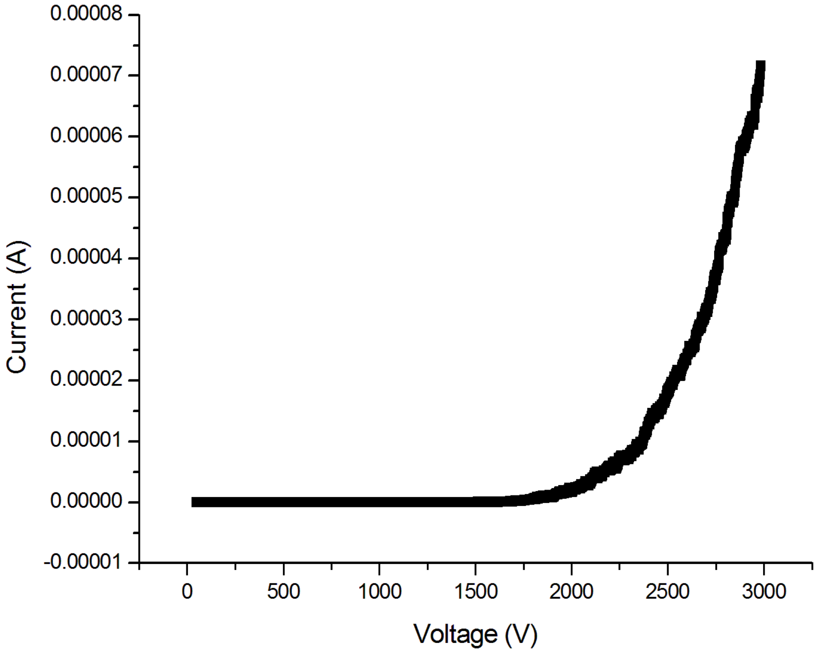

Figure 5.27: I-V curve for ZrN thin film

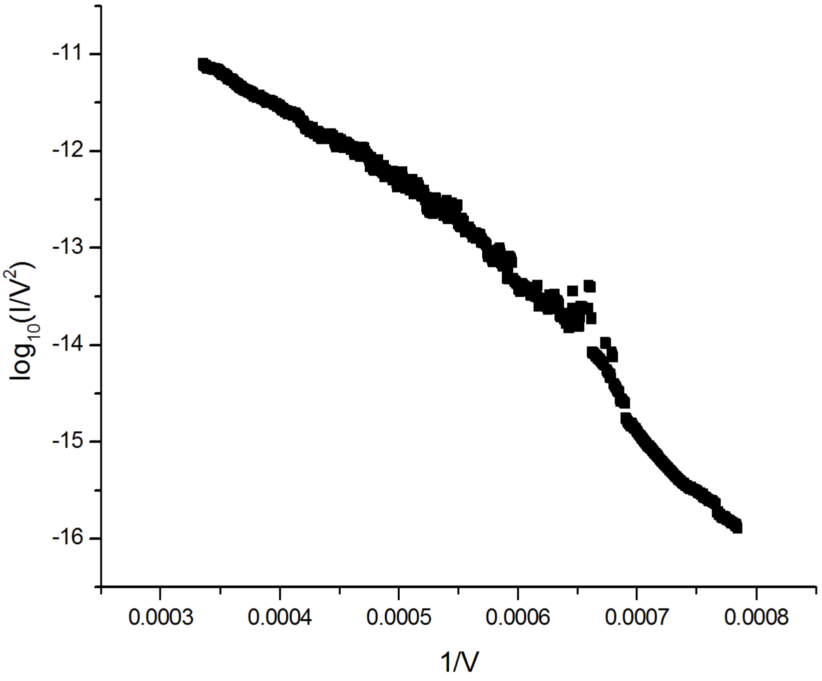

Figure 5.28: FN plot for ZrN thin film

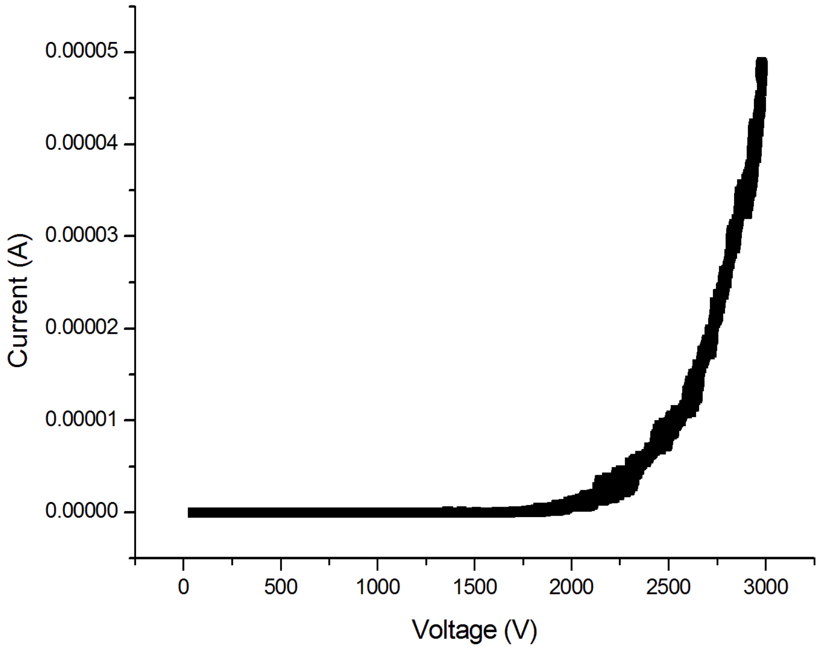

Figure 5.29: I-V curve for ZrC thin film

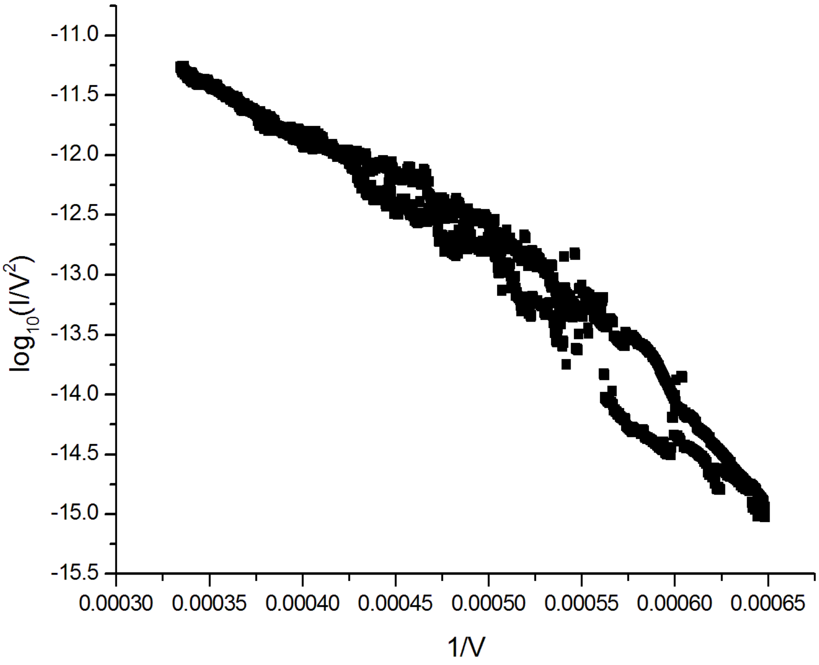

Figure 5.30: FN plot for ZrC thin film

Having a known γ factor means that the work function can be determined from Equation (2.37). Performing this analysis gives values of $\sim$0.09 eV for both types of sample. This value seems unrealistic, and from this we can conclude that the samples do not behave as planar emitters. If we assume the work functions of 2.9 eV and 3.5 eV for ZrN and ZrC, respectively, we can analyse the samples using our treatment, and determine γ factors, current densities, and emission areas. The γ values determined by our iterative method for the ZrN and ZrC thin films are $\sim$336 and $\sim$415, respectively. Plots of the current densities and emission areas against the applied voltage are seen in Figures 5.31 - 5.34. We see current densities on the order of $\sim 10^{11}$ Am^{-2}, and emission areas on the order of $\sim 10^{-16}$ m^2.

The samples were analysed by SEM after field emission characterisation. The results are presented in Figures 5.35 - 5.40. We see localised areas of melting and delamination on both samples. The presence of melting on materials with such high melting points gives an indication of the high temperatures reached during field emission testing. There is a large amount of delamination compared to the zinc oxide samples tested, which may indicate weaker bonding between the thin film and substrate, or higher currents/temperatures resulting in more damage. These features disrupt the flat surface, which leads to the deviation from planar emitter behaviour described above.

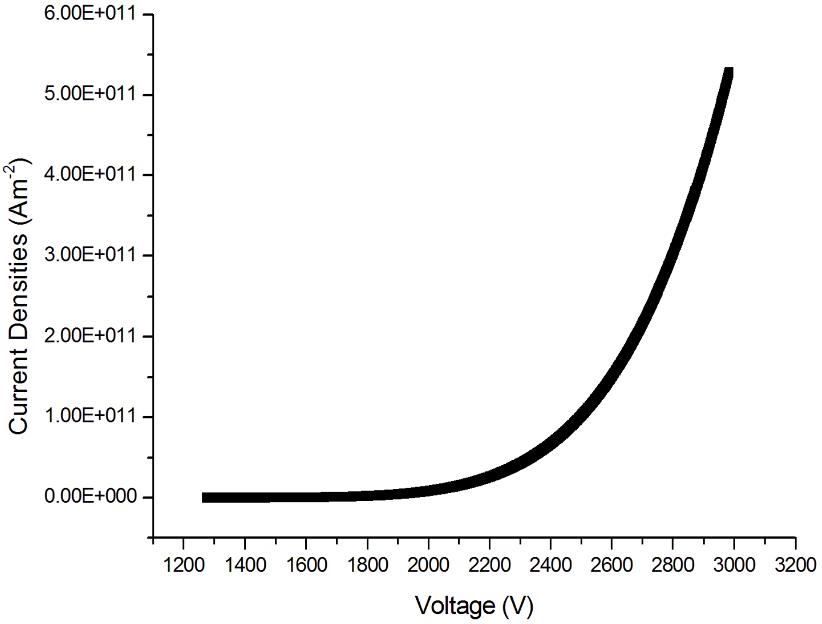

Figure 5.31: Current density vs. voltage for the ZrN thin film

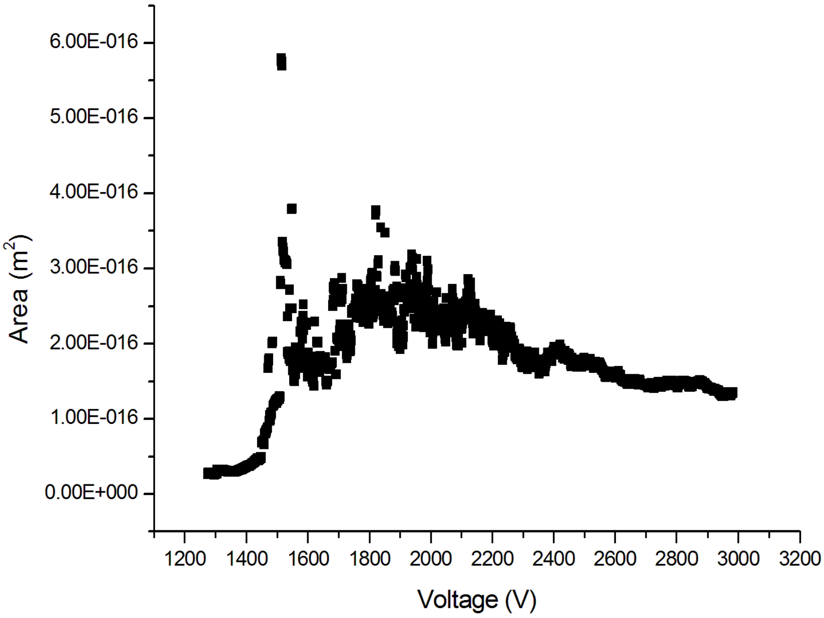

Figure 5.32: Emission area vs. voltage for the ZrN thin film

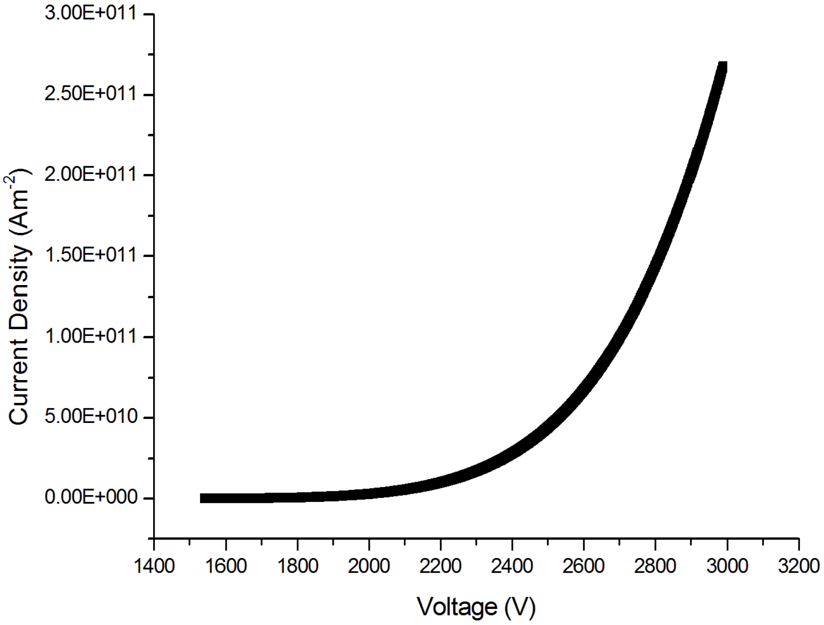

Figure 5.33: Current density vs. voltage for the ZrC thin film

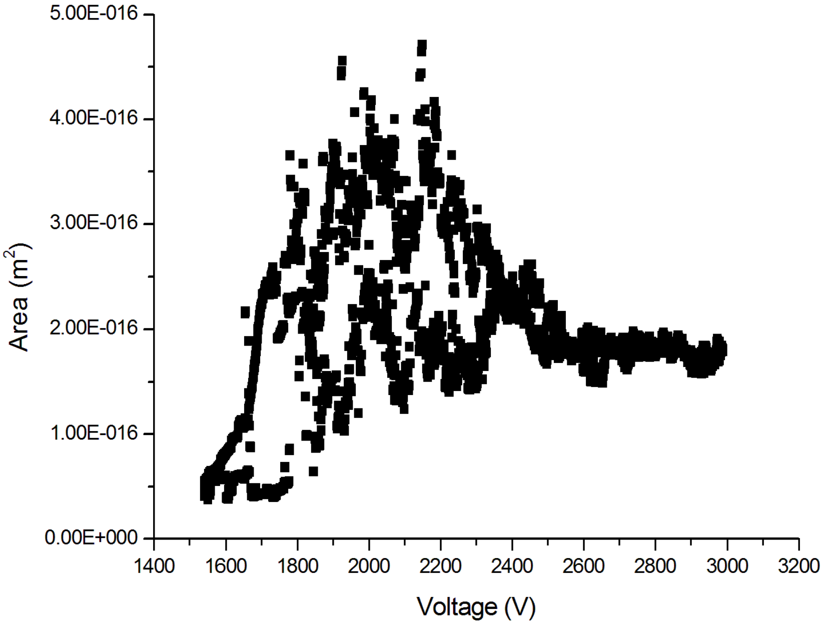

Figure 5.34: Emission area vs. voltage for the ZrC thin film

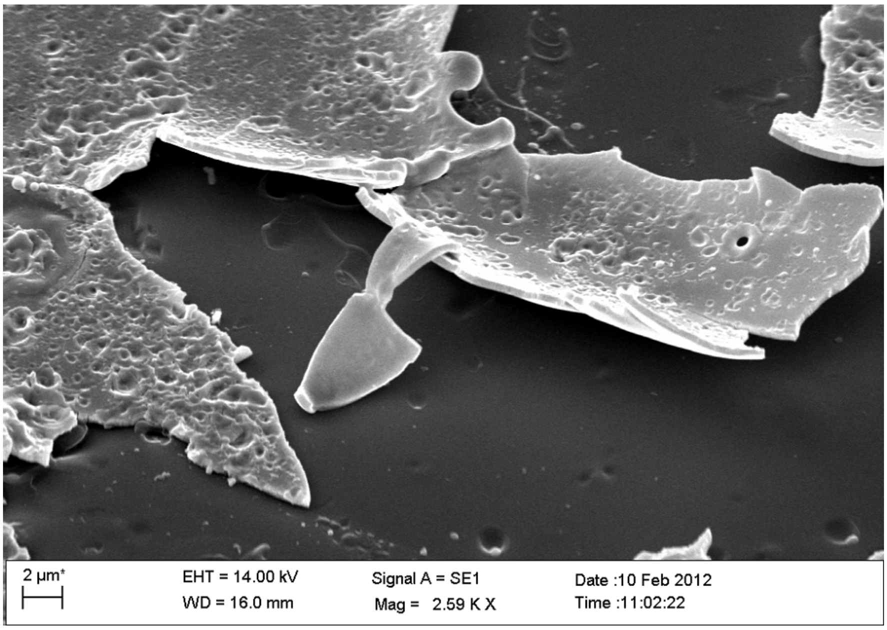

Figure 5.35: SEM image of the ZrN thin film at 30 ° observation angle

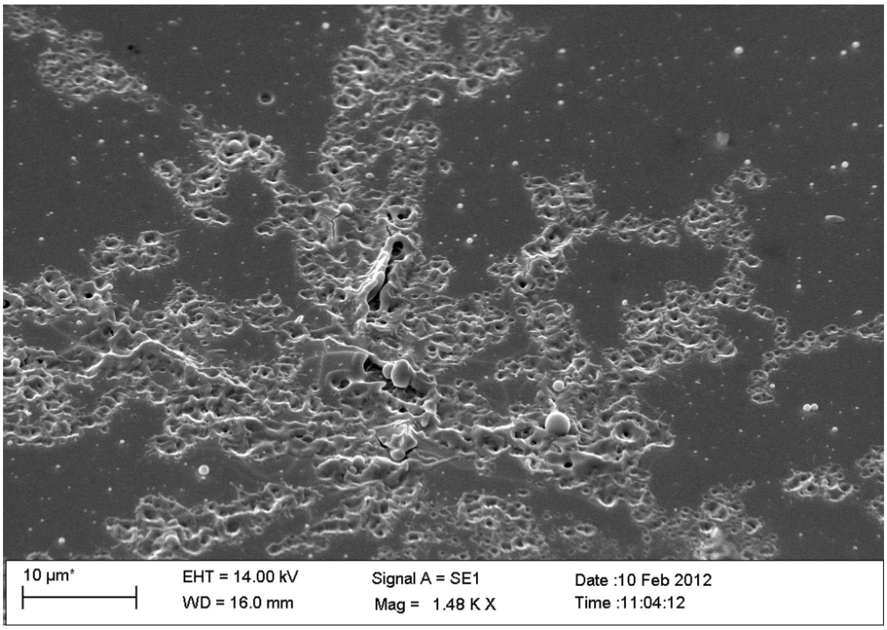

Figure 5.36: SEM image of the ZrN thin film at 30 ° observation angle

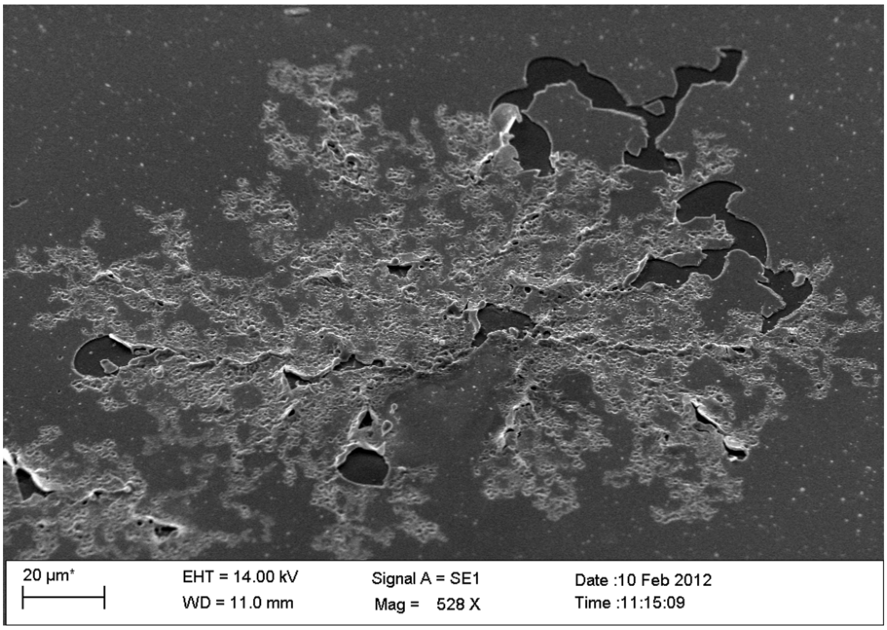

Figure 5.37: SEM image of the ZrN thin film at 30 ° observation angle

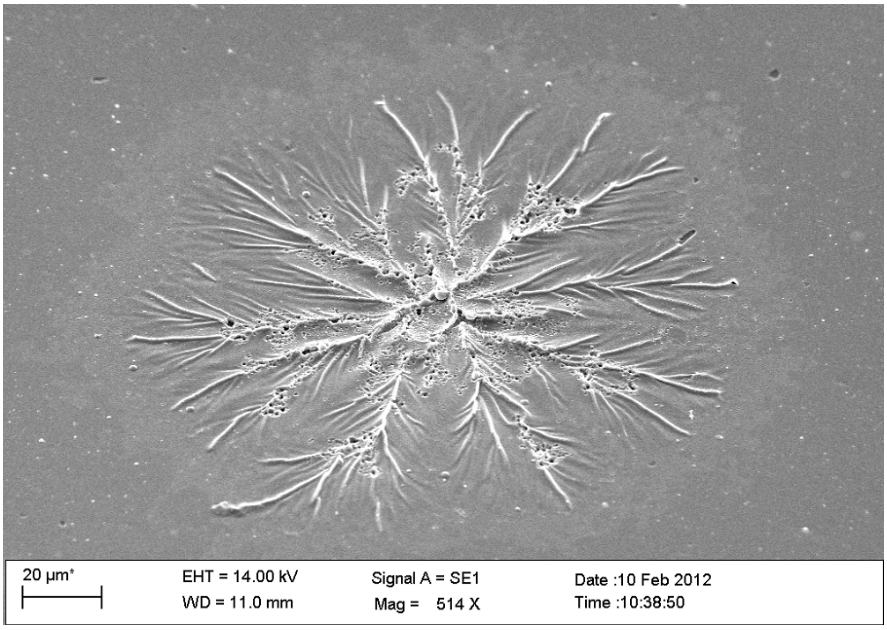

Figure 5.38: SEM image of the ZrC thin film at 30 ° observation angle

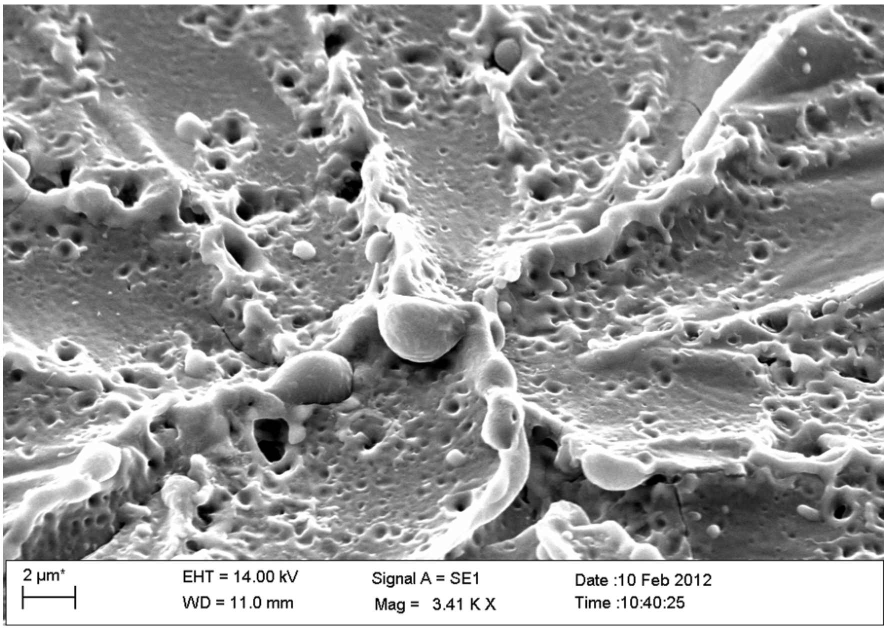

Figure 5.39: SEM image of the ZrC thin film at 30 ° observation angle

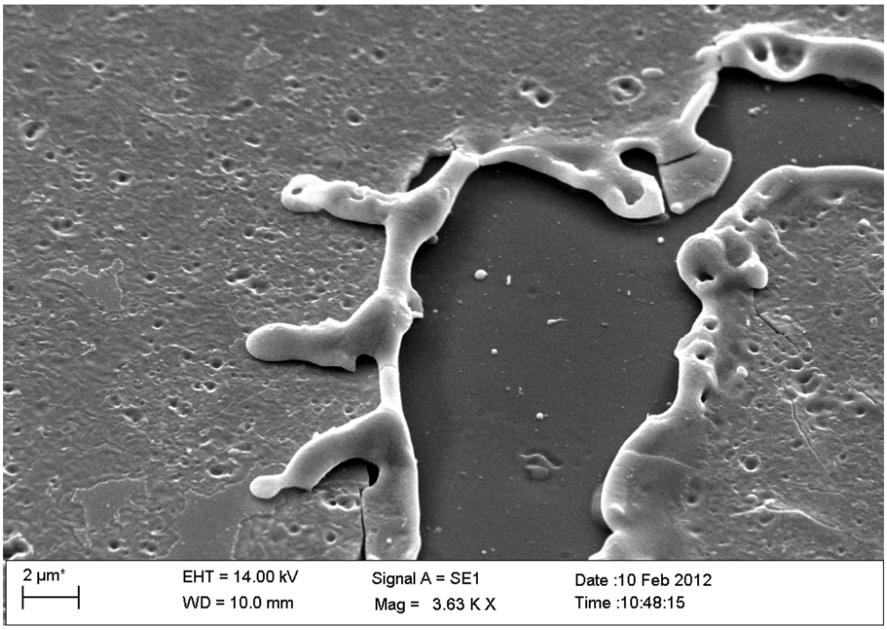

Figure 5.40: SEM image of the ZrC thin film at 30 ° observation angle

Chapter 6

Conclusions and Outlook

The work presented in this thesis is concerned with the field emission characterisation of zinc oxide nanostructures, with a view to their potential use in field emission applications, such as flexible displays or small x-ray sources. A system was designed and built during the course of this study to experimentally characterise the field emission properties of various samples, with either a stainless steel electrode or a transparent phosphor electrode, to investigate I-V characteristics or distribution and uniformity of emission, respectively. Results were presented from a number of ZnO nanostructures grown by vapour phase transport, chemical bath deposition, and pulsed laser deposition. A new treatment for analysing field emission results, based on recently discovered analytical approximations, was developed and applied to the data. Samples were also characterised with SEM and XRD.

A VPT and NSL grown ordered zinc oxide nanowire array was characterised, and the I-V data analysed using the treatment we have developed. A number of work function values were applied, based on a review of the values commonly used for zinc oxide in the literature. The enhancement factors determined experimentally were compared with values for a number of geometry based models. The agreement between experimental and modelled valuess was found to be poor, with hemi-ellipsoidal models giving closest agreement. The effect of shielding from neighbouring nanowires was estimated to be a reduction by ∼0.5 of the field enhancement factors. The treatment used provided values of the current density and emission area, which were on the order of 10^{11} $\mathrm{Am^{-2}}$ and 10^{-17} $\mathrm{m^2}$, respectively. These low area values may support the physical model according to which field emission takes place from an area of atomic dimensions at the tip of the emitter. Possible explanations for the 2-stage FN plot obtained, and frequently observed in the literature, were explored. Images of the transparent phosphor electrode at various voltages were presented and analysed, and the results contrasted with the I-V analysis. Estimates for the maximum and minimum number of emitters could be determined, and from this estimates of maximum and minimum values for the emission area and current density, ranging from $\sim 10^{-13}$ - 10^{-6} $\mathrm{m^2}$ and ~ 10 - 10^{7} $\mathrm{Am^{-2}}$, respectively. These values were then applied to the FN equation, to obtained estimates of the field enhancement factor, γ, which gave greater agreement with the modelled values than values determined from the I-V data.

The effect of inter-wire spacing of ordered zinc oxide nanowire arrays on their field emission properties was investigated for a number of samples grown by VPT and CBD, with NSL patterning. Our treatment was applied, giving current densities and emission areas of $\sim 10^{10}$ - 10^{13} $\mathrm{Am^{-2}}$, and $\sim 10^{-19}$ - 10^{-16} $\mathrm{m^2}$, respectively. The field enhancement factors (γ) determined were compared with the model of the effect of spacing on the field enhancement. The samples were found to show signs of damage after field emission testing. The distinct types of damage were investigated with SEM and discussed in the context of their potential to affect the field emission. The types of damage were classified into those are likely or unlikely to significantly affect the field emission. The samples which exhibited extensive melting damage were found to generally fail to agree with the model. Reasonable agreement with the model was found for samples that exhibited only minor melting damage.

The effect of doping on field emission properties was investigated for a number of PLD grown nanostructured columnar films. Depositions were carried out using a pure ZnO target for a variety of growth parameters to determine which gave the morphology most favourable for field emission testing. The best parameters were then used to grow 4 samples using 4 different targets: pure ZnO, ZnO with 0.02 wt% Al_2O_3, ZnO with 0.2 wt% Al_2O_3, and ZnO with 2 wt% Al_2O_3. The morphology of the 4 samples was found to be consistent using SEM. Increasing amounts of Al_2O_3 present in the target was correlated with increased electron concentration by measurement with a 4-point Hall effect probe, consistent with n-type doping. The field emission properties of the samples were characterised. Work functions were determined for the doped samples, on the assumption of a roughly equivalent surface morphology and an undoped work function of 3.7 eV, and found to be 5.51 eV, 5.35 eV, and 3.56 eV for the 0.02 wt%, 0.2 wt%, and 2 wt% samples, respectively. This did not agree with the expected trend of decreasing work function with increasing doping. Our treatment was applied to the data using these work function values to determine current densities and emission areas, which were found to be within typical range. The samples were examined with SEM after field emission testing, and found to have extensive signs of melting, which would disrupt the surface morphology, and may explain the deviation from expected behaviour.

The field emission properties of thin films of ZrN and ZrC were tested. The data were analysed in the context of planar emitters, and which gave unrealistic results. Work function values were assumed for the materials, and the field enhancement factors (γ), current densities, and emission areas determined. Despite the high melting points of both materials, they exhibited signs of melting and delamination after field emission testing. This gives a clear indication of the high temperatures reached during testing.

All samples tested exhibited melting to some degree after field emission testing. Such melting has been reported in the literature, and is generally considered to have negligible effect on the field emission. However, in our experiments we see both significant and insignificant melting. The scale of the largest disturbances, and their presence in materials of high melting point, suggest that these features are created during arcs between the sample and anode. Spindt [9] suggests these arcs proceed from a melting of tip releasing vapour which allows the arc to take place. Arcing could also be caused by the release of adsorbates from the emitter surface. In the most striking feature, the deposited material is completely removed, and the silicon substrate beneath melted, forming into a cone shape that resembles a Spindt valve. This sharply terminated cone shape is well suited to field emission. In cases where the cone is significantly lower than the surrounding material it is unlikely that it will contribute significantly to the emission current. However, in other cases the cone is approximately at the height of the nanowires or above. In these cases the cone may contribute significantly, or even dominate, the emission current.

Another consideration is the duration of conditioning a sample must undergo, before hysteresis-free, reproducible I-V data can be obtained. As previously stated, this is commonly attributed to adsorbates. Our results suggest that deformation of the emitters is also a factor. The number of 'cycles' of ramping up and down the voltage needed is on the order of hundreds, in most cases taking between one and two weeks of constant cycling.

There are some key avenues for further work. One such avenue would be to implement varied conditioning procedures on a number of similar samples, to investigate how best to minimise the time needed to obtain reliable data, and minimise the amount of and severity of melting damage caused during testing. Another possibility is the use of cleaning or treatment of samples before testing. If hysteresis is caused by adsorbates, their removal may reduce conditioning times, and also decrease the incidence of arcing. If arcing due to vapour released from melting tips is the source of major melting damage, annealing samples prior to testing may allow tips to melt safely, without risk of arcing. The apparatus could be augmented to include multiple electrodes, so that mulitple samples could be conditioned concurrently. Testing a reduced area could decrease conditioning time, for example by masking samples which would also allow for a greater degree of selection in choosing the area of the samples to test. Other avenues for future work include investigating the effect of surface treatments on field emission, plasma etching of nanospheres before silica deposition to adjust nanowire diameters for arrays of the same spacing, and investigation of larger spacings by use of larger nanospheres.

Bibliography

[1] R. Gomer. *Field Emission and Field Ionisation.* American Vacuum Society Classics, 1993.

[2] J. D. Carey. Engineering the next generation of large-area displays: prospects and pitfalls. *Philosophical Transactions of the Royal Society of London Series A-Mathematical Physical and Engineering Sciences*, 361(1813):2891–2907, 2003.

[3] S. Wang, X. Calderon, R. Peng, E. C. Schreiber, O. Zhou, and S. Chang. A carbon nanotube field emission multipixel x-ray array source for microradiotherapy application. *Applied Physics Letters*, 98(21):213701, 2011.

[4] C. J. Lee, T. J. Lee, S. C. Lyu, Y. Zhang, H. Ruh, and H. J. Lee. Field emission from well-aligned zinc oxide nanowires grown at low temperature. *Applied Physics Letters*, 81(19):3648–3650, 2002.

[5] R. W. Wood. *Phys Rev*, 5:1, 1897.

[6] R. H. Fowler and L. Nordheim. Electron emission in intense electric fields. *Proceedings of the Royal Society of London. Series A*, 119:173, 1928.

[7] A. G. J. Van Oostrum. *Phillips Res. Rep.*, Suppl. 1(1), 1966.

[8] F. Charbonnier. Developing and using the field emitter as a high intensity electron source. *Applied Surface Science*, 94-5:26–43, 1996.

[9] C. A. Spindt, I. Brodie, L. Humphrey, and E. R. Westerberg. Physical-properties of thin-film field-emission cathodes with molybdenum cones. *Journal of Applied Physics*, 47(12):5248–5263, 1976.

[10] X. Wang, J. Zhou, C. Lao, J. Song, N. Xu, and Z. L. Wang. In situ field emission of density-controlled zno nanowire arrays. *Advanced Materials*, 19(12):1627–+, 2007.

[11] A. C. Mofor, A. S. Bakin, B. Postels, M. Suleiman, A. Elshaer, and A. Waag. Growth of zno layers for transparent and flexible electronics. *Thin Solid Films*, 516(7):1401–1404, 2008.

[12] C. Sui, N. Chen, X. Xu, G. Wei, P. Cai, and H. Zhou. High-temperature-dependent optical properties of zno film on sapphire substrate. *Thin Solid Films*, 516(6):1137–1141, 2008.

[13] F. Pan, C. Song, X. J. Liu, Y. C. Yang, and F. Zeng. Ferromagnetism and possible application in spintronics of transition-metal-doped zno films. *Materials Science and Engineering R-Reports*, 62(1):1–35, 2008.

[14] Z. L. Wang. Zinc oxide nanostructures: growth, properties and applications. *Journal of Physics-Condensed Matter*, 16(25):R829–R858, 2004.

[15] M. S. Tyagi. *Introduction to Semiconductor Materials and Devices*. John Wiley and Sons, 1991.

[16] L. Liao, W. F. Zhang, H. B. Lu, J. C. Li, D. F. Wang, C. Liu, and D. J. Fu. Investigation of the temperature dependence of the field emission of zno nanorods. *Nanotechnology*, 18(22):225703, 2007.

[17] M. Herrera-Zaldivar, J. Valenzuela-Benavides, and U. Pal. Stm and sts characterization of zno nanorods. *Optical Materials*, 27(7):1276–1280, 2005.

[18] U. Ozgur, Y. I. Alivov, C. Liu, A. Teke, M. A. Reshchikov, S. Dogan, V. Avrutin, S. J. Cho, and H. Morkoc. A comprehensive review of zno materials and devices. *Journal of Applied Physics*, 98(4):041301, 2005.

[19] P. J. Brown and J. B. Forsyth. *The Crystal Structure of Solids*. Edward Arnold Ltd., 1973.

[20] Web elements.

[21] L. E. Greene, M. Law, D. H. Tan, M. Montano, J. Goldberger, G. Somorjai, and P. D. Yang. General route to vertical zno nanowire arrays using textured zno seeds. *Nano Letters*, 5(7):1231–1236, 2005.

[22] R. T. Kumar, E. McGlynn, C. McLoughlin, S. Chakrabarti, R. Smith, J. D. Carey, J. P. Mosnier, and M. O. Henry. Control of zno nanorod array density by zn supersaturation variation and effects on field emission. *Nanotechnology*, 18(21):215704, 2007.

[23] D. C. Look, D. C. Reynolds, J. W. Hemsky, R. L. Jones, and J. R. Sizelove. Production and annealing of electron irradiation damage in zno. *Applied Physics Letters*, 75(6):811–813, 1999.

[24] Q. Zhao, H. Z. Zhang, Y. W. Zhu, S. Q. Feng, X. C. Sun, J. Xu, and D. P. Yu. Morphological effects on the field emission of zno nanorod arrays. *Applied Physics Letters*, 86(20):203115, 2005.

[25] Y. H. Yang, B. Wang, N. S. Xu, and G. W. Yang. Field emission of one-dimensional micro- and nanostructures of zinc oxide. *Applied Physics Letters*, 89(4):043108, 2006.

[26] J. Singh, S. S. Patil, M. A. More, D. S. Joag, R. S. Tiwari, and O. N. Srivastava. Formation of aligned zno nanorods on self-grown zno template and its enhanced field emission characteristics. *Applied Surface Science*, 256(21):6157–6163, 2010.

[27] J. S. Jeong, J. Y. Lee, and H. K. Cho. Investigation of 2d/3d defects in controlled-growth oxygen-deficient zno nanowires and their field emission. *Chemical Physics Letters*, 503(4-6):266–271, 2011.

[28] L. Yao, M. Zheng, L. Ma, W. Li, M. Li, and W. Shen. Morphology-dependent field emission properties and wetting behavior of zno nanowire arrays. *Nanoscale Research Letters*, 6:74, 2011.

[29] T. Minami, T. Miyata, and T. Yamamoto. Work function of transparent conducting multicomponent oxide thin films prepared by magnetron sputtering. *Surface and Coatings Technology*, 108109(0):583–587, 1998.

[30] K. Jacobi, G. Zwicker, and A. Gutmann. Work function, electron affinity and band bending of zinc oxide surfaces. *Surface Science*, 141(1):109–125, 1984.

[31] J. Marien. Field-emission study of specificity of zinc-oxide polar surfaces (0001) and (000-bar1) - work function and hydrogen adsorption. *Physica Status Solidi A-Applied Research*, 38(2):513–522, 1976.

[32] C. F. Klingshirn, B. K. Meyer, A. Waag, and A. Hoffman. *Zinc Oxide: From Fundamental Properties Towards Novel Applications.* Springer, Berlin, 2010.

[33] Z. Q. Yu, Y. Zhang, C. M. Wang, V. Shutthanandan, I. V. Lyubinetsk, M. H. Engelhard, Ln Saraf, D. E. McCready, C. H. Henager Jr.,

P. Nachimuthu, and S. Thevuthasan. Synthesis and characterization of compositionally graded si1-xgex layers on si substrate. *Nuclear Instruments and Methods in Physics Research Section B-Beam Interactions with Materials and Atoms*, 261(1-2):723–726, 2007.

[34] V. Semet, V. T. Binh, T. Pauporte, L. Joulaud, and F. J. Vermersch. Field emission behavior of vertically aligned zno nanowire planar cathodes. *Journal of Applied Physics*, 109(5):054301, 2011.

[35] M. Biswas, E. McGlynn, M. O. Henry, M. McCann, and A. Rafferty. Carbothermal reduction vapor phase transport growth of zno nanostructures: Effects of various carbon sources. *Journal of Applied Physics*, 105(9):094306, 2009.

[36] Z. M. Zhu, T. L. Chen, Y. Gu, J. Warren, and R. M. Osgood. Zinc oxide nanowires grown by vapor-phase transport using selected metal catalysts: A comparative study. *Chemistry of Materials*, 17(16):4227–4234, 2005.

[37] R. T. R. Kumar, E. McGlynn, M. Biswas, R. Saunders, G. Trolliard, B. Soulestin, J. R Duclere, J. P. Mosnier, and M. O. Henry. Growth of zno nanostructures on au-coated si: Influence of growth temperature on growth mechanism and morphology. *Journal of Applied Physics*, 104(8):084309, 2008.

[38] R. T. R. Kumar, E. McGlynn, C. McLoughlin, S. Chakrabarti, R. C. Smith, J. D. Carey, J. P. Mosnier, and M. O. Henry. Control of zno nanorod array density by zn supersaturation variation and effects on field emission. *Nanotechnology*, 18(21):215704, 2007.

[39] D. F. Liu, Y. J. Xiang, X. C. Wu, Z. X. Zhang, L. F. Liu, L. Song, X. W.

Zhao, S. D. Luo, W. J. Ma, J. Shen, W. Y. Zhou, G. Wang, C. Y. Wang, and S. S. Xie. Periodic zno nanorod arrays defined by polystyrene microsphere self-assembled monolayers. *Nano Letters*, 6(10):2375–2378, 2006.

[40] D. Lan, Y. Zhang, and Y. Wang. From hexagonally arrayed nanorods to ordered porous film through controlling the morphology of zno crystals. *Applied Surface Science*, 254(18):5849–5853, 2008.

[41] S. Zoppel, H. Huber, and G. A. Reider. Selective ablation of thin mo and tco films with femtosecond laser pulses for structuring thin film solar cells. *Applied Physics A-Materials Science and Processing*, 89(1):161–163, 2007.

[42] B. Doggett, S. Chakrabarti, R. O'Haire, A. Meaney, E. McGlynn, M. O. Henry, and J. P. Mosnier. Electrical characterisation of phosphorus-doped zno thin films grown by pulsed laser deposition. *Superlattices and Microstructures*, 42(1-6):74–78, 2007.

[43] T. Premkumar, Y. S. Zhou, Y. F. Lu, and K. Baskar. Optical and field-emission properties of zno nanostructures deposited using high-pressure pulsed laser deposition. *Acs Applied Materials and Interfaces*, 2(10):2863–2869, 2010.

[44] L. C. Tien, S. J. Pearton, D. P. Norton, and F. Ren. Synthesis and microstructure of vertically aligned zno nanowires grown by high-pressure-assisted pulsed-laser deposition. *Journal of Materials Science*, 43(21):6925–6932, 2008.

[45] Y. Sun, K. E. Addison, and M. N. R. Ashfold. Growth of arrays of

al-doped zno nanocones by pulsed laser deposition. *Nanotechnology*, 18(49):495601, 2007.

[46] S. Kahraman, F. Bayansal, H. A. Cetinkara, H. M. Cakmak, and H. S. Guder. Characterization of cbd grown zno films with high c-axis orientation. *Materials Chemistry and Physics*, 134(2-3):1036–1041, 2012.

[47] S. H. Yi, S. K. Choi, J. M. Jang, J. A. Kim, and W. G. Jung. Low-temperature growth of zno nanorods by chemical bath deposition. *Journal of colloid and interface science*, 313(2):705–710, 2007.

[48] S. L. Cheng, S. L. Wong, S. W. Lu, and H. Chen. Large-area co-silicide nanodot arrays produced by colloidal nanosphere lithography and thermal annealing. *Ultramicroscopy*, 108(10):1200–1204, 2008.

[49] J. C. Hulteen and R. P. Vanduyne. Nanosphere lithography - a materials general fabrication process for periodic particle array surfaces. *Journal of Vacuum Science and Technology A-Vacuum Surfaces and Films*, 13(3):1553–1558, 1995.

[50] X. Zhang, D. Liu, L. Zhang, W. Li, M. Gao, W. Ma, Y. Ren, Q. Zeng, Z. Niu, W. Zhou, and S. Xie. Synthesis of large-scale periodic zno nanorod arrays and its blue-shift of uv luminescence. *Journal of Materials Chemistry*, 19(7):962–969, 2009.

[51] X. Zhang, D. Liu, L. Zhang, W. Li, M. Gao, W. Ma, Y. Ren, Q. Zeng, Z. Niu, W. Zhou, and S. Xie. Synthesis of large-scale periodic zno nanorod arrays and its blue-shift of uv luminescence. *Journal of Materials Chemistry*, 19(7):962–969, 2009.

[52] D. Byrne, E. McGlynn, J. Cullen, and M. O. Henry. A catalyst-free

and facile route to periodically ordered and c-axis aligned zno nanorod arrays on diverse substrates. *Nanoscale*, 3(4):1675–1682, 2011.

[53] H. J. Fan, B. Fuhrmann, R. Scholz, F. Syrowatka, A. Dadgar, A. Krost, and M. Zacharias. Well-ordered zno nanowire arrays on gan substrate fabricated via nanosphere lithography. *Journal of Crystal Growth*, 287(1):34–38, 2006.

[54] N. D. Lang and W. Kohn. Theory of metal surfaces - work function. *Physical Review B*, 3(4):1215–and, 1971.

[55] O. W. Richardson. *Proc. Roy. Soc. A*, 117:719, 1928.

[56] N. A. de Bruyne. *Proc. Roy. Soc. A*, 120:423, 1928.

[57] E. L. Murphy and R. H. Good. *Phys. Rev.*, 102:1464, 1956.

[58] V. Sahni and K. P. Bohnen. Image charge at a metal-surface. *Physical Review B*, 31(12):7651–7661, 1985.

[59] L. W. Nordheim. The effect of the image force on the emission and reflexion of electrons by metals. *Proc. Roy. Soc. London A*, 121(788):626, 1928.

[60] S. C. Miller and R. H. Good. A wkb-type approximation to the schrodinger equation. *Physical Review*, 91(1):174–179, 1953.

[61] A. Modinos. *Field, Thermionic, and Secondary Electron Emission Spectroscopy.* Plenum Press, New York and London, 1984.

[62] F. M. Charbonnier and E. E. Martin. Simple method for deriving, from measured i(v) data, information on geometry of a field emission current source of unknown characteristics. *Journal of Applied Physics*, 33(5):1897–and, 1962.

[63] R. G. Forbes. Simple good approximations for the special elliptic functions in standard fowler-nordheim tunneling theory for a schottky-nordheim barrier. *Applied Physics Letters*, 89(11):113122, 2006.

[64] G. Ulisse, F. Brunetti, A. Vomiero, M. M. Natile, G. Sberveglieri, and A. Di Carlo. Hybrid thermal-field emission of zno nanowires. *Applied Physics Letters*, 99(24):243108, 2011.

[65] E. L. Murphy and R. H. Good. Thermionic emission, field emission, and the transition region. *Physical Review*, 102(6):1464–1473, 1956.

[66] W. B. Nottingham. Remarks on energy losses attending thermionic emission of electrons from metals. *Phys. Rev.*, 59:907, 1941.

[67] F. M. Charbonnier, R. W. Strayer, L. W. Swanson, and E. E. Martin. Nottingham effect in field and t-f emission: heating and cooling domains, and inversion temperature. *Phys. Rev. Lett.*, 13(13):397, 1964.

[68] J. Paulini, T. Klein, and G. Simon. Thermo-field emission and the nottingham effect. *Journal of Physics D-Applied Physics*, 26(8):1310–1315, 1993.

[69] A. A. Al-Tabbakh, M. A. More, D. S. Joag, I. S. Mulla, and V. K. Pillai. The fowler-nordheim plot behavior and mechanism of field electron emission from zno tetrapod structures. *Acs Nano*, 4(10):5585–5590, 2010.

[70] A. A. Al-Tabbakh, M. A. More, D. S. Joag, N. S. Ramgir, I. S. Mulla, and V. K. Pillai. Energy analysis of field emitted electrons from a zno tetrapod. *Applied Physics Letters*, 90(16):162102, 2007.

[71] G. Fursey. *Field Emission in Vacuum Microelectronics.* Kluwer Academic/Plenum Publishers, New York, 2005.

[72] Z. Zhang and J. T. Yates. Band bending in semiconductors: Chemical and physical consequences at surfaces and interfaces. *Chemical reviews*, 112(10):5520–5551, 2012.

[73] H. Z. Zhang, R. M. Wang, and Y. W. Zhu. Effect of adsorbates on field-electron emission from zno nanoneedle arrays. *Journal of Applied Physics*, 96(1):624–628, 2004.

[74] W. L. Bragg. The diffraction of short electromagnetic waves by a crystal. *Proceedings of the Cambridge Philosophical Society*, 17:43, 1913.

[75] Z. Q. Yu, Y. Zhang, C. M. Wang, V. Shutthanandan, I. V. Lyubinetsky, M. H. Engelhard, L. V. Saraf, D. E. McCready, C. H. Henager Jr., P. Nachimuthu, and S. Thevuthasan. Synthesis and characterization of compositionally graded si1xgex layers on si substrate. *Nuclear Instruments and Methods in Physics Research Section B: Beam Interactions with Materials and Atoms*, 261(12):723–726, 2007.

[76] B. H. Hwang. Calculation and measurement of all (002) multiple diffraction peaks from a (001) silicon wafer. *Journal of Physics D-Applied Physics*, 34(16):2469–2474, 2001.

[77] A. Bogner, P. H Jouneau, G. Thollet, D. Basset, and C. Gauthier. A history of scanning electron microscopy developments: Towards "wet-stem" imaging. *Micron*, 38(4):390–401, 2007.

[78] J. M. Bonard, K. A. Dean, B. F. Coll, and C. Klinke. Field emission of individual carbon nanotubes in the scanning electron microscope. *Physical Review Letters*, 89(19):197602, 2002.

[79] A. Rahm, M. Lorenz, T. Nobis, G. Zimmermann, M. Grundmann, B. Fuhrmann, and F. Syrowatka. Pulsed-laser deposition and charac-

terization of zno nanowires with regular lateral arrangement. *Applied Physics A-Materials Science and Processing*, 88(1):31–34, 2007.

[80] L. Chen, J. Huang, Z. Ye, H. He, Y. Zeng, S. Wang, and H. Wu. Controllable synthesis of ordered zno nanodots arrays by nanosphere lithography. *Crystal Growth and Design*, 8(8):2917–2920, 2008.

[81] L. Chen, J. Huang, Z. Ye, H. He, Y. Zeng, S. Wang, and H. Wu. Controllable synthesis of ordered zno nanodots arrays by nanosphere lithography. *Crystal Growth and Design*, 8(8):2917–2920, 2008.

[82] Z. M. Xiao, J. C. She, Z. B. Li, Y. H. Yang, G. W. Yang, S. Z. Deng, J. Chen, and N. S. Xu. Oscillating current observed in field emission from a single zinc oxide nanostructure and the physical mechanism. *Journal of Applied Physics*, 106(1):014310, 2009.

[83] D. A. Kirkpatrick, A. Mankofsky, and K. T. Tsang. Analysis of field-emission from 3-dimensional structures. *Applied Physics Letters*, 60(17):2065–2067, 1992.

[84] F. H. Read and N. J. Bowring. Field enhancement factors of random arrays of carbon nanotubes. *Nuclear Instruments and Methods in Physics Research Section A-Accelerators Spectrometers Detectors and Associated Equipment*, 519(1-2):305–314, 2004.

[85] R. G. Forbes, C. J. Edgcombe, and U. Valdre. Some comments on models for field enhancement. *Ultramicroscopy*, 95(1-4):57–65, 2003.

[86] R. G. Forbes and K. L. Jensen. New results in the theory of fowler-nordheim plots and the modelling of hemi-ellipsoidal emitters. *Ultramicroscopy*, 89(1-3):17–22, 2001.

[87] D. Byrne, E. McGlynn, K. Kumar, M. Biswas, M. O. Henry, and

G. Hughes. A study of drop-coated and chemical bath-deposited buffer layers for vapor phase deposition of large area, aligned, zinc oxide nanorod arrays. *Crystal Growth and Design*, 10(5):2400–2408, 2010.

[88] J. S. Suh, K. S. Jeong, J. S. Lee, and I. T. Han. Study of the field-screening effect of highly ordered carbon nanotube arrays. *Applied Physics Letters*, 80(13):2392–2394, 2002.

[89] S. H. Jeong, S. Kno, D. Jung, S. B. Lee, and J. H. Boo. Deposition of aluminum-doped zinc oxide films by rf magnetron sputtering and study of their surface characteristics. *Surface and Coatings Technology*, 174:187–192, 2003.

[90] R. N. Gayen, S. Dalui, A. Rajaram, and A. K. Pal. Modulation of field emission properties of vertically aligned zno nanorods with aspect ratio and number density. *Applied Surface Science*, 255(9):4902–4906, 2009.

[91] T. E. Stern, B. S. Gossling, and R. H. Fowler. *Proc. Roy. Soc. London A*, 124:699, 1929.

[92] P. H. Cutler, J. He, J. Miller, N. M. Miskovsky, B. Weiss, and T. E. Sullivan. Theory of electron-emission in high fields from atomically sharp emitters - validity of the fowler-nordheim equation. *Progress in Surface Science*, 42(1-4):169–185, 1993.

[93] P. H. Cutler, J. He, N. M. Miskovsky, T. E. Sullivan, and B. Weiss. Theory of electron-emission in high fields from atomically sharp emitters - validity of the fowler-nordheim equation. *Journal of Vacuum Science and Technology B*, 11(2):387–391, 1993.

[94] G. N. Fursey and D. V. Glazanov. Deviations from the fowler-nordheim theory and peculiarities of field electron emission from small-scale ob-

jects. *Journal of Vacuum Science and Technology B*, 16(2):910–915, 1998.

[95] R. G. Forbes. Use of the concept "area efficiency of emission" in equations describing field emission from large-area electron sources. *Journal of Vacuum Science and Technology B*, 27(3):1200–1203, 2009.

[96] Q. Ahsanulhaq, J. H. Kim, and Y. B. Hahn. Controlled selective growth of zno nanorod arrays and their field emission properties. *Nanotechnology*, 18(48):485307, 2007.

[97] Y. Nakayama and S. Akita. Field-emission device with carbon nanotubes for a flat panel display. *Synthetic Metals*, 117(1-3):207–210, 2001.

[98] S. C. Wang and B. C. Huang. Field emission properties of ag/sio2/carbon nanotube films by pulsed voltage co-electrophoretic deposition. *Thin Solid Films*, 517(3):1245–1250, 2008.

[99] M. Nagao, K. Utsumi, Y. Gotoh, H. Tsuji, J. Ishikawa, T. Nakatani, T. Sakashita, and K. Betsui. Dependence of emission characteristics of spindt-type field emitters on cathode material. *Applied Surface Science*, 146(1-4):182–186, 1999.

[100] N. Gopalakrishnan, B. C. Shin, H. S. Lim, T. Balasubramanian, and Y. S. Yu. Effect of gan doping on zno films by pulsed laser deposition. *Materials Letters*, 61(11-12):2307–2310, 2007.

[101] S. S. Lin, Z. Z. Ye, J. G. Lu, H. P. He, L. X. Chen, X. Q. Gu, J. Y. Huang, L. P. Zhu, and B. H. Zhao. Na doping concentration tuned conductivity of zno films via pulsed laser deposition and electrolumines-

cence from zno homojunction on silicon substrate. *Journal of Physics D-Applied Physics*, 41(15):155114, 2008.

[102] A. Wang, Z. Zhong, C. Lu, L. Lv, X. Wang, and B. Zhang. Study on field-emission characteristics of electrodeposited co-doped zno thin films. *Physica B-Condensed Matter*, 406(5):1049–1052, 2011.

[103] Y. Huang, Y. Zhang, Y. Gu, X. Bai, J. Qi, Q. Liao, and J. Liu. Field emission of a single in-doped zno nanowire. *Journal of Physical Chemistry C*, 111(26):9039–9043, 2007.

[104] M. Ahmad, H. Sun, and J. Zhu. Enhanced photoluminescence and field-emission behavior of vertically well aligned arrays of in-doped zno nanowires. *Acs Applied Materials and Interfaces*, 3(4):1299–1305, 2011.

[105] Y. Kim and S. Kang. Aluminum-doped zno nanorod array by thermal diffusion process. *Materials Letters*, 63(12):1065–1067, 2009.

[106] R. Eason. *Pulsed Laser Deposition of Thin Films.* John Wiley and Sons, New Jersey, 2007.

[107] M. Lorenz, R. Johne, T. Nobis, H. Hochmuth, J. Lenzner, M. Grundmann, H. P. D. Schenk, S. I. Borenstain, A. Schon, C. Bekeny, T. Voss, and J. Gutowski. Fast, high-efficiency, and homogeneous room-temperature cathodoluminescence of zno scintillator thin films on sapphire. *Applied Physics Letters*, 89(24):243510, 2006.

[108] M. Lorenz, H. Hochmuth, J. Lenzner, T. Nobis, G. Zimmermann, M. Diaconu, H. Schmidt, H. von Wenckstern, and M. Grundmann. Room-temperature cathodoluminescence of n-type zno thin films grown by pulsed laser deposition in n-2, n2o, and o-2 background gas. *Thin Solid Films*, 486(1-2):205–209, 2005.

[109] M. Kawakami, AB Hartanto, Y. Nakata, and T. Okada. Synthesis of zno nanorods by nanoparticle assisted pulsed-laser deposition. *Japanese Journal of Applied Physics Part 2-Letters*, 42(1A-B):L33–L35, 2003.

[110] M. Lorenz, E. M. Kaidashev, A. Rahm, T. Nobis, J. Lenzner, G. Wagner, D. Spemann, H. Hochmuth, and M. Grundmann. Mgxzn1-xo (0 ¡= x ¡ 0.2) nanowire arrays on sapphire grown by high-pressure pulsed-laser deposition. *Applied Physics Letters*, 86(14):143113, 2005.

[111] T. Premkumar, P. Manoravi, K. Panigrahi, and K. Baskar. Particulate assisted growth of zno nanorods and microrods by pulsed laser deposition. *Applied Surface Science*, 255(15):6819–6822, 2009.

[112] T. Minami, Y. Ohtani, T. Miyata, and T. Kuboi. Transparent conducting al-doped zno thin films prepared by magnetron sputtering with dc and rf powers applied in combination. *Journal of Vacuum Science and Technology a*, 25(4):1172–1177, 2007.

[113] M. J. Alam and D. C. Cameron. Preparation and properties of transparent conductive aluminum-doped zinc oxide thin films by sol-gel process. *Journal of Vacuum Science and Technology A-Vacuum Surfaces and Films*, 19(4):1642–1646, 2001.

[114] C. P. Constable, J. Yarwood, and W. D. Munz. Raman microscopic studies of pvd hard coatings. *Surface and Coatings Technology*, 116:155–159, 1999.

[115] R. Hubler, A. Cozza, T. L. Marcondes, R. B. Souza, and F. F. Fiori. Wear and corrosion protection of 316-l femoral implants by deposition of thin films. *Surface and Coatings Technology*, 142:1078–1083, 2001.

[116] D. F. Arias, Y. C. Arango, and A. Devia. Study of tin and zrn thin films grown by cathodic arc technique. *Applied Surface Science*, 253(4):1683–1690, 2006.

[117] G. W. C. Silva, A. A. Kercher, J. D. Hunn, R. C. Martin, G. E. Jellison, and H. M. Meyer. Characterization of zirconium carbides using electron microscopy, optical anisotropy, auger depth profiles, x-ray diffraction, and electron density calculated by charge flipping method. *Journal of Solid State Chemistry*, 194:91–99, 2012.

[118] J. Vetter and R. Rochotzki. Tribological behavior and mechanical-properties of physical-vapor-deposited hard coatings - tinx, zrnx, ticx, ticx i-c. *Thin Solid Films*, 192(2):253–261, 1990.

[119] S. Kanamori. Investigation of reactively sputtered tin films for diffusion-barriers. *Thin Solid Films*, 136(2):195–214, 1986.

[120] B. Karlsson, R. P. Shimshock, B. O. Seraphin, and J. C. Haygrath. Optical-properties of cvd-coated tin, zrn and hfn. *Physica Scripta*, 25(6):775–779, 1982.

[121] W. A. Mackie, R. L. Hartman, M. A. Anderson, and P. R. Davis. Transition-metal carbides for use as field-emission cathodes. *Journal of Vacuum Science and Technology B*, 12(2):722–726, 1994.

[122] G. W. C. Silva, A. A. Kercher, J. D. Hunn, R. C. Martin, G. E. Jellison, and H. M. Meyer. Characterization of zirconium carbides using electron microscopy, optical anisotropy, auger depth profiles, x-ray diffraction, and electron density calculated by charge flipping method. *Journal of Solid State Chemistry*, 194:91–99, 2012.